UNIVERSITY OF SOUTHAMPTON

FACULTY OF PHYSICAL AND APPLIED SCIENCES

Optoelectronics Research Centre

Novel Optical Fibre Fabrication Techniques for Yb-doped High-Power Fibre Lasers and Sensing Applications

by Andrew Simon Webb

Submitted for the degree of Doctor of Philosophy

March 2012

UNIVERSITY OF SOUTHAMPTON

ABSTRACT

FACULTY OF PHYSICAL AND APPLIED SCIENCES

Optoelectronics Research Centre

Doctor of Philosophy

NOVEL OPTICAL FIBRE FABRICATION TECHNIQUES FOR Yb-DOPED HIGH-POWER FIBRE LASERS AND SENSING APPLICATIONS

by Andrew Simon Webb

The work presented in this thesis reports on four novel techniques for fabricating speciality silica preforms and optical fibres. The project aims were to conceive new fabrication methods by adapting conventional Modified Chemical Vapour Deposition (MCVD) and optical fibre drawing equipment, and to demonstrate fibre devices for ytterbium (Yb)-doped high-power fibre lasers (HPFL) and optical sensing applications.

Firstly, a new *in-situ solution doping* technique is presented for fabricating actively-doped fibre-preforms of complex design. The fabrication and characterisation of several multilayered rare-earth (RE)-doped fibres suitable for HPFL applications are reported, including an Yb-doped (>18,000 ppm, by weight) fibre with a low effective-NA, which incorporates a pedestal refractive index profile and a unique aluminosilcate (Al:Si) inner-cladding. The vapour-phase deposition of RE ions in fibre-preforms has also been demonstrated using a novel *chemical-in-crucible* process that is intended for use with precursors of low volatility. Modifications to the standard MCVD setup were made which allows the dopant source to be placed within the substrate glassware and in close proximity to the reaction zone. Preforms with dopant concentrations of up to 25,000 ppm (by weight) of Yb^{3+} ions have been attained using an organometallic precursor, whilst passive Al:Si preforms containing >16 mol% of Al have been achieved using gaseous aluminium chloride.

A straightforward fabrication technique for producing silica *suspended-core holey fibre* (SC-HF) is also presented. The drawn fibre exhibits a relatively low optical loss (of 0.3 $dB.m^{-1}$ at $\lambda = 1550$ nm), and the high air-filling fraction, which was predicted as ~30 % (for a core size of 0.8 µm), is believed to the highest reported value at the time the work was undertaken. The sensing capability of SC-HF has been demonstrated by constructing an all-fibre acetylene-filled gas cell. The final experimental chapter describes the first example of a novel *flat fibre* concept. Extended lengths of low-loss planar glass substrates were produced using MCVD and conventional fibre drawing equipment. In combination with direct UV-writing, multifunctional planar waveguiding devices can be fabricated that are mechanically flexible. The potential of the flat fibre platform for sensing applications is discussed.

The reported fabrication techniques have been implemented through the successful demonstration of several fibre devices suitable for Yb-doped HPFLs and optical sensing applications. The developed techniques have future potential in industry and manufacturing, and it is anticipated that the work presented will enable fibres with novel properties and glass compositions to be researched.

Contents

Academic Thesis: Declaration Of Authorship

I, **Andrew Simon Webb** …………………………………………. [please print name]

declare that this thesis and the work presented in it are my own and has been generated by me as the result of my own original research.

Thesis title: **Novel Optical Fibre Fabrication Techniques for Yb-doped High-Power Fibre Lasers and Sensing Applications**

I confirm that:

1. This work was done wholly or mainly while in candidature for a research degree at this University;

2. Where any part of this thesis has previously been submitted for a degree or any other qualification at this University or any other institution, this has been clearly stated;

3. Where I have consulted the published work of others, this is always clearly attributed;

4. Where I have quoted from the work of others, the source is always given. With the exception of such quotations, this thesis is entirely my own work;

5. I have acknowledged all main sources of help;

6. Where the thesis is based on work done by myself jointly with others, I have made clear exactly what was done by others and what I have contributed myself;

7. Either none of this work has been published before submission, or parts of this work have been published as: [please list references below]:

Signed:…………………………………………………………………………………

Date: ……………………………………………………………………………….

Acknowledgements

My PhD studies and employment at the Optoelectronics Research Centre have been inextricably linked from day one, and I therefore owe thanks to all members of the ORC who have assisted and contributed to my progression over the years.

It is a pleasure to thank all of the Silica group members, both past and present. In particular, Alex Boyland and Laurence Cooper, who I have worked and studied alongside for much of my time at the ORC, and who have provided a soundboard for ideas, thoughts, and frustrations – and to Rob Standish, who has remained the steadfast technician of the Silica group. I am sincerely grateful to Seongwoo Yoo for providing the laser-based fibre results, and to the latest addition to the Silica flock – Tim May-Smith – whose proof-reading and editorial guidance ensured that this thesis finally reached fruition! My special thanks go to my supervisor Jayanta Sahu for allowing me to pursue this PhD alongside the frenzy that is the daily workings of the Silica group, and without whose support none of this would have been possible.

For their practical contributions and scientific input, I would like to show my gratitude to Rafiq Adikan, James Gates, Sumiaty Ambran, Francesco Poletti and Anna Peacock – and it would be a travesty not to acknowledge Ed Weatherby, Kenton Knight, Neil Sessions, and Mark Lessey for their eclectic mix of technical support, hindrance, and amusement since I started at the ORC.

Finally, I would like to acknowledge the unwavering patience and support of my partner Zoë – and last, but by no means least, to my parents for their encouragement and ceaseless attempts to try and understand exactly what it is that I do, which will no doubt continue beyond this work.

Chapter 1

Introduction

1.1 History of optical fibre fabrication

In 1970, researchers at Corning Glass Works published their seminal paper on low-loss optical fibres [1]. The concept of transmitting light through glass had been known for many years, but it was not until a pivotal report a few years earlier by Kao et al. [2], that research into high-purity glasses intensified. Kao et al. predicted that the impurities in silica-based glass could be reduced sufficiently to produce waveguides with an attenuation of less than 20 $dB.km^{-1}$; a threshold that was, at the time, considered practical for optical communications.

The fabrication method that Corning Glass Works used involved high-temperature oxidation of precursor vapours to form glassy soot particles that were deposited on the outside of target rod, a process known as Outside Vapour Deposition (OVD) [3]. The soot body that was formed was subsequently consolidated and drawn into low-loss optical fibre. In 1974, John MacChesney and co-workers at Bell Laboratories [4] published a modified process for fabricating high-purity glass, a process that was also being investigated by David Payne and Alec Gambling at the University of Southampton [5] and was called Modified Chemical Vapour Deposition (MCVD).

MCVD utilises a similar vapour-phase reaction of silica precursors to that of OVD, but the optically transparent glass layers are deposited in a single step on the inside of a cylindrical glass tube. Although the OVD process supplied the increased demand for optical fibre at the time, it is MCVD that is most widely used for preform manufacture today.

Whilst MCVD technology was still in its infancy, an alternative fibre structure that featured micron-scale air holes running along its length was being explored, again for the purpose of optical data transmission [6]. These early microstructured optical fibres consisted of a solid silica core supported by two or more thin membranes. Unlike the germanium-doped fibres produced by Corning Glass Works, microstructured fibres were fabricated from a single-material (silica) and were also capable of attaining low-loss levels similar to those achieved by OVD. The promising, yet challenging, fabrication route of microstructured optical fibres was soon overshadowed by the low-loss fibres that were possible using the MCVD process, and the relative ease in which the technique could be implemented.

However, in 1996 there was a resurgence in the field of microstructured fibres, largely pioneered by Philip Russell and the advent of the stack-and-draw technique [7]. The emphasis had shifted to the tantalising optical guidance properties that these exotic fibres could offer, which were difficult to achieve with any other types of fibre. Modern microstructured fibres now comprise of an intricate array of holes, with their size and placement creating unprecedented transmission characteristics, such as the well-known ‘endlessly single-mode’ fibre [8].

Alongside the mainstream development of low-loss fibres for optical communications, there have been countless other fabrication techniques that allow optical fibres with unconventional structures and glass compositions to be realised for a range of applications [9]. Many of these speciality fibres rely on existing technology to create the glass preform, notably MCVD, but adopt a fabrication route which involves assembling the fibre-preform, rather than depositing the glass. The main constituent is normally silica, but the core and cladding materials can be of dissimilar composition. The core can therefore be derived from more unusual materials, such as bulk crystals of silicon [10] or YAG [11]. Fabrication techniques such as rod-in-tube (RIT), or powder-in-tube (PIT) [12, 13], are used in these particular examples, and are more akin with traditional glass-melting methods. The motivations that drive the development of new fabrication techniques are the changing applications for optical fibres, which are still being discovered.

1.2 Applications of optical fibre

In modern society, optical fibres are well known as the transmission medium for optical communications. It is optical amplifiers and lasers, however, that have helped to functionalise this infrastructure, with perhaps the most eminent example being the erbium doped fibre amplifier (EDFA) [14]. The EDFA, which consists of a laser active gain medium that enables optical signals at a wavelength (λ) of 1.55 μm to be amplified, was developed in the late 1980s and has been a resounding triumph. Closely-related to the optical fibre amplifier is the rare-earth (RE) doped fibre laser, which has, in recent years, experienced similar levels of success as the EDFA. Multi-kilowatts of stable output power combined with a diffraction-limited beam has meant that fibre lasers are now used routinely in industry for material processing [15].

The first fibre laser was reported in 1964 [16], but it was not until 1985, and the progress made by David Payne and co-workers at the University of Southampton [17], that serious interest was generated. The fibre platform has several advantages over solid state lasers. The attraction lies in the superior beam quality and thermal management that the fibre laser geometry allows. The demonstration of a cladding-pumped fibre laser a few years later [18], using semiconductor laser diodes as the pump light source, enabled the achievable output power to increase dramatically. The first fibre laser to reach 100 W of single-mode output power was reported in 1999 [19], with the following decade seeing an impressive year-by-year increase which is now in the multi-kilowatt regime [15].

In parallel with the development of fibre lasers and amplifiers, optical sensing has also received considerable scientific attention over the years. Optical fibres already play an important part in manufacturing and industrial processes for analysing and monitoring chemical and biological materials [20]. Although optical fibre sensors can take many forms, the architecture that is of relevance in this work is an ‘intrinsic’ system, where the fibre itself is the sensing medium as opposed to merely a light carrier to and from an external modulator. These devices tend to be compact, stable, and integrate easily into fibre networks. Sensing in optical fibres is achieved by altering the fibre structure so as to gain access to the evanescent-field of the light propagating in the core. This can be most straightforwardly achieved by removing a section of the glass cladding material. The exposed region is then sensitive to its surroundings and can be used to discern external properties such as the refractive index of a liquid [21] or a particular gas species [22].

Embedded in the mechanism by which index-guiding microstructured optical fibres operate is the interaction between the core mode and the surrounding medium, and it was soon realised that the air holes provided an ideal platform for sensing elements in the voids. The innately long optical path length enhanced their sensitivity, and the early work by Tanya Monro et al. predicted optical fibres with overlapping fractions of up to 20 – 30 % [23]. Since then, numerous microstructured fibre designs have been suggested for sensing gases and liquids [24, 25] and the principle has given rise to an entirely new class of fibre sensing devices, so-called evanescent-field devices.

1.3 Thesis aims and structure

The broad aims of the work presented in this thesis were to develop new fabrication methods for silica optical fibres that are compatible with existing MCVD and fibre drawing technologies. Applications in ytterbium (Yb)-doped high-power fibre lasers and optical fibre sensing were targeted, which are of current interest in both academia and industry. The objectives were to conceive and refine novel fabrication techniques, as well as exemplify their potential by demonstrating speciality optical fibres designs that can not easily be obtained using existing methods. Underpinning the research was the intention to develop straightforward approaches, rather than elaborate and complex solutions, which would be more widely accessible and have a greater impact for optical fibre fabrication outside the research environment.

This PhD was studied on a part-time basis, and was undertaken alongside employment at the Optoelectronics Research Centre (ORC). The author is currently a member of the Silica Fibre Fabrication group, supporting the development of preform and fibre processes in the capacity of Senior Engineer. The experimental and development work reported in this thesis, including the design and construction of bespoke apparatus, was undertaken by the author, unless otherwise stated.

The thesis is organised into seven chapters, including this introduction. Prior to the presentation of any practical work, the background information relevant to silica optical fibre fabrication is provided. Although the outcome of this work will involve implementation of optical fibres as devices, it is predominantly advances in their fabrication that have been studied, and as such the information in Chapter 2 concentrates on these aspects. Any subsequent work that requires an understanding of how the resultant optical fibre can be integrated into a particular application is addressed in the individual chapter. Having introduced the appropriate technical background, the experimental work is then split into four distinct chapters, each covering a separate fabrication technique. The presentation structure of these chapters broadly follows the same form: an introduction to the topic followed a description of the developed fabrication technique, a report of the characterisation results from the fabricated preforms and fibres, and finally a summary and a list of the references used in the text.

Chapter 3 presents an *in-situ solution doping* technique for incorporating RE ions into preforms fabricated using MCVD [26]. The current types of optical fibre used in high-power fibre lasers are introduced and the limitations of current fabrication methods are highlighted. The experimental work reports on the realisation and characterisation of selected Yb-doped fibre designs, including a large-core fibre suitable for large mode area (LMA) operation, and a selectively RE-doped fibre with a raised inner-cladding. The use of multiple Yb and aluminium (Al)-doped layers has been advocated in all of the designs, and represents a format that is impracticable to achieve with conventional doping techniques.

In chapter 4, a vapour-phase RE-doping process for MCVD preform fabrication is reported, termed *chemical-in-crucible* (CIC) [27]. The CIC process enables dopant precursors that have a low volatility to be prototyped for their suitability in preform fabrication. The CIC process uses a new approach of electrically heating the dopant precursor within the substrate glassware, and accordingly a dedicated setup was developed and constructed by the author. The demonstration of preforms fabricated using the CIC process are reported and the characterisation results from the resultant fibres are presented. The work on the CIC process was supported by Engineering and Physical Sciences Research Council grant, EP/EO33725/1.

Chapter 5 describes a straightforward fabrication technique for silica *suspended-core holey fibre* (SC-HF) [28] that was developed by the author. The fibre design exhibits a small diameter core and a high air-filling fraction. Modelling of the fibre confirmed that the modal overlap is greater than 29 % (at $\lambda = 1.5$ μm) which, at the time that the work was undertaken, was significantly higher than any previously reported index-guiding structure used in this way. The fabrication and characterisation of an all-fibre acetylene-filled gas cell based on SC-HF is reported.

The work presented in the final experimental chapter relates to an entirely new type of optical fibre, termed *flat fibre* [29]. Flat fibre is fabricated using conventional MCVD and fibre drawing equipment and represents a new platform for extended length planar devices. The first proof-of-concept for flat fibre is reported and waveguiding channels were defined using direct-UV writing [30]. The written waveguides were characterised and ways to improve the material properties of the core layer are discussed. The progress towards realising an evanescent-field sensor using flat fibre is summarised.

Chapter 7 details the conclusions and future work. An overall account of the work is given, which is in addition to the summary provided at the end of each individual chapter. The possible directions for future work are discussed based on a continuation of the current themes. Appendices A, B and C, provide a list of published articles, a summary of the individual preforms and fibres that have been fabricated, and the effects of the Mountbatten fire, respectively.

1.4 References

1. F.P. Kapron, D.B. Keck, and R.D. Maurer. "Radiation losses in glass optical waveguides". *Applied Physics Letters*, 17(10): 423-425, (1970).
2. K.C. Kao and G.A. Hockham. "Dielectric-fibre surface waveguides for optical frequencies". *Proceedings of the IEE*, 113: 1151-1158, (1966).
3. M.G. Blankenship and C.W. Deneka. "Outside Vapor Deposition Method of Fabricating Optical Waveguide Fibers". *IEEE Journal of Quantum Electronics*, 18(10): 1418-1423, (1982).
4. J.B. MacChesney, P.B. O'Connor, and H.M. Presby. "A new technique for the preparation of low-loss and graded-index optical fibers". *Proceedings of the IEEE*, 62(9): 1280-1281, (1974).
5. D.N. Payne and W.A. Gambling. "Silica-based low-loss optical fibre". *Electronics Letters*, 10(15): 289-290, (1974).
6. P. Kaiser and H.W. Astle. "Low-loss single-material fibers made from pure fused silica". *Bell System Technical Journal*, 53(6): 1021, (1974).

7. J.C. Knight, T.A. Birks, P. St.J. Russell, and D.M. Atkin. "All-silica single-mode optical fiber with photonic crystal cladding". *Optics Letters*, 21(19): 1547, (1996).
8. T.A. Birks, J.C. Knight, and P.S.J. Russell. "Endlessly single-mode photonic crystal fiber". *Optics Letters*, 22(13): 961-963, (1997).
9. A. Mendez and T.F. Morse, *Speciality Optical Fibers Handbook.* Academic Press. (2007).
10. J. Ballato, T. Hawkins, P. Foy, R. Stolen, B. Kokuoz, M. Ellison, C. McMillen, J. Reppert, A.M. Rao, M. Daw, S. Sharma, R. Shori, O. Stafsudd, R.R. Rice, and D.R. Powers. "Silicon optical fiber". *Optics Express*, 16(23): 18675-18683, (2008).
11. Y.-C. Huang, Y.-K. Lu, J.-G. Chen, Y.-C. Hsu, Y.-M. Huang, S.-L. Huang, and W.-H. Cheng. "Broadband emission from Cr-doped fibers fabricated by drawing tower". *Optics Express*, 14(19): 8492-8497, (2006).
12. M. Neff, V. Romano, and W. Luthy. "Metal-doped fibres for broadband emission: Fabrication with granulated oxides". *Optical Materials*, 31(2): 247-251, (2008).
13. R. Renner-Erny, L. Loredana Di, and W. Luthy. "A novel technique for active fibre production". *Optical Materials*, 29(8): 919-922, (2007).
14. R.J. Mears, L. Reekie, I.M. Jauncey, and D.N. Payne. "Low-noise erbium-doped fibre amplifier operating at 1.54 um". *Electronics Letters*, 23(19): 1026-1028, (1987).
15. Y. Jeong, A.J. Boyland, J.K. Sahu, S. Chung, J. Nilsson, and D.N. Payne. "Multi-kilowatt single-mode ytterbium-doped large-core fiber laser". *Journal of the Optical Society of Korea*, 13(4): 416-422, (2009).
16. C.J. Koester and E. Snitzer. "Amplification in a fibre laser". *Applied Optics*, 3(10): 1182-1186, (1964).
17. R.J. Mears, L. Reekie, S.B. Poole, and D.N. Payne. "Neodymium-doped silica single-mode fibre lasers". *Electronics Letters*, 21(17): 738-740, (1985).

18. E. Snitzer, H. Po, F. Hakimi, R. Tumminelli, and B.C. McCollum. "Double-clad, offset core Nd fiber laser." in *OSA Technical Digest Series, Optical Fiber Sensors*. paper PD5, (1988).
19. V. Dominic, S. MacCormack, R. Waarts, S. Sanders, S. Bicknese, R. Dohle, E. Wolak, P.S. Yeh, and E. Zucker. "110 W fibre laser". *Electronics Letters*, 35(14): 1158-1160, (1999).
20. J.M. López-Higuera, *Handbook of optical fibre sensing technology*. Wiley-Blackwell (2002).
21. J. Villatoro and D. Monzon-Hernandez. "Low-cost optical fiber refractive-index sensor based on core diameter mismatch". *Journal of Lightwave Technology*, 24(3): 1409-1413, (2006).
22. G. Stewart, W. Jin, and B. Culshaw. "Prospects for fibre-optic evanescent-field gas sensors using absorption in the near-infrared". *Sensors and Actuators B: Chemical*, 38(1-3): 42-47, (1997).
23. T.M. Monro, D.J. Richardson, and P.J. Bennett. "Developing holey fibres for evanescent field devices". *Electronics Letters*, 35(14): 1188-9, (1999).
24. G. Pickrell, W. Peng, and A. Wang. "Random-hole optical fiber evanescent-wave gas sensing". *Optics Letters*, 29(13): 1476-1478, (2004).
25. R.S. Windele, Y.L. Hoo, W. Jin, H.L. Ho, and D.N. Wang. "Evanescent wave gas sensing using microstructure fibre." in *4th Pacific Rim Conference on Lasers and Electro-Optics, Chiba*. 8-9, (2001).
26. A.S. Webb, A.J. Boyland, R.J. Standish, S. Yoo, J.K. Sahu, and D.N. Payne. "MCVD in-situ solution doping process for the fabrication of complex design large core rare-earth doped fibers". *Journal of Non-Crystalline Solids*, 356: 848-851, (2010).
27. A.J. Boyland, A.S. Webb, S. Yoo, F.H. Mountfort, M.P. Kalita, R.J. Standish, J.K. Sahu, D.J. Richardson, and D.N. Payne. "Optical Fiber Fabrication Using Novel Gas-Phase Deposition Technique". *Journal of Lightwave Technology*, 29(6): 912-915, (2011).
28. A.S. Webb, F. Poletti, D.J. Richardson, and J.K. sahu. "Suspended-core holey fiber for evanescent-field sensing". *Optical Engineering Letters*, 46(1), (2007).

29. A.S. Webb, F.R. Mahamd Adikan, J.K. Sahu, R.J. Standish, C.B.E. Gawith, J.C. Gates, P.G.R. Smith, and D.N. Payne. "MCVD planar substrates for UV-written waveguide devices". *Electronics Letters*, 43(9): 517-519, (2007).

30. G.D. Emmerson, S.P. Watts, C.B.E. Gawith, V. Albanis, M. Ibsen, R.B. Williams, and P.G.R. Smith. "Fabrication of directly UV-written channel waveguides with simultaneously defined integral Bragg gratings". *Electronics Letters*, 38(24): 1531-2, (2002).

Chapter 2

Silica Optical Fibre Fabrication

2.1 Introduction

This chapter reviews the technologies behind preform and optical fibre fabrication, and describes the equipment and techniques that relate to the work in the subsequent chapters. A brief introduction to silica and rare-earth (RE) glasses is firstly provided, which outlines the transmission characteristics and suitability for use as an optical waveguide. The major preform fabrication processes are then examined, and a more detailed account of Modified Chemical Vapour Deposition (MCVD) is provided owing to its significance throughout this thesis. As a large proportion of the experimental work also focuses on incorporating RE ions into silica preforms, specifically ytterbium, the numerous techniques associated with this are presented as well as the practical considerations and limitations of the different approaches.

The second half of this chapter discusses optical fibre drawing and measurement techniques, and the fibre requirements for deployment in lasing and sensing applications. The configuration and operation of a research-grade fibre drawing tower is described, which is typical of those used for the experimental work. The subject matter in the first half of this chapter is relevant to the entire thesis, whereas the final two sections look specifically at ytterbium-doped fibre lasers (YDFL) and evanescent-wave sensing, and relate to Chapters 3 and 4 and Chapters 5 and 6, respectively. The brief introduction to these topics is expanded upon within the relevant chapters.

2.2 Silica and rare-earth doped glasses

Silicon dioxide (SiO_2) is one of nature's most abundant compounds, occurring naturally in a crystalline form as quartz. The crystal unit cell of quartz consists of a silicon (Si) atom bonded to four oxygen (O) atoms in a tetrahedral configuration. In a solid glass phase, SiO_2, referred to as silica, is an amorphous material that exhibits no long-range uniformity in its atomic arrangement and has only limited short-range periodicity (see Figure 2.1). As a result of the lack of periodicity in glassy/amorphous silica, the voids are irregular which controls the glass viscosity.

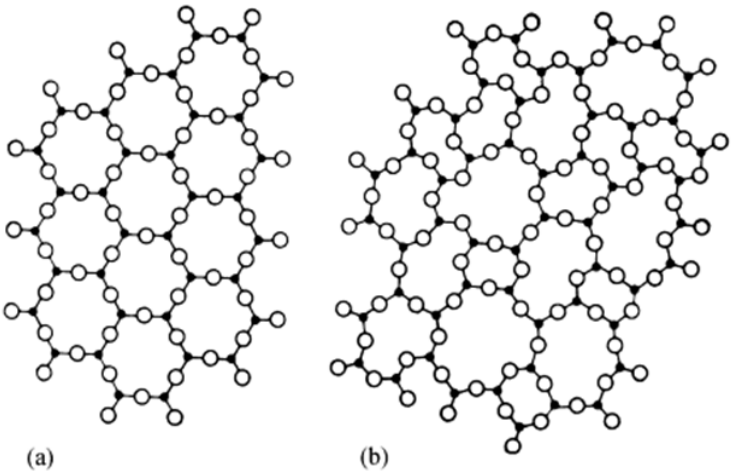

Figure 2.1: Representations of the sp^3 hybridized silicon (dark circles) with oxygen (open circles) in (a) silica crystal and (b) in amorphous or glassy silica [2]. The crystalline structure depicts a 3-dimensional periodic array of Si and O atoms, which is absent in the amorphous or glassy silica.

Transforming a crystal into a glass can be achieved by traditional 'melt-quenching', whereby the material is heated until it forms a viscous liquid and is then rapidly cooled. With insufficient time for a regular lattice to reform, the disordered molecular structure is frozen-in. The temperature at which the viscous liquid becomes a solid glass is known as the transition temperature (T_g) and can be regarded as the temperature below which the molecules have relatively little mobility. For pure SiO_2, T_g is in the region of 1200 °C [1]. However, this value will depend on the rate of cooling, and therefore the properties of a glass will differ depending on the thermal history of the material.

In principle, nearly all materials will form a glass if cooled sufficiently fast, however, relativity few can do so on their own in the same manner as SiO_2. These types of oxides are known as ‘glass formers’, and include germanium dioxide (GeO_2), phosphorus pentoxide (P_2O_5), and boron trioxide (B_2O_3). In addition to glass formers, dopant elements in oxide glasses can also be classed as ‘network modifiers’ or ‘intermediates’, which are often classified by their atomic bond strength. Network modifiers sit in interstitial positions within the glass network, breaking the Si-O-Si bonds and modifying the chemical and optical properties of the glass, but are not able to form a glass themselves. These include alkali and alkaline earth metal oxides, of which sodium (Na) is perhaps the most important as it reduces the working temperature of the glass [2]. An intermediate oxide is a conditional glass former which does not form a glass independently but can combine with other oxides in the glass network.

Amorphous silica glass has a very high optical transparency over a broad wavelength (λ) range of 0.8 μm to 2.0 μm, making it ideal for optical waveguiding applications. This low-loss window is bound by fundamental absorption edges in the ultraviolet (UV) and near-infrared (IR) regions as a result of favourable electron transitions and molecular vibrations in the glass. The dominant loss mechanism within the transparent region is Rayleigh scattering, which defines the theoretical minimum loss in silica as 0.125 $dB.km^{-1}$ at $\lambda = 1.55$ μm [2]. Rayleigh scattering is an intrinsic loss mechanism that is caused by inhomogeneities in the glass which are of a similar length scale as the wavelength of light, and introduces an optical loss that is proportional to λ^{-4}. In contrast, extrinsic losses arise from impurities such as metal ions and hydroxyl (OH) groups that are present in the glass structure. Transition metal ions such as chromium (Cr), copper

(Cu) and iron (Fe) introduce to a considerable absorption in optical fibres that is of the order 1 dB.km^{-1} for every part per million (ppm) of impurity [3]. However, it is OH groups that account for the highest contribution to the absorption in silica, and which are most difficult to eradicate. OH molecules that are embedded in silica glass structure have a fundamental stretching vibration at $\lambda = 2.73$ µm. This fundamental vibration, in combination with harmonic vibrations, manifests as characteristic absorption peaks centred at wavelengths of 1.39 µm, 1.24 µm and 0.95 µm, with every ppm responsible for an absorption of 54 dB.km^{-1}, 2.3 dB.km^{-1}, and 0.83 dB.km^{-1}, respectively [2].

Reducing the attenuation in optical fibres that is caused by the presence of OH groups is addressed at the start of the preform fabrication process. In the case of MCVD, the substrate itself can be a major source of contamination and is partially suppressed by careful selection of the starting material. A glass type that is widely used as a substrate and jacketing tube, both commercially and in the laboratory is SUPRASIL-F300 (Heraeus, Germany), which is synthetic fused quartz. It is manufactured from the oxidation of silicon-rich precursors (as opposed to naturally fused quartz) to form a porous soot body that can be efficiently dehydrated before being sintered into glass. Thereafter, it is ground and drilled to the required dimensions. F300 glass exhibits only trace metal impurities, at the sub-parts per billion (ppb) level, and the manufacturing process is regulated so as to maintain the OH content at <1 ppm [4].

Whilst considerable efforts are made to remove impurities from the glass to reduce unwanted absorption and scattering losses, the deliberate incorporation of RE ions into the silica structure is desirable for the purpose of light amplification. RE ions are optically active, enabling them to absorb and emit light at different wavelengths. Lasing is based on the process of stimulated emission, and in the case of RE-doped silica fibre used in applications for telecommunications the emission wavelengths typically lie within the favourable ‘eye-safe’ range between 1.5 µm and 2.0 µm. Furthermore, RE ions are relatively insensitive to their host material by virtue of their electronic structure; the outer 5s and 5p electrons shield the electronic structure when incorporated into the glass matrix whilst the 4f inner shell is responsible for optical absorption and emission.

In a purely silica host glass, trivalent RE ions can only be incorporated homogenously in low concentrations owing to a lack of non-bridging oxygen sites. In the ‘continuous random network’ model proposed by Zacharison [5], each corner of the silica tetrahedron shares a ‘bridging’ oxygen ion to form a rigid network. Trivalent RE ions in oxide glasses require the coordination of 6 to 8 oxygen ions and are therefore not easily dissolved in pure silica. When RE ions such as erbium (Er^{3+}) are introduced into the glass, the silica tetrahedron are displaced so that the dopant ion is bonded to six O atoms (see Figure 2.2(a)) [6]. The coordination balance is achieved by the 3+ erbium and the three -1 oxygens, where two oxygen atoms behave as one in terms as charge. Since the Si^{4+} tetrahedron donates one electron to each O neighbour, the Er^{3+} ion does not fit well in the silica network [7]. Owing to the insufficient number of ‘non-bridging’ oxygen ions in silica, RE ions tend to share oxygen ions which leads to ‘clustering’. The close proximity of the RE then permits energy to be transferred through RE-O-RE bonds [8]. This limits the maximum concentration of RE ions that can be incorporated homogenously in pure silica to around 100 ppm, by weight.

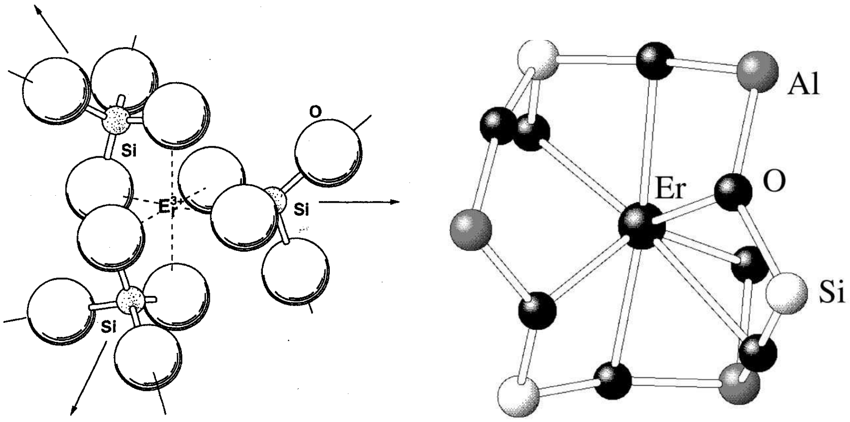

Figure 2.2: Illustration showing (a) the inclusion of an Er^{3+} ion in the pure silica network, indicating the movement of the silica tetrahedron to accommodate the RE ion [6], and (b) the coordination of an Er ion in an Al co-doped silica glass [7].

It is well known that the solubility of RE ions in silica can be increased by incorporating aluminium and phosphorous co-dopants into the glass, which surround the RE ion and shield its charge. In the case of aluminium, trivalent Al^{3+} ions substitute for Si^{4+} ions in the glass network, and with three Al ions in close proximity a RE ion can provide the charge compensation (Figure 2.2(b)) [7]. Phosphorous provides a similar structural role to aluminium and is incorporated as a P_2O_5 tetrahedron. An in-depth model of the effect of co-doping on the structural properties in RE-doped silica glass is given by Arai et al. [9]. The authors describe that RE ions that can not coordinate sufficiently to non-bridging oxygens cluster together to form ‘ill-coordinated’ ions. The addition of Al ions, coupled with the Si ions, surround the RE ion achieving charge compensation and resulting in ‘well-coordinated ions’. As both aluminium and phosphorus are soluble in silica glass, they are used extensively in RE-doped silica fibres to allow RE constituents to be incorporated in relatively high concentrations.

2.3 Preform fabrication

The industrial processes used in manufacturing silica optical fibres have been developed over many years and are now well established [10]. Optical fibre is manufactured in two-stages. The first stage involves fabricating the glass preform with the compositional and waveguiding refractive index profile (RIP) that is required for the resultant fibre. Fibre is then pulled from the preform in a drawing tower, with a reduction in diameter of more than two orders of magnitude. Producing the preform arguably poses a greater challenge in terms of fabrication than the fibre drawing stage, and has consequently given rise to a handful of disparate techniques that are widely used.

The leading preform manufacturing processes are broadly categorised as Chemical Vapour Deposition (CVD), and involve the high-temperature reaction of precursor vapours to deposit silica particles on a substrate. The three main CVD methods are: Outside Vapour Deposition (OVD) [11], Vapour-phase Axial Deposition (VAD) [12] and MCVD [13]. VAD and OVD are well known as the industry standards for mass-producing transmission optical fibre, and although MCVD endures a comparatively lower deposition rate, it is a highly versatile process and relatively simple to implement. A photograph of the MCVD system used for the majority of the experimental work presented in this thesis is shown in Figure 2.3. Other noteworthy preform fabrication processes are Plasma-activated Chemical Vapour Deposition (PCVD) [14] and Direct Nanoparticle Deposition (DND) [15]. PCVD is similar to MCVD except that instead of a fuel burner, microwave-generated plasma provides the necessary energy to initiate the chemical reactions inside the substrate tube. DND is the proprietary technology of LIEKKI (Finland) and is a variant of the OVD process that was developed to improve aspects of the deposition efficiency and control over the preform RIP.

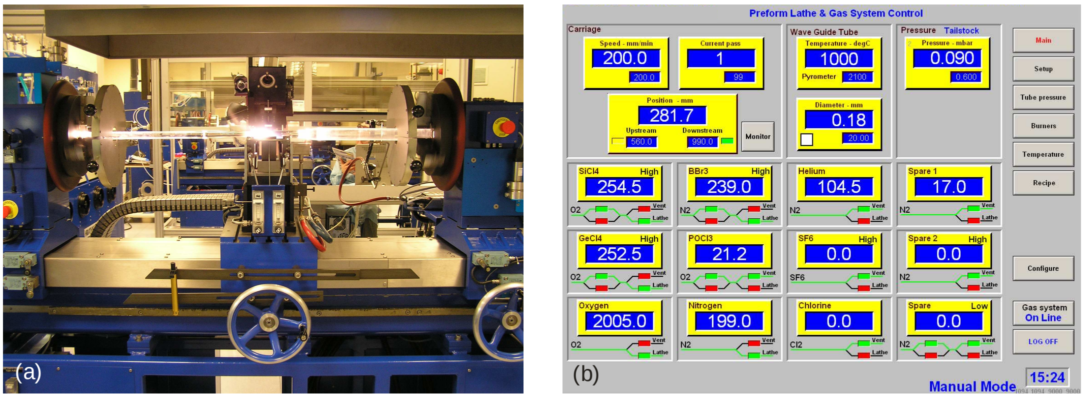
Preform Lathe & Gas System Control

Carriage
Speed - mm/min: 200.0 (200.0)
Current pass: 1 (99)
Position - mm: 281.7
Upstream: 560.0
Downstream: 990.0

Wave Guide Tube
Temperature - degC: 1000
Pyrometer: 2100
Diameter - mm: 0.18 (20.00)

Pressure Tailstock
Pressure - mbar: 0.090 (0.600)

SiCl4 High: 254.5
BBr3 High: 239.0
Helium: 104.5
Spare 1: 17.0
GeCl4 High: 252.5
POCl3: 21.2
SF6 High: 0.0
Spare 2 High: 0.0
Oxygen: 2005.0
Nitrogen: 199.0
Chlorine: 0.0
Spare Low: 0.0

Gas system On Line
Manual Mode
15:24

Figure 2.3: (a) Photograph of a MCVD lathe in operation, and (b) a snap-shot image of the graphical interface used for its control.

The CVD processes used in preform fabrication can be further categorised according to the type of chemical reaction that is responsible for producing the silica particles. In MCVD, the precursor vapour is mixed with an oxygen carrier gas and transported inside a glass tube to the heat source where it undergoes a high-temperature oxidation reaction. By contrast, in OVD and VAD processes the precursor vapour is fed directly into a burner flame and a hydrolysis reaction is initiated. The resultant glass particles are then deposited on to a rotating target rod. Hydrolysis is the same mechanism that takes place in other CVD techniques, such as Flame Hydrolysis Deposition (FHD) [16]. FHD can be regarded as the equivalent deposition process for producing planar silica layers, and is revisited in Chapter 6 in the context of alternative deposition techniques for planar devices.

The final distinction between MCVD, OVD and VAD, is that the former is a single-step fabrication process, whereas OVD and VAD require a deposition, or soot stage, as well as a combined dehydration and consolidation stage. The latter stage entails drying the porous soot to remove OH ion impurities before it is consolidated into glass. Dehydration is achieved by immersing the soot body in a controlled atmosphere of helium (He) and chlorine (Cl_2) gas at an elevated temperature of between 950 °C and 1250 °C [17]. This is sufficient to effectuate a reaction between the Cl_2 gas and the OH ions, but is low enough not to densify the soot. Following dehydration, the temperature is increased to 1200 – 1600 °C and the soot body is viscously sintered into a dense, bubble-free glass preform.

2.3.1 Modified chemical vapour deposition

The MCVD process involves flowing the vapour from halide precursors down the centre of an externally heated rotating glass tube (see Figure 2.4). The precursors undergo a high-temperature reaction upon reaching the burner, and deposit amorphous particles on the inside surface which are sintered by the trailing burner as it traverses along the length of the tube [18]. After the required layers have been deposited, the tube is collapsed at a high temperature into a solid rod known as a preform. The MCVD process is described in detail below.

The glassware is assembled between two synchronously rotating chucks of a glassworking lathe, along which an oxy-hydrogen burner carriage traverses. The precursors are located remotely in a chemical enclosure and are delivered through a heated umbilical line (30 – 40 °C) and gas-tight rotating seal to the substrate tube. The main chemical precursors used in the MCVD process are the halide compounds: silicon tetrachloride ($SiCl_4$), germanium tetrachloride ($GeCl_4$), phosphorus oxychloride ($POCl_3$) and boron tribromide (BBr_3). These precursors are characterised by their high vapour pressures at room temperature (~100 kPa) and can be efficiently vaporised by passing a carrier gas, such as oxygen (O_2) or nitrogen (N_2), through a 'bubbler' containing the liquid reagent. This approach takes advantage of the comparatively lower vapour pressure of the unwanted metallic impurities and effectively purifies the precursor. Supplementary process gases include Cl_2, He, N_2 and sulphurhexafluoride (SF_6), which are entrained in the gas stream within the chemical enclosure to ensure that they are homogenously mixed and in a laminar flow upon reaching the substrate. The flow rates of all gases are accurately regulated by computer controlled mass flow controllers (MFC).

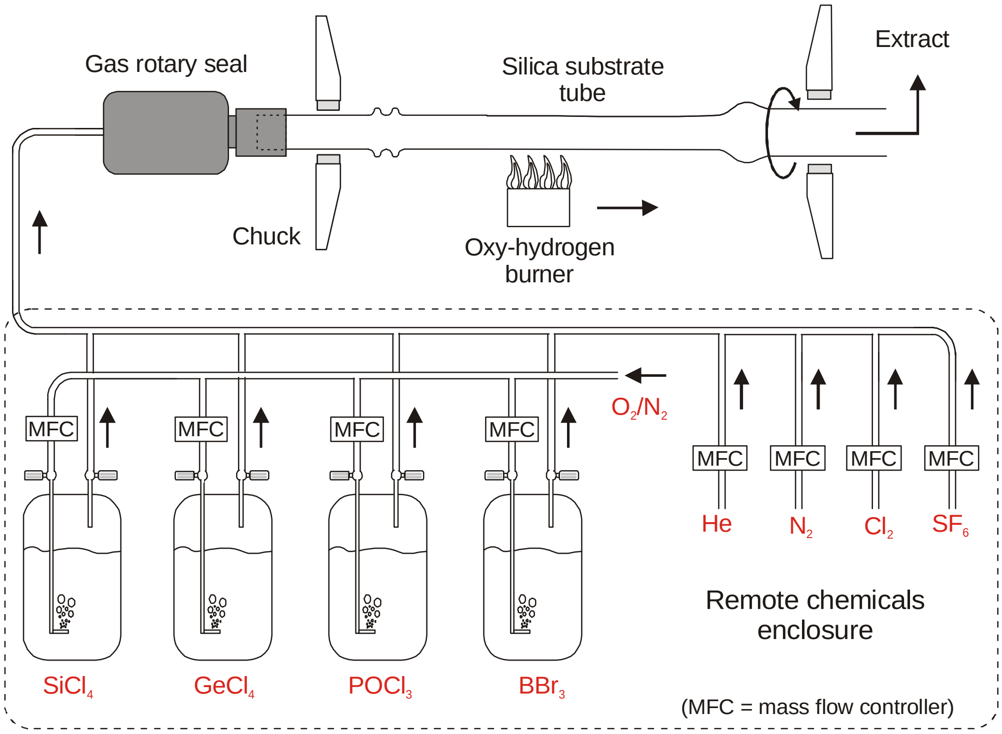

Figure 2.4: Schematic of the MCVD process showing the glassworking lathe and chemical delivery system.

The temperature of the substrate tube is measured by an infrared pyrometer, which provides feedback to the computer and controls the flow of hydrogen (H_2) and O_2 to the burner in order to maintain the required temperature. The pyrometer is usually focused on the axial centre of the tube, at a point which corresponds to the peak glass temperature when the carriage traverse speed is set to 150 mm.min^{-1}. The position of the hot-zone, however, will shift depending on the carriage speed, and thus a fixed pyrometer can sometimes lead to an incorrect temperature reading. The measurement becomes even less accurate if the burner is translated in the upstream direction, as is necessary for depositing phosphosilicate soot layers [19]. For these reasons, a thermal imaging camera can be used, in addition to the pyrometer, which is able to measure the temperature over a wider field of view and ascertain the peak glass temperature irrespective of its location on the tube surface. A thermal imaging system was available for most of the experimental work reported in this thesis. The correlation between the temperature measured by the thermal imaging camera and that of the fixed position pyrometer was experimentally determined and the effect of carriage speed is illustrated in Figure 2.5.

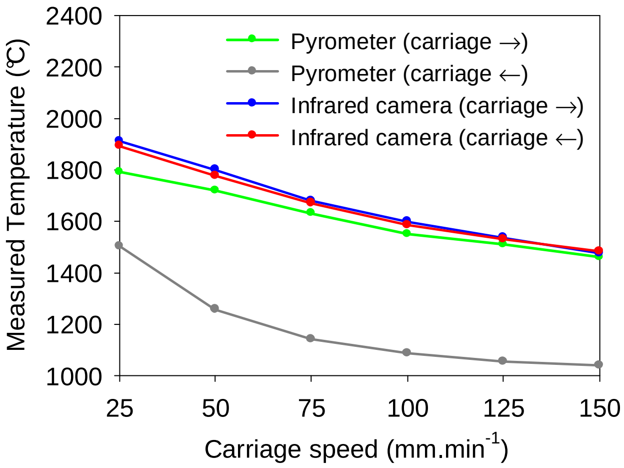

Figure 2.5: Comparsion of the glass temperature measured by the pyrometer and the infrared camera at various burner carriage speeds, in both downstream (→) and upstream (←) directions (the burner flow rates were fixed at H_2 = 30 L.min^{-1} and O_2 = 15 L.min^{-1}).

The substrate tube used for preform fabrication is normally F300-quality glass with a nominal outside diameter of 20 mm and an inside diameter of 16 mm. A variation in diameter of <0.1 mm is tolerated and the tube should additionally exhibit a high tolerance on the ovality, siding, and bow along its length. After the substrate tube has been chemically cleaned, it is assembled on the lathe and undergoes further preparation with a gas-phase etching pass using SF_6, or similar fluorinated compound, to eliminate any remaining contamination. This is followed by a high-temperature flame-polishing pass (2000 –2100 °C) to smooth out the microscopic irregularities that were formed during the etching. Prior to the core layer, several silica cladding layers are deposited to provide a low-loss barrier which prevents OH ions, or any other contaminants, from diffusing inwards.

The core layer is produced by adding $GeCl_4$ or $POCl_3$ to the $SiCl_4$ gas stream in order to raise the index of the glass in accordance with the fibre design. At high-temperatures, $SiCl_4$ vapour reacts with oxygen to form the silica network, whilst $GeCl_4$ oxidises into GeO_2. Similarly, $POCl_3$ is converted into P_2O_5 which also increases the refractive index of the glass, but reduces the processing temperature and allows multiple glass layers to be deposited without significant tube distortion. BBr_3 is incorporated into silica as B_2O_3 and reduces the refractive index of the glass. Boron doping also significantly increases the thermal expansion coefficient of the glass and is therefore normally reserved for speciality fibre structures. Its use is studied further in Chapters 3 and 6.

The balanced oxidation reactions for the four main precursors are shown below.

$$SiCl_4 + O_2 \rightarrow SiO_2 + 2Cl_2 \tag{2.1}$$

$$GeCl_4 + O_2 \rightarrow GeO_2 + 2Cl_2 \tag{2.2}$$

$$4POCl_3 + 3O_2 \rightarrow 2P_2O_5 + 6Cl_2 \tag{2.3}$$

$$4BBr_3 + 3O_2 \rightarrow 2B_2O_3 + 6Br_2 \tag{2.4}$$

These chemical reactions are initiated at temperatures in the region of 1300 °C to 1600 °C, although the overall efficiency of material incorporation, even above 1600 °C, is typically only around 40 – 70 % [18]. The conversion of $SiCl_4$ and $POCl_3$ into their oxide forms is effectively unity at temperatures above around 1475 °C [20]. However, the conversion of $GeCl_4$ to GeO_2 is incomplete at temperatures above ~1125 °C as the excess of Cl_2 from the oxidation of $SiCl_4$ shifts the reaction equilibrium in favour of $GeCl_4$. The excess of Cl_2 in the tube, which is typically between 3 – 10 % during processing [10], is however beneficial as it reacts favourably to remove OH ions.

The dominant mass transfer mechanism responsible for glass deposition is thermophoresis [21]. As the oxy-hydrogen burner slowly traverses along the length of the substrate tube in the same direction as the gas flow, it produces a temperature gradient within the tube with the hottest point marginally lagging behind the centre of the burner. As the precursors reach this hot-zone they undergo a high-temperature oxidation reaction resulting in the growth of submicron-sized amorphous particles. These are subsequently deposited downstream where the tube wall is cooler and are viscously sintered into a glassy layer as the burner passes over them.

Thermophoresis describes how a particle suspended in a laminar gas flow acquires a velocity towards a lower temperature as a result of being bombarded by gas molecules of different average energies [21]. Following the oxidation reaction, the initial direction of the particles is towards the centre of the tube where the gas is cooler. However, as they travel further downstream, the tube temperature is lower than that of the gas and the particles are deposited on the glass wall. Most particle paths lead to deposition, whilst those particles travelling at, or close to, the axial centre of the tube travel directly to the extract. As the oxide particles travel downstream, they continually collide and combine with other particles to produce a range of sizes. Once sintered, this particle size variation has no effect on the resulting glass layer, but it has profound implications for soot deposition which is discussed further in the next subsection.

The temperature profile inside the tube means that the position at which a particle is formed dictates the trajectory it will follow downstream. Consequently, factors such as the tube wall thickness, gas flow rate, burner carriage, and to a lesser extent the tube rotation speed, will all influence the temperature profile and play a role in the deposition efficiency [22]. Methods to enhance the deposition efficiency by force cooling of the gas after it has passed through the reaction zone [23], or introducing internal directional gas jets downstream of the burner [24] have been reported but add complexity to the system and are normally unnecessary for most research work.

Following deposition of the cladding and core layers, the glass temperature is increased to around 2200 °C and the tube is collapsed solid. The tube collapses under surface tension effects which prevail at high temperatures as the viscosity of the glass exponentially decreases. The collapsing stage typically requires several passes with the carriage speed being reduced in each consecutive pass. This compensates for the increased wall thickness in the glass and ensures that the inside surface temperature of the tube is sufficiently high to allow deformation. A slightly positive pressure (relative to atmospheric) is maintained within the tube during the collapse stage so that the surface tension dominates the collapse, rather than the reduced pressure, and in this way the core remains circularly symmetric in the final preform.

There is an abundance of reports in the literature that describe how the aforementioned variables affect the deposition process [18, 21, 23]. Many of these provide an excellent grounding in understanding the process parameters; however, the complex nature of the MCVD process means that experience and empirically derived recipes are of most practical use to the fabricator.

2.3.2 Solution doping

Transporting the vapour from RE precursors such as $YbCl_3$ and $ErCl_3$, in the same way as $SiCl_4$, $GeCl_4$, $POCl_3$ and BBr_3, is impractical owing to their naturally low vapour pressure at room temperature. Appreciable vapour can be produced from RE halide compounds at elevated temperatures, but the need for high temperature delivery lines precludes their use in a MCVD process. An alternative, and more accessible route for doping preforms with RE ions, is to impregnate the glass with a solution in which the dopant ions are dissolved. This process is known as solution doping [25] and is regarded as the principal method for fabricating RE-doping silica preforms by MCVD, both in industry and research alike. The solution doping technique is simple to implement and enables an extensive range of dopant ions to be incorporated into the glass structure. It is reviewed in-depth here owing to its importance to the work presented in Chapter 3.

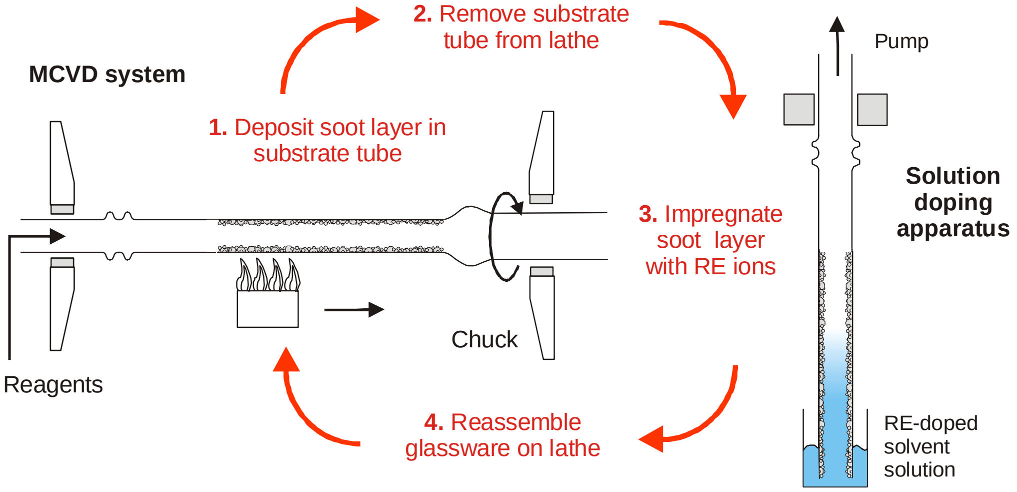

Figure 2.6: Depiction of the solution doping technique used for RE-doping silica preforms, illustrating that the substrate tube needs to removed from the lathe for each doped layer required.

The solution doping technique is an addendum to the conventional MCVD process and begins with the deposition of a porous oxide layer, known as a ‘soot’, on the inside of the substrate tube (see Figure 2.6). The soot layer is deposited using a reduced burner temperature which oxidises the $SiCl_4$ vapour but is insufficient to consolidate the resultant particles. The substrate tube is then removed from the lathe and soaked vertically in a solvent solution containing the desired RE chlorides. After soaking for 1 hour, the solution is drained, and the residual liquid is left to evaporate. The glassware is then reassembled on the lathe. To achieve a low level of OH impurity in the resultant glass a dehydration stage is required, which involves flowing Cl_2 gas through the substrate tube whilst heating to ~600 °C [26]. At this temperature, the Cl_2 gas reacts readily with the water molecules, liberating hydrogen chloride (HCl) vapour in the process (see equation 2.5). After dehydration, the soot layer is sintered at around 2000 °C and the tube is subsequently collapsed in the usual manner.

$$2H_2O + 2Cl_2 \rightarrow 4HCl + O_2 \tag{2.5}$$

The characteristics of the deposited soot layer are dictated by the burner temperature, which directly affects the porosity of the soot as well as its adhesion to the inner glass surface. If the burner temperature is too high, the soot layer becomes partially sintered;

whereas, if the burner temperature is inadequate, the soot layer may not adhere to glass surface [27]. Therefore, an optimum soot deposition temperature exists for a particular set of process conditions (e.g. precursor gas flow rates, carriage traverse speed etc.).

Silica is doped with germanium or phosphorous primarily to raise the refractive index of the glass, but is also used to enhance the solubility of RE ions in the structure. $GeCl_4$ and $POCl_3$ are combined with $SiCl_4$ in the vapour-phase and deposited at a reduced burner temperature to produce a doped soot layer. The addition of GeO_2 and P_2O_5 to the glass, however, lowers its melting point and consequently the porosity of the soot layer is more sensitive to the deposition temperature than an undoped soot layer. It has been reported that an increase of 40 ºC in the deposition temperature used for a Ge-doped soot reduces the layer thickness by 45 %, and translates into a significant reduction in the RE absorption of the resultant fibre [28]. In the case of a soot layer doped with P_2O_5, the situation is even more problematic: within the temperature range needed for the oxidation reaction to occur, the traversing burner substantially sinters the soot as it passes. To overcome this problem, the soot is deposited by translating the burner carriage in the opposite direction to the gas flow, thus preventing premature consolidation of the deposited particles. A low temperature pre-sintering pass, in the conventional downstream direction, is subsequently needed to sufficiently adhere the soot layer to the glass surface [19].

As well as the soot porosity, variations in the particle sizes, both radially and longitudinally along the tube, will strongly influence the dopant incorporation and uniformity in the final preform. The effects of the temperature gradient and the thermopheretic forces in the tube direct the particles along different trajectories. The temperature the particles experience, and the distance they travel, will influence their growth and produce a distribution of particle sizes that follow different trajectories towards the tube wall (see Figure 2.7). The larger soot particles (of the order of 150 nm) are deposited close to the burner whilst smaller particles (of the order of 15 nm) are deposited further downstream [30]. During normal (high temperature) deposition, this variation is inconsequential as the particles are immediately consolidated by the burner.

However, in a soot layer, the outcome is a hierarchy of particle sizes with the largest particles nearest the layer surface and gradually smaller particles located towards the substrate wall. Moreover, smaller particles will fuse more easily, which further contributes to the porosity gradient. The continued deposition of smaller particles downstream also introduces a thickness gradient along the length of the substrate. This longitudinal thickness variation can be as large as 25 μm to 35 μm over a distance of 350 mm, and results in a slightly tapered core in the final preform [31].

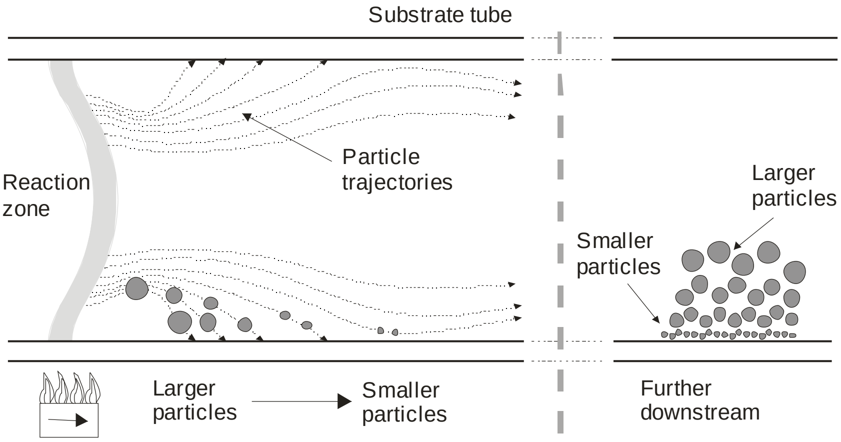

Figure 2.7: Illustration of the thermopheretic effect on the growth and distribution of particle sizes inside a substrate tube. The lefthand side shows the trajectories of particles due to the temperature gradients inside the tube, and the righthand side shows the hierarchy of sizes in the soot layer deposited downstream [18, 29].

In comparison to establishing the optimum soot deposition temperature, the soaking and drying stages in the solution doping technique are comparatively straightforward. However, consideration should be given to the viscosity of the dopant solution, which increases with dopant concentration. Peeling of the soot may occur if it is soaked in a high viscosity solution, especially if the layer is poorly adhered to the glass substrate. Furthermore, a high viscosity solution may require an extended soaking duration to ensure it fully penetrates the soot layer. Dhar et al. [32] reported that the soaking duration can be used to control the desired RE concentration, however, the outcome is strongly dependent on the morphology of the soot layer. For this reason, the soot is usually left immersed in the solution for 1 hour, which is sufficient for most soot and solution compositions to reach a saturation point [27].

The use of aluminium (Al) as an index-raising co-dopant offers certain advantages over GeO_2 and P_2O_5, and is used extensively for the experimental work reported in Chapter 3. Al is added to the RE solution directly, in the form of hydrated $AlCl_3$, which allows a pure silica soot to be deposited thus simplifying the soot preparation stage. Furthermore, Al-doping increases the solubility of RE ions in the silica glass network, and the high melting point of Al_2O_3 has a further benefit of preventing a central dip in the RIP that manifests itself during the collapse stage of the MCVD process.

The incorporation of Al_2O_3 into silica preforms using the solution doping technique has been studied extensively by Tang et al. [29, 31]. For the aforementioned reasons, the soot deposition temperature significantly affects the intake of $AlCl_3$ and consequently the resultant NA of the preform. For example, a 40 ºC decrease in burner temperature, for a pure silica soot and a fixed Al-concentration, increases the preform NA from 0.14 to 0.18 [31]. As described previously, the radial variation of particle sizes in a soot layer also affects its porosity. Considering an Al-only dopant solution, the lower porosity of the layer near the glass surface impedes penetration and results in a gradient in the Al concentration. Analysis shows that there is a slight increase in Al close to the exposed surface which then dramatically decreases towards the glass wall [30]. The maximum concentration is seen at a depth of ~25 % from the exposed surface. The slight reduction close to the surface suggests that $AlCl_3$ can be lost to evaporation, assisted by the drying process and the gas flow in the tube [29]. Interestingly, for a preform NA of around 0.12 this central depletion of Al is not replicated in the final preform RIP [31], but does manifest itself as ‘ripples’ that are visible in the RIP of multi-layered preforms.

2.3.3 Vapour-phase deposition of rare-earth ions

The previous section describes a liquid preparation technique for incorporating RE ions into silica preforms that are fabricated using MCVD. In this subsection, methods for delivering RE precursors in the vapour-phase for the purposes of preform fabrication are discussed and the key chemical reactions involved are outlined. Over the years, numerous methods have emerged, and although the intricacies of these designs differ, they can usually be classified into one of the regimes illustrated in Figure 2.8 [33].

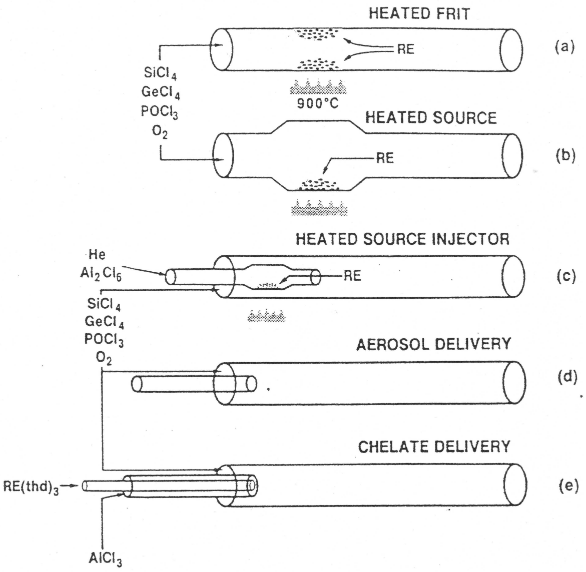

Figure 2.8: Classification of methods used for vapour-phase deposition of RE constituents in silica preforms: (a) heated frit, (b) heated source, (c) heated source injector, (d) aerosol delivery (e) and organometallic chelate delivery [33].

The 'heated frit' and 'heated source' techniques shown in Figure 2.8(a) and (b), respectively, both introduce the dopants through the evaporation of RE chlorides that are situated upstream of the substrate tube [33, 34]. In the case of the heated frit design, the vapour source is an unsintered soot layer that has been previously impregnated with a solvent solution containing the RE ions; whereas the heated source method uses a solid form of the RE compound. For both techniques, it is first necessary to dehydrate the RE precursor in a chlorinated atmosphere to remove the bonded OH ions. The RE dopant is then evaporated into the gas stream by heating the tube externally to several hundred degrees. Concentrations of up to 300 ppm of Nd^{3+} ions have been reported using the technique [34]. However, achieving appreciably higher concentrations than this is impractical owing to the RE chlorides converting into a less volatile oxide form when heated in the presence of oxygen. The reason that any RE vapour at all is produced whilst oxygen gas is flowing in the tube is most likely due to vaporisation of the more volatile oxyhalide compounds which constitute the intermediate products in the oxidation reaction [35].

The ‘heated source injector’ method shown in Figure 2.8(c) addresses the problem of unintended oxidation by segregating the RE chloride source from the conventional precursors. However, any advancement from glass delivery designs that involve multiple tubes in this way is offset by the need to heat the external glassware to an even higher temperature to reach the same temperature within the internal glassware. This then risks oxidising the $SiCl_4$ vapour in the outer glass tube. The problem can be overcome by simply swapping the chemical input lines, and locating the RE within the outer glassware, although it is not believed that this approach has been reported in the literature.

The aerosol delivery method illustrated in Figure 2.8(d) eliminates the need for volatile precursors, as well as high temperature heating, and uses an ultrasonic nebuliser to produce aerosol particles from a RE solution [36]. The generated particles are of the order of several microns in diameter, and are sufficiently buoyant to be generated remotely and transported to the reaction zone through a normal chemical delivery line. The RE chlorides can be dissolved in an aqueous or organic-based liquid although a solution with a low viscosity and surface tension is desirable to enable easy nebulisation. Tetraethylorthosilicate (TEOS) is commonly used for this purpose, and is available in high purity [37]. Glass oxides containing Nd, Er, Al, and P have all been demonstrated using this method [38], although no recent reports have been found. Given the relative ease with which the technique can be implemented, it is presumed that researchers have probably explored the use of aerosol delivery, but were either unsuccessful or are aware of significant limitations of the process for preform fabrication.

In Figure 2.8(e), a delivery system based on RE-chelates is shown. Chelates are organometallic compounds that have a significantly higher vapour pressure than RE chlorides and are volatized at a more manageable temperature of around 150 – 200 ºC

[39]. Although the chelate vapour source can be located external to the lathe, it still requires the entire line, including the rotary joint, to be maintained at around 150 ºC to prevent condensation during vapour transport.

The different preform fabrication routes described above address the need to transport dopant vapour to the reaction zone in a controllable manner as well as the specific properties of the precursor. The vapour pressure of the chosen precursor is critical to the method used and a comparison of the aforementioned precursors is shown in Figure 2.9. For RE chelate compounds the vapour pressures have been characterised by Sicre et al. and can range from approximately 0.1 kPa to 1 kPa (at 200 ºC) for the lanthanide series, with Yb among the highest at 1 kPa [39]. In contrast, the vapour pressure of RE chlorides is considerably lower and typically requires a temperature of around 1000 ºC to achieve 1 kPa [40], although data extrapolated from a publication by Moriarty [41] suggests that in the case of $YbCl_3$ the vapour pressure at this temperature is nearer 0.2 kPa.

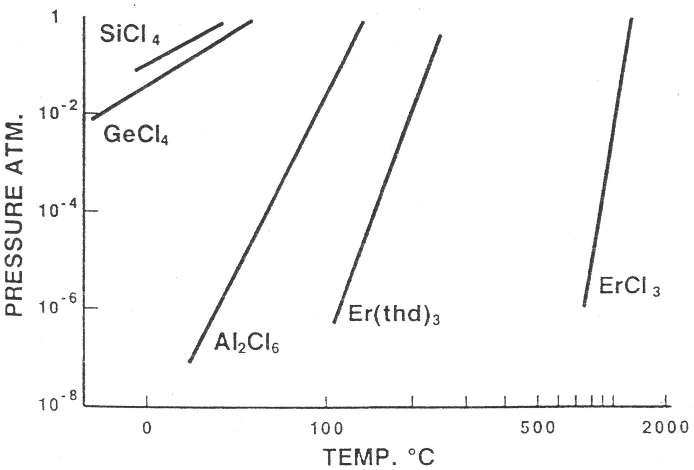

Figure 2.9: Comparison of the vapour pressures of conventional halide precursors ($SiCl_4$ and $GeCl_4$), aluminium chloride (Al_2Cl_6), RE chelate ($Er(thd)_3$) and erbium chloride ($ErCl_3$) [33].

As well as the difference between the vapour pressure of RE chlorides and chelate complexes, the oxidation reactions that take place are also important in understanding their use in MCVD. At elevated temperatures, RE chlorides undergo an oxidation reaction and in the case of ytterbium the conversion from $YbCl_3$ to Yb_2O_3 is shown below,

$$4YbCl_3 + 3O_2 \rightarrow 2Yb_2O_3 + 6Cl_2 \tag{2.6}$$

The temperature at which the reaction occurs is important for determining the correct oxidation temperature to use during preform fabrication. To calculate the likelihood of a chemical reaction, an equilibrium constant can be calculated for the reaction at a specific temperature using,

$$\ln K = \frac{\Delta G}{-RT} \tag{2.7}$$

where K is the equilibrium constant, G is the Gibbs free energy ($J.mol^{-1}$), R is the ideal gas constant ($J.K^{-1}.mol^{-1}$), and T is the temperature (K).

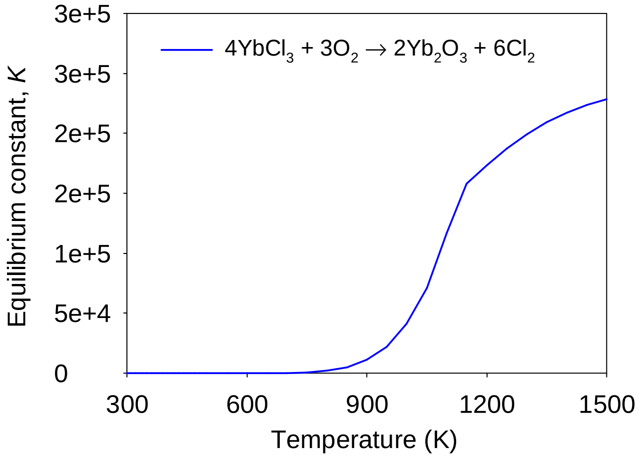

Figure 2.10: Equilibrium constant for the oxidation reaction of ytterbium chloride over the temperature range of 300 K up to 1500 K.

An equilibrium constant that is much larger than 1 indicates that the reaction has a strong tendency to lie in the product side of the reaction, whereas if K is much smaller than 1 then the reaction will consist of largely unchanged reactants. The equilibrium constant has been calculated for the reaction shown in (2.6) using on-line software [42] and is plotted in Figure 2.10. It is important to note that the oxidation of $YbCl_3$ can occur at temperatures lower than that at which significant vapour would evolve, and is key in understanding why the heated-source injector approach (shown in Figure 2.8(c)) separates the precursor vapour from the oxygen initially.

The high temperature reactions that take place with chelate compounds in the presence of oxygen are more complicated and have been studied by Xiong et al. [43]. Thermogravimetric (TG) and Differential Thermal Analysis (DTA) was conducted on Yb chelate samples ($Yb(O_2C_{11}H_{19})_3$) above their melting point of 169 ºC. It is reported that between a temperature of 200 ºC and 250 ºC the complex remains in the gas phase, with decomposition beginning at around 278 ºC. At specific temperatures of 423 ºC and 548 ºC, the decomposition products of hydrocarbon and carbon undergo oxidation, and at temperatures of above 650 ºC the decomposition and oxidation of the precursor is complete. These findings have been vital in understanding the use of chelate compounds in MCVD preform fabrication and this process is studied further in Chapter 4.

2.4 Optical fibre drawing

The second stage of the fabrication process is to convert the solid glass preform into fibre using a drawing tower. The exact configuration and specification of the equipment will depend on whether it is designed for manufacturing or research, although the basic components are essentially the same irrespective of the application. The major difference is that in commercial establishments, where hundreds of kilometres of fibre can be produced in a single day, the drawing speed can be in excess of 600 $m.min^{-1}$ in order to minimise operational costs. As the maximum drawing speed required increases, the physical height of the tower needs to be extended to ensure that the temperature of the fibre is sufficiently low upon reaching the coating applicator. Even at a distance of several metres from the furnace exit, the glass temperature can be >100 °C at a draw speed of 600 $m.min^{-1}$ [44]. Therefore, the height of the tower needs to be appropriate for the drawing speeds that are required. When increasing the tower height becomes impractical, forced cooling of the fibre is employed [44]. Additionally, specially-designed coating applicators and high-power curing ovens are required to cope with the high drawing speeds.

In stark contrast to a production environment, the drawing speeds used for fabricating speciality silica fibres within the Optoelectronics Research Centre (ORC) are typically in the range of 3 $\mathrm{m.min^{-1}}$ to 25 $\mathrm{m.min^{-1}}$. As such, the equipment specification is less demanding and a modest tower height of around 6 m is preferable so as to allow the operator to access all parts of the tower quickly. Moreover, the challenges in coating the fibre tend to be towards large diameters (up to 800 μm) and non-cylindrical geometries rather than high draw speeds. The key attributes of a drawing tower are detailed below and reflect the typical configuration of the towers that were used for the experimental work reported within this thesis.

A schematic of a research-grade drawing tower is shown in Figure 2.11. The preform is attached to a motorised chuck at the top of the drawing tower that slowly feeds the glass into the furnace at a rate of between 0.1 $\mathrm{mm.min^{-1}}$ and 10 $\mathrm{mm.min^{-1}}$. The furnace, which is resistively heated, is continually purged with argon during operation to prevent the graphite elements from oxidising (burning). An adjustable aperture at the top and bottom of the furnace reduces turbulent gas flows which would otherwise contribute to fluctuations in fibre diameter. To begin the drawing process, a sacrificial length of glass welded to the end of the preform, known as the ‘drop’, is positioned directly below the hot-zone of the furnace. The furnace temperature is then increased, and as the glass softens it tapers to form a necked-down region. The drop falls under gravity and is pulled downwards, by hand, before removing and transferring the fibre on to the capstan. The motorised mini-capstan is used for large diameter (>0.5 mm) uncoated glass fibres or capillaries and was utilised for the experimental work presented in Chapters 5 and 6.

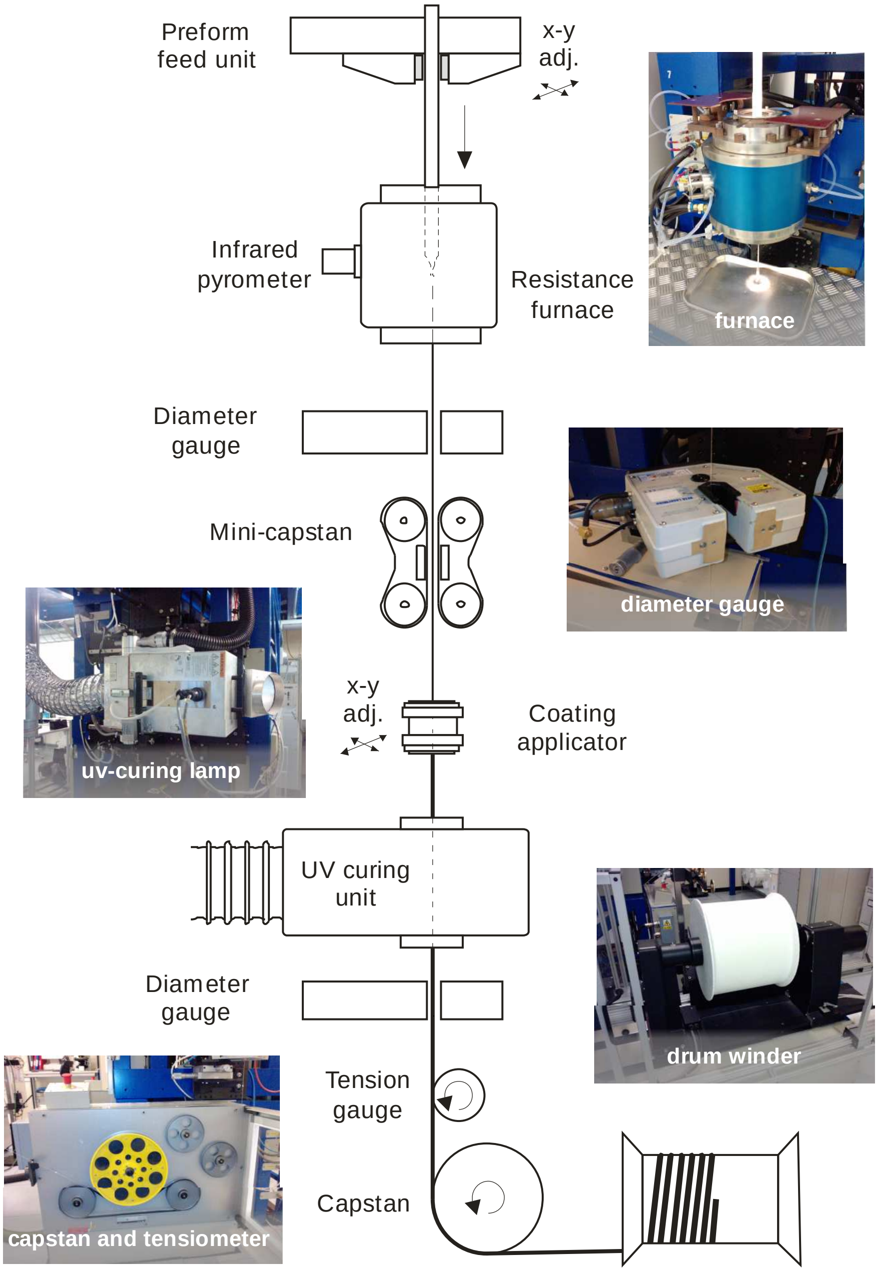

Figure 2.11: Illustration of a research-grade optical fibre drawing tower and identification of the key equipment.

Situated directly beneath the furnace is a laser diameter and position gauge that continuously monitors the fibre. Through a feedback loop to the control computer, the preform feed rate (υ_p) and capstan speed (υ_f) are varied in order to maintain a constant fibre diameter, typically to within ±1 μm. Once the draw reaches a steady state, the law of mass conservation can be applied, where the volume of the glass entering the furnace is equal to the volume of glass exiting the furnace. Thus the preform diameter (d_p) and fibre diameter (d_f) are related to feed rate and capstan speed by,

$$\frac{\upsilon_p}{\upsilon_f} = \frac{{d_f}^2}{{d_p}^2} \tag{2.8}$$

A liquid polymer or silicone-based coating is applied to the glass fibre during the drawing process which is subsequently cured, either thermally or with ultraviolet (UV) radiation. The function of the coating is predominantly to protect the optical fibre from abrasion and scratches and preserve its mechanical strength, but it also provides an optical interface for double-cladding fibre (section 2.6.3). For this purpose, the cured coating should exhibit low optical loss around the wavelength range of interest, and ideally be as thin as possible to aid heat extraction in high-power applications.

The two main types of UV-cured polymer coating used for the work described in this thesis are: DeSolite® 3471-3-14 (DSM Desotech, The Netherlands) and EFIRON® PC-373 (Luvantix, Korea), and are categorised by their cured refractive index (n) relative to that of silica ($n = 1.458$ at $\lambda = 633$ nm). DeSolite® 3471-3-14 coating, abbreviated to DSM-314 hereafter, has a higher refractive index than undoped silica ($n = 1.51$) and is designed for transmission fibre where it is necessary to ‘strip out’ any higher-order cladding modes which might otherwise couple with the signal in the core. PC-373 has a lower refractive index than silica ($n = 1.37$) and is applied to double-cladding fibre to enable the pump-light to be guided in the silica glass cladding region via total internal reflection.

The coating assembly can either be a gravity-assisted applicator or a closed pressurised system. Both comprise of a reservoir of liquid coating and a precision-engineered die through which the fibre is pulled. The pressurised applicator was introduced to combat the increased slip between the fibre and coating that occurs at high line speeds

(>300 $m.min^{-1}$) [45, 46]. The pressure required to force the liquid coating on to fibre is proportional to the capstan speed, for a fixed viscosity, and to a certain extent can be used to tailor the coating thickness [47]. However, an optimum pressure is reached when the shear rate is minimum, at which point the coated fibre diameter is a function of the fibre and die dimensions only [45]. The optimum pressure needed for the coating applicator is strongly influenced by the viscosity of the liquid coating. In the case of PC-373, the viscosity of the liquid coating is 7500 mPa.s at a temperature of 25 °C, and reduces to 2100 mPa.s at 40 °C. The viscosity of the higher-index DSM-314 is 7700 mPa.s at 25 °C, and has a comparable dependence on temperature. These coatings are typically heated to around 35 – 40 °C so that the pressures required during their application are within the practical range of the equipment.

Before the fibre passes on to the drum winder, the tension in the line is measured. This is performed on the coated fibre and relates to a combination of the bare fibre and coating tension. The measured tension will increase with reducing furnace temperature, as well as increasing draw speeds, and is normally kept within the range of 20 – 80 g. The measured tension provides additional information about the temperature of the glass in the hot-zone and complements the measurement of the furnace temperature obtained by the pyrometer.

A final additional piece of equipment, which is mainly found on a drawing tower designed for research and development, is a preform pressurisation and vacuum facility. This is used for microstructured optical fibre drawing, where it is necessary to control and manipulate the shape of air holes in the preform, and is used for the work presented in Chapters 5 and 6. The pressure inside the preform tube is monitored and controlled through a hollow preform handle, on to which a pipeline is connected. The control mechanism can take the form of a closed loop MFC which continually adjusts the flow of N_2 or He to maintain a specific pressure, or equally, can comprise of a simple arrangement of manual gas valves and a sensitive pressure gauge. It is usual to be able to switch the pipeline to a vacuum pump in order to obtain pressures below atmosphere.

Pressure ranges of ±50 mbar (relative to atmospheric), which are controllable to within ±0.1 mbar, are typical.

2.5 Measurement techniques

The need to qualitatively assess the optical properties of different fibres in a comparable way has led to professional organisations developing various standardised procedures for their measurement. These procedures are now widely recognised, as too are the measurement techniques and equipment involved. The equipment and analytical methods that were used throughout this thesis are based on these standards and are described below.

2.5.1 Preform analysis

During the MCVD preform fabrication process there is no reliable means of measuring the composition or thickness of the deposited layers. Therefore, the material properties are analysed once the process is complete and tube has been collapsed into a solid preform. The refractive index and geometry of the deposited glass are evaluated using an industry standard Preform Analyzer (Photon Kinetics, US). The model used for the measurements reported herein was the PK2600HP as is shown in Figure 2.12(a).

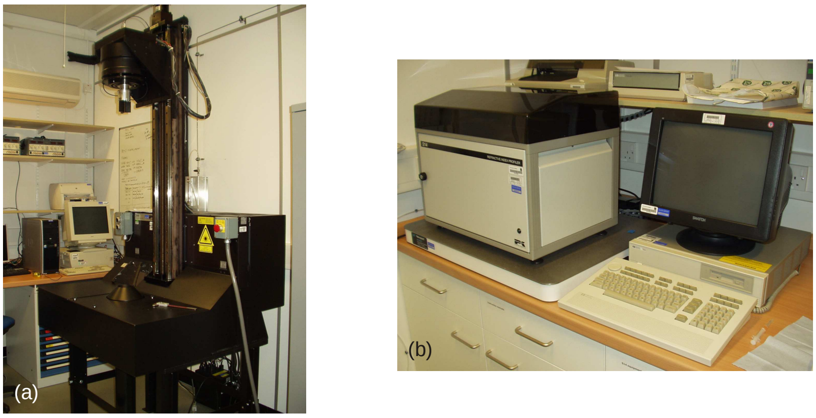

Figure 2.12: Photographs of the preform and fibre measurment equipment used throughout the experimental work. (a) Preform Analyser PK2600HP and (b) Refractive Index Profiler S14, both manufactured by Photon Kinetics (US).

The principle of operation involves scanning a focussed laser beam across the diameter of the preform and measuring its deflective angle at various points [48]. From this data a RIP is calculated which expresses the measured index difference relative to a liquid of known refractive index in which the preform is immersed. The PK2600HP is fully automated and can perform multiple measurements longitudinally along the preform, as well as at different rotational angles to assess any ovality in the deposited core.

2.5.2 Fibre analysis

The RIP of an optical fibre should mimic that of the original perform (with the core features scaled down proportionately) and so profiling the fibre is not necessarily required. However, if it is suspected that the core dopants in the fibre have diffused radially, or a more accurate measurement of the core diameter is required, a RIP measurement can be performed [49]. The equipment used for the experimental work was the S14 Refractive Index Profiler (Photon Kinetics, US), shown in Figure 2.12(b). The measurement is performed by inserting a cleaved fibre sample inside a specially designed cell which contains a refractive index gel. A focussed laser beam then scans through a transparent window at the base of the cell on to the fibre end and the refracted light is collected by an optical sensor. The measured angle of refraction is used to determine the index of the fibre at a given point and a 3-dimensional profile of the fibre is constructed.

2.5.3 Fibre transmission measurements

The properties of an optical fibre such as the spectral loss and the RE constituents can all be measured with a ‘white-light’ set-up, and this method was used extensively during the experimental work. The apparatus consists of a light source (typically a tungsten-bulb) which is free-space coupled into the sample fibre via an objective. The light exiting the fibre is then captured by an optical spectrum analyser (OSA) and the intensity recorded as a function of the wavelength. By monitoring the transmission characteristics of a fibre across the visible and near-infrared wavelength range (typically from 400 nm to 1700 nm) the OSA can provide information about the RE concentration as well as any OH ion impurity. This is conveyed by absorption bands which are observed at frequencies that are specific to a particular atom or molecule. From the intensity of the absorption, the ion concentration can then be calculated.

To measure the attenuation in fibre samples a cutback method can be performed using a white-light setup. Light is launched into the longest length of fibre possible without incurring excessive degradation of the signal light and the spectrum is recorded on the OSA. The fibre is then cut to a length of ~1 m and the light exiting the fibre is re-measured. The loss in the fibre is then a subtraction of the two spectra and is normally converted to a logarithmic scale and expressed as decibels per kilometre (dB.km^{-1}). By using this approach, where the launch conditions in both measurements remain unaltered, the emission characteristics of the light-source itself are eliminated from the measurement.

The loss in an optical fibre can also be evaluated using Optical Time Domain Reflectometry (OTDR) [50]. This method involves injecting optical pulses into a fibre and measuring the backscattered Rayleigh signal. The intensity and arrival time of the detected signal then allows a loss to be calculated as a function of fibre length. A long optical pulse width with return a higher intensity signal, whereas a shorter pulse will provide better spatial information. A high resolution v-OTDR (Luciol Instruments, Switzerland) with a laser source at a wavelength of 1285 nm was available during the experimental work and was used to compare the results obtained using the white-light set-up.

2.6 Ytterbium doped fibre lasers

The motives for introducing RE ions into silica fibre for the purpose of light amplification are numerous. Optical fibre lends itself well to a lasing medium, and the inherent geometry means that it is robust, can be compactly coiled, and unlike bulk materials, it has a large surface-to-volume ratio allowing it to dissipate excess heat generated during lasing.

The foremost RE dopants used in silica optical fibre are neodymium (Nd), ytterbium (Yb) and erbium (Er). Nd^{3+} ions were one of the first RE dopants to be incorporated into silica fibres for the purpose of light amplification. They can be pumped at around $\lambda = 0.80\ \mu m$ with laser diodes, and have an emission wavelength of $\sim 1.08\ \mu m$ [51]. Glasses doped with Er^{3+} ions have a laser transition around $\lambda = 1.53\ \mu m$ and are most renowned for their use as the erbium-doped fibre amplifier (EDFA) [52]. These glasses can also be sensitised with Yb^{3+} to produce an Yb co-doped Er fibre laser [53]. This symbiotic relationship allows the fibre to be pumped with alternative light sources within the Yb^{3+} absorption band, and the energy is subsequently transferred to the Er^{3+} ions. The typical emission wavelength of Yb^{3+} in a silica glass is around $\lambda = 1.06\ \mu m$, and for most modern high-power laser applications Yb-doped fibres are the preferred choice. Yb^{3+} ions in silica benefit from a broad-gain bandwidth, a long lifetime in the excited state (~1 ms), and can be incorporated into a silica host in relatively high concentrations [8].

The experimental work on RE incorporation detailed within this thesis focuses exclusively on Yb because of the current interest in high-power fibre lasers. This section provides a brief background on amplification and lasing in RE-doped glasses and introduces the concept of a double-cladding optical fibre which is relevant to Chapters 3 and 4.

2.6.1 Electronic structure of ytterbium

The energy level structure of Yb^{3+} is relatively simple compared to other lanthanides owing to only one missing electron from the 4f shell. Yb^{3+} comprises of only two manifolds: the upper $^2F_{5/2}$ level and a lower $^2F_{7/2}$ level, which are split further into three upper and four lower Stark levels (see Figure 2.13). Yb^{3+} ions in a silica host absorb over a wide wavelength range and produce two distinct maxima centred at 915 nm and

975 nm, which correspond to transitions originating from the ground level *a* up to levels *e*, *f* and *g* [54]. The emission spectrum of Yb^{3+} ions also extends over a broad wavelength range from 970 nm up to 1200 nm and exhibits two peaks at around 975 nm and 1030 nm. The narrow emission line seen at 975 nm is characterised by a transition that returns the electron to its ground state (*e* to *a*) and in a laser configuration this corresponds to a quasi-three level system. However, owing to re-absorption at this wavelength, Yb-doped fibres are typically operated as a quasi-four level laser system, where the lower level is situated above the ground state. Here, the ions are pumped at 915 nm into the upper sublevels *f* and *g* which then decay into the $^2F_{7/2}$ manifold above the ground level and emission is observed at around 1030 nm [54].

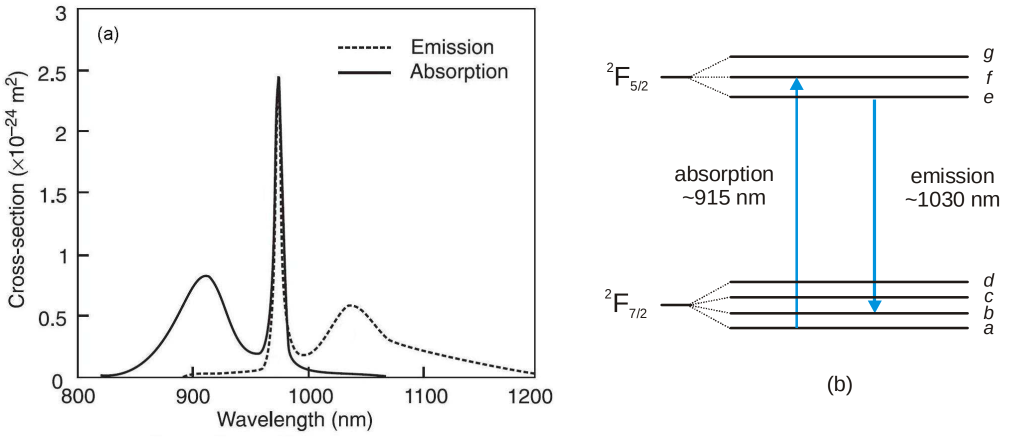

Figure 2.13: (a) Absorption and emission cross-section of Yb-doped silica glass [55], and (b) an illustration of the energy level structure of Yb^{3+} showing the upper and lower Stark levels.

In addition to the laser transitions described above, there are also non-radiative transitions which can impair the performance of RE-doped fibre lasers. These transitions arise from interactions between either the host glass and RE ions or, when the RE ion separation is small, between the dopant ions themselves. RE ions which interact with vibrations in the host lattice result in relaxation of the excited atom through the emission of multiple phonons. The number of phonons will depend on the gap between the energy states of the RE ion and the phonon energy of the glass. The probability of non-radiative relaxation is low when a large number of phonons are required to bridge the energy gap, whereas the relaxation rate is comparably higher in a high phonon energy glass such as silica.

Interactions that occur between multiple RE ions also lead to non-radiative transitions and are a type of concentration quenching. When RE ions within the glass are in close proximity, energy can be transferred to adjacent ions through processes such as cross-relaxation and cooperative up-conversion [6]. Although this process is beneficial for devices such as Er:Yb fibre amplifiers [53], the sharing of energy in an excited ion usually leads to non-radiative decay back to the ground level. Energy transfer can also occur between RE ions and other impurities in the glass such as OH. OH quenching is a parasitic effect that greatly reduces the radiative transition rate in actively-doped fibres and provides a motivation for reducing impurities in doped silica glass.

2.6.2 Optical amplification and lasing

Light amplification exploits a process known as stimulated emission. Radiation, of the correct wavelength, incident on an atom is absorbed causing excitation of an electron into a higher energy state. The arrival of another photon then relaxes the electron back to the minimum energy ground level, prompting the emission of a second photon. The optical properties of this second photon are identical to those of the incident photon and its wavelength is dictated by the difference between the two energy levels. For optical amplification to occur, proportionally more electrons must reside in an upper energy level than the lower energy level, a condition known as population inversion. Stimulated emission then dominates over absorption, and a net gain can be achieved.

The principle of light amplification can be used to construct a RE-doped laser oscillator by placing mirrors (or typically Bragg gratings in the case of a fibre laser) at each end of the gain medium. The mirrors are selected to be highly reflective at the emission wavelength and of low reflectivity at the wavelength of the pump light. The lasing medium is then pumped continuously to maintain a population inversion and a small proportion of the emitted photons then exit the cavity as the laser output.

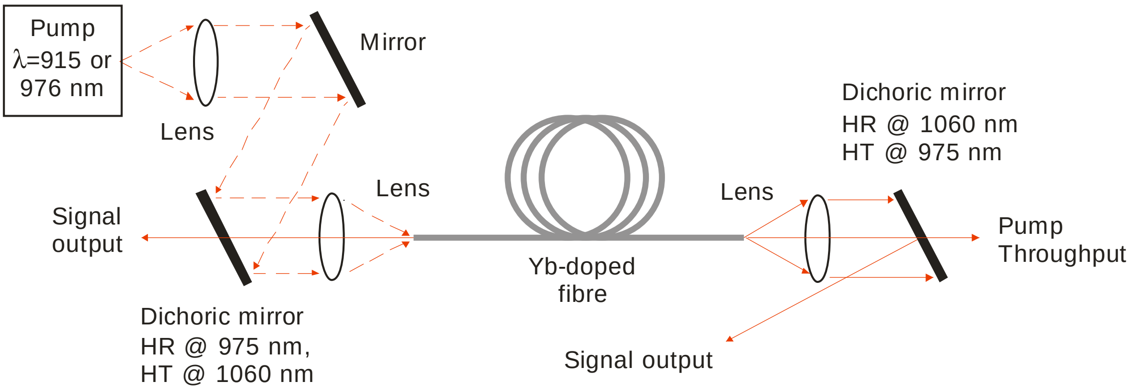

Figure 2.14: Schematic of the experimental setup for measuring the laser efficiency in a Yb-doped fibre. HR and HT correspond to high reflection and high transmission, respectively, at the stipulated wavelength.

Figure 2.14 shows a schematic of an experimental setup for measuring the laser efficiency of an Yb-doped fibre, and is referenced in Chapters 3 and 4. The laser efficiency is defined as the ratio of the output power to the input pump power. The pump source, which is typically a laser diode with an operating wavelength of 976 nm, is free-space coupled into the Yb-doped fibre via collimating and focusing lenses. The fibre ends are cleaved perpendicularly to its axis and the 4 % Fresnel reflections form the laser cavity. The output signal is then separated from the pump beam using dichroic mirrors at each end.

2.6.3 Double-cladding fibre

Achieving increasingly higher output powers in fibre lasers is ultimately limited by the need to launch high pump powers directly into the active core of the optical fibre. Core-pumping schemes that require single-mode (SM) output from the fibre also necessitate SM pump sources. The double-cladding fibre (DCF) was developed to allow high-power multi-moded sources with a low beam quality, such as diode bars and stacks, to be used for the pump light, and is now the accepted geometry for high-power fibre lasers.

A schematic of a DCF is shown in Figure 2.15. The laser light travels in the central core of the fibre which is doped with active ions. Surrounding the core region is the inner-cladding, into which the multi-moded pump light is launched. The pump is confined to the inner-cladding region by the lower refractive index of the polymer cladding and absorbed by the active ions in the core as it propagates.

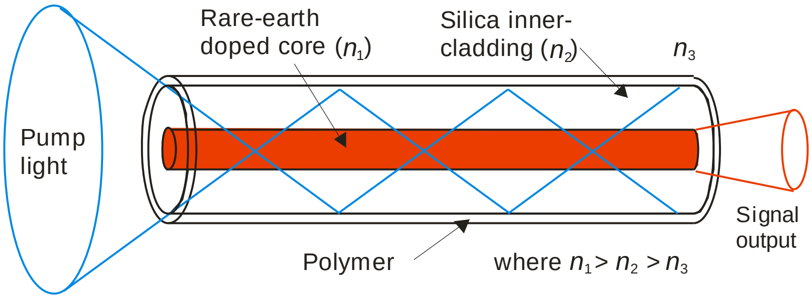

Figure 2.15: Illustration showing the operation of a cladding-pumped optical fibre laser. Pump light is launched into the inner-cladding which crosses the rare-earth doped core as it propagates.

The area of the inner-cladding in a DCF is significantly larger than that of the core, and therefore supports many modes. Most of these optical modes will intersect the core region as intended, but some will follow a helical path along the fibre length and exhibit a negligible overlap with the active ions. Furthermore, the mode distribution in the inner-cladding also becomes sensitive to the launch conditions and influences the absorption in the fibre. To resolves these issues, the circular symmetry of the inner-cladding is removed. There are numerous reports in the literature of geometric designs that initiate a break in the symmetry of the fibre including, off-centre core, rectangular inner-cladding, hexagonal cladding and D-shaped [56] (see Figure 2.16). All of these fibre structures provide a significant improvement in the absorption efficiency which, compared to a circularly symmetric profile, is more than doubled [57]. However, it is a simple D-shaped design that is generally adopted and which ensures an efficient overlap of the pump light with the fibre core. Also, the shape is not too dissimilar to conventional fibres that splicing becomes an issue [56].

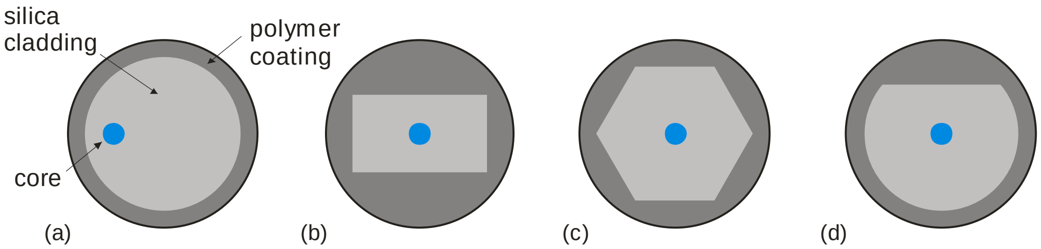

Figure 2.16: Cross-sectional representations of DCF geometries, (a) offset core, (b) square, (c) hexagonal and (d) D-shaped, used to improve the pump absorption efficiency in RE-doped fibres..

The D-shape in the fibre is produced by machining a flat indentation on the surface of the glass preform. The preform is secured horizontally on a reference block, and a rotating grinding tool traverses back and forth removing around 200 µm of glass in each pass. An overall reduction in preform diameter of ~10 % is normally targeted and typically takes 1 – 2 hours to complete. The milling process can be repeated on multiple faces in order to produce square or hexagonal cross-sectional profiles.

2.7 Sensing using optical fibre

Sensing devices that are based on optical fibres can be found in countless applications. Their abundance can be largely attributed to the potential of improved functionality and better suitability for demanding applications, compared to electrical sensors. The physical attributes of optical fibres make them an attractive candidate for sensing applications: they are robust, can be compactly coiled, and can withstand hostile environments and high temperatures. Furthermore, the inherently low optical loss of silica fibres means that sensing points can be distributed over long distances without incurring deterioration of the signal light.

Optical fibre sensors can be classified on the basis of their application and the properties that are being measured or distinguished. The application of a sensor may be based on physical (e.g. pressure, strain and displacement), chemical (e.g. pH content, gas analysis) or biomedical (e.g. endoscopy) measurements, which are detected through modulation of the transmitted light [58]. Another important distinction is whether the sensing mechanism is ‘intrinsic’ or ‘extrinsic’. Intrinsic sensors use the fibre itself as the sensing element, which directly interacts with the measurand, whereas extrinsic sensors rely on an external optical device to detect changes in its surroundings, and the optical fibres relay the information.

The sensing architecture can consist of measurements that are made at single or multiple points along the length of the fibre, or distributed over the entire length. In Chapter 5, gas sensing that uses the entire length of a MOF as the sensing element is reported, whereas the work reported in Chapter 6 was aimed at a multiple point, or quasi-distributed, sensing arrangement. Both of these approaches are based on the principle of evanescent-field sensing which is described below.

2.7.1 Evanescent-field sensing

The light in conventional optical fibre propagates in the central core and is confined by the lower refractive index of the surrounding cladding by total internal reflection. At the boundary between these two media, a small percentage of the propagating wave, known as the evanescent-field, penetrates into the silica cladding. Outside the confines of the core, the electric-field strength decreases exponentially and a small proportion of the total energy travels unhindered in the low-loss silica cladding [3]. If the cladding material of an optical waveguide is partially removed, the evanescent-field is able to interact with its surroundings. The properties of the medium outside the core can then be discerned by detecting a change in the transmitted light at the output end of the fibre. For example, a simple refractive index sensor can be constructed using this principle, where a change in the index contrast between the core material and that of the surrounding medium is conveyed as an intensity modulation of the guided light. This type of approach can be expanded to quantify numerous properties about the material surrounding the core [59].

The detection sensitivity of an optical fibre sensor will depend predominantly on the extent that the light overlaps the sample being measured, and the interaction length. The distance that the evanescent-field extends outside the core region is known as the penetration depth, and is defined as the distance required for the electric-field amplitude to drop to e^{-1} of its value at the interface [20]. For a modest index contrast, such as that in a conventional SM fibre, the penetration depth will be only a few microns, at most.

2.7.2 Realisation of optical fibre sensors

To realise an evanescent-field sensor using an optical fibre, the glass cladding must be removed in order to access the light in the core. Chemical or mechanical means can be employed for this purpose, but both methods require the process to be accurately controlled so that an appreciable proportion of the evanescent-field is exposed without causing severe disruption to the light guiding properties of the fibre. Side-polishing the fibre is one such method, and is achieved using abrasive powders to polish an isolated section of the optical fibre which is held secure in a solid block [59]. The benefit of this approach is that the transmission in the fibre can be simultaneously monitored whilst the cladding is being removed to reveal when the polished facet is near the core.

As previously stated, the detection sensitivity also depends on the interaction length, and in side-polished fibres, where only a small region of glass cladding is removed, the interaction length is typically a few centimetres. However, if the polishing is performed on the glass preform prior to fibre drawing, the interaction length can be increased to several metres [60]. This extended interaction length is a significant advancement for sensing applications but the overall sensitivity of side-polished fibre is still relatively low, and heavily dependent on the accuracy of the initial glass removal in the preform. Furthermore, the resultant fibre shape is difficult to splice to conventional circular fibre, and although side-polished fibre has been around for many years, integration difficulties have limited its appeal for most applications.

Microstructured optical fibres (MOF) offer one of the most attractive options for a sensing platform. The intrinsic overlap between the propagating light and the air-cladding makes them ideal for sensing gases and liquids residing in the holes. The long interaction length also means that MOF-based sensors are able to characterise a variety of trace elements within the transmission window of silica glass. For example, resolving the absorption lines of a known gas species within the holes of the fibre can be used to create a compact alternative to the free-space gas cells used for wavelength references [61]. Although most early index guiding silica MOF designs exhibited a weak interaction with the sample (<1 %) [62], in recent years new fibre designs have seen this figure increase significantly. Evanescent-field gas sensing is the focus of the work presented in Chapter 5, and a new technique for fabricating MOF with a high air-filling fraction is reported.

2.8 References

1. R.H. Doremus. "Viscosity of silica". *Journal of Applied Physics*, 92(12): 7619-7629, (2002).
2. A. Yamane and Y. Asahara, *Glasses for photonics*. Cambridge University Press. (2000).
3. J.M. Senior, *Optical Fiber Communications: Principles and Practise.* International Series in Optoelectronics: Pearson Education, Prentice Hall. (1992).
4. O. Humbach, H. Fabian, U. Grzesik, U. Haken, and W. Heitmann. "Analysis of OH absorption bands in synthetic silica". *Journal of Non-Crystalline Solids*, 203: 19-26, (1996).
5. W.H. Zachariasen. "The atomic arrangement in glass". *Journal of American Chemical Society*, 54(10): 3841-3851, (1932).
6. S. Sudo, *Optical Fiber Amplifiers: Materials, Devices, and Applications.* Artech House. (1997).

7. J. Laegsgaard. "Dissolution of rare-earth clusters in SiO2 by Al codoping: A microscopic model". *Physical Review B (Condensed Matter and Materials Physics)*, 65(17): 174114-1, (2002).

8. P. Barua, E.H. Sekiya, K. Saito, and A.J. Ikushima. "Influences of Yb^{3+} ion concentration on the spectroscopic properties of silica glass". *Journal of Non-Crystalline Solids*, 354(42-44): 4760-4764, (2008).

9. K. Arai, H. Namikawa, K. Kumata, T. Honda, Y. Ishii, and T. Handa. "Aluminium or phosphorus co-doping effects on the fluorescence and structural properties of neodymium-doped silica glass". *Journal of Applied Physics*, 59(10): 3430-3436, (1986).

10. T. Li, *Optical Fibre Communications.* AT&T Bell Laboratories: Academic Press. (1985).

11. P.C. Schultz. "Fabrication of optical waveguides by the outside vapor deposition process". *Proceedings of the IEEE*, 68(10): 1187-1190, (1980).

12. T. Izawa and N. Inagaki. "Materials and processes for fiber preform fabrication-Vapor-phase axial deposition". *Proceedings of the IEEE*, 68(10): 1184-1187, (1980).

13. J.B. MacChesney, P.B. O'Connor, and H.M. Presby. "A new technique for the preparation of low-loss and graded-index optical fibers". *Proceedings of the IEEE*, 62(9): 1280-1281, (1974).

14. P. Geittner, D. Kuppers, and H. Lydtin. "Low-loss optical fibers prepared by plasma-activated chemical vapor deposition (CVD)". *Applied Physics Letters*, 28(11): 645-646, (1976).

15. S. Tammela, M. Soderlund, J. Koponen, V. Philippov, and P. Stenius. "The potential of direct nanoparticle deposition for the next generation of optical fibers." in *Proceedings of SPIE - Optical Components and Materials III San Jose, CA*. 61160G-9, (2006).

16. Y. Wu, H. Xin, L. Zhang, Z. Zhuo, Y. Yu, W. Zheng, G. Liu, and Y. Zhang. "Fabrication of planar optical waveguide material on silicon by flame hydrolysis deposition." in *Proceedings SPIE - Optoelectronics, Materials, and Devices for Communications, China*. 251, (2001).

17. M.G. Blankenship and C.W. Deneka. "Outside Vapor Deposition Method of Fabricating Optical Waveguide Fibers". *IEEE Journal of Quantum Electronics*, 18(10): 1418-1423, (1982).
18. S.R. Nagel, J.B. MacChesney, and K.L. Walker. "Overview of the modified chemical vapor deposition (MCVD) process and performance". *IEEE Journal of Quantum Electronics*, QE-18(4): 459-476, (1982).
19. M. Pal, R. Sen, M.C. Paul, S.K. Bhadra, S. Chatterjee, D. Ghosal, and K. Dasgupta. "Investigation of the deposition of porous layers by the MCVD method for the preparation of rare-earth doped cores of optical fibres". *Optics Communications*, 254(1-3): 88, (2005).
20. A. Mendez and T.F. Morse, *Speciality Optical Fibers Handbook.* Academic Press. (2007).
21. K.L. Walker, F.T. Geyling, and S.R. Nagel. "Thermophoretic deposition of small particles in the modified chemical vapor deposition (MCVD) process". *Journal of the American Ceramic Society*, 63(9-10): 552-558, (1980).
22. Y.T. Lin, M. Choi, and R. Greif. "An analysis of the effect of the solid layer for the modified chemical vapor deposition process ". *Heat and Mass Transfer*, 28(4): 169-176, (1993).
23. I. Kasik and V. Mateijec. "New ways for influencing thermophoretic efficiency in the MCVD process". *Journal of Aerosol Science*, 26(3): 399-399, (1995).
24. M. Choi, C. Hong, and K.H. Lee. "Jet assisted aerosol chemical vapor deposition for optical fiber synthesis". *Aerosol Science and Technology*, 36(3): 300-307, (2002).
25. J.E. Townsend, S.B. Poole, and D.N. Payne. "Solution-doping Technique for Fabrication of Rare-earth Doped Optical Fibres". *Electronics Letters*, 23(7): 329-331, (1987).
26. S.B. Poole, D.N. Payne, R.J. Mears, M.E. Fermann, and R.I. Laming. "Fabrication and charaterization of low-loss optical fibers containing rare-earth ions". *Journal of Lightwave Technology*, LT-4(7): 870-876, (1986).
27. J.E. Townsend. "Thesis: The development of optical fibres doped with rare-earth ions". *Optoelectronics Research Centre*, (1990).

28. A. Dhar, M.C. Paul, M. Pal, A.K. Mondal, S. Sen, H.S. Maiti, and R. Sen. "Characterization of porous core layer for controlling rare earth incorporation in optical fiber". *Optics Express*, 14(20): 9006-9015, (2006).
29. F.Z. Tang, P. McNamara, G.W. Barton, and S.P. Ringer. "Nanoscale characterization of silica soots and aluminium solution doping in optical fibre fabrication". *Journal of Non-Crystalline Solids*, 352(36-37): 3799-3807, (2006).
30. F.Z. Tang, P. McNamara, and G.W. Barton. "Enhanced Al Incorporation in solution-doped Optical fibre Fabrication." in *ECOC European Conference on Optical Communications, Cannes, France*. 24-28 September, 1-2, (2006).
31. F.Z. Tang, P. McNamara, G.W. Barton, and S.P. Ringer. "Microscale inhomogeneities in aluminum solution-doping of silica-based optical fibers". *Journal of the American Ceramic Society*, 90(1): 23-8, (2007).
32. A. Dhar, M.C. Paul, M. Pal, S.K. Bhadra, H.S. Maiti, and R. Sen. "An improved method of controlling rare earth incorporation in optical fiber". *Optics Communications*, 277(2): 329-334, (2007).
33. M.J.F. Digonnet, *Rare Earth Doped Fiber Lasers and Amplifiers.* New York: Marcel Dekker. (1993).
34. S.B. Poole, D.N. Payne, and M.E. Fermann. "Fabrication of low-loss optical fibres containing rare-earth ions". *Electronics Letters*, 21(17): 737-738, (1985).
35. J. Kirchhof, S. Unger, and A. Schwuchow. "Fiber lasers: materials, structures and technologies." in *Proceedings of the SPIE - Optical Fibers and Sensors for Medical Applications III, USA*. 1-15, (2003).
36. T.F. Morse, L. Reinhart, A. Kilian, W. Risen, Jr., and J.W. Cipolla, Jr. "Aerosol doping technique for MCVD and OVD". *Proceedings of the SPIE - Fiber Laser Sources and Amplifiers*, 1171: 72-79, (1990).
37. T.F. Morse, A. Kilian, L. Reinhart, and J.R. Cipolla, Jr. "Aerosol transport for optical fiber core doping: a new technique for glass formation". *Journal of Aerosol Science*, 22(5): 657-666, (1991).
38. T.F. Morse, A. Kilian, L. Reinhart, W. Risen, Jr., and J.W. Cipolla, Jr. "Aerosol techniques for glass formation". *Journal of Non-Crystalline Solids*, 129: 93-100, (1991).

39. J.E. Sicre, J.T. Dubois, K.J. Eisentraut, and R.E. Sievers. "Volatile Lanthanide Chelates. II. Vapour Pressures, Heats of Vaporization, and Heats of Sublimation". *Journal of the American Chemical Society*, 91(13): 3476-3481, (1969).

40. R.C. Weast, *CRC Handbook of Chemistry and Physics.* CRC Press. (1984).

41. J.L. Moriarty. "Vapor Pressures of Yttrium and Rare Earth Chlorides Above Their Melting Points". *Journal of Chemical and Engineering Data*, 8(3): 422-424, (1963).

42. *Reaction-web*. Available from: http://www.crct.polymtl.ca/reacweb.htm.

43. L. Xiong, E.H. Sekiya, and K. Saito. "Mass fabrication of homogeneously Yb-doped silica nanoparticles and their spectroscopic properties". *Nanotechnology*, 20(1), (2009).

44. C.M.G. Jochem and J.W.C. Van Der Ligt. "Method for cooling and bubble-free coating of optical fibres at high drawing rates". *Electronics Letters*, 21(18): 786-787, (1985).

45. S. Sakaguchi and T. Kimura. "High-speed drawing of optical fibers with pressurized coating". *Journal of Lightwave Technology*, LT-3(3): 669-673, (1985).

46. L. Stormbom, R. Pennanen, and J. Kurki, *A high speed optical fibre double pressure coating system*, in *Wire and Cable Panorama*. 1986.

47. K. Chida, S. Sakaguchi, M. Wagatsuma, and T. Kimura. "High-speed coating of optical fibres with thermally curable silicone resin using a pressurised die". *Electronics Letters*, 18(16): 713-715, (1982).

48. P.L. Chu and T. Whitbread. "Measurement of refractive index profile of optical fibre preform". *Electronics Letters*, 15(10): 295-296, (1979).

49. K.W. Raine, J.G. Baines, and R.J. King. "Comparison of refractive index measurements of optical fibres by three methods". *IEE Proceedings*, 135(3): 190-195, (1988).

50. K. Aoyama, K. Nakagawa, and T. Itoh. "Optical time domain reflectometry in a single-mode fiber". *IEEE Journal of Quantum Electronics*, QE-17(6): 862-8, (1981).

51. R.J. Mears, L. Reekie, S.B. Poole, and D.N. Payne. "Neodymium-doped silica single-mode fibre lasers". *Electronics Letters*, 21(17): 738-740, (1985).
52. R.J. Mears, L. Reekie, I.M. Jauncey, and D.N. Payne. "Low-noise erbium-doped fibre amplifier operating at 1.54 um". *Electronics Letters*, 23(19): 1026-1028, (1987).
53. M.E. Fermann, D.C. Hanna, D.P. Shepherd, P.J. Suni, and J.E. Townsend. "Efficient operation of an Yb-sensitised Er fibre laser 1.56 um". *Electronics Letters*, 24(18): 1135-1136, (1988).
54. A.S. Kurkov, V.M. Paramonov, and O.I. Medvedkov. "Ytterbium fiber laser emitting at 1160 nm". *Laser Physics Letters*, (10): 503-506, (2007).
55. J. Swiderski, A. Zajac, M. Skorczakowski, Z. Jankiewicz, and P. Konieczny. "Rare-earth-doped high-power fiber lasers generating in near infrared range". *Opto-Electronics Review*, 12(2): 169-173, (2004).
56. H.R. Muller, J. Kirchhof, V. Reichel, and S. Unger. "Fibers for high-power lasers and amplifiers". *Academie des Sciences. Comptes Rendus, Physique*, 7(2): 154-62, (2006).
57. P. Filip, A. Grobelny, and J.S. Witkowski. "Efficiency of active double-clad fiber pumping in different types of fibers." in *International Conference on Transparent Optical Networks ICTON, NJ*. 353-356, (2008).
58. J.M. López-Higuera, *Handbook of optical fibre sensing technology*. Wiley-Blackwell (2002).
59. A. Gaston, I. Lozano, F. Perez, F. Auza, and J. Sevilla. "Evanescent wave optical-fiber sensing (temperature, relative humidity, and pH sensors)". *IEEE Sensors Journal*, 3(6): 806-811, (2003).
60. F.A. Muhammad and G. Stewart. "D-shaped optical fibre design for methane gas sensing". *Electronics Letters*, 28(13): 1205-1206, (1992).
61. Y.L. Hoo, W. Jin, H.L. Ho, D.N. Wang, and R.S. Windeler. "Evanescent-wave gas sensing using microstructure fiber". *Optical Engineering*, 41(1): 8-9, (2002).
62. T.M. Monro, D.J. Richardson, and P.J. Bennett. "Developing holey fibres for evanescent field devices". *Electronics Letters*, 35(14): 1188-9, (1999).

Chapter 3

In-situ Solution Doping Technique

3.1 Introduction

The conventional Modified Chemical Vapour Deposition (MCVD) process used for silica preform fabrication does not support the delivery of rare-earth (RE) chemicals with a standard bubbler system, owing to the low vapour pressure of RE halide compounds at room temperature. To overcome this limitation, a liquid-phase preparation of the preform is used, known as solution doping [1]. Almost since its conception, solution doping has been the leading technique for incorporating RE ions into silica preforms as a result of its simplicity and low cost to implement. Its drawbacks, however, arise when multiple layers or complex preform structures are required, as the substrate tube must be removed from the preform-making lathe for each doped layer, progressively reducing the usable length of preform. Moreover, there is the potential for introducing contamination and disturbing the fragile porous soot layer when the glassware is transferred to the apparatus for solution infiltration. When combined with the duration needed for the dopant solution to fully saturate the soot layer, the entire process becomes a time consuming operation and only practicable for a maximum of 3 RE-doped layers.

In this chapter, a new doping technique is presented, termed *in-situ solution doping*, which is suitable for fabricating actively-doped preforms with complex refractive index profiles (RIP) using conventional RE halide precursors [2, 3]. The need to dismantle, and reassemble the glassware from the preform-making lathe is removed, which considerably reduces the processing time for each layer, and increases the overall preform yield compared to traditional solution doping.

The first section is a prelude to the experimental work and introduces some of the existing RE-doped fibre designs that are currently favoured for high-power fibre laser applications. The work that has been conducted on simulating these fibre designs, and understanding their preform fabrication requirements, is then presented. In particular, those preforms that incorporate a large diameter RE-doped core or a pedestal RIP were targeted. The in-situ solution doping technique is then described and the process refinements that have been made are highlighted. Thereinafter, demonstrations of specific RE-doped preform designs are reported, all of which are based around multiple ytterbium (Yb)- and aluminium (Al)-doped glass layers, and which represent preform structures that are unobtainable using conventional solution doping. Details of the preform fabrication process are explained in each case, and characterisation results from the drawn fibres are presented. Finally, a summary of the work is provided.

3.2 Rare-earth doped fibre designs

Recent advances in the design of RE-doped fibre lasers have been pivotal in attaining the high output powers that are now possible, and were achieved principally through optimising the refractive index and doping concentration profile [4, 5]. Increasing the output power from silica fibres in to the kilowatt regime, however, is hindered by the onset of nonlinear effects, such as stimulated Brillouin scattering (SBS) and stimulated Raman scattering (SRS). SBS and SRS limit the power scaling ability and performance of fibre laser systems, and improvements to the fibre design are needed to suppress these unwanted effects. The existing approaches to fibre design, and the difficulties in fabrication, are reviewed below.

Progress in scaling the output power of double-cladding fibre (DCF) lasers has largely been possible due to the large mode-area (LMA) fibre design [6]. LMA fibres are characterised by a step-function RIP and an extended core diameter (in the region of 20 to 30 μm), which reduces the power density and staves off the onset of parasitic nonlinear effects. Furthermore, as the size of the core region containing the active ions is increased, so too is the absorption per unit length, and consequently the overall length of the fibre device can be reduced. To maintain intrinsic single-mode (SM) guidance in a LMA fibre, it is necessary to reduce the numerical aperture (NA) of the core to ~0.06. The relationship between the number of guided modes in a fibre and the core NA is expressed by the normalised frequency parameter, V,

$$V = \frac{2\pi a}{\lambda} \mathrm{NA} \tag{3.1}$$

where a is the fibre radius and λ is the operating wavelength. For SM guidance to occur, the condition $V < 2.405$ must be satisfied. Core NA values <<0.06 lead to a high bending sensitivity (i.e. loss) and compromise the waveguiding capacity of the fibre. Therefore, there is a practical upper limit on the core diameter for purely SM operation.

If the geometry and operating wavelength of the fibre are such that higher-order modes are confined in the core, then mode filtering techniques can be used to institute SM guidance. Coiling the fibre is a convenient way in which to discriminate against higher-order modes, as the fundamental mode (LP_{01}) is least sensitive to the effect of bending [7]. In a fibre with a 40 μm diameter core and a NA of 0.05, a modest bend radius of 0.12 m is sufficient to impart a bend-induced loss in the LP_{11} mode of around 1 $dB.m^{-1}$ whilst the effect on the LP_{01} mode is negligible [8]. SM guidance can also be achieved by tailoring the launch conditions into the fibre so that the LP_{01} mode is preferentially excited [9]. Or alternatively, selective core doping, or differential mode gain, can be achieved by confining the active ions in the fibre to the central region of the core. The distribution of RE dopants is then tailored so that it closely matches the intensity field of the LP_{01} mode, and thus gain in higher-order modes is significantly reduced.

The power threshold for SBS is inversely proportional to the effective fibre length [10], and consequently a high RE absorption is normally targeted in order to minimise the limitations imposed by nonlinear effects. In combination with co-dopants, such as aluminium and phosphorous, the silica glass network has the capacity to accommodate relatively high concentrations of RE ions. The addition of these co-dopants, however, increases the refractive index of the glass and precludes the fabrication of fibres with a low-NA core. This has led to the development of a ‘pedestal’ RIP, which incorporates an inner-cladding region with a raised refractive index that surrounds the core [5]. It is then the effective refractive index between the core and the inner-cladding of the fibre that is responsible for optical guidance, and which can be designed to be of low-NA.

Applications where the polarisation of the signal light in a RE-doped fibre laser needs to be conserved are achieved through stress-induced birefringence, which decouples the polarisations of a SM core. The two main types of polarisation-maintaining (PM) fibres are ‘bow-tie’ and PANDA [11]. Both bow-tie and PANDA fibres incorporate borosilicate stress-applying regions to induce birefringence, but are fabricated in very dissimilar ways. Bow-tie fibres are fabricated entirely by MCVD, in a single-step process, with the stress regions deposited in-situ, prior to the core layer. Conversely, PANDA fibres are fabricated using a multi-step process, which involves drilling holes into a solid preform and inserting pre-fabricated borosilicate ‘stress rods’. Bow-tie fibres generally allow the most accurate control over the separation between the stress members and the core, although it is PANDA fibres that are considered to give the best preform scalability and reproducibility as a result of the decoupled fabrication stages [12]. The fabrication process for PANDA fibres is detailed further in subsection 3.3.8, with the demonstration of a pedestal RIP fibre featuring a unique aluminosilicate (Al:Si) inner-cladding.

The fibre types described above all present challenges when using MCVD and the solution doping process to fabricate the preform. The issues relate to an inability to deposit multiple RE-doped glass layers, which invariably means that before the preform can be drawn into fibre, it has to be sleeved or chemical etched to achieve the correct cladding-to-core diameter ratio. For preforms that incorporate a pedestal RIP, the raised refractive index of the inner-cladding is achieved using phosphorous (P) or germanium (Ge), as a plurality of glass layers can be deposited in the vapour-phase. However, the high concentration of Ge or P dopants in the glass leaves the final preform inherently stressed, due to the mismatch in thermal expansion compared to that of the undoped silica cladding. This consequently precludes any post-processing of the preform, and in particular, prevents holes from being drilled into the glass to fabricate PANDA fibres.

Although the solution doping technique is widely adopted, future high-power fibre laser designs will require complex RIPs and compositions, and the inherent constraints of the current approach are preventing these fibres from being realised. This has been the motivation behind developing the in-situ solution doping technique, and in particular, the work has concentrated on the use of multiple Yb-doped and Al-doped silica layers [3]. This composition leaves the preform non-stressed and allows post-processing of the glass to be performed in order to achieve novel fibre structures [13, 14].

3.3 Experimental Work

This section describes the experimental work that has been undertaken to develop the in-situ solution doping technique and demonstrate RE-doped preforms that have complex RIPs. Subsection 3.3.1 presents the computer simulation work that was performed on large-core and pedestal RIP fibres. Subsection 3.3.2 then examines the preform fabrication requirements based on these findings. Following a description of the in-situ solution doping technique in subsection 3.3.3, the fabricated preforms and fibres are described and the characterisation results are reported. The computer simulation work and modelling of large-core multi-layered preforms was all undertaken by the author, including the development of the process and fabrication of the preforms. The passive fibre characterisation was also completed by the author, whilst the laser performance measurements were conducted by Dr. Seongwoo Yoo.

3.3.1 Simulation of optical fibre modes

To understand the design criteria for large-core and pedestal RIP fibres, a study was conducted using numerical mode-solving software (OptiFiber) to analyse the optical modes that propagate in fibres with idealised RIPs. OptiFiber proprietary software operates by fibre mode solving of LP modes by finite difference and transfer matrix methods. The findings formed the basis of the fabricated preforms reported in the subsequent sections. Firstly, the condition for single-mode guidance was obtained by simulating a series of step-index RIPs, and varying the core diameter and refractive index contrast (Δn) between 6 – 34 μm and 0.001 – 0.005, respectively. Figure 3.1 shows the results of this computation, which was performed at operating wavelengths of 1550 nm and 1060 nm. The index of refraction used for the undoped silica cladding was taken as 1.458.

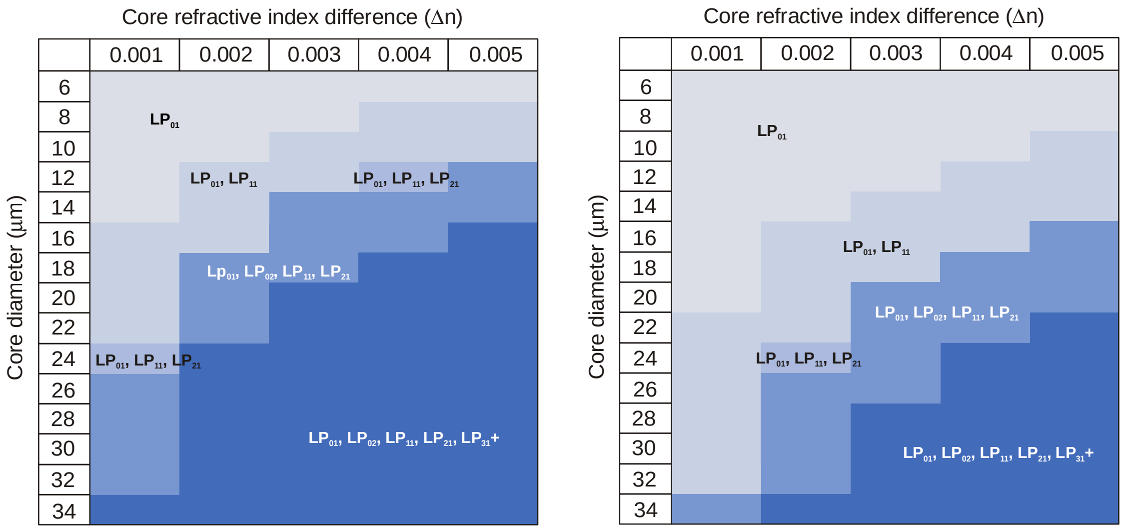

(a) Wavelength = 1060 nm (b) Wavelength = 1550 nm

Figure 3.1: The theoretical linearly polarised modes propagating in a step-function optical fibre, calculated using OptFiber software, at wavelengths of (a) 1060 nm and (b) 1550 nm.

It if is assumed that $\Delta n = 0.001$ represents the lowest practical index difference that can be achieved using the MCVD process, the maximum core diameter of a fibre that will support solely the LP_{01} mode at wavelengths of 1060 nm and 1550 nm is 14 μm and 20 μm, respectively. This means that a LMA fibre with a core diameter in the region of 20 – 30 μm, as is often quoted in the literature, will be multimoded, or few-moded, at this wavelength.

The simulation data shown in Figure 3.1 can also be applied to a fibre with a pedestal RIP, where the effective refractive index between the core and the inner-cladding (Δn_{eff}) is modelled as a simple step-function with an infinite cladding. This assumption, however, assumes that the medium surrounding the core, in this case the inner-cladding, behaves as a ‘true’ optical cladding and is of sufficient width. The diameter threshold for the inner-cladding was regarded as the point at which any further increase in its width had a negligible effect on the modal properties of the core [5].

In a step-index fibre with a core diameter of 25 μm and Δn of 0.001, it was predicted that four core modes will be supported at $\lambda = 1.06$ μm (Figure 3.1). Using OptiFiber software, a pedestal RIP was simulated with the dimensions of the effective core matching those of the step-index above. The overall core Δn was set to 0.01, which is indicative of the index rise in a highly RE-doped fibre. The mode field diameter (MFD), which describes the transverse distribution of the optical intensity, was then computed for inner-cladding widths that ranged from 1 μm to 30 μm. These results are plotted in Figure 3.2 for the lower-order modes.

The results indicate that the influence the inner-cladding width has on the MFD of the core modes reduces as its width increases. As the inner-cladding width is extended, it begins to behave as a ‘true’ optical cladding and not merely an extended core feature. The MFD of the modes in the simulated RIP are constant, to within <0.1 %, beyond an inner-cladding width of 17 μm. This equates to inner-cladding and core diameters of 59 μm and 25 μm, respectively, and a diameter ratio of 2.4.

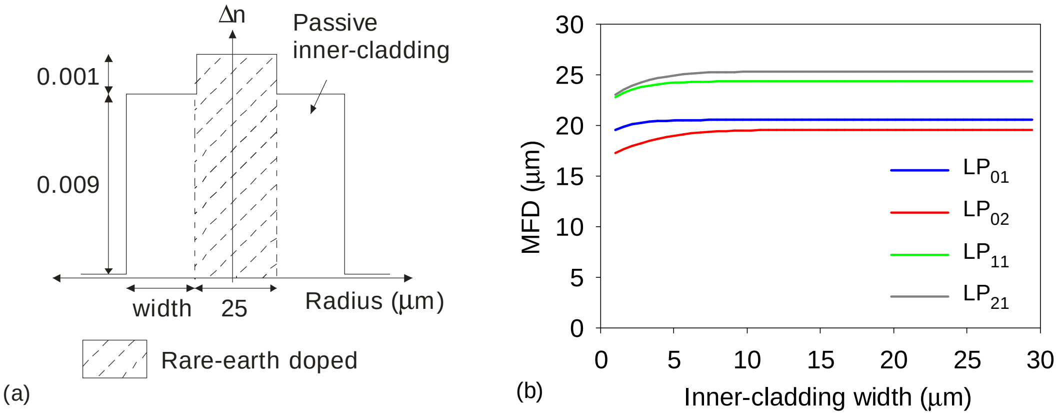

Figure 3.2: OptiFiber simulation analysing the effect of inner-cladding width on the core modes of a pedestal RIP fibre. (a) The simulated RIP, and (b) the MFD of the lower-order modes as a function of inner-cladding width.

The appropriate inner-cladding-to-core diameter ratio in the pedestal RIP will also depend on Δn_{eff} of the core. The core modes will spatially spread outwards as the Δn_{eff} is reduced, and therefore a larger inner-cladding width will be needed. The extent of this effect was investigated by applying the same type of MFD analysis as performed previously, with Δn_{eff} varied between 0.001 and 0.005. The results of the simulation are shown in Figure 3.3. For clarity of illustration, only the LP01 is shown.

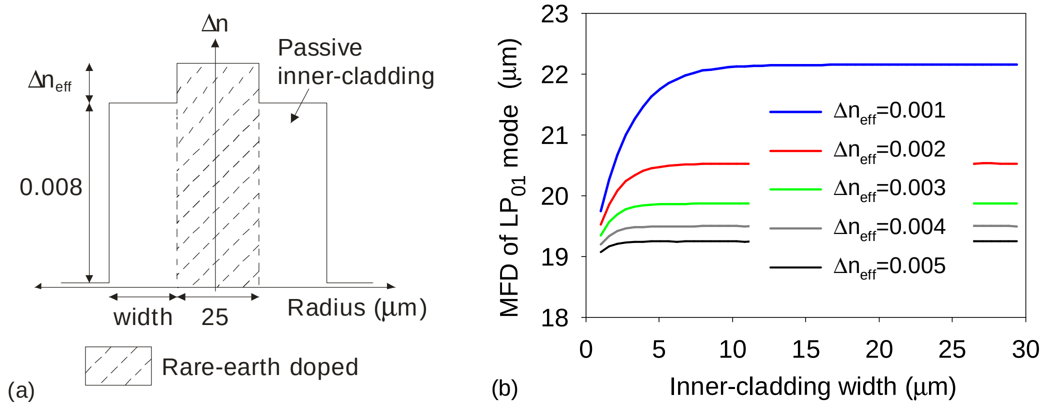

Figure 3.3: OptiFiber simulation analysing the effect of inner-cladding width on the LP_{01} mode of a pedestal RIP with different effective core indices. (a) The simulated RIP, and (b) the MFD of the LP_{01} mode as a function of inner-cladding for effective core indices of between 0.001 and 0.005.

The results indicate that as Δn_{eff} is reduced, a larger inner-cladding width is needed to ensure that optical guidance occurs in the designated core. For a Δn_{eff} of 0.001, 0.002, 0.003, 0.004 and 0.005, the inner-cladding width at which any further increase ceases to change the MFD of the LP_{01} mode (to within <0.1 %), was measured from the graph as 17.2 μm, 9.7 μm, 7.9 μm, 5.1 μm and 4.9 μm, respectively. This equates to a minimum inner-cladding-to-core diameter ratio of 2.4, 1.8, 1.6, 1.4 and 1.1 for a corresponding Δn_{eff} of 0.001, 0.002, 0.003, 0.004 and 0.005, respectively. It is believed that such a quantitative study has not been reported previously in the literature, and the findings formed the basis for design of the pedestal RIP fibre reported in section 3.3.6.

3.3.2 Modelling of multi-layered preforms

The motivations behind depositing multiple RE-doped layers in MCVD preforms were explained in section 3.2. This subsection presents practical and theoretical work that was undertaken to explore the relationship between the number of deposited layers and the size of the core in the final preform. This information was required in order to arrive at the preform recipes reported later in this chapter, and in particular those with a large diameter core and pedestal RIP.

In the MCVD process, the thermophoretic efficiency can be defined as the ratio between the amount of glass deposited on the tube wall and that formed by the initial chemical reaction, and will depend on many factors [15]. These include the burner velocity and flame profile, the wall thickness of the substrate glass, and the total gas flow inside the tube. Nagel et al. [16] reported that if the temperature inside the tube is sufficient for complete oxidation of the precursors, then the deposition efficiency will be strongly dependent on the burner parameters, but only weakly dependent on the gas flow rate and tube radius.

During preform fabrication, most of the lathe parameters such as the burner velocity and flame profile remain constant throughout the process, and in most cases are fixed for a particular MCVD system in order to promote reproducibility. Therefore, providing that the temperature inside the tube is high enough for complete oxidation (i.e. conversion of $SiCl_4$ into SiO_2) the deposition efficiency will be the same for each layer that is deposited. The emphasis of the work in this chapter, however, is on the deposition of soot layers (which are required for Yb-doping), and instead constitutes a regime where the particle formation may be limited by an incomplete reaction. In this case, the gas flow rate and tube radius are relevant, and Nagel et al. reported that the deposition efficiency will be dependent on effective transfer of particles to the tube wall [16]. As the tube radius will change between successive passes, through viscous collapse, the amount of glass deposited on the tube wall may vary between layers.

A pragmatic approach was taken to evaluate how the tube dimensions and reagent vapour flow rate used in MCVD influence the thickness of the core layers in the final preform. For the purpose of modelling, the deposited layers were viewed (at any given position along the tube length) as a circular ‘ring’ with a defined thickness and cross-sectional area (CSA). Figure 3.4 shows the parameters that were used for the calculations. Note that for clarity, the layer numbering is the reverse of the order in which they are deposited so as to ensure that the central layer is always denoted ‘layer 1’, regardless of the quantity of layers considered.

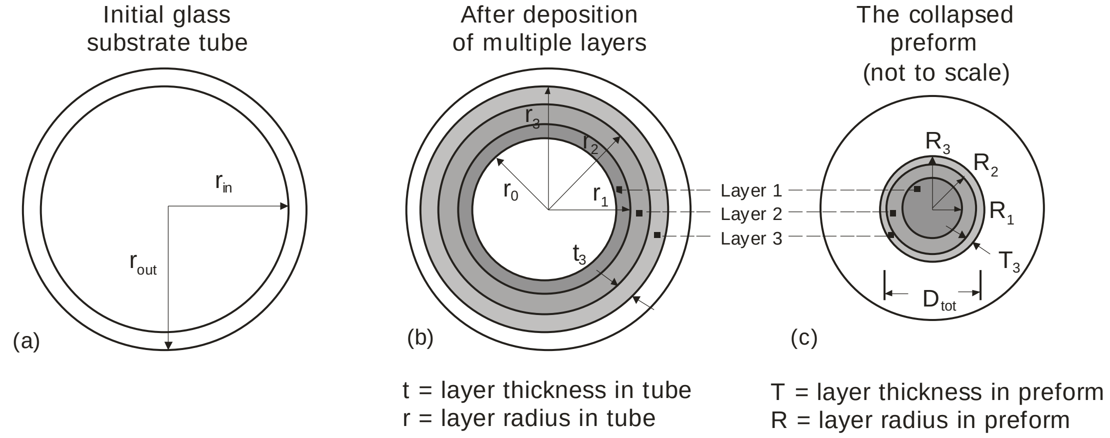

Figure 3.4: Cross-sectional depiction of the layer deposition process, with the parameters used to describe the layer and tube geometry in the (a) substrate tube, (b) after deposition, (c) and in the collapsed preform.

Following deposition of the required number of layers in the substrate, the tube is radially collapsed to form the solid preform. By applying conservation of mass, the CSA of each deposited layer in the substrate tube is equal to that of the corresponding layer in the collapsed preform. This is illustrated in Figure 3.4 and the relationship is expressed mathematically below,

$$\text{Layer 1:} \qquad CSA_1 = \pi(r_1^2 - r_0^2) = \pi R_1^2 \tag{3.2}$$

$$\text{Layer 2:} \qquad CSA_2 = \pi(r_2^2 - r_1^2) = \pi(R_2^2 - R_1^2) \tag{3.3}$$

$$\text{Layer n:} \qquad CSA_n = \pi(r_n^2 - r_{n-1}^2) = \pi(R_n^2 - R_{n-1}^2) \tag{3.4}$$

where CSA is the layer cross-sectional area (mm^2) and n denotes the layer number.

Similarly, the thicknesses of the layers deposited in the substrate, t, and the thicknesses of the collapsed layers in the preform, T, are related by,

$$t_1 = r_1 - r_0, \text{ and } t_2 = r_2 - r_1, \text{ and } t_n = r_n - r_{n-1} \tag{3.5}$$

$$T_1 = R_1, \text{ and } T_2 = R_2 - R_1, \text{ and } T_n = R_n - R_{n-1} \tag{3.6}$$

By applying the mathematical rule of 'difference of two squares' to equation (3.4), and substituting into the general form of equations (3.5) and (3.6), the following relationships were derived,

$$t_n = CSA_n / \pi (r_n + r_{n-1}) \tag{3.7}$$

$$T_n = CSA_n / \pi (R_n + R_{n-1}) \tag{3.8}$$

Using the equations above, the dimensions of a theoretical preform comprising of 10 layers deposited inside a substrate tube with r_{out} = 10 mm and r_{in} = 8 mm was modelled. The CSA used for each of the deposited layers was estimated to be 0.5 mm^2, and was arrived at retrospectively from examining many previously fabricated preforms. It was assumed that there was no collapse between each pass. Figure 3.5 and Figure 3.6 predict the CSA and thickness in each of 10 layers in the uncollapsed tube and the collapsed preform, respectively. The CSA of the individual layers remains constant in both the substrate tube and the collapsed preform, however, the thickness of each layer decreases as the number of layers increases. In the solid preform, this means that each individual layer contributes less to the overall core thickness than the previous one, with the thickest layer being closest to the axial centre.

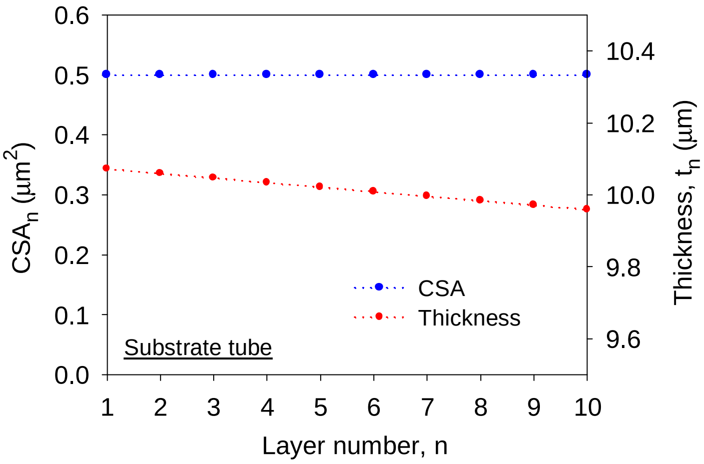

Figure 3.5: Properties of the layers in a theoretical uncollapsed substrate tube with 10 deposited layers (note: layer 1 is closest to the central axis of the tube). Dotted lines indicate trend only.

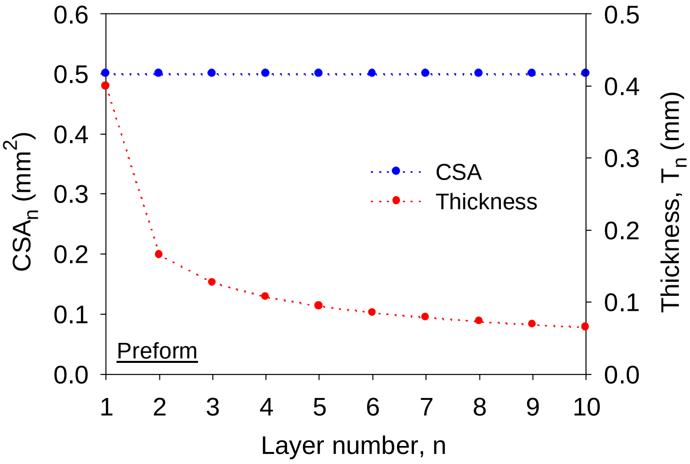

Figure 3.6: Properties of the layers in a theoretical collapsed preform with 10 deposited layers (note: layer 1 is closest to the central axis of the preform). Dotted lines indicate trend only.

To check the validity of this model, the findings were compared with the RIP of a multilayered preform (L30154). The preform consisted of 10 Al:Si layers, each deposited initially as a soot layer with identical process conditions, and doped using the in-situ solution doping technique. The cross-sectional area and thickness of the layers was measured from a RIP of the preform obtained using a PK2600HP Preform Analyzer (Photon Kinetics, US). The findings are plotted in Figure 3.7, together with the theoretical layer CSA and thickness. The predicted trends in the layer CSA and thickness are in good agreement with the measured values, and support the proposition that with unvarying fabrication conditions, the CSA of multiple soot layers is approximately constant.

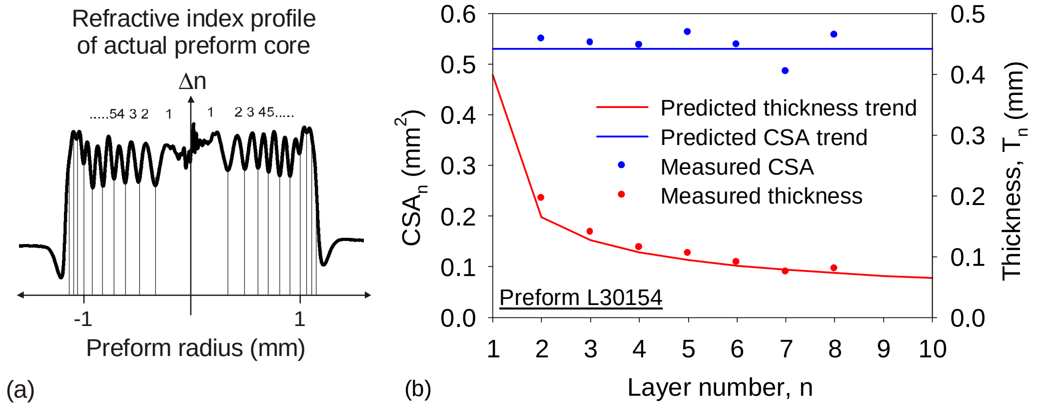

Figure 3.7: (a) Refractive index profile of 10-layered preform L30154, indicating the boundaries of the deposited layers. (b) Comparison of measured CSAs and thicknesses in the preform to the predicted values.

These results imply that the core diameter in the collapsed preform is independent of the substrate tube dimensions at the time of deposition. This means that there is no advantage in selecting a larger diameter substrate tube in order to produce a larger diameter core in the resultant preform. To verify these findings, a single Ge-doped core layer was deposited in 3 differently sized substrate tubes, measuring a nominal 28 × 24 mm, 20 × 16 mm and 16 × 12 mm. Following the core deposition, half of each glass tube was removed from the lathe while the remaining glass was collapsed into a solid preform in the normal manner. Small sections from both the uncollapsed tubes and the solid preforms were then sawn and polished, and the dimensions of the Ge-doped layer measured using an optical microscope. Figure 3.8 shows the results, plotted together with the theoretical trends fitted using equations (3.7) and (3.8). Error bars have been applied to the measured values to reflect the limitations of the microscope and how accurately the Ge-doped layers could be discerned. The findings show that the core diameter in the final preform is independent of the substrate tube size.

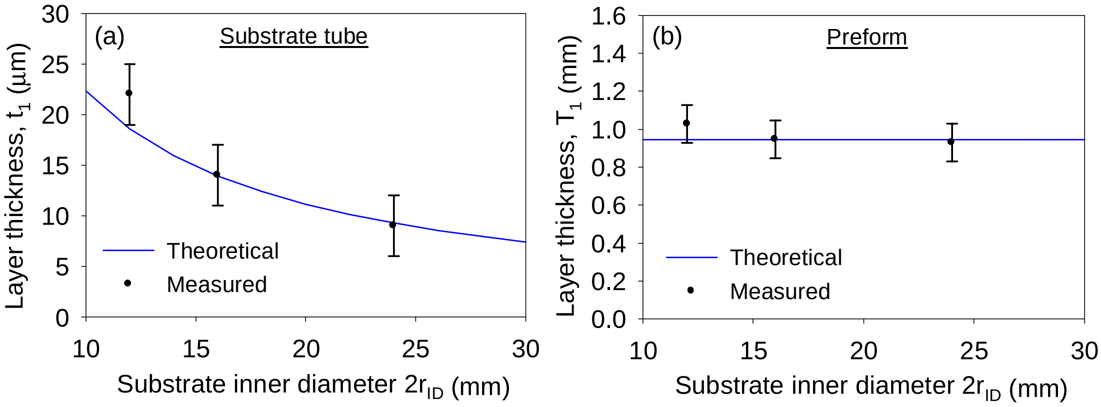

Figure 3.8: Experimentally determined dimensions of a single Ge:Si layer, deposited under the same process conditions, in 3 differently sized substrate tubes. The thickness of the layers in the (a) uncollapsed tube and (b) solid preform were measured using an optical microscope. The curves represent the theoretical trends.

The results obtained are in good agreement with the hypothesis that the CSA of the deposited layer, at a given point along the tube, is the same irrespective of the substrate tube dimensions at the time of deposition. In other deposition trials, an apparent reduction in the final core diameter has been observed when the layer was deposited on a small internal diameter tube (e.g. ~5 – 7 mm), compared to the more conventional 20 × 16 mm tube. This, however, can be attributed to an increased gas velocity through the tube which decreases the resident time of the reagent in the hot zone and thus reduces the reaction efficiency [17], and is not a deviation from the current theory.

The expected CSA of a glass layer in a preform has been equated to the precursor flow rate used during deposition. The data for this was obtained retrospectively, by measuring the RIP of existing preforms, and relating the layer thickness to the initial $SiCl_4$ flow rate. Only preforms where the soot layer was deposited on a 20 × 16 mm substrate tube, using a burner velocity of 100 mm.min^{-1}, and doped with a relatively low concentration solution, were examined. The average measured CSA of layers deposited using a $SiCl_4$ flow rate of 50, 100, 150 and 200 ml.min^{-1}, were (to within ~10 %) 0.35, 0.48, 0.61 and 0.75 mm^2, respectively (and a bubbler temperature of 28 °C). These results predict that a single core layer, deposited using a $SiCl_4$ gas flow of 50 ml.min^{-1}, will produce a core diameter in the resultant preform that measures 0.67 mm. This is compared to a layer deposited with a $SiCl_4$ flow rate of 200 ml.min^{-1}, which results in a core diameter of 0.98 mm.

The correlation between the $SiCl_4$ flow rate and expected layer CSA can be expressed numerically. If the total core diameter in the preform, D_{tot} (see Figure 3.4), consists of multiple individual layers, each with the same CSA, then the total number of layers, N is related to the total core diameter by,

$$N = \frac{\pi}{4} \times \frac{{D_{tot}}^2}{CSA_n} \tag{3.9}$$

By inserting the predicted CSA values for a particular $SiCl_4$ flow rate, as deduced previously, into equation (3.9), the number of layers required to produce a specific preform core diameter can be calculated. This is shown in Figure 3.9 for $SiCl_4$ flow rates of 50, 100, 150 and 200 ml.min^{-1}. The graph reveals that several or more layers are needed to realise even a modest core diameter of 2 mm. (Higher flow rates of $SiCl_4$ can be used, but introduce an undesirable dopant gradient, which is discussed further in subsection 3.3.5).

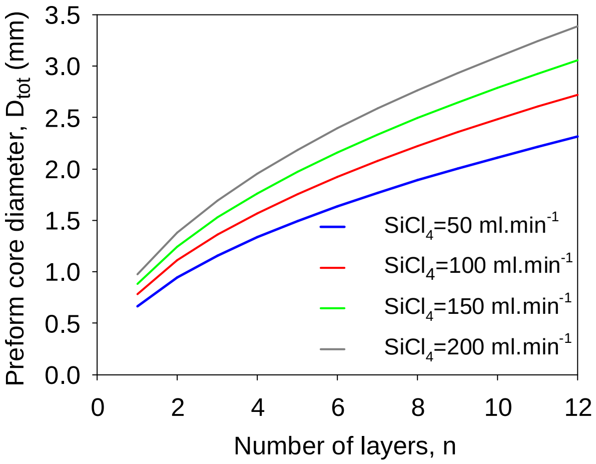

Figure 3.9: Graph illustrating the predicted correlation between the number of deposited layers in a substrate tube and the core diameter in the resultant preform. The difference in D_{tot} is shown for $SiCl_4$ flow rates of 50, 100, 150 and 150 ml.min^{-1}.

3.3.3 In-situ solution doping technique

The in-situ solution doping technique was developed for incorporating RE and co-dopant ions into preforms fabricated using the MCVD process. The technique involves impregnating a soot layer deposited on the inside of a silica substrate tube with a solution containing the dopant ions. The liquid is delivered through a small diameter glass tube, which is inserted into the open end of the glassware while the substrate tube remains on the lathe. Once the soot layer is saturated, the delivery tube is removed and the solvent left to evaporate, leaving the dopant ions behind. The soot layer is then oxidised and consolidated into a glassy layer. These steps are shown schematically in Figure 3.10 and the process used for fabricating the preforms reported in this chapter is described in detail below.

The glassware was arranged in the normal manner adopted for MCVD preform fabrication. A SUPRASIL-F300 (Heraeus, Germany) substrate tube was used for all performs, which measured a nominal 20 × 16 mm in diameter and 500 mm in length, and exhibited a high diameter tolerance (typically ±0.1 mm over 1 m). Before joining the exhaust glassware, the tip of the substrate tube was heated and deftly flared outwards using a graphite rod. Once assembled, preparation of the substrate glass involved the standard etching, polishing and cladding layers as described in Chapter 2.

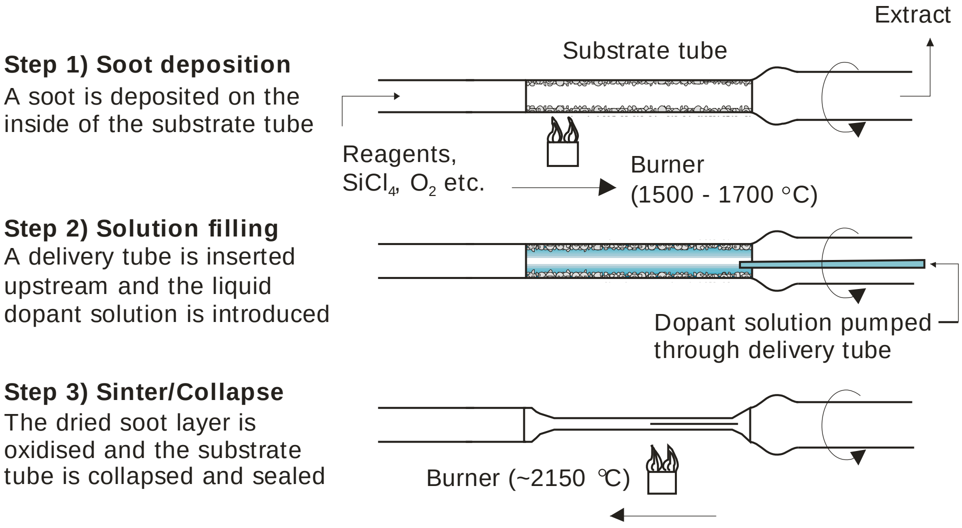

Figure 3.10: Process steps for in-situ solution doping of preforms fabricated using MCVD.

A soot layer was deposited on the inside of the substrate tube using a burner temperature that was sufficiently low to ensure good porosity, and was typically in the range of 1500 – 1700 °C. The required concentration of RE and Al co-dopant chlorides were dissolved in a methanol solution and delivered to the soot layer through a small diameter glass tube inserted into the exhaust tube. The other end of the glass delivery tube was attached to a peristaltic pump via a silicon rubber hose and the solution was pumped slowly into the rotating substrate tube. The liquid flow was halted once the soot layer visibly darkened in colour, indicating that the layer was saturated. The delivery rate was chosen so that the entire soot surface was soaked evenly, but was slow enough that the peristaltic pump could be stopped promptly upon the liquid reaching the end of the soot layer. Depending on the soot thickness, it was found that a flow rate of between 10 – 15 $ml.min^{-1}$ was adequate to soak the porous layer uniformly, and took around 15 – 30 seconds to complete. After infiltration, the delivery tube was withdrawn and the solvent left to evaporate.

To accelerate the drying process, a nitrogen (N_2) gas flow of around 2000 $ml.min^{-1}$ was directed through the substrate tube. It was found that the soot layer appeared visibly dry after around 15 mins, although a total drying time of between 30 and 60 mins was typically required. This drying period was extended further for thicker soot layers or if a high viscosity solution had been used. If the soot layer was not sufficiently dry before processing continued, the residual methanol ignited, irreparably damaging the soot layer. After the required drying period, the doped layer was oxidized and sintered. The soot deposition and soaking steps were then repeated if multiple layers were required, after which the tube was collapsed and sealed in the usual manner.

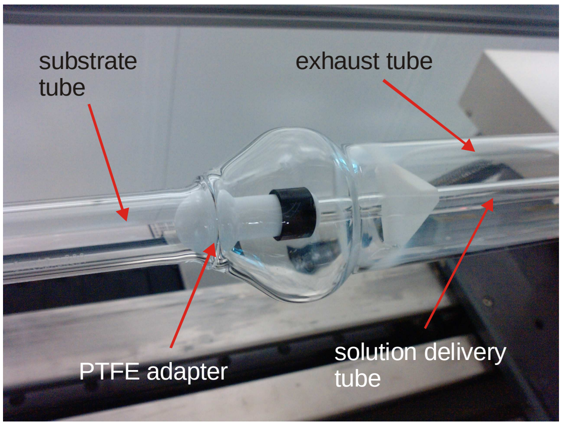

Figure 3.11: Photograph showing the final design of the PTFE adapter used to deliver the RE solution in the in-situ solution doping technique.

Two important refinements were subsequently made to the technique described above, relating to the delivery tube and the soot drying conditions. To improve the repeatability in soaking the soot layer, and to avoid disturbing the fragile layer with the tip of the glass tube, a bespoke adapter was designed which connected to the end of the delivery tube. Figure 3.11 shows a photograph of the final adapter which was machined from polytetrafluoroethylene (PTFE) by Mr. Ken Frampton. The PTFE adapter fitted on to an 8 × 4 mm diameter glass tube and the dopant solution was directed through a small central hole. The spherical shape and design of the PTFE adapter enabled it to self-locate when pushed into the flared end of the substrate tube and rotate independently of the delivery tube.

To establish the optimum soot drying conditions, 3 preforms were fabricated and the concentration of hydroxyl (OH) ions in the resultant fibre was measured. Identical processing parameters were used in each case except for a disparity in the soot drying conditions. Preform L10009 was dried for 60 mins, with a continuous N_2 gas flow of 2000 $ml.min^{-1}$ directed downstream through the tube. Preform L10010 included the same 60 min drying, but with an additional 30 mins period where the gas species was O_2 and the burner traversed back and forth along the tube at a low temperature (<500 °C). Preform L10011 included both of the aforementioned drying steps, as well as an extra step where the O_2 gas was heated for 30 mins by a stationary burner before it passed into the substrate tube.

Fibre was drawn from each of the preforms and the OH concentration was evaluated using a standard white-light setup. The fibre from preforms L10009, L100010 and L10011 revealed OH impurity levels of 5.3 ppm, 3.7 ppm and 2.7 ppm, by weight, respectively, indicating that the inclusion of all three drying stages aided removal of OH groups. Other drying regimes were explored, albeit in a less systematic manner, but it was found that using the current MCVD system the minimum achievable OH concentration was ~2.5 ppm. It was concluded that drying periods extending beyond ~3 hours were of limited benefit, and that chlorination would be necessary to eradicate the OH impurities any further.

3.3.4 Evaluation of the in-situ solution doping technique

The developed in-situ solution doping technique has been directly compared against the traditional solution doping method by fabricating two RE-doped preforms with a single core layer prepared using the respective techniques [2]. A F300-quality substrate tube measuring 20 × 16 mm, and with a diameter tolerance of ±0.1 mm, was used in each case. Following the conventional glass polishing and cladding steps, a silica soot layer was deposited in each substrate using the same conditions to ensure identical soot porosity. The same solution containing 12 g of $AlCl_3.6H_2O$ and 4 g of $YbCl_3.6H_2O$ dissolved in 200 ml of methanol was used to dope both soot layers. Preform L30186 was fabricated using the in-situ solution doping technique. The solution was fed into the substrate tube at a flow rate of 12 ml.min^{-1}, and after infiltration, the oxide layer was subject to a drying period of 30 mins with a N_2 gas flow of 2000 ml.min^{-1} passing through the tube. The substrate tube remained on the lathe throughout the process. L30196 was fabricated using the traditional solution doping method and was soaked vertically in the dopant solution for 60 mins, after which it was left to dry vertically for a further 60 mins in the atmosphere.

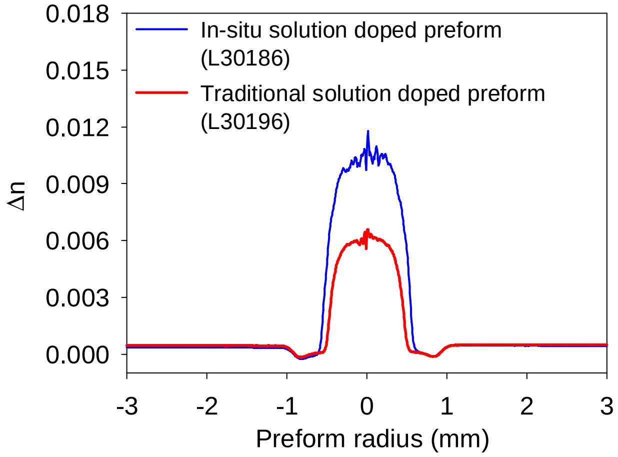

Figure 3.12: Comparison of the refractive index profiles from preforms fabricated using the in-situ solution doping technique and the traditional solution doping method. The same dopant solution was used in both cases.

The RIPs of the collapsed preforms were measured using PK2600HP equipment and the results can be seen in Figure 3.12. The average NA of preform L30186 and L30196 was 0.17 and 0.13, respectively. The core diameter of preform L30186 and L30196 was 0.99 mm and 0.86 mm, respectively, measured at the full-width half-maximum (FWHM). The variation in refractive index along the length of the preform was $<5 \times 10^{-4}$. The difference between the core diameters is attributed to an increase in the volume of glass resulting from the additional incorporation of dopant ions in the case of L30186 [18].

To assess the Yb concentration, both preforms were drawn into DCF and denoted as T0296 (for the in-situ solution doped preform) and T0308 (for the solution doped preform). The fibres were 120 μm in diameter and a PC-373 coating was applied. The RIP of the fibres was measured by using a S14 Fiber Profiler (Photon Kinetics, US) and was found to be consistent with the preform RIP. The Yb concentration was evaluated as 10,700 ppm for T0296 and 4,700 ppm for T0308, by weight, based on Yb-induced absorption at $\lambda = 976$ nm. The background losses in both fibres were measured using optical time-domain reflectometer (OTDR) equipment (model: ν-OTDR, Datacom) operating at $\lambda = 1285$ nm. Losses of 38 dB.km^{-1} and 21 dB.km^{-1} were measured for T0296 and T0308, respectively. The higher background loss evaluated for T0296 is attributed to scattering losses from the increased dopant incorporation. In addition, Figure 3.13 shows the loss spectrum for T0296 obtained with a white-light cut-back measurement. The OH concentration in the fibre was calculated as 2.3 ppm, by weight, which compared to 2.1 ppm for fibre T0308. The difference in OH levels is attributed to the higher Al concentration in preform L30186 as a result of the increased retention of $AlCl_3.6H_2O$ during soaking.

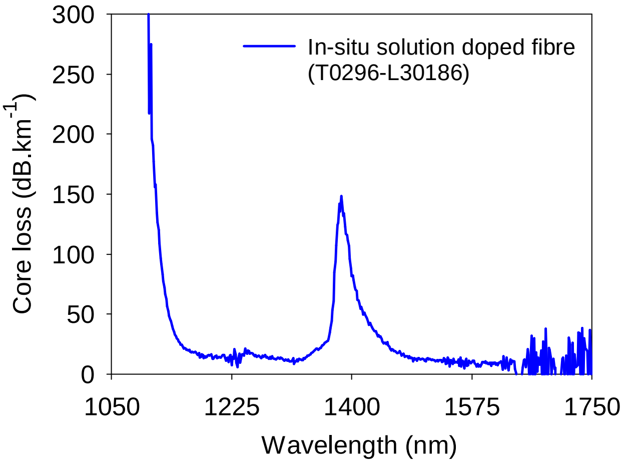

Figure 3.13: Loss spectrum of fibre T0296-L30186 obtained using a white-light cut-back measurement. The visible peak at 1380 nm corresponds to absorped OH ions in the fibre.

Both fibres were tested in a laser configuration by Dr. Seongwoo Yoo using the experimental setup depicted in Chapter 2. The fibres were cladding-pumped by a fibre-coupled laser diode operating at $\lambda = 975$ nm. The output power was found to increase linearly with the launched pump power, and the output of the in-situ solution doped fibre (T0296) reached 13.7 W for a launched pump power of just over 17 W. A slope efficiency of 79 % was calculated. This result compares to a similar laser measurement performed on T0308, where the maximum output power was 13.6 W, and the slope efficiency was 78 %.

From the RIP measurements of the preforms, it is evident that for a given solution concentration, the in-situ solution doping technique produces a comparatively higher NA than using traditional vertical solution doping. This effect has been observed for all fabricated performs irrespective of the soot composition, liquid delivery flow rate, or soot drying regime. The fibre absorption measurements show that there is a marked increase in the Yb concentration, and it is predicted that the increase in Al concentration will be in-line with that of Yb. A summary of the complete comparison between the two techniques is shown in Table 3.1.

	In-situ solution doping (L30186/T0296)	**Conventional solution doping** (L30196/T0308)
Soaking/drying time	30 mins	120 mins
Average preform NA	0.17	0.13
Preform core diameter	0.99 mm	0.86 mm
Preform NA variation	$<5 \times 10^{-4}$	$<5 \times 10^{-4}$
Nominal fibre diameter	120 μm	120 μm
Yb concentration	10,700 ppm	4,700 ppm
Loss (at λ=1285 nm)	38 dB.km^{-1}	21 dB.km^{-1}
OH concentration	2.3 ppm	2.1 ppm
Laser slope efficiency	79 %	78 %

Table 3.1 – Comparison of the measured properties of Yb-doped Al:Si preforms, L30186 and L30196, and fibres, T0296 and T0308, fabricated using the in-situ solution doping technique and the traditional solution doping method.

3.3.5 Multi-layered preform fabrication

One of the salient features of the in-situ solution doping technique is the ability to deposit a plurality of RE-doped layers. This capability is needed when fabricating preforms that require a large core diameter or complex RIP. To demonstrate that several layers can be deposited using the in-situ solution doping technique, an Yb-doped Al:Si preform with a low-NA core, suitable for LMA applications, was fabricated.

Preform L30154 consisted of 10 individual layers, each deposited at a temperature of 1475 °C and with a $SiCl_4$ flow rate of 100 $ml.min^{-1}$. The soot layers were doped with a solution containing 2.5 g of $AlCl_3.6H_2O$ and 2.5 g of $YbCl_3.6H_2O$ dissolved in 1000 ml of methanol, which from previous experience was expected to produce a core NA of ~0.06. The RIP of the resultant preform was measured at different points along its length, and the longitudinal position of $z = 150$ mm (where $z = 0$ represents the beginning-of-deposition end of the preform) is shown in Figure 3.14(a). The average NA and diameter of the core was measured as 0.07 and 2.6 mm, respectively, and the refractive index was found to vary $<0.5 \times 10^{-4}$ along the 300 mm length of the preform. The fabrication process was optimised to eliminate any 'central dip' by carefully controlling the soot drying and oxidation stages to avoid dopant depletion. The processing time needed to fabricate all 10 Yb-doped Al:Si layers was ~8 hours, in addition to the standard time taken to deposit the initial cladding layers and collapse the preform.

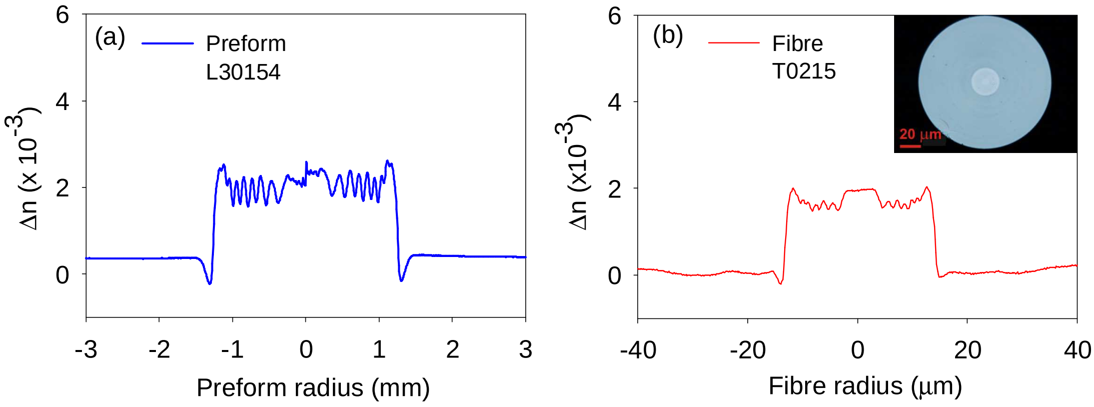

Figure 3.14: Refractive index profiles of 10-layered Yb-doped Al:Si (a) preform L30154, and (b) fibre T0215 (inset: image of cross-section).

The preform was drawn into fibre (T0215) of glass diameter 125 µm and coated with PC-373. A sample of the fibre was measured by Mr. Robert Standish using S14 equipment, and revealed that the radial undulation seen in the preform RIP was reduced to generally less than 1×10^{-4} as shown in Figure 3.14(b). The core and cladding diameters of the fibre were 24 μm and 125 μm, respectively. Comparing these measured values to the step-index computer simulations performed in subsection 3.3.1, it was predicted that a fibre with these dimensions will support 4 modes (i.e. LP_{01}, LP_{02}, LP_{11} and LP_{21}) at $\lambda = 1.06$ μm.

Preform L30154 demonstrates the scalable nature of the in-situ solution doping technique for RE-doped fibre fabrication, showing that many RE-doped layers can be deposited, almost indefinitely. Nevertheless, it is still beneficial to maximise the thickness of each soot layer to limit the overall number of layers that are required. The soot thickness can be increased by either, increasing the $SiCl_4$ gas flow rate, or reducing the burner traverse speed during deposition. However, it was found that to avoid blocking the tube with the generated soot, the practical limit for the $SiCl_4$ flow rate was 200 $ml.min^{-1}$ (when using a standard-sized substrate tube).

Three preforms were fabricated to explore whether a thick soot layer could be achieved from multiple individual layers, each deposited with a relatively low $SiCl_4$ flow rate (i.e. <200 $ml.min^{-1}$). A thick soot layer that is produced in this way has been termed as a 'soot-set'. Each preform was fabricated with a standard-sized substrate tube and the usual glass preparation and cladding layer steps were applied. All soot layers were deposited using a $SiCl_4$ flow rate of 100 $ml.min^{-1}$ at a deposition temperature of 1600 °C. A soot-set consisting of 10, 5, and 1 individual soot layers was applied to preforms L30200, L30202 and L30207, respectively. Each soot-set was subject to a single doping step using the in-situ solution doping technique. The RIP of the resultant preforms was measured. The peak Δn was slightly different in each case, and so for the purposes of comparing the core diameter, the RIPs have been normalised with respect to the undoped silica cladding (see Figure 3.15). A summary of the preform fabrication parameters and measured results are shown in Table 3.2.

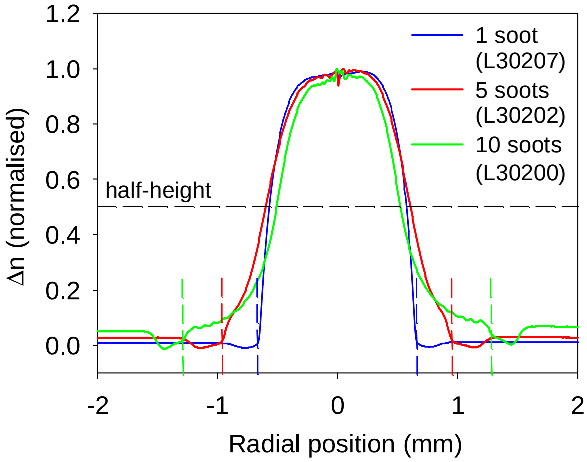

Figure 3.15: Refractive index profiles of Yb-doped Al:Si preforms L30207, L30202 and L30200, which incorporate a soot-set comprised of 1, 5 and 10 individual layers, respectively. Each soot-set was doped using the in-situ solution doping technique. (Dotted vertical lines indicate the deposited glass thickness of each preform).

	Preform L30207	Preform L30202	Preform L30200
Number of soot layers in soot-set	1	5	10
$SiCl_4$ flow rate	100 ml.min^{-1}	100 ml.min^{-1}	100 ml.min^{-1}
Soot deposition temperature	1600 °C	1600 °C	1600 °C
Solution doping steps	1	1	1
Core diameter (deposited glass)	1.31 mm	1.85 mm	2.48 mm
Core diameter (FWHM)	1.14 mm	1.20 mm	1.03 mm

Table 3.2: Fabrication parameters and resultant core sizes. Preforms L30207, L30202 and L30200 were fabricated using soot-sets that comprised of 1, 5 and 10 individual soot layers, respectively.

Figure 3.15 illustrates that, although the deposited glass region (depicted as vertical dotted lines on the graph) increases with the number of soot layers deposited, the core thickness measured at the FWHM is similar for each preform. This suggests that each deposition pass in the soot-set partially sinters the previously laid soot layer, thus reducing its porosity and the ability to take up dopant from the solution. Therefore, soot-sets are not necessarily suitable for fabricating preforms with a large diameter step-index core, but have been used effectively to increase the thickness of the inner-cladding region in pedestal RIP preforms where a dopant gradient is tolerable (as detailed in subsection 3.3.7).

3.3.6 Pedestal refractive index profile fibre

A pedestal RIP preform with a low effective NA core has been fabricated using the in-situ solution doping technique. The RIP was based on that shown in that Figure 3.2(a), and the target dimensions for the fibre were derived using the information presented in subsection 3.3.1. The preform features a highly Yb-doped Al:Si core and a unique Al:Si inner-cladding. Details of how the preform fabrication recipe was determined and characterisation of the resultant fibre are presented below.

In subsection 3.3.1, it was shown that for a pedestal RIP with a core Δn_{eff} of 0.001, the inner-cladding-to-core diameter ratio must be >2.4 to ensure that guidance occurs in the designated core region. In subsection 3.3.2, it was calculated that a single layer deposited using a $SiCl_4$ flow rate of 50 $ml.min^{-1}$ results in a core diameter in the final preform of 0.67 mm. Therefore, to achieve the correct diameter ratio, the inner-cladding diameter must be >1.61 mm. From the data shown in Figure 3.9, it was calculated that the required diameter ratio required >4 inner-cladding layers.

To achieve a Δn_{eff} of 0.001 in the preform, the targeted index rise for the core and inner-cladding was 0.010 and 0.009, respectively. The concentration of Al and Yb required for the core was calculated from previously fabricated performs, and the chosen solution was expected to result in an Yb concentration of around 17,000 ppm, by weight. The dopant concentration of Al required for the inner-cladding was then adjusted accordingly to produce the correct index contrast with that of the core.

In addition to the dopant concentration in the solutions, the temperature at which the soot layer is deposited influences its porosity and consequently its dopant uptake. This effect was found to be more significant than anticipated. To illustrate the problem, preforms L30186 and L30187 were fabricated using identical recipes except for a disparity in the soot deposition temperature. A $SiCl_4$ flow rate of 100 ml.min^{-1} was used in both cases, but a burner temperature of 1550 °C ±3 °C was used for L30186 compared to 1650 °C ±3 °C for preform L30187. Measurements of the resultant preforms revealed that the Δn of L30186 was 8×10^{-3} compared to Δn of 10×10^{-3} for L30187, demonstrating that a change in soot deposition temperature of 100 °C can alter the final refractive index by as much as 2×10^{-3}. This issue is further compounded as the pyrometer measures the temperature of the outer glass surface, which will differ from that inside the substrate, and is dependent on the tube wall thickness and gas flow rate.

Deposition pass	$SiCl_4$ flow (ml.min^{-1})	O_2 flow (ml.min^{-1})	Burner temperature (°C)	Carriage speed (mm.min^{-1})	Dopant solution ($AlCl_3.6H_2O$+$YbCl_3.6H_2O$ in 200 ml methanol)
Clad layers 1 to 3	200	600	2025	150	N/A
Pedestal layer 1	200	400	1575	100	20g Al
Pedestal layer 2	200	400	1585	100	20g Al
Pedestal layer 3	200	400	1595	100	20g Al
Pedestal layer 4	200	400	1605	100	20g Al
Pedestal layer 5	200	400	1615	100	20g Al
Buffer layer	20	600	2025	150	N/A
Core layer	50	550	1625	100	12g Al + 4g Yb

Table 3.3: Summary of the recipe used for fabricating pedestal RIP preform L30225.

Numerous trials preforms were fabricated in order to optimise the process requirements. The final recipe for pedestal RIP preform L30225 is shown in Table 3.3, and was fabricated on a 20 × 16 mm diameter F300 substrate tube. The measured RIP of the collapsed preform revealed an average core Δn of 0.008 and a Δn_{eff} of 0.002. The measured core and inner-cladding diameters were 0.75 mm and 2.8 mm, respectively. This diameter ratio of 3.7 is higher than anticipated, but is very dependent on where the core and cladding boundaries are defined in the RIP trace. Fibre (T0361) was drawn from the preform in a DCF configuration to an outer diameter of 400 μm. Measurements of the fibre RIP revealed that the core and inner-cladding diameters were 27 μm and 87 μm, respectively, equating to an inner-cladding-to-core ratio of 3.1 and indicating that diffusion between the two regions took place during the drawing process (see Figure 3.16(a)). The radial index variation (i.e. ripples) in the inner-cladding was also reduced compared to the preform RIP, again as a result of diffusion effects.

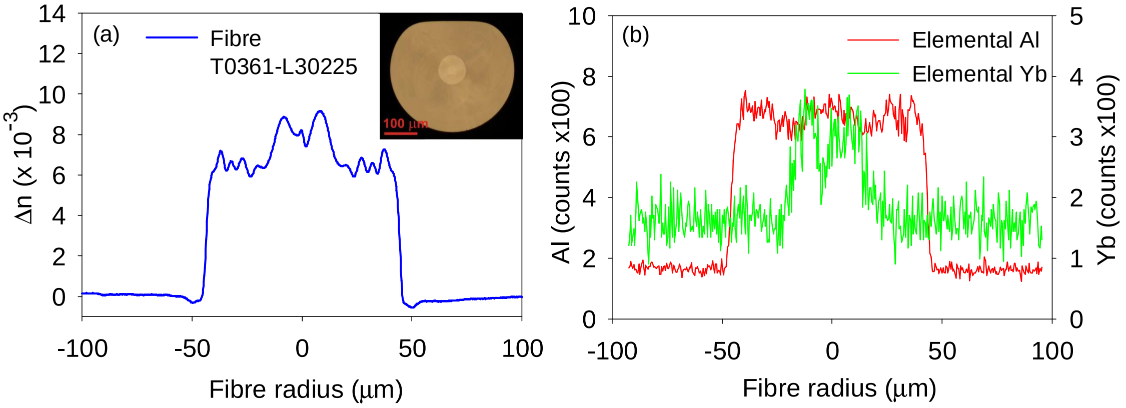

Figure 3.16: Pedestal fibre T0361. (a) Refractive index profile with inset of fibre cross-section, and (b) radial analysis of the dopant distribution using energy-dispersive X-ray spectroscopy.

To verify that the diffusion effects were not substantial, and that the Yb ions were still confined to the central core region following fibre drawing, the glass composition of fibre T0361 was analysed using energy-dispersive X-ray spectroscopy (EDX). The obtained results for the elemental concentrations of Yb and Al in the fibre are shown in Figure 3.16(b) and confirm that the Yb ions are predominantly confined to the core.

The Yb concentration in fibre was measured as 18,160 ppm, by weight, using a white-light experimental set-up and is good agreement with the anticipated value. The background loss was evaluated as 40 dB.km^{-1} at $\lambda = 1550$ nm, using a cut-back measurement, and the OH concentration was calculated as ~4 ppm, by weight. The performance of the fibre was tested in a laser configuration by Dr. Seongwoo Yoo (see Chapter 2 for a schematic of a fibre laser setup). The pump source ($\lambda = 976$ nm) was coupled into a 1.6 m length of the fibre. The slope efficiency of the fibre was measured as 82 % and the laser output power characteristics, including the output spectrum, are shown in Figure 3.17.

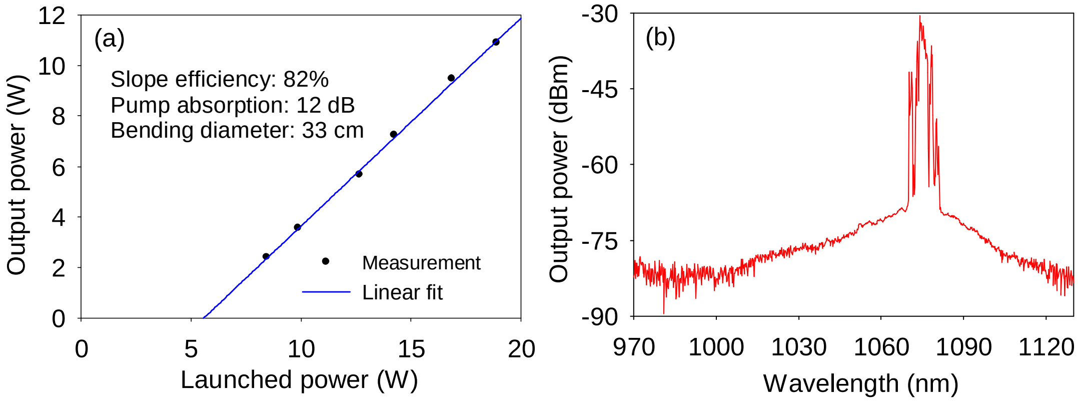

Figure 3.17: (a) Laser characteristics of pedestal RIP fibre T0361 indicating a slope efficiency of 82%, and the (b) output spectrum.

The data from the fibre RIP shown in Figure 3.16(a) was imported into the OptiFiber software and the intensity fields of the predicted core modes LP_{01}, LP_{11}, LP_{02} and LP_{12} were simulated (see Figure 3.18). The results illustrate that the lower-order modes are well confined to the central gain region by the effective refractive index contrast of the core, and exhibit a negligible overlap with the inner-cladding. The higher-order modes, which propagate predominantly in the inner-cladding region, can be suppressed by coiling the fibre.

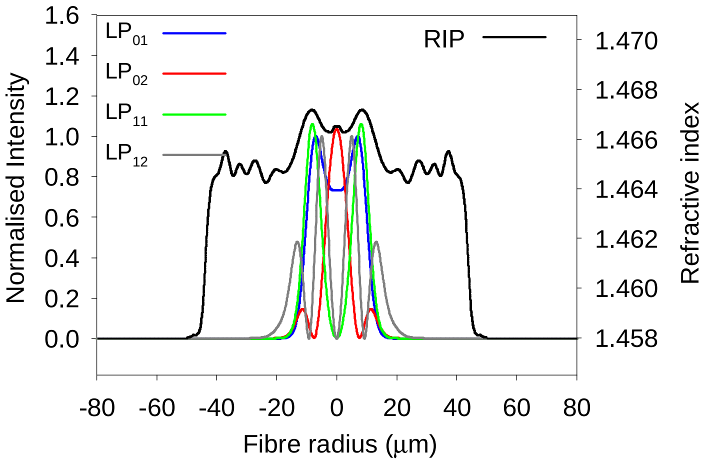

Figure 3.18: OptiFiber simulation of fibre T0361, illustrating that the supported modes, LP_{01}, LP_{02}, LP_{11} and LP_{12} are confined to the core region.

3.3.7 Non-circular pedestal refractive index profile fibre

The natural circular symmetry of DCF is removed by introducing a D-shape in the glass preform. This suppresses helical modes from propagating in the cladding and promotes interaction of the pump light with the doped core region [19]. It is logical to assume that a similar situation exists in fibre that has a pedestal RIP, whereby unwanted helical modes propagate in the circular inner-cladding. In this subsection, a novel way to remove the circular symmetry of the inner-cladding is presented, and the effect on the pump absorption efficiency is reported.

Pedestal RIP preforms with a pedestal RIP that are fabricated using MCVD and the traditional process and solution doping are not suitable for post-processing owing to the high concentrations of P_2O_5 or GeO_2 that are incorporated into the inner-cladding glass. Any post-processing that is attempted near the core would most likely shatter the preform. The preform demonstrated in the previous section, however, is considerably less stressed, as the Al:Si inner-cladding has a thermal expansion coefficient that is closer to that of the pure silica cladding [14]. Post-processing has been investigating in pedestal RIP preform L30184, which was fabricated with an Al:Si inner-cladding and a Yb-doped Al:Si core. The inner-cladding was deposited using 4 soot-sets, each comprising of 3 soot layers, and a single layer was deposited for the core. The inner-cladding and core diameters of the preform were measured as 0.79 and 3.1 mm, respectively, representing a diameter ratio of 3.9. The average Δn of the inner-cladding and core was measured from the RIP as 0.004 and 0.010, respectively.

To remove the circular symmetry of the inner-cladding in the preform, holes were drilled longitudinally into the preform. The placement and size of the holes were chosen so that they intersected equally with both the inner-cladding and outer-cladding glass regions. The holes were drilled to staggered depths of between 50 mm and 75 mm to produce three separate structures for comparison (see Figure 3.19). Once the machined surfaces had been polished, pure silica (F300) glass rods were inserted into the holes to produce a solid preform. Generating multiple fibre geometries from adjacent sections of a single preform ensured that any minor longitudinal variations in the dopant concentration were minimised.

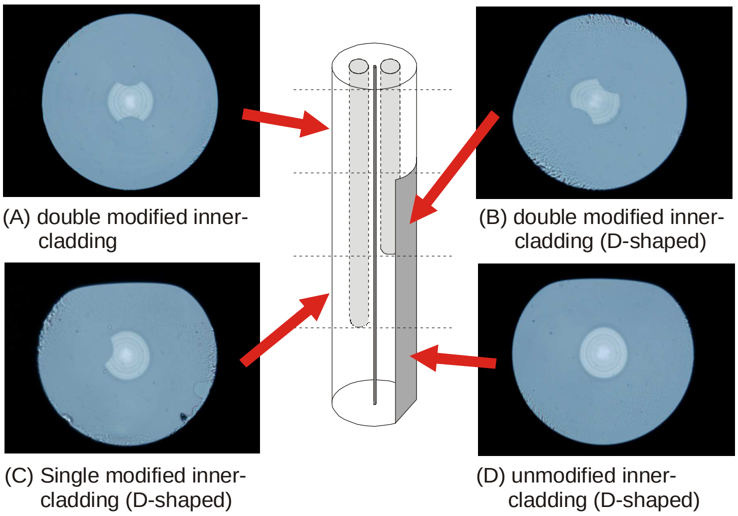

(A) double modified inner-cladding

(B) double modified inner-cladding (D-shaped)

(C) Single modified inner-cladding (D-shaped)

(D) unmodified inner-cladding (D-shaped)

Figure 3.19: Cross-sectional images of fibres T0285-A, T0285-B, T0285-C and T0285-D, drawn from pedestal RIP preform L30184, and their respective positions in the preform.

The entire preform was drawn into 120 μm diameter fibre, in a single run, and a low-index coating (PC-373) was applied. The nominal preform feed and capstan speeds were 0.5 mm.min^{-1} and 8 m.min^{-1}, respectively. A vacuum of 2 mbar (below atmospheric pressure) was applied to the top of the preform handle during the fibre draw to ensure that the air voids were removed. For each fibre structure, a length of between 50 m and 100 m was drawn, and the individual modified sections were denoted as A, B, C and D as shown in Figure 3.19. The RIP was measured from a sample of each fibre structure and revealed that the core diameter of ~8 μm and an inner-cladding diameter of ~30 μm in the unmodified axis.

The Yb concentration in the fibres was evaluated using a standard white-light experimental setup and the results are summarised in Figure 3.20. The peak core absorption at $\lambda = 976$ nm was measured as 10.68 dB.m^{-1}, 10.16 dB.m^{-1} and 10.69 dB.m^{-1} for fibres B, C and D, respectively.

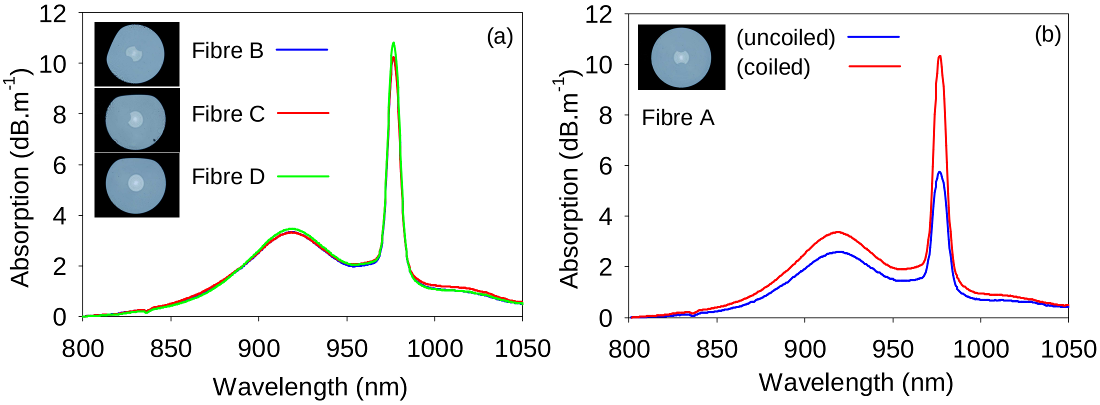

Figure 3.20: Graphs showing the absorption from Yb ions in pedestal RIP fibres (a) T0285-B, T0285-C, T0285-D, and (b) T0285-A, illustrating the effect of a non-circular inner-cladding.

The unexpected similarity in the measured absorption values for fibres B, C and D suggests that the removal of the circular symmetry in the inner-cladding does not have any measurable effect on the absorption. The reasons for this have been attributed to three possible origins:

1) The higher-order inner-cladding modes that have a low modal overlap with the core are of sufficiently low energy that they are undetectable with the white-light absorption measurements.

2) The ‘ripples’ seen in the fibre RIP instigate mode-mixing, even in the unmodified inner-cladding of fibre sample D.

3) The dissymmetry in the outer-cladding (D-shape) is sufficient to introduce enough perturbation to the propagating light that any helical modes in the inner-cladding region are suppressed.

The measured RE absorption in fibre A is shown in Figure 3.20(b). Owing to the circularly symmetric outer-cladding, the measurement was conducted on uncoiled and tightly coiled fibre samples. The peak absorption in the tightly coiled sample is 10.31 dB.m^{-1}, which, to within the error of the measurement, is the same as that obtained for fibres B, C and D. It has not yet been concluded which of the three possible reasons above is correct. However, if it is assumed that tightly coiling the fibre is a definitive way to ensure mode-mixing, then this suggests that the D-shape in fibres B, C and D is adequate to prevent helical modes from propagating, both in the outer-cladding as well as the inner-cladding.

3.3.8 Polarisation-maintaining (PANDA) optical fibre

Polarisation-maintaining (PM) optical fibres are used where there is a need to conserve the polarisation of the signal light, and the methods for their fabrication were introduced in section 3.2. In this subsection, a PANDA fibre with a pedestal RIP and an Al:Si inner-cladding is reported. Conventional pedestal RIP preforms are fabricated using P or Ge to raise the index of the inner-cladding, as explained previously, and are not suitable for post-processing owing the thermal expansion mismatch with that of the undoped silica. The fibre reported here is believed to be the first demonstration of a PANDA fibre with a pedestal RIP that permits the stress-applying parts (SAPs) to be positioned within the inner-cladding region to maximise the birefringence [13].

The placement and size of the SAPs in a PANDA fibre will dictate its birefringence and PM capabilities. Sasaki et al. numerically modelled the effect that the diameter of the SAPs, and their proximity to the core, has on the modal birefringence of a fibre with twin circular stress regions [20]. Sasaki et al. reported that a ratio of 0.7 between the diameter of the stressed region, t, and the fibre radius, b, is desirable. Similarly, a ratio of 3 is deemed optimum for r/a, where r is the distance from the geometric centre of the fibre to the edge of the SAP and a is the core radius. Adhering to this specification yields a theoretical birefringence in the fibre of $\sim 4.5 \times 10^{-4}$, although this value is dependent on the core refractive index and the operating wavelength [20].

A PANDA fibre has been fabricated using preform L30184 and the target diameter ratios recommended by Sasaki et al. [20]. The preform was first ‘squashed’ on a glass-working lathe to increase the outer glass diameter from 12.1 mm to 14.8 mm. The holes for the SAPs were then drilled diametrically into the preform to a positional accuracy approaching 50 μm, using in-house ultrasonic drilling equipment. Pre-fabricated borosilicate stress rods were used for the SAPs, and were chemically etched to a diameter of 4.8 mm to remove the majority of the silica cladding. A cladding-to-core diameter ratio of 1.05 was achieved. The clearance between the stress rods and the drilled holes was found to be critical and, a gap of 0.2 mm to 0.3 mm was deemed to be optimum. It was found that if the clearance was too large, the holes collapsed during the draw to eliminate the void and tended to deform the core elliptically. Conversely, if the gap was too small, there was the potential for trapping air between the surfaces owing to the inevitable slight non-uniformity along the length of the stress rods.

The surface quality of the holes following ultrasonic drilling was reasonable, but it was found that if the visible scratches were not removed before drawing, small holes developed in the fibre at the interface of the stress regions as a result of trapped gas between the fused glass surfaces. A similar effect was also seen if the contaminants from the coolant used in the drilling process were not adequately removed prior to fibre drawing. Both issues were resolved for preform L30184 by performing a high-temperature flame polish on the lathe after drilling. During this process, the pressure inside the holes was controlled to avoid any collapse or deformation.

The preform was assembled with a glass handle tube attached to the upper end to allow the air inside to be evacuated during the draw. The applied vacuum ensured that the surfaces between the stress rods and the holes sealed. An applied vacuum of 15 mbar (below atmospheric) was found to be sufficient. The final fibre drawing parameters, included, a furnace temperature of 2030 °C, a draw speed of 10 $\mathrm{m.min^{-1}}$ and a preform feed speed of 0.7 $\mathrm{mm.min^{-1}}$. A 200 m length of fibre (T0283) was successfully drawn at a diameter of 120 μm which was coated with PC-373. A cross-section of the fibre is shown in Figure 3.21(a).

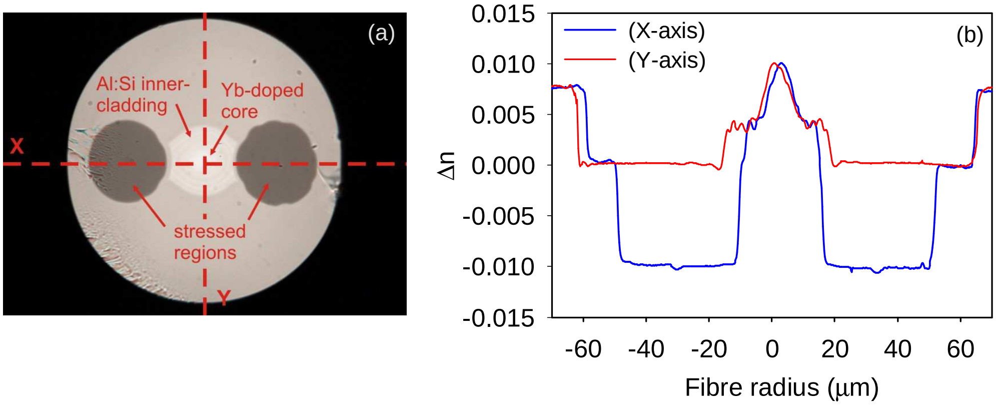

Figure 3.21: PANDA fibre T0283(a) cross section and (b) refractive index profiles in the modified and unmodified axes.

The RIP of fibre T0283 was measured by Mr. Robert Standish using S14 equipment (see Figure 3.21(b)) and the average inner-cladding diameter was evaluated 25 μm and 31 μm along the modified and unmodified axes, respectively. A diameter ratio of 3.2 and 0.6 were obtained for *r*/*a* and *t*/*b*, respectively, which are in good agreement with the targeted values as defined by Sasaki et al. [20]. Using a standard white-light setup, the induced cladding absorption from the Yb ions in the fibre was measured as 12.7 dB.m^{-1} at $\lambda = 976$ nm.

The birefringence and laser performance of the fibre was assessed by Dr. Seongwoo Yoo. The birefringence in the fibre was measured using a cross-polariser method and a value of 2.4×10^{-4} was calculated, based on the beat length from the measured spectrum of a 1.02 m length of fibre [14]. The laser performance of the fibre was determined using an experimental setup based on that shown in Chapter 2. The measured output power versus launched pump power is shown in Figure 3.22. A linear increase was observed which represented a slope efficiency of 79 %. The maximum output power was 14.7 W, which was limited by the pump power available. The fibre length was 2.5 m and 98 % of the pump was absorbed. The polarisation extinction ratio (PER) was also measured by placing a polariser in the signal output. A figure of 12 dB was obtained at maximum output power.

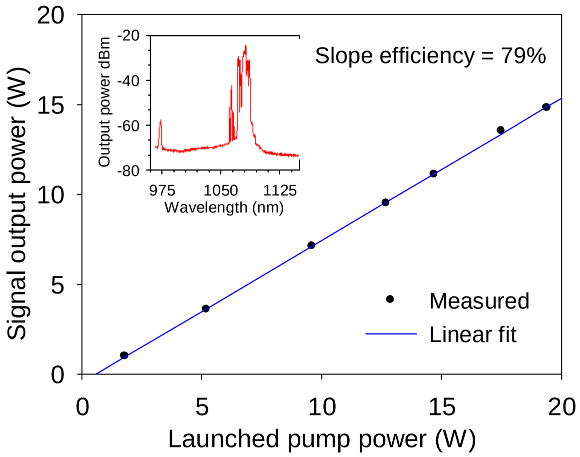

Figure 3.22: Laser output power versus launched pump power for PANDA fibre T0283 indicating a slope efficiency of 79 % (inset: emission spectrum).

3.4 Summary

In this chapter, a novel in-situ solution doping technique has been presented. The developed technique allows RE-doped preforms with complex design to be fabricated using the MCVD process. A direct comparison between the two methods showed an enhancement in dopant incorporation when using in-situ solution doping, without any deterioration in the fibre performance. The in-situ solution doping technique is a viable alternative to traditional solution doping that provides a vast improvement on the preform yield and labour investment [2].

The ability to produce multiple RE-doped silica layers using the in-situ solution doping technique was demonstrated with the fabrication of a 10-layered Yb-doped step-index preform. The core measured 2.6 mm in diameter and the low-NA of 0.07 was free from any central dip, making it suitable for LMA applications. A slight undulation was observed in the RIP as a result of either, the solution not fully penetrating the soot layer during soaking, or evaporation of Al during the oxidation passes. This effect has also been documented by Tang et al. [21], and it is believed that an adjustment to the burner temperature used during the soot deposition as well as further optimisation of the drying conditions would be beneficial in flattening the RIP of low-NA multilayered preforms.

To further increase the core diameter, the feasibility of using soot-sets was investigated. Preliminary results indicated that without further optimisation of the burner temperature a detrimental porosity gradient was introduced. This was a result of the previously laid soot layer being sintered during the following deposition pass. It may be possible to lessen the porosity gradient by optimising the soot deposition temperature for each subsequent layer. By reducing the burner temperature for each soot layer it would ensure that the porosity of the layers nearest the tube wall would be maintained, however trials would be needed to ascertain if this approach detrimentally affects the overall adhesion of the soot body.

A large proportion of the experimental work involved the fabrication of pedestal RIP preforms that included a unique Al:Si inner-cladding. The multilayered inner-cladding was achieved using the in-situ solution technique and resulted in a glass preform which was tolerant to post-processing. Using this approach, a fibre with a high Yb concentration (>18,000 ppm, by weight) and a low effective-NA (~0.06) was demonstrated for what is believed to be the first time [3]. The fibre was testing in a lasing configuration and slope efficiency of 82 % was measured at 11 W of output power. Computer simulation of the fibre RIP confirmed that the lower-order modes were confined to the central core region and exhibited a negligible overlap with the inner-cladding.

The use of Al:Si for the inner-cladding of a pedestal RIP preform, as opposed to Ge:Si or P:Si, results in a reduced thermal expansion mismatch with that of the silica cladding. The benefits of this were demonstrated by fabricating Yb-doped fibres featuring an asymmetric inner-cladding, and which have not been seen in the literature previously. The post-processing was intended to break the symmetry of the inner-cladding to enhance the pump absorption, although, in the fibres tested, the absorption measurements suggested that the D-shaped outer-cladding was sufficient to suppress helical modes from propagating even without modifying the inner-cladding symmetry. These findings were contrary to expectations. To ascertain the origin of the results, a repeat of the experiments is needed using a pedestal structured preform with a comparatively larger diameter inner-cladding. If a similar outcome is observed in this fibre it would eliminate the remaining possibilities that were raised in subsection 3.3.7 and allow a more accurate interpretation of the results.

The ability to conduct post-processing on a pedestal RIP preform was also demonstrated with the fabrication of a PANDA design fibre [13, 14]. The preform glass was tolerant to drilling and therefore placement of the SAPs was not restricted. The birefringence in the fibre was measured as 2.4×10^{-4} and a slope efficiency of 79 % was achieved. It is believed that this is the first demonstration of a pedestal RIP PANDA fibre, where the SAPs are permitted to overlap with the inner-cladding region to maximise the birefringence.

3.5 References

1. J.E. Townsend, S.B. Poole, and D.N. Payne. "Solution-doping Technique for Fabrication of Rare-earth Doped Optical Fibres". *Electronics Letters*, 23(7): 329-331, (1987).
2. A.S. Webb, A.J. Boyland, R.J. Standish, S. Yoo, J.K. Sahu, and D.N. Payne. "MCVD in-situ solution doping process for the fabrication of complex design large core rare-earth doped fibers". *Journal of Non-Crystalline Solids*, 356: 848-851, (2010).
3. A.S. Webb, A.J. Boyland, R.J. Standish, D. Lin, S. Alam, and J.K. Sahu. "In situ Solution Doping Technique for Novel Geometry Rare-Earth Doped Fiber Fabrication." in *Conference on Lasers and Electro-Optics (CLEO), San Jose, CA* 16-21 May, JTuD35, (2010).
4. J.K. Sahu, S. Yoo, A.J. Boyland, A.S. Webb, M. Kalita, J.-N. Maran, Y. Jeong, J. Nilsson, W.A. Clarkson, and D.N. Payne. "Fiber design for high-power fiber lasers." in *Photonics West, San Jose, CA*. (2009).
5. K. Tankala, B. Samson, A. Carter, J. Farroni, D. Machewirth, N. Jacobson, U. Manyam, A. Sanchez, M.Y. Cheng, A. Galvanauskas, W. Torruellas, and Y.

Chen. "New developments in high power eye-safe LMA fibers." in *Proceedings of SPIE: Fiber Lasers III: Technology, Systems, and Applications San Jose, CA*. (2006).

6. B. Samson, G. Frith, A. Carter, and K. Tankala. "High-power large-mode area optical fibers for fiber lasers and amplifiers." in *Piscataway, NJ 08855-1331, United States*. 4528625, (2008).
7. J.P. Koplow, D.A.V. Kliner, and L. Goldberg. "Single-mode operation of a coiled multimode fiber amplifier". *Optics Letters*, 25(7): 442-444, (2000).
8. Y. Jeong, J.K. Sahu, D.N. Payne, and J. Nilsson. "Ytterbium-doped large-core fiber laser with 1.36 kW continuous-wave output power". *Optics Express*, 12(25): 6088-6092, (2004).
9. B. Morasse, S. Chatigny, C. Desrosiers, E. Gagnon, M.-A. Lapointe, and J.-P. De Sandro. "Simple design for singlemode high power cw fiber laser using multimode high NA fiber." in *Proceedings of SPIE: Fiber Lasers VI: Technology, Systems, and Applications, San Jose, CA*. January 26-29, (2009).
10. M.J.F. Digonnet, *Rare Earth Doped Fiber Lasers and Amplifiers.* New York: Marcel Dekker. (1993).
11. M.C. Li, L.H. Liu, T.P. Xiao, J.J. Xue, L.T. Liang, H.L. Wang, and M. Xiong. "Single-polarization polarization maintaining optical fiber with large stress birefringence and high homogeneity". *Applied Physics Letters*, 89(10), (2006).
12. A. Mendez and T.F. Morse, *Speciality Optical Fibers Handbook.* Academic Press. (2007).
13. S. Yoo, A.S. Webb, A.J. Boyland, R.J. Standish, A. Dhar, and J.K. Sahu. "Polarization-maintaining Ytterbium-doped Fibre With an Aluminosilicate Inner-cladding Fabricated Using In-situ Doping Technique." in *European Conference on Lasers and Electro-Optics CLEO*. paper CJ2_4, (2011).
14. S. Yoo, A.S. Webb, A.J. Boyland, R.J. Standish, A. Dhar, and J.K. Sahu. "Linearly polarized ytterbium-doped fiber laser in a pedestal design with aluminosilicate inner cladding". *Laser Physics Letters*, 8(6): 453-457, (2011).
15. I. Kasik and V. Mateijec. "New ways for influencing thermophoretic efficiency in the MCVD process". *Journal of Aerosol Science*, 26(3): 399-399, (1995).

16. S.R. Nagel, J.B. MacChesney, and K.L. Walker. "Overview of the modified chemical vapor deposition (MCVD) process and performance". *IEEE Journal of Quantum Electronics*, QE-18(4): 459-476, (1982).
17. M. Pal, R. Sen, M.C. Paul, S.K. Bhadra, S. Chatterjee, D. Ghosal, and K. Dasgupta. "Investigation of the deposition of porous layers by the MCVD method for the preparation of rare-earth doped cores of optical fibres". *Optics Communications*, 254(1-3): 88, (2005).
18. F.Z. Tang, P. McNamara, G.W. Barton, and S.P. Ringer. "Multiple solution-doping in optical fibre fabrication I - Aluminium doping". *Journal of Non-Crystalline Solids*, 354(10-11): 927-937, (2008).
19. L. Philippe, V. Doya, R. Philippe, P. Dominique, M. Fabrice, and L. Olivier. "Experimental study of pump power absorption along rare-earth-doped double clad optical fibres". *Optics Communications*, 218(4-6): 249-54, (2003).
20. Y. Sasaki, T. Hosaka, M. Horiguchi, and J. Noda. "Design and Fabrication of Low-Loss and Low-Crosstalk Polarization-Maintaining Optical Fibers". *Journal of Lightwave Technology*, LT-4(No. 8): 1097-1102, (1986).
21. F.Z. Tang, P. McNamara, G.W. Barton, and S.P. Ringer. "Nanoscale characterization of silica soots and aluminium solution doping in optical fibre fabrication". *Journal of Non-Crystalline Solids*, 352(36-37): 3799-3807, (2006).

Chapter 4

Chemical-in-Crucible Process

4.1 Introduction

In this chapter, a novel method for incorporating dopant ions into silica preforms is presented. The process, which has been termed *chemical-in-crucible* (CIC), enables a range of dopant precursors with low vapour pressures to be prototyped for their suitability in preform fabrication using Modified Chemical Vapour Deposition (MCVD) [1]. The originality of the process resides in the placement of the dopant precursor, which is within the substrate glassware and in close proximity to the reaction-zone. The precursor is heated directly by an electrical resistive-element heater rather than the vapour being generated and transported from an external source, as is conventional with MCVD. This approach means that the CIC process has numerous advantages over traditional preform doping techniques: the extended temperature range, up to several hundred degrees Celsius, allows less volatile precursors to be vaporised. Small amounts of dopant precursor can also be used in single-use trials, which avoids any unwanted reactions that may arise with larger quantities that are subject to repeated thermal cycles. There is also the potential for more homogeneous RE incorporation.

This chapter begins with a review of existing vapour delivery schemes used in preform fabrication and builds on the introduction provided in Chapter 2. Commercially available deposition systems, as well as those techniques confined to the scientific literature are discussed, and their practicalities and limitations are highlighted. The focus of the work presented in this chapter was to develop a vapour-phase deposition technique for ytterbium- and aluminium-based precursors. The experimental work was intended to provide proof for the underlying concept of the CIC process, as well as the chosen precursors, rather than targeting a specific fibre design. Several preforms have been successfully fabricated using the CIC process, including preforms doped using an organometallic ytterbium precursor. It was found that understanding the properties and behaviour of rare-earth organometallic precursors at high temperatures was paramount to their successful implementation in MCVD and, as such, a section has been dedicated to these findings. Fibres have been drawn from both ytterbium- and aluminium-doped silica preforms and the characterisation results are presented. Finally, a highly ytterbium-doped phosphosilicate fibre was tested in a laser configuration and the optical-to-optical conversion efficiency is reported [1].

4.2 Motivation and prior art

A MCVD-based system capable of delivering rare-earth (RE) dopants in the vapour-phase, analogous to the conventional bubbler chemicals $SiCl_4$, $GeCl_4$, $POCl_3$ and BBr_3, is a tantalising prospect for active preform fabrication. This capability would permit an arbitrary number of glassy layers to be deposited, each with a specific RE concentration, and with a greater control over the refractive index than with solution doping [2]. Furthermore, it would remove the dependence of dopant incorporation on soot characteristics. As oxidation of the glass-forming and rare-earth components occurs simultaneous at the reaction-zone, it would also have the potential for creating a more homogeneous distribution of RE ions in the layer structure and improving the lasing efficiency of the resultant fibre.

The RE chemical precursors that are used in the solution doping process are metal halides, such as erbium and ytterbium chloride, and have the molecular form of $RECl_3$. These compounds are solid at room temperature and available commercially in the high purities that are needed for fibre fabrication (i.e. up to 99.9999 %, from RE metals analysis). Rare-earth chlorides are hygroscopic, readily oxidising in air, and therefore require stringent chemical handling practices. However, hydrated rare-earth chlorides ($RECl_3.xH_2O$) are highly soluble in water, as well as solvents such as methanol, and are therefore easily integrated into a solution doping process.

Although rare-earth chlorides are appropriate for solution doping, their intrinsically low volatility means that they are less attractive as a vapour source. Anhydrous RE chlorides have a vapour pressure in the region of 1 kPa (at 1000 °C) and require a temperature of at least several hundred degrees Celsius to produce appreciable vapour [3]. Therefore, a system capable of efficiently transporting gaseous RE chloride to a rotating substrate tube on a lathe, and integration of this into conventional MCVD equipment, requires considerable engineering investment. Notably, the entire delivery line, from the chemical bubblers through to the rotary seal and the glass tube, must be heated to prevent the vapour from condensing en-route and clogging the pipe-work.

For the reasons mentioned above, organometallic chelate complexes are an attractive candidate for a dopant vapour-source owing to their favourable physical properties [4]. Chelates, (the name of which refers to the specific chemical bonding of the compound) are solid at room temperature and evolve vapour in quantities comparable to $SiCl_4$ (at room temperature) at a temperature of only 100 – 200 °C, thus considerably simplifying the specification on heated lines. The vapour pressure of three lanthanide chelate compounds in the range of 150 – 250 °C is shown in Figure 4.1.

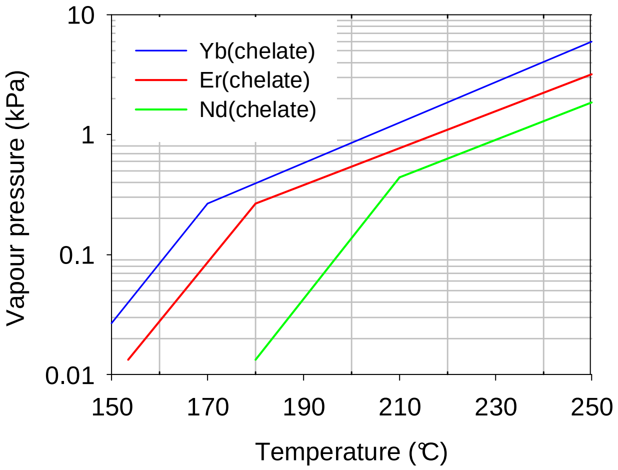

Figure 4.1: Vapour pressure of rare-earth chelate compounds, ytterbium, erbium, and neodymium. Data taken from [4].

Complexes based on metal chelates are well known in the field of organic chemistry and were proposed for use in silica optical fibre fabrication as early as 1990 [5]. However, the complexity of the equipment required for vaporising and delivering chelate vapour at elevated temperatures is thought to be the reason why they have not yet been fully exploited in MCVD. In recent years, vapour delivery systems that are compatible with preform fabrication equipment and chelate precursors have become available commercially. The Norwegian company Nextrom, which specialises in fibre optic fabrication equipment, now offer a high temperature vapour delivery system (NHS) [6] that is compatible with up to four dopant sources. Figure 4.2 shows a photograph of the NHS system, alongside a schematic of the internal pipe work illustrating the inherent sophistication of the equipment.

A similar, Advanced Chelate Delivery System is also available from Optacore (Slovenia), a company that provides MCVD-based solutions for speciality fibre fabrication [7]. Optacore adopt the same design approach as Nextrom, whereby the chelate source is located and vaporised in a dedicated cabinet and delivered through heated lines to the preform-making lathe. A major difficultly is heating the rotary seal assembly to the same temperature as the delivery line, whilst maintaining its gas-tight integrity, and Optacore have developed a proprietary design to overcome this problem.

Additionally, the rotary seal assembly incorporates a heated sliding injection tube which protrudes into the substrate glassware to bring the point of reagent mixing closer to the reaction-zone.

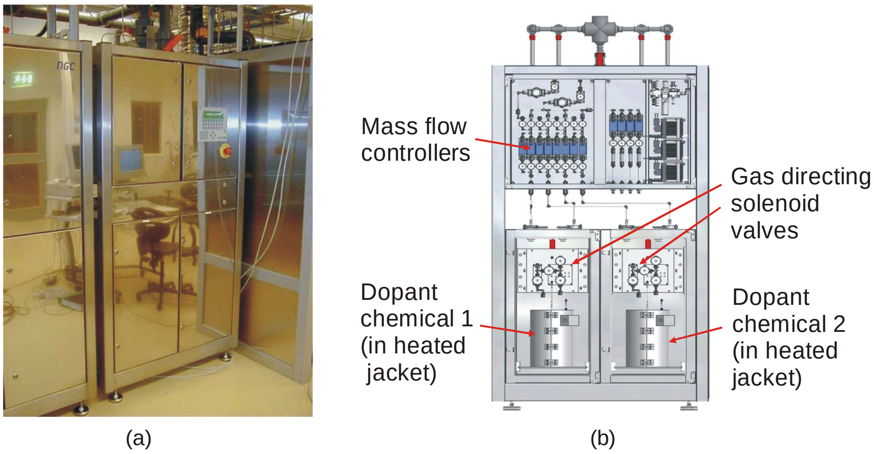

Figure 4.2: The external (a) and internal (b) view of Nextrom's high-temperture delivery system (NHS) which is suitable for up to 4 dopant chemicals [6].

Despite high-temperature delivery systems being commercially available for MCVD, there are only a handful of reports in the literature of their successful implementation. A summary of the known progress in the area of active preform fabrication using chelate precursors is given in the following paragraphs.

The fabrication of RE-doped preforms using chelate precursors was first reported by Tumminelli et al. [5]. Silica fibres containing either neodymium oxide (Nd_2O_3), ytterbium oxide (Yb_2O_3) or erbium oxide (Er_2O_3) were presented, all co-doped with aluminium oxide (Al_2O_3) and prepared using TRIS(2,2,6,6,-tetramethyl-3,5-heptane-dione) RE chelate compounds. The experimental setup used by Tumminelli et al. located the RE precursors externally to the MCVD lathe and transported the dopant vapour with a helium (He) carrier gas through a heated rotary seal to the reaction-zone. An additional ribbon burner, spanning the length of the substrate tube, was used to warm the glassware during deposition. An erbium-ytterbium co-doped fibre was reportedly fabricated using this method and exhibited a RE concentration of >11 wt% of Yb_2O_3, which was calculated by comparing the Yb-induced optical absorption in the fibre with that of a known glass composition. The work by Tumminelli et al. was undertaken at a time when the solution doping technique was in its infancy and can arguably be regarded as proof-of-concept for preform fabrication using vapour-phase deposition of RE ions. Moreover, no information on the obtained preform refractive index profile or dopant uniformity was disclosed, and only limited data has been provided on the laser results of a fibre doped with 1 wt% of Nd_2O_3.

Over a decade later, Jackson et al. [8] reported on a thulium (Tm)-doped preform fabricated using a chelate-based MCVD technique. Optical fibre was drawn into a double-cladding geometry from the preform which contained ~0.35 wt% of Tm_2O_3 in an aluminosilicate (Al:Si) host glass. An output power of >1.5 W at a wavelength (λ) of ~2 μm was demonstrated with a slope efficiency of 13 %.

In 2008, a more explicit account of preform fabrication using RE chelates was reported. Sekiya et al. [9] described how vapour from chelate precursors, which were located externally to the lathe, were transported through heated lines in the same way as depicted by Tumminelli et al. and Jackson et al. The experimental setup also included a ‘nickel-chrome heated nozzle’, which protruded into the glassware to ensure that the dopant vapour did not condense prematurely. Sekiya et al. targeted a large-mode area (LMA) Yb-doped preform structure, using $Yb(DPM)_3$ chelate (essentially the same compound as TRIS(2,2,6,6,-tetramethyl-3,5-heptanedione)) co-doped using $AlCl_3$. The focus of the article was on validating their fabrication technique and around 40 doped layers were deposited, forming a 5 – 6 mm diameter core with a maximum Yb concentration of 1.2 wt%. Sekiya et al. cite that the early difficulties in achieving good radial and longitudinal dopant uniformity in the preform were overcome with improved process control. Confirmation of their improvements was presented by way of Scanning Electronic Microscopy-Electron Probe Microscopy Analysis (SEM-EPMA) measurements, which showed a radial variation in dopant concentration of less than ±10 %.

Sekiya et al. omit any reference to fibre being drawn from the preforms, and instead the continuing results were reported separately by Petit et al. [10]. In this article, Petit et al. correlated the chelate temperature used during glass deposition the Yb-incorporation in the resultant fibre. A concentration of 0.12 wt% and 1.2 wt% was achieved using a furnace temperature of 200 °C and 250 °C, respectively. It was also demonstrated that the solubility limit of Yb in silica, without any co-doping, was 0.2 wt%. A LMA fibre with ~0.3 wt% Yb_2O_3 and ~0.4 wt% Al_2O_3 was tested in a laser configuration, and a slope efficiency of 73 %, with respect to launched pump power, was reported.

An alternative vapour deposition technique has been reported by Lenardic et al. (of Optacore) [11], termed 'flash vaporization', which is based on a hybrid delivery method for MCVD and was developed in conjunction with Kemstream (France). Lenardic et al. proposed that the sublimation of some solid chelate precursors does not yield a stable and reproducible vapour flow, and that the materials may thermally degrade when subjected to prolonged direct contact heating. These issues can reportedly be evaded by using the flash vaporization technique. The process is an amalgamation of aerosol and chelate doping techniques. Dopant precursors are first dissolved in a solvent which is then atomised and directly injected into a high-temperature (up to 250 °C) evaporation chamber. The aerosol is instantly vaporised and the dopant mixture is transported through heated lines and a high temperature rotary seal to the substrate tube. Rare-earth organometallic precursors are typically dissolved in TEOS (tetraethylorthosilicate $Si(OC_2H_5)_4$), which is readily available in high-purity and also acts as a silica precursor, thus removing the need for $SiCl_4$. The layer deposition step can be repeated as required, and 20 or more RE-doped layers are achievable [12].

An Yb-doped aluminosilicate fibre fabricated using the flash vaporization technique has been reported by Lenardic et al. [11]. The fibre had a measured Yb_2O_3 content of up to 3.2 wt% and a background loss of 20 $dB.km^{-1}$ in the $\lambda = 1100 – 1300$ nm transmission window. A subsequent article by Lenardic et al. expands the repertoire of precursors that can be deposited using flash vaporization to include, bismuth (Bi), iron (Fe) and cobalt (Co) [12]. A Bi-doped aluminosilicate preform was fabricated using $Bi(tmhd)_3$ and $Al(acac)_3$ precursors. Analysis of the preform samples, however, showed only trace amounts of Bi_2O_3, and no explanation for the low concentration was given. Similarly, the preforms doped with iron and cobalt, achieved using $Fe(thmd)_3$ and $Co(acac)_3$ precursors, also showed low concentrations and the absence of characterisation from the drawn fibres suggests that the process still requires refinement.

The accounts in the literature of MCVD preform fabrication using RE chelate compounds provide encouraging results, however, it is apparent from the lack of publications and underwhelming results in this area, that the employed schemes harbour certain problems. It is also possible that the institutions that possess these specialist facilities do not wish to openly publicise their development, but the inherent complexity of the currently available equipment is believed to be a contributing factor. Locating the dopant source external to the preform-making lathe appears to be symptomatic of many of the cited problems. A logical step, therefore, is to situate the chemical precursor closer to the substrate tube initially. Techniques such as the heated frit and heated source, which were alluded to in Chapter 2, both adopt this approach. However, the exponential dependence of vapour pressure on temperature, and the potential for premature oxidation of the dopant, means that heating the chemical from the glass exterior does not allow a steady flow of dopant vapour to be maintained.

The CIC process presented in this chapter addresses all of the issues that are encountered with the existing technologies. First and foremost, the CIC setup uses relatively simple components that remove the need for the remote vaporiser and heated delivery lines that are integral to the previously mentioned systems. Instead, the precursors are situated in a glass crucible that is in close proximity to the reaction-zone and heated directly, rather than by an external burner. This strategy gives the crucible its superior temperature stability and, moreover, it can be heated to several hundred degrees Celsius, allowing a wider range of precursors with low volatility to be used.

4.3 Experimental work

This section presents the experimental work undertaken in developing the CIC process, and silica preform fabrication using vapour-phase deposition of ytterbium and aluminium dopants. Identifying a suitable precursor for Yb and Al is equally as important as the process itself, and three chemicals have been selected for investigation: aluminium chloride, ytterbium chloride and ytterbium TRIS(2,2,6,6,-tetramethyl-3,5-heptane-dionato). Preforms have been successfully fabricated using two of these precursors. The preforms and the fibres drawn from them have been characterised and the findings are discussed. The modified rotary seal and glassware arrangement was conceived and engineered by the author and the preforms were fabricated solely or in conjunction with Dr. Alex Boyland. The passive fibre characterisation was also conducted by the author, whilst the laser results were obtained by Dr. Seongwoo Yoo.

4.3.1 Preform fabrication using chemical-in-crucible process

The experimental setup used for the CIC process and preform fabrication is shown schematically in Figure 4.3. The dopant precursors are situated in a glass crucible, which is positioned within the glassware a small distance from the start of the substrate tube. The crucible is electrically heated using a resistive-element, and a flow of He carrier gas is directed over the heated precursor and transports the vapour downstream to the reaction-zone. The dopant vapours are initially separated from the conventional reagent chemicals (i.e. $SiCl_4$, $GeCl_4$, $POCl_3$ and BBr_3) which pass through the outer glassware. Segregating the solid dopant material from that of the glass-forming vapours prevents the contents of the crucible from oxidising prematurely. A novel rotary seal permits the inner glass tube to remain stationary and gas tight whilst the outer tube rotates. The final design of the rotary seal arrangement, with a dual-gas input adapter and provisions for the electrically heated crucible, required extensive engineering to reach its developed stage and is the key part of the CIC process.

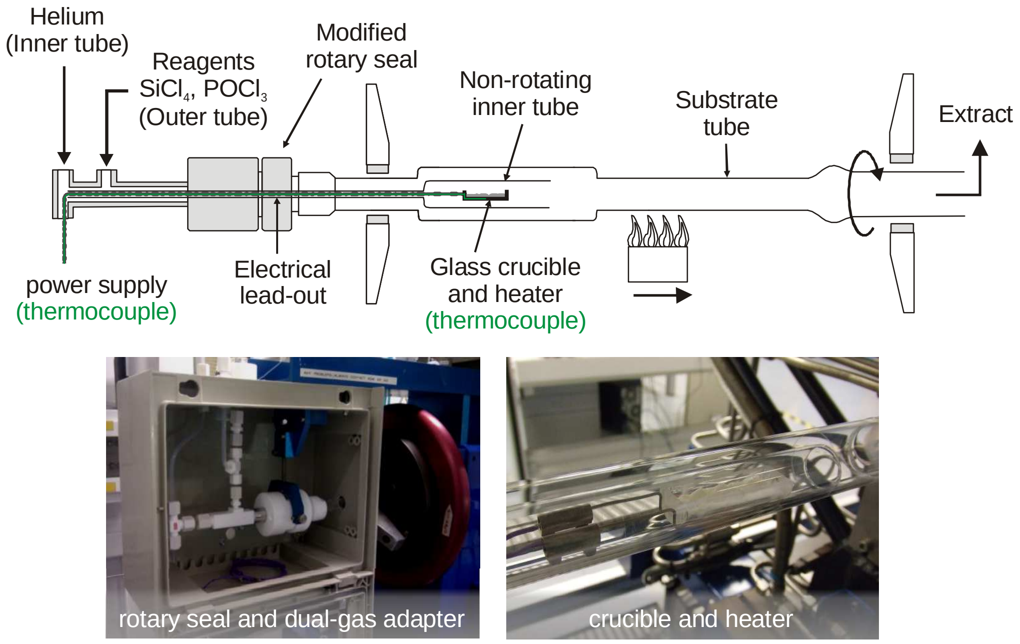

Figure 4.3: Schematic of CIC apparatus designed and built by the author showing (below) photographs of the modified rotary seal and heated chemical crucible.

The CIC process avoids the need to heat the rotary seal by situating the chemical crucible close to the reaction-zone and heating it in-situ. The rotary seal was initially purchased from Production Techniques (Hampshire, UK) and modified to allow for two gas inputs as well as accommodating an 8 mm diameter glass tube through which electric wires can be fed. An additional T-adapter allows the wires from the crucible heater to be accessed whilst maintaining gas-tight integrity. Owing to a practical limitation in the size of the inner glass tube, and the required compatibility with a 20 × 16 mm diameter substrate tube, the crucible and heater needed to be miniature in size. No suitable commercial products were found, so the items were designed and constructed in-house.

The basic heater design consisted of an electrical resistance wire that was formed around a glass crucible. This straightforward approach avoided any complications with out-gassing from glues or complex materials which may have subsequently been incorporated into the preform as impurities. Nickel-chromium (nichrome 80/20) wire was used as the heating element, which has a high melting point (1400 °C) and good resistance to oxidation. A custom-made low-voltage variable power supply, with a feedback temperature control mode via a thermocouple input, was purchased from EFI (Suffolk, UK).

The specifications of the power supply and resistance wire depended on a number of factors, such as the final heater design and rate of gas flow around the crucible, which would be dictated by the fabrication process and were not known initially. As a starting point, preliminary trials performed using existing power supplies and heating wires suggested that a power in the region of 100 W, as deduced from the measured voltage and current, was needed to achieve a temperature in the region of 200 – 300 °C. This temperature range and identified power rating was used as the basis for selecting the power supply and resistance wire, and is elaborated upon below.

The resistivity (ρ) of nichrome wire is $\sim 1 \times 10^{-6}\ \Omega.\mathrm{m}^{-1}$, which is related to its physical dimension by $\rho = R(A/l)$, where R is the resistance, and A and l are the area and length, respectively. The power (P) transferred to the wire can be calculated from $P = V^2/R$. The maximum power dissipated, using a set voltage, is therefore a trade-off between the length of the resistance wire and its cross-sectional area. i.e. a thicker, or shorter length, wire will result in an increased power. For reasons of safety, the output voltage of the power supply was limited to <10 V. At maximum output voltage, a wire with a resistance of 1 Ω would therefore dissipate a power of 100 W. The electrical current drawn through the wire under these conditions would be 10 A (from $P = I^2R$). The anticipated length of the wire was around 0.15 m, and so a diameter of 0.5 mm was chosen which complied with the required electrical resistance, as well as being sufficiently ductile that it could be shaped as required. The power supply and nichrome wire was specified based on these calculations.

During the course of the research, a number of glass crucible designs were tested. The evolution of these designs is shown in Figure 4.4. Crucible A was the first incarnation, and employed a quartz crucible with a volume of $\sim 1\ \mathrm{cm}^3$, around which the nichrome wire was wound. The coiled wire arrangement concentrated the generated heat, in a similar way as a filament bulb, and was capable of reaching a maximum temperature of ~650 ºC (at 10 V). Crucible B was intended for larger dopant quantities and had a larger internal volume than crucible A. However, it was found that its increased thermal mass and simplistic heating-wire arrangement reduced its operating temperature to <400 ºC. Crucible C was made from borosilicate glass and was supplied by a third party. This was the first attempt at actively monitoring the temperature of the crucible by means of a glass sheath in which a thermocouple was inserted. Modest control of the temperature was possible, but the semi-circular profile meant that the surface area reduced as the quantity of chemical decreased. Crucible design D was the final design, and was made by milling a parallel-walled trench in a glass rod (12 mm diameter), on to which glass end faces were welded. A hole was drilled into the solid glass region beneath the trench to accommodate a thermocouple. An operating temperature of up to ~450 ºC could be achieved, and with feedback control this temperature was stable to better than ±2 ºC.

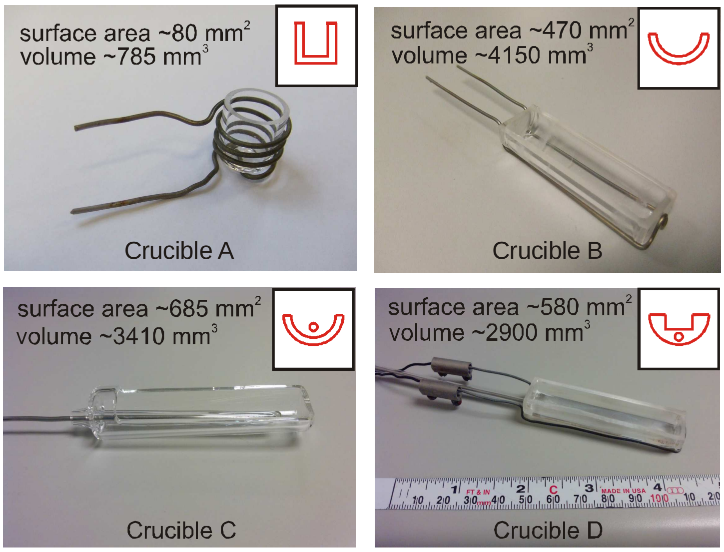

Figure 4.4: Crucible designs trialled with the CIC apparatus. The measured surface area and volume of the chemical in a fully filled crucible is shown. The insets illustrate the cross-sectional shapes of the designs.

MCVD preform fabrication using the CIC apparatus is conducted in the conventional manner, with the main reagent flows and lathe control functions all operated from the standard computer interface. The process begins with the customary preparation steps of gas-phase etching of the substrate glass (SUPRASIL-F300, from Heraeus, Germany) using sulphur hexafluoride (SF_6), followed by the deposition of several undoped silica cladding layers. At the core deposition stage, the crucible heater is ramped to temperature and allowed to stabilise. Once vapour is seen exiting the inner tube, the carrier gas flow can be varied to ensure that the vapour is efficiently transported downstream and without significant turbulence. Once set, the crucible temperature is adjusted to control the dopant concentration and the He gas flow remains fixed. Numerous preforms have been fabricated using this technique to validate and optimise the CIC process. In each case, a standard step refractive index profile consisting of one or more core layers was targeted. Specific preforms are reported in the following sections, whereas a full list of the fabrication runs can be found in Appendix B.2.

4.3.2 Preform fabrication using gaseous aluminium chloride

Aluminium chloride ($AlCl_3$) is widely used in industry and can be produced by passing chlorine gas over metallic aluminium at an elevated temperature [13]. $AlCl_3$ is also the primary precursor for incorporating aluminium, in the form of Al_2O_3, into fibre-preforms. It acts as an index-rising glass modifier ion in optical fibres as well as improving the RE solubility in silica [14]. The hydrated form of $AlCl_3$ (e.g. $AlCl_3.6H_2O$), however, is most familiar to MCVD preform fabricators through the role it plays in the solution doping process [2].

The fundamental chemical differences between anhydrous and hydrated $AlCl_3$ renders the latter compound ineffective as a vapour source. Owing to the interaction forces within hydrated $AlCl_3.6H_2O$ (which can also be written $[Al(H_2O)_6]Cl_3$), heating of the chemical does not yield Al-vapour, but instead the tendency is for the compound to hydrolyze resulting in the decomposition reaction shown in (4.1) [15]. This reaction reportedly occurs at a temperature of 90 °C, but is most rapid around 150 °C, and decomposition is still incomplete at 350 °C.

$$2AlCl_3.6H_2O \rightarrow Al_2O_3 + 6HCl + 3H_2O \qquad (4.1)$$

Hydrated aluminium chloride is therefore unsuitable for use in the CIC process, as the reaction product, Al_2O_3, is a non-volatile compound with a melting point of 2054 °C and a boiling point of almost 2977 °C [16]. The properties of anhydrous aluminium chloride, however, are more favourable. $AlCl_3$ sublimes above 100 °C and has a vapour pressure of around 1 kPa at ~100 °C [16]. It is also readily available with a purity of up to 99.999 % (Sigma Aldrich product). $AlCl_3$ does, however, require careful handling practises as it is corrosive and hydroscopic, and contact with water initiates a violent hydrolysis reaction that releases HCl fumes and heat.

Preform L30114 has been fabricated using the CIC process and anhydrous $AlCl_3$ as the precursor for the Al-doped core. To avoid contamination, a dry nitrogen (N_2) purged glovebox was used to decant ~0.5 g of $AlCl_3$ into crucible A, which was then transferred to the preform-making lathe in a sealed N_2-filled container. Once in the glassware setup, a dry gas flow over the crucible was maintained. A silica substrate tube, measuring 20×16 mm in diameter was prepared in the usual manner. The crucible was heated to a temperature of 200 – 230 ºC (the ambiguity relates to the absence of temperature feedback with the particular crucible used) and a single core layer was deposited using a burner temperature of 1950 ºC. The carriage traverse speed was 80 $mm.min^{-1}$, the $SiCl_4$ flow rate was 100 $ml.min^{-1}$, and the He flow rate directed over the crucible was 200 $ml.mim^{-1}$. By the end of the core pass the entirety of the $AlCl_3$ had been exhausted. The tube was subsequently collapsed and sealed in to a solid preform.

The refractive index profile (RIP) of the preform was measured at intervals along its length, Z, (where Z = 0 designates the preform position at the beginning of deposition) using PK2600HP (Photon Kinetics, US) equipment. The measured refractive index difference (Δn) and core diameters are plotted in Figure 4.5. A significant variation along the length can be observed. It was also noted that a section of the preform, between length positions Z = 70 and 140 mm, appeared white and corresponds to the region of highest refractive index. The large variation in Δn, ranging from 0.007 to 0.018, is attributed to a diminishing amount of available $AlCl_3$ in the crucible towards the end of the deposition pass.

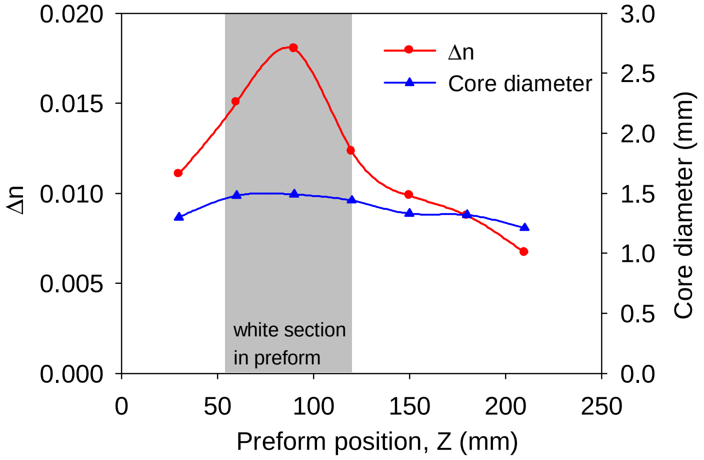

Figure 4.5: Peak refractive index and core diameter of preform L30114, measured at 30 mm intervals along its length.

Preform L30114 was drawn from position Z = 150 mm into fibre (T0171) of 80 μm in diameter and coated with a high-index polymer (DSM-314). The RIP of the fibre was measured by Mr. Robert Standish using S14 (Photon Kinetics, US) equipment, which revealed a core diameter of 8.2 μm and a calculated peak NA of 0.17 (Figure 4.6). The optical loss was measured using optical time-domain reflectometery (OTDR) equipment (model: ν-OTDR, Datacom) and was calculated to be 2.5 $dB.km^{-1}$ at the operating wavelength of 1285 nm. The absorption at $\lambda = 1380$ nm, resulting from hydroxyl (OH) ions, has been measured as ~2 $dB.km^{-1}$ using a white-light set up over a fibre length of 100 m. This equates to an impurity of <<1 part per million (ppm), by weight.

These fibre results assert the use of $AlCl_3$ and the CIC process for producing passively-doped preforms with various NA values and relatively low optical losses. Further preforms have since been fabricated, in collaboration with Dr. Alexander Boyland, to explore the upper concentration limit of Al-incorporation using the CIC method.

Preforms L30258, L30259 and L30260 were produced using the same process parameters as those described for L30114, except for the crucible temperature which was 140 °C, 175 °C and 190 °C, respectively. The improved crucible design D (see Figure 4.4) was also used in these experiments and the thermal stability achieved at the target temperature was ±1 °C.

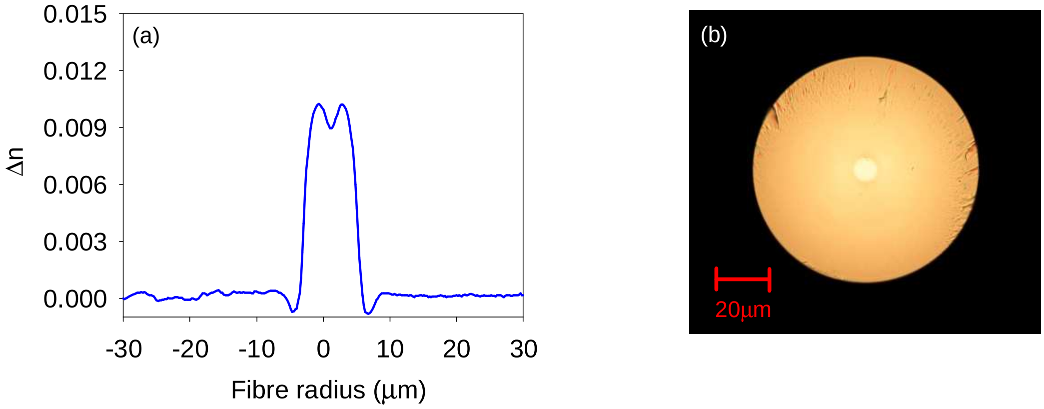

Figure 4.6: Aluminosilicate fibre T0171 fabricated using the CIC proces showing (a) the measured refractive index profile and (b) a cross-sectional image.

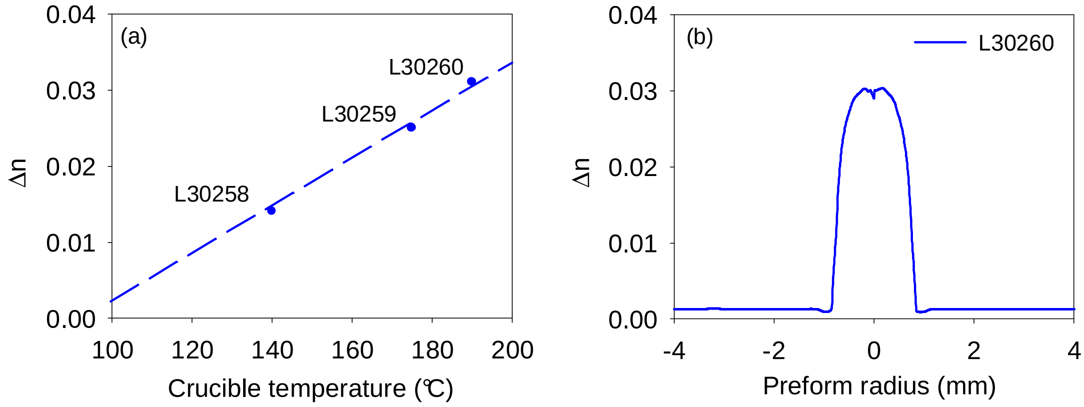

Figure 4.7: (a) Graph showing the average Δn for aluminosilicate preforms fabricated using crucible temperatures of 140 °C, 175 °C and 190 °C, respectively and (b) the RIP of preform L30260.

The RIP of the collapsed preforms was measured at intervals along their length. The average Δn is indicated in Figure 4.7(a) and is plotted against the crucible temperature that was used during fabrication. The longitudinal variation in the refractive index, for all cases, was significantly less than in the first preform (L30114), and typically less than 5×10^{-3} over a nominal 300 mm length. The vast improvement in uniformity is attributed to the temperature feedback control that was possible with the newer design of crucible. The RIP of preform L30260 is shown in Figure 4.7(b) and shows the highest index contrast achieved, to date, of 0.03, which corresponds to an NA of 0.30. This represents an addition to the silica glass from Al_2O_3 of ~16.5 mol%, and is higher than previously reported results using either a modified solution doping method [17] or an external Al-source delivery system [18].

4.3.3 Suitability of ytterbium chloride for vapour deposition

Hydrated ytterbium chloride ($YbCl_3.6H_2O$) is the conventional precursor used for incorporating Yb ions in MCVD preform fabrication, and is administered through a solution doping step [2]. It is available in high purity (99.998+ %, based on trace metal and rare-earth analysis) and is used extensively in research and industry alike for high power fibre lasers, with proven results. This subsection examines whether $YbCl_3.6H_2O$ is suitable for use as a vapour source.

The chemical $YbCl_3.6H_2O$ has a specified melting point of 150 °C, at which point decomposition of the compound also begins [16]. In contrast, dehydrated $YbCl_3$ has a melting point of 854 ºC and a vapour pressure of ~1 kPa at 1000 °C [16]. It is therefore crucial to understand the differences between hydrated and anhydrous ytterbium chloride, in the same way as defined for aluminium chloride in the previous section, and whether the compound can be used in the CIC process.

There are numerous studies on the thermal decomposition of hydrated lanthanide chlorides, including the chemical $YbCl_3.6H_2O$ [19-21]. The dehydration scheme reportedly depends on the atmosphere in which the compound is heated, although some of the studies in the literature are specifically aimed at those in the field of analytical chemistry and use unfamiliar experimental techniques. Wendlandt et al. [21] uses a thermobalance to examine the decomposition of $YbCl_3.6H_2O$, among other compounds, at temperatures of up to several hundred degrees Celsius in the presence of air. Decomposition of the starting material undergoes multiple reactions, characterised by intermediate species approximating to the form YbOCl, but the final product is Yb_2O_3 when the reaction is complete at a temperature of 585 °C. As Yb_2O_3 has a melting point of 2355 °C and a boiling point of over 4000 °C [16], it is unsuitable as a vapour source for ytterbium. Ashcroft et al. [19] and Hong et al. [20] separately examined the dehydration scheme of lanthanide chloride ($LnCl_3$) hydrates in atmospheres containing 1% hydrogen chloride (HCl) gas as well as nitrogen-only. Both articles reported an integer reduction in the number of bonded water molecules as the compound was heated up to 200 °C, characterised by the reaction $LnCl_3.nH_2O \rightarrow LnCl_3.mH_2O + (n\text{-}m)H_2O$. The final product was anhydrous lanthanide chloride.

The results in the literature indicate that as $YbCl_3.6H_2O$ is gradually heated, it passes through notable stages where water molecules are removed from the starting material. The final product is $YbCl_3$, but the reduction happens in combination with the production of other oxychloride-based compounds. The exact form of these intermediate species appears to be dependent on factors such as the surrounding atmosphere, the heating scheme, the rare-earth element, and even its initial purity [20, 21]. It is not entirely clear whether the reported experiments were carried out in a dry atmosphere, however, the results suggest that hydrolysis is taking place simultaneously with the dehydration (i.e. the water evolving at discrete temperatures is reacting and converting the starting compound to oxychloride).

The dehydration scheme of $YbCl_3.6H_2O$ has been experimentally determined. Two approaches were followed: the first used thermogravimetric (TG) equipment to accurately monitor the mass change in a sample that was subjected to a heating cycle, whilst the second provided a visible indication of the process and involved heating a sample inside a glass tube placed on the preform-making lathe.

The thermal decomposition of $YbCl_3.6H_2O$ was analysed using Perkin Elmer Diamond TG equipment. The apparatus consists of a sample and reference crucible enclosed in a furnace through which an inert gas is flowed. Each crucible is attached to a microbalance and thermocouple that allows the sample weight and temperature to be monitored by a computer. A sample of $YbCl_3.6H_2O$ weighing 6.6 mg was placed in a alumina crucible, within the TG equipment, and the furnace was purged with dry N_2 gas at a flow rate of 200 ml.min^{-1}. The furnace temperature was increased from ambient up to 900 °C, at a ramp rate of 10 °C.min^{-1}, and the measurement data logged. The results showed that the sample weight had reduced rapidly from its starting value to around 4.4 mg upon reaching ~225 °C. Thereafter, the weight decreased slowly to 3.4 mg at 900 °C. Overall, the trace displayed a gradual drop in the sample weight but without any distinguishing features. Further information was revealed when the data was differentiated (with respect to time), as shown in Figure 4.8.

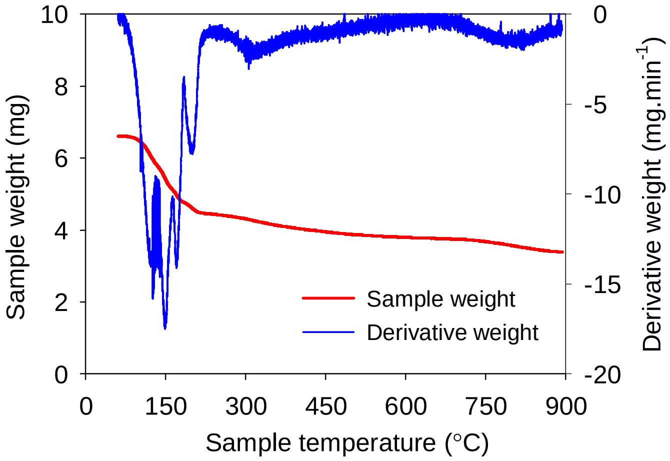

Figure 4.8: Thermogravimetric analysis of $YbCl_3.6H_2O$ sample (ramp rate = 10 °C.min^{-1}).

The graph shows sharp dips, corresponding to rapid weight loss, centred at sample temperatures of 122 °C, 150 °C, 170 °C and 200 °C. A broad dip is also evident around 310 °C. Comparing these results with those reported in the literature [19, 20], it is concluded that the abrupt changes in sample weight represent the integer reduction of H_2O from the sample. Comparable TG data was obtained by Kipouros et al. in a similar experiment analysing $NdCl_3$ [22]. From Figure 4.8, it is also evident that no significant weight reduction occurs above a temperature of ~800 °C. This suggests that hydrolysis reactions are taking place with the compound that is left behind in parallel with the H_2O release. The end product of these reactions is believed to be predominantly Yb_2O_3.

The second experiment to investigate the dehydration of $YbCl_3.6H_2O$ adopted a more rudimentary method. A silica glass tube was assembled on the preform-making lathe through which a flow of dry N_2 was passed. Midway along the tube a small section of the glass was expanded, into which ~1 g of $YbCl_3.6H_2O$ was placed. The tube was rotated at a slow speed and the carriage burner was used to gradually heat the glass from room temperature up to around 700 °C (this corresponded to the lower temperature limit of the optical pyrometer). This temperature was maintained for 30 minutes, after which the temperature was increased to ~1600 °C. During the initial temperature ramp, a significant amount of clear liquid, presumably water, collected in the tube downstream of the chemical sample. At no point was vapour seen evolving from the sample, or any visible deposits observed on the inner surface of the glass tube. During the subsequent temperature rise to 1600 °C, no vapour or evidence of chemical deposits was seen, indicating that the chemical had been converted to a non-volatile form, presumably Yb_2O_3. This was further substantiated by emptying the powdery remains into a beaker of water. The particles were insoluble, consistent with the properties of Yb_2O_3.

These findings concluded that the conventional hydrated ytterbium chloride chemical used in solution doping is not suitable as a vapour source or starting material for use in the CIC process. Anhydrous $YbCl_3$ may be suitable, but the intrinsically low volatility of the compound still means a temperature of between 800 – 1000 °C is required to produce sufficient vapour thus a and meaningful dopant incorporation in the preform. This temperature regime was not possible using the existing crucible designs, but preliminary work towards a high temperature crucible design is discussed in Chapter 7.

4.3.4 Ytterbium(TRIS) and the chemical-in-crucible process

The majority of the preforms that have been fabricated using the CIC process have been doped using the chemical precursor ytterbium(TRIS(2,2,6,6-tetramethyl-3,5-

heptanedionato)). This organic chelate compound, which is abbreviated to Yb(TRIS) hereafter, has the chemical formula $C_{33}H_{57}O_6Yb$ and can be readily purchased from chemical suppliers that specialise in precursors for chemical vapour deposition (CVD) applications. It is available with a purity of up to 99.9 % (Strem Chemicals product) and its material properties include a melting point of 167 – 169 ºC and a boiling point of 300 ºC [4]. Yb(TRIS) sublimes from its solid form, and has a vapour pressure of around 1 kPa at a temperature of 200 ºC [4].

During the conventional MCVD process, the chloride-based precursors, $SiCl_4$, $GeCl_4$ and $POCl_3$ undergo a well documented oxidation reaction in the hot-zone of the burner which results in amorphous particles of SiO_2, GeO_2 and P_2O_5, respectively. In contrast, the high-temperature chemical reactions that take place with RE chelate compounds in the presence of oxygen are less well understood. The experimental work in preform fabrication using Yb(TRIS) has uncovered a number of practical and material-based considerations pertaining to its use. These findings have helped to better understand the deposition process with RE chelates and some of the important process variables are described below. The experimental setup refers to that shown in Figure 4.3.

Firstly, the position of the crucible within the glassware was found to be crucial for the chelate vapour to be transported efficiently to the reaction-zone. When the separation between the crucible and the substrate tube was insufficient, the spatial ‘spread’ of the burner flame inadvertently heated the precursor at the start of each pass. However, if the distance between the crucible and substrate was excessive, then the vapour tended to condense on the cool glass wall before reaching the reaction-zone. A separation of between 175 mm and 200 mm was found to be optimum, and was adopted for the glassware set up in all preform runs to improve their repeatability.

Before the core deposition pass commenced, the crucible was heated to its target temperature. During this period, of between 30 and 120 seconds, any chelate vapour evolving from the crucible had the tendency to condense on the cold inner surface of the substrate tube. It was found that repeatedly traversing the carriage at a high speed

(>1000 mm.min^{-1}) along the length of the glassware using a burner temperature of 100 – 300 ºC was an effective way to re-evaporate the dopant and prevent any further deposits on the glass surface.

The flow rates of the dopant carrier gas (He) through the central glassware, and the oxygen (O_2) in the outer tube, were set once the chelate vapour was visible, and were adjusting independently to achieve efficient transport of the vapour downstream and without any obvious turbulence. Suitable He and O_2 gas flows were found to be around 1200 ml.min^{-1} and 1000 ml.min^{-1}, respectively. Failure to achieve a net flow downstream resulted in the undesired ignition of the Yb(TRIS) vapour as the burner commenced its pass. Once the He and O_2 gas flows were set appropriately, the required concentration of Yb was adjusted by means of the crucible temperature.

Following the core layer deposition pass, many of preform fabrication runs exhibited a distinct section near the start of the substrate tube of white and dark coloured deposits that still remained in the final preform. The origin of this contamination is believed to be inhomogeneous carbon- and RE-rich particles from the premature decomposition of Yb(TRIS), and is reasoned as follows:

When the core deposition pass commences, the carriage is stationary at the beginning of the substrate tube, and undergoes a dwell (of ~12 seconds) whilst the glass surface reaches its target temperature (typically in the region of 1950 – 2100 ºC). During this period, chelate vapour is already flowing downstream in a steady state together with $SiCl_4$. As the internal gas temperature reaches ~650 ºC, the Yb(TRIS) compound decomposes into its metallic and organic constituents [23], but the temperature is insufficient to oxidise the $SiCl_4$ vapour. This results in carbon- and RE-rich deposits several centimetres downstream of the burner (there are also the combined reactions with $SiCl_4$ vapour to consider, although the described effect was still apparent in trials where initiating the $SiCl_4$ flow was delayed). Once the burner has reached its target temperature it then traverses downstream and passes over the contaminated region. The carbon deposits should readily evaporate in the oxygen atmosphere at above ~600 ºC, but the Yb ions are more likely to be oxide in form and are therefore less volatile. From the experiments performed, it appears that acquiring some contaminates on the glass tube during the burner start-up sequence is unavoidable. However, by extending the length of the original substrate tube so as to include a 'sacrificial' region, these problems were not transferred into the final preform.

It should be noted that the decomposition of Yb(TRIS) described above is the intended mechanism for doping the deposited glass with Yb-ions, but with the desired reaction taking place at high temperature and in combination with $SiCl_4$ oxidation. The thermopheretic deposition process occurs once the glass temperature and chelate vapour flow have stabilised and the carriage velocity is constant. The Yb(TRIS) and $SiCl_4$ vapours (and $POCl_3$ in the case of the preforms reported in the following sections) then undergo a high-temperature oxidation reaction upon reaching the hot-zone and form glassy particles downstream that are sintered as the burner passes over them.

4.3.5 Preform fabrication using ytterbium(TRIS)

In order to establish the appropriate process conditions for using chelate compounds within the CIC process, numerous trial preforms were fabricated. These are tabulated in Appendix B.2. The understanding acquired from these experiments has subsequently been used to produce two phosphosilicate preforms, using Yb(TRIS), which demonstrate the capability for low and high RE-dopant concentrations. Their fabrication and characterisation is reported here.

Preforms L30193 and L30194 were fabricated using the glassware arrangement shown in Figure 4.3 and crucible design D (see Figure 4.4). Feedback control of the crucible temperature was possible through the integral thermocouple, and the temperature stability was to be maintained to within ±1 °C. Both preforms were fabricated with a F300-quality substrate tube measuring a nominal 20×16 mm in diameter and 500 mm in length. The standard glass preparation steps and cladding layers were applied before a single core layer was deposited. The gas flow rates used during deposition of the Yb-doped core were, $SiCl_4$ = 150 ml.min^{-1}, $POCl_3$ = 450 ml.min^{-1}, O_2 = 1200 ml.min^{-1} and He = 1200 ml.min^{-1}. The crucible was heated to a temperature of 200 °C in the case of preform L30193, and 250 °C for L30194, as measured by the thermocouple. The temperature of the burner was maintained at 1800 ±3 °C during deposition and the carriage traverse was set to 100 mm.min^{-1}. Following deposition the tube was collapsed and sealed in the normal manner.

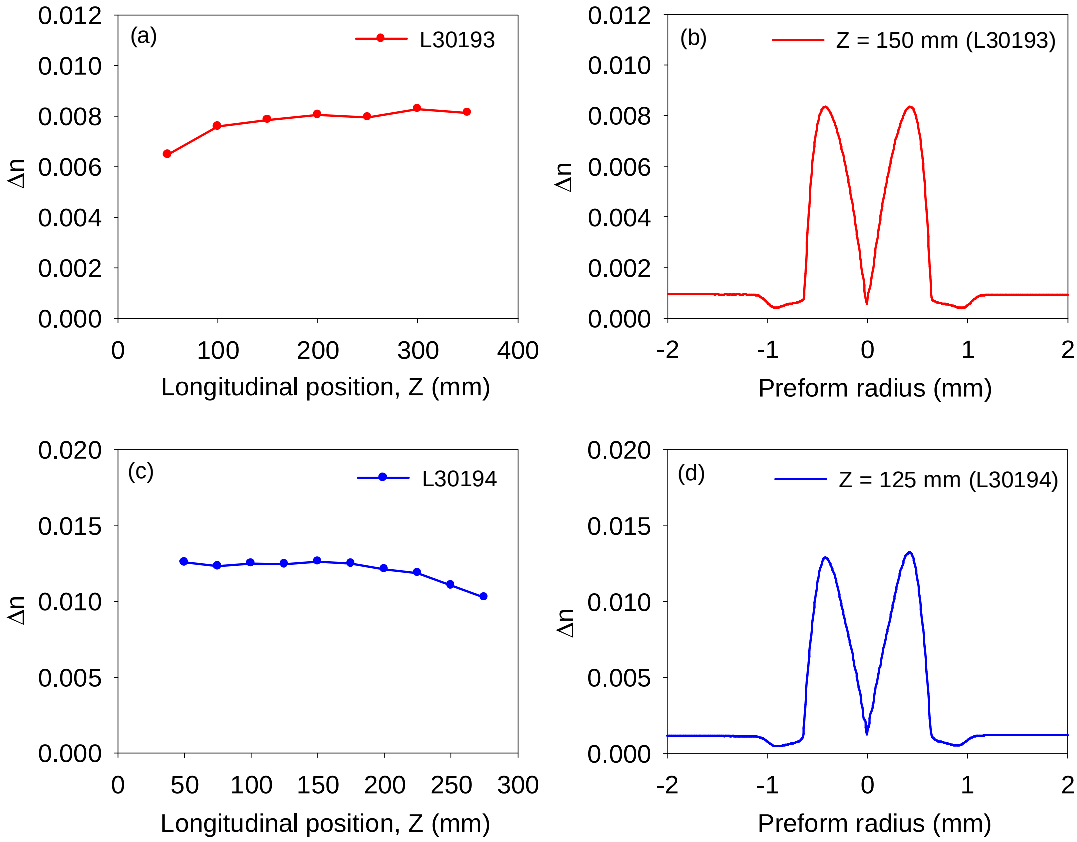

Figure 4.9: Variation in Δn along the length of preforms (a) L30193 and (c) L30194, and an example refractive index profile (b) and (d), respectively. Z = 0 corresponds to the preform position at the beginning of deposition.

Multiple RIP measurements were made spanning the length of each preform. A plot of the peak Δn versus longitudinal position can be seen in Figure 4.9, alongside which is an example of the preform RIP. The prominent central dip in the RIP is a result of P_2O_5 evaporation during the seal pass, as the equipment was not equipped for ‘over-doping’ during this final step. Although the variation in refractive index along the preform shows reasonably good uniformity, it is primarily an indication of the phosphorous incorporation rather than the Yb-concentration.

Preform	Fibre	Position drawn	Core/cladding diameter (μm)	Yb-concentration
L30193	T0299	BOD	12/126	8,000 ppm
L30193	T0383	MOD	12/125	-
L30193	T0300	EOD	13/129	7,200 ppm
L30194	T0302	BOD	13/128	24,000 ppm
L30194	T0327	MOD	40/400	20,100 ppm
L30194	T0303	EOD	12/120	15,700 ppm

Table 4.1 – Summary of fibre draws from Yb-doped phosphosilicate preforms L30193 and L30194. (BOD, MOD and EOD denote the positions from the beginning, middle, and end of deposition).

A series of fibres were drawn from each preform for the purpose of assessing the Yb-concentration and the background optical loss, as well as for subsequent device implementation (see Table 4.1). Fibres T0299 and T0300 were drawn from the beginning-of-deposition (BOD) and end-of-deposition (EOD) regions of L30193, respectively, whilst the fibre originating from the BOD and EOD of preform L30194 are denoted as T0302 and T0303. The target fibre diameter in each case was 125 μm and the fibres were drawn in a double-cladding (DCF) geometry with a low-index (PC-373) coating. The induced absorption from Yb^{3+} ions at a wavelength of 976 nm was evaluated from white-light measurements. Fibres drawn from preform L30193 (crucible temperature = 200 °C) reveal a concentration of ~8,000 ppm, by weight, whilst those fibres drawn from preform L30194 (crucible temperature = 250 °C) reveal a higher concentration of ~20,000 ppm, by weight. A variation in the measured values from alternative ends of the preforms is observed, and in each case the RE incorporation is lower from the EOD section.

The background loss in the fibres was established using OTDR. The results from fibres belonging to both preforms indicate that the losses are in the region of 100 – 175 $dB.km^{-1}$ (at $\lambda = 1285$ nm), but with seemingly incompatible values. For example, a background loss of 148 dB.km^{-1} and 102 dB.km^{-1} was obtained for fibres T0300 and T0303, respectively, and points towards a higher material loss for the fibre with a lower Yb incorporation. Additional loss measurements of T0302 and T0383, which was drawn with a high-index coating, were performed using a standard white-light setup and the results are shown in Figure 4.10. The loss spectrum from an existing undoped F300-quality rod, drawn with the same low-index coating, is also plotted for comparison to illustrate the expected wavelength dependent transmission of the silica glass. The graph depicts an uncharacteristic lowest loss region in the visible wavelength range for both Yb-doped fibres (~29 dB.km^{-1} at λ = 715 nm) which increases significantly towards the near-infrared.

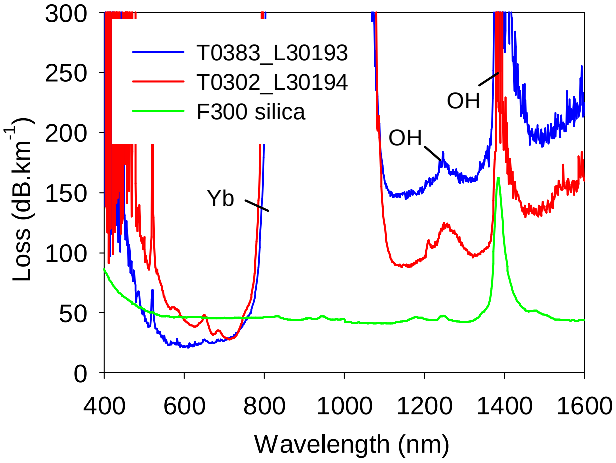

Figure 4.10: Loss spectra of fibres T0383-L30193 and T0302-L30194 showing a trend of higher loss towards the near-infrared region. A plot of the optical loss from an undoped F300-quality glass rod, coated with a low-index polymer, is included for comparison.

The obtained loss trend is hypothesised to be a result of absorption bands which mask what would be a more conventional looking trace with a low-loss region around λ = 1550 nm. Absorption from OH groups are visible at λ = 1380 nm as well as at λ = 1240 nm, which can be equated to 7.4 ppm, by weight, of impurity in the core glass. The relatively low purity starting precursor of 99.9 % is also a potential source of contamination. A detailed chemical certificate of analysis of the impurities within the precursor was unavailable from the supplier, but absorption peaks seen at wavelengths of around 530 nm, 654 nm and 1543 nm suggest the presence of Er^{3+} ions. The intensity of the assumed Er^{3+} peak at $\lambda = 530$ nm is equivalent to a concentration in the region of 1 ppm, by weight, and is entirely consistent with the manufacturers specified purity for Yb(TRIS). It is believed that absorption from these, and other impurities, are responsible for the high background loss seen in the near-infrared range.

A large diameter fibre (T0303), drawn from the high Yb-concentration preform L30194, has been tested in a lasing configuration by Dr. Seongwoo Yoo. The experimental setup was based on that shown in Chapter 2. The fibre was cladding-pumped by a fibre-coupled 975 nm laser diode via collimating and focusing lenses. A coupling efficiency of over 85 % was obtained. The laser output power characteristics for the fibre are shown in Figure 4.11, together with the spectrum taken at maximum output power. The output of the fibre reached 16 W for a launched pump power 20 W. The output power linearly increased with the launched pump power with a slope efficiency of 84 %.

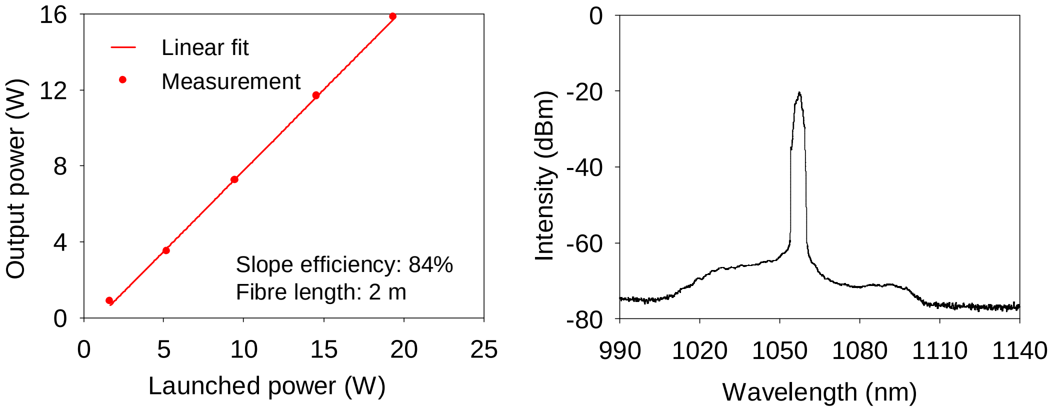

Figure 4.11: Laser efficiency measurement of Yb-doped fibre T0303-L30194 showing (a) the slope efficiency and (b) emission spectrum.

The laser result shows good optical-to-optical conversion efficiency at modest pump power. This result compares well against an Yb doped fibre fabricated by Petit et al. using Yb(TRIS) [10]. Petit et al. reported the slope efficiency in the fibre as 74 % with an output power of approximately 100 W. Further device work has been carried out, by others, on fibre T0327 (drawn from preform L30194) which has generated an output power of 200 W although initial results indicate that the slope efficiency is 72 % [24].

4.4 Summary

A novel fabrication process for doping preforms using precursors that have a low vapour pressure has been conceived and studied. The CIC experimental setup is compatible with conventional MCVD apparatus and allows new and unusual dopants to be assessed for their suitability in preform fabrication. The prior art in vapour-phase deposition of RE dopants was firstly reviewed, and the drawbacks of existing schemes were highlighted. The CIC process possesses many advantages over its counterpart methods, including the option to trial small quantities of potentially expensive or untested dopant materials, and the innate capability to use higher temperatures than are possible with external-source delivery systems.

A passively-doped preform was fabricated using anhydrous $AlCl_3$ and the CIC process. The measured refractive index profiles showed a maximum NA of 0.23, corresponding to an Al_2O_3 concentration of 10.5 mol%. Fibre drawn from the preform revealed an optical loss of 2 $dB.km^{-1}$, at $\lambda = 1285$ nm, and an OH impurity of <1 ppm, by weight. This demonstrates that relatively low loss fibre can be achieved using the CIC process and the results compare well against similar results in the literature. Simpson et al. reported on the fabrication of an Al-only fibre using a gas-phase technique with a measured loss of 0.75 $dB.km^{-1}$ at 1.6 μm. The NA of this fibre was 0.18, and although a fibre with a higher NA of 0.29 was also reported this was achieved with the addition of phosphorous to the core composition. Simpson et al. reported a considerably higher value of 4 – 12 $dB.km^{-1}$ for the OH impurity in their fibres compared to the 2 $dB.km^{-1}$ experimentally determined in fibre T0171. The measurement on fibre T0171 however was only performed on a 100 m long sample and therefore includes a scaling error.

The feasibility of using either hydrated or anhydrous ytterbium chloride as a vapour delivery source was explored. The thermal decomposition of $YbCl_3.6H_2O$ was examined using TG equipment as well as by direct heating within a silica tube on the perform-making lathe. TG analysis revealed a modest reduction in weight as the sample temperature was increased, whilst a transparent liquid was seen evolving from the chemical when it was heated on the lathe. These findings were consistent with the evaporation of water from the chemical and the non-soluble residue suggested that it had combined with the sample to form a non-volatile compound consistent with Yb_2O_3. It was concluded that $YbCl_3.6H_2O$ was unsuitable for use in the CIC process and anhydrous ytterbium chloride would be better suited as a RE precursor.

The main part of the experimental work involved the use of the chemical compound Yb(TRIS). The fabrication and characterisation of two Yb-doped phosphosilicate preforms have been reported, which represent low and high RE concentrations. Optical measurements on the fibre drawn from these preforms revealed an Yb concentration of ~8,000 ppm and ~20,000 ppm, by weight, obtained with a crucible temperature of 200 °C and 250 °C, respectively. The achieved Yb concentrations are higher than those reported by Sekiya et al. [9] using the same precursor, although their work predominantly focussed on optimising the radial and longitudinal uniformity of the deposited layers and no attempts at higher concentrations were discussed. They report good radial uniformity of refractive index in a preform with 40-50 deposited layers and negligible longitudinal variation in the Yb concentration over a length of 340 mm. This compares to the preforms reported here which have a variation in the refractive index of up to 0.002 over the same length of preform.

The background loss in the fibres depicted an uncharacteristic lowest loss region (~29 dB.km^{-1} at λ = 715 nm) in the visible wavelength range, which increased significantly towards the near-infrared (~152 dB.km^{-1} at λ = 1550 nm). It was suggested that this loss trend was caused by the relatively low purity of the starting precursor (99.9 %). There is no mention of the loss in the recent reports by either Sekiya et al. or Petit et al. on the fibre fabricated using their gas-phase deposition using Yb(TRIS).

Finally, a length of fibre with a high Yb-concentration of 15,700 ppm, by weight, was tested in a lasing configuration. The output of the fibre reached 16 W for a launched pump power 20 W, and a slope efficiency of 84 % was obtained. Further device work on a larger diameter fibre (400 μm) drawn from the same preform was tested up to 200 W, which demonstrates the potential of the CIC process to produce Yb-doped fibre for high-power applications [24].

4.5 References

1. A.J. Boyland, A.S. Webb, S. Yoo, F.H. Mountfort, M.P. Kalita, R.J. Standish, J.K. Sahu, D.J. Richardson, and D.N. Payne. "Optical Fiber Fabrication Using Novel Gas-Phase Deposition Technique". *Journal of Lightwave Technology*, 29(6): 912-915, (2011).
2. J.E. Townsend, S.B. Poole, and D.N. Payne. "Solution-doping Technique for Fabrication of Rare-earth Doped Optical Fibres". *Electronics Letters*, 23(7): 329-331, (1987).
3. M.J.F. Digonnet, *Rare Earth Doped Fiber Lasers and Amplifiers*. New York: Marcel Dekker. (1993).
4. J.E. Sicre, J.T. Dubois, K.J. Eisentraut, and R.E. Sievers. "Volatile Lanthanide Chelates. II. Vapour Pressures, Heats of Vaporization, and Heats of Sublimation". *Journal of the American Chemical Society*, 91(13): 3476-3481, (1969).
5. R.P. Tumminelli, B.C. McCollum, and E. Snitzer. "Fabrication of high-concentration rare-earth doped optical fibers using chelates". *Journal of Lightwave Technology*, 8(11): 1680-1683, (1990).
6. Nextrom. *www.nextrom.com*.
7. Optacore. *www.optacore.si*.
8. S.D. Jackson, T. Ryan, and S. Mossman. "High power Tm^{3+} doped silica fibre laser fabricated using chelate delivery deposition". *Optics Communications*, 216(4-6): 401-404, (2003).

9. E.H. Sekiya, P. Barua, K. Saito, and A.J. Ikushima. "Fabrication of Yb-doped silica glass through the modification of MCVD process". *Journal of Non-Crystalline Solids,* 354(42-44): 4737-4742, (2008).
10. V. Petit, E.H. Sekiya, T. Okazaki, R. Bacus, P. Barua, B. Yao, K. Ohsono, and K. Saito. "Improvement of Yb^{3+} doped optical fiber preforms by using MCVD method." in *Proceedings of SPIE - Solid State Lasers and Amplifiers III, Strasbourg, France*. April 8-10, 69980A-8, (2008).
11. B.K. Lenardic, Miha; Guillon, Herv; Bonnafous, Samuel. "Fabrication of Rare-Earth Doped Fibers by Flash Vaporization Method." in *European Conference and Exhibition on Optical Communication, Berlin, Germany*. 45, (2007).
12. B. Lenardic, M. Kveder, H. Guillon, and S. Bonnafous. "Fabrication of specialty optical fibers using flash vaporization method." in *Proceedings of SPIE - Passive Components and Fiber-based Devices V, Hangzhou, China*. (2008).
13. J. Kotz and K. Purcell, *Chemistry and chemical reactivity (second edition).* Saunders College Publishing. (1991).
14. K. Arai, H. Namikawa, K. Kumata, T. Honda, Y. Ishii, and T. Handa. "Aluminium or phosphorus co-doping effects on the fluorescence and structural properties of neodymium-doped silica glass". *Journal of Applied Physics*, 59(10): 3430-3436, (1986).
15. M. Hartman, O. Trnka, and O. Šolcová. "Thermal Decomposition of Aluminum Chloride Hexahydrate". *Industrial & Engineering Chemistry Research*, 44(17): 6591-6598, (2005).
16. R.C. Weast, *CRC Handbook of Chemistry and Physics.* CRC Press. (1984).
17. F.Z. Tang, P. McNamara, G.W. Barton, and S.P. Ringer. "Multiple solution-doping in optical fibre fabrication I - Aluminium doping". *Journal of Non-Crystalline Solids,* 354(10-11): 927-937, (2008).
18. J.R. Simpson and J.B. Macchesney. "Optical fibres with an Al_2O_3-doped silicate core composition". *Electronics Letters*, 19(7): 261-262, (1983).
19. S.J. Ashcroft and C.T. Mortimer. "The thermal decomposition of lanthanide(III) chloride hydrates". *Journal of Less-Common Metals*, 14(4): 403-406, (1968).

20. V. Van Hong and J. Sundstroem. "The dehydration schemes of rare-earth chlorides". *Thermochimica Acta*, 307(1): 37, (1997).
21. W.W. Wendlandt. "The thermal decomposition of the heavier rare earth metal chloride hydrates". *Journal of Inorganic and Nuclear Chemistry*, 9: 136-139, (1959).
22. G.J. Kipouros and R.A. Sharma. "Characterization of neodymium trichloride hydrates and neodymium hydroxychloride". *Journal of the Less-Common Metals*, 160(1): 85-99, (1990).
23. L. Xiong, E.H. Sekiya, and K. Saito. "Mass fabrication of homogeneously Yb-doped silica nanoparticles and their spectroscopic properties". *Nanotechnology*, 20(1), (2009).
24. A.J. Boyland, A.S. Webb, M.P. Kalita, S. Yoo, C.A. Codemard, R.J. Standish, J. Nilsson, and J.K. Sahu. "Rare-earth doped optical fiber fabrication using novel gas phase deposition technique." in *CLEO/QELS Lasers and Electro-Optics/Quantum Electronics and Laser Science Conference, San Jose, CA*. May 16-21, (2010).

Chapter 5

Suspended-Core Holey Fibre

5.1 Introduction

In this chapter, a new fabrication technique is presented for producing a relatively simple type of optical fibre that is suitable for sensing applications. The fibre, which has been called *suspended-core holey fibre* (SC-HF), has a geometry similar to that of an air-suspended rod with three thin struts supporting a solid core. The motivation for developing SC-HF was drawn from a similar fibre structure, often referred to as wagon-wheel fibre, which has been reported previously in a compound glass and is fabricated using a glass extrusion method [1]. The structure of these fibres incorporates a high air-filling fraction that makes them an ideal platform for sensing gas and liquid species entrained in the holes. However, at the time the work presented in this chapter was undertaken, it is not believed that the distinctive three-holed fibre design had been demonstrated previously in a silica host.

A fabrication technique for SC-HF has been developed which utilises a straightforward drilling method to define the preform, rather than the labour intensive route conventionally used for fabricating silica holey fibres. The fabrication technique is described in the experimental section and the optical characterisation that has been performed on SC-HF is reported [2]. To evaluate the fraction of light that overlaps with the air holes in a SC-HF, and to assess its suitability for sensing applications, computer simulation was performed based on a profile of the SC-HF. The sensing capability of the SC-HF was then demonstrated using acetylene gas owing to its strong absorption lines in the low-loss wavelength range (1510 –1540 nm) of silica glass. The practical issues relating to fusion splicing air-cladding fibres were also addressed and a robust all-fibre acetylene gas cell was constructed which showed good stability over an extended time period.

Finally, the SC-HF architecture was used as the foundation to develop a novel type of holey fibre with a germanium-doped core. Unlike other holey fibre designs that incorporate a germanium core, the fibre reported in this chapter exhibits a small-core diameter (<2 μm) initially, which is expanded into a larger high-index region (of several microns in diameter) when the cladding holes are collapsed during conventional fusion splicing. This ability provides an easy method of sealing gas species inside the fibre for sensing applications whilst retaining a high-index core that is compatible with conventional solid core fibre.

5.2 Overview of holey fibre

Since optical guidance was first demonstrated in a microstructured fibre over a decade ago [3], it has attracted widespread interest from the scientific community eager to exploit the unique optical properties it possesses. The term microstructured optical fibre (MOF) is used to refer to any fibre, normally of single material (i.e. undoped), which has a structure that utilises air-holes along its length to facilitate light propagation. Holey fibre (HF) generally refers to those fibres which are index guiding and are categorised by a solid central core and an air-cladding (Figure 5.1(a)). It is also possible for hollow core MOFs to guide light despite having a core of lower refractive index than the cladding. These photonic bandgap fibres (PBGF) operate by bandgap effects and confine light to the air core at frequencies where propagation into the cladding is not possible (Figure 5.1(b)). PBGFs have the potential for lower transmission loss than conventional fibres and are also candidates for sensing applications. However, the work within this thesis focuses only on the properties of solid core HFs.

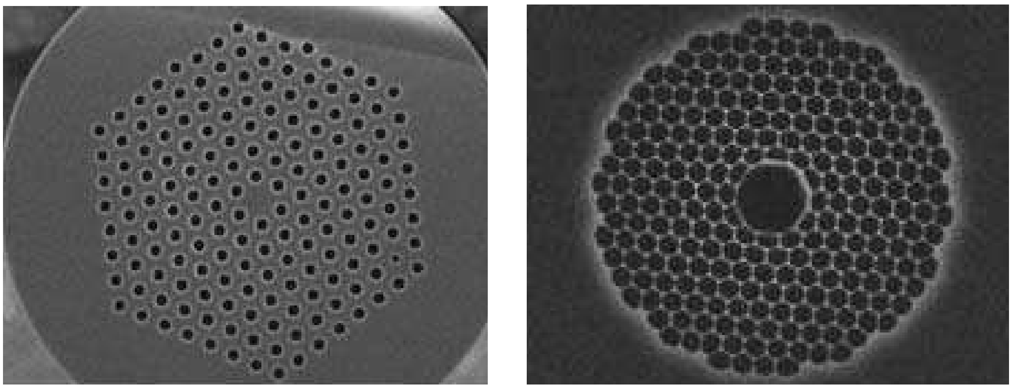

Figure 5.1: Photographs showing the cross-sectional structure of (left) a solid core HF and (right) a photonic bandgap fibre (PBGP) [4].

Solid core HFs have a guidance mechanism analogous to conventional optical fibre with an array of holes in the cladding that forms an average refractive index lower than that of the core. The effective index model of a HF was first proposed by Birks et al. [5] and approximates the complex structure to that of a step index fibre, with an effective refractive index for the air-cladding region (n_{eff}) and a higher refractive index for the central solid region where a hole is missing (n_{core}). As the guided modes in the fibre will extend further into the cladding at longer wavelengths, thus producing a larger index contrast, n_{eff} is strongly wavelength dependent. At shorter wavelengths, the modes are tightly confined to the core and sample less of the air-cladding, and consequently n_{eff} is only slightly lower than n_{core}. The effective index model enables an effective V value (normalised frequency), V_{eff}, to be determined for a HF to predict the criteria for single-mode (SM) operation [5]. This also reveals how the explicit dependence of V on wavelength is counteracted by the effective index contrast of the air-cladding, and creates the potential for SM guidance over an extended wavelength range.

The cladding of a conventional HF consists of an array of circular air holes that are arranged in a hexagonal lattice with a hole diameter, d, and pitch (i.e. hole-to-hole spacing), Λ, which determines the optical properties of the fibre. A stack-and-draw technique [3] (which is explained in the following section) is most commonly used to define the initial preform structure, and permits complete freedom in the placement and size of the holes. The fibre can therefore be tailored to produce an effective core area (A_{eff}) to match a particular application. For example, a large effective mode area is achieved by either decreasing the diameter of the holes or spacing them further apart (essentially smaller values of d/Λ). Engineering the structure in this manner can produce fibre with a very large A_{eff} (>600 μm^2 at $\lambda = 1.55$ μm) and a numerical aperture (NA) less than 0.05 [6], which would be difficult to accomplish in conventional optical fibre using dopant control methods such as Modified Chemical Vapour Deposition (MCVD). Large mode area HFs are attractive for high-power light generation or delivery, where the unwanted nonlinear effects and thermal damage are minimised by virtue of the reduced power density in the core [7].

HFs that contain features on the same scale as the wavelength of the light being transmitted, and incorporate a high air-filling fraction (large values of d/Λ), create a tight modal confinement in the core and give rise to a high refractive index contrast. This generates a high nonlinearity per unit length and these small-core HFs are appropriate for nonlinear optical fibre applications [8]. The effective nonlinearity parameter, γ, is most conveniently related to the effective area through the equation $\gamma = 2\pi n_2 / (\lambda A_{eff})$, where n_2 is the nonlinear refractive index of the material. Although the intrinsic value of n_2 in silica glass is relatively low, the mode confinement in high NA fibres can result in an effective nonlinearity that is many times higher than that of a conventional optical fibre [8]. Moreover, a small-core HF fabricated using the developed technique reported in this chapter has achieved an effective nonlinearity of 60 $W^{-1}.km^{-1}$ (at $\lambda = 1.55$ μm) [9], compared to the theoretical maximum for a pure silica HF at this wavelength of ~60 $W^{-1}.km^{-1}$, as predicted by Finazzi et al. [10].

5.2.1 Sensing in holey fibre

The intrinsic overlap between the propagating light and the air-cladding in HFs allows them to be used for sensing applications by exploiting the interrogating properties of the evanescent-field. Using this approach, the presence of gases and liquids entrained within the holes of a HF may be detected through optical absorption of the transmitted light at specific wavelengths. As well as identifying chemicals, this principle has stimulated a number of innovative optical devices where exotic materials, such as polymers, are permanently infused into the holes of the silica fibre to intentionally sensitise the guidance properties to a particular environment [11]. The potential of these ideas has given rise to an entirely new class of HFs designed for sensing, known as evanescent-field devices.

HFs that employ evanescent-field sensing for gas detection [12-14] possess numerous beneficial qualities: they offer a high sensitivity owing to the potential for long optical interaction lengths, require extremely small sample volumes to fill the holes in the fibre (in the region of μL per metre), and have the ability to be compactly coiled. However, despite these credentials, at the time the research presented here was undertaken, most of the index-guiding fibres exhibited a modal overlap with the air holes of only a few percent [15].

The most important prerequisite for HF as a sensing platform is that there exists a significant overlap between the light propagating in the core and the air-cladding. In a conventional HF, which incorporates multiple rings of air holes, the design criterion is towards a high value of d/Λ (i.e. the air-filling fraction). Monro et al. showed that the proportion of the fundamental mode located in the air-cladding increases significantly with the parameter d/Λ,.particularly at longer wavelengths, and predicted that the modal overlap is up to 30 % for $d/\Lambda = 0.8$ and $\Lambda = 0.75$ μm (at $\lambda = 1.55$ μm) [15].

Theoretical studies on HFs have also been conducted by Finazzi et al. who examined the properties of small-core holey fibres with a high air-filling fraction [10]. The condition for highly non-linear silica fibres was investigated and the concept of a jacketed air-suspended rod (JASR) was introduced. The JASR represents a holey fibre with an air-filling fraction of 100 % and is close to the structure of SC-HF. As previously stated, the effective non-linearity parameter is inversely proportional to the A_{eff}, and so small-core holey fibres with a tight modal confinement are desirable for non-linearity devices. The diagram shown in Figure 5.2 illustrates how the A_{eff} varies with core (rod) diameter for a JASR. For non-linear applications the A_{eff} should be minimised in order to maximise γ. However, for the purpose of evanescent-field sensing the A_{eff} needs to be maximised so that a large proportion of the light is located outside the core. The preferred method for increasing the A_{eff} is therefore to significantly reduce the core diameter, which has been shown to increase almost exponentially below a core diameter below ~1.2 µm [10]. It is this regime together with the idealised geometry of the JASR that was targeted in the development of the SC-HF, and provided the motivation behind the work reported in this chapter.

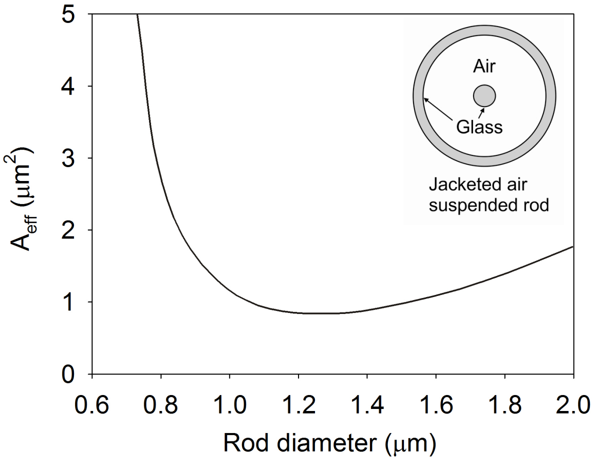

Figure 5.2: Simulation of how the effective area (A_{eff}) in a jacketed air suspended rod (JASR) varies with rod diameter [10]. The graph illustrates that the A_{eff} increases significantly below a rod diameter of 1.2 µm, which makes the small-core JASR ideal for evanescent-field sensing applications.

Although HFs with a small core diameter and a high air-filling fraction are desirable for sensing and nonlinear applications, they generally incur an additional optical loss over more conventional structures. Finazzi et al. reported that small-core HFs suffer from high confinement loss which increases as the core size reduces. This effect can be significant and is the dominant loss mechanism in silica when the core diameter is less than ~1 μm [10]. Furthermore, HFs with a large A_{eff} potentially have a large scattering loss caused by the roughness at the air-silica boundaries which is accentuated by the high intensity of light at the interface [16]. Interface roughness scattering is now well known in HFs and is attributed to surface fluctuations of the molten glass surface which occur during drawing and are frozen-in as the fibre cools. These fundamental effects consequently place a lower limit on the loss that can be achieved in HFs and are also applicable to SC-HF.

5.2.2 Fabrication techniques

Conventional HFs are generally fabricated by employing either a drilling [17] or stacking [3] technique to define the preform structure. The former method is a straightforward approach that was used predominantly in the early days of silica HF development, but with the advent of the stack-and-draw technique, its appeal has diminished. However, drilling is still used for compound glass HF, where producing long uniform lengths of capillaries is not viable, and remains popular for manufacturing preform geometries that have up to around 20 well-spaced holes [17]. For silica HFs that have a complex transverse profile the stack-and-draw method is the obvious route.

A stacked HF preform consists of a large number of thin hollow glass capillaries that are packed inside an outer jacket tube. The capillaries are firstly manufactured using a standard optical fibre drawing tower and originate from a high-purity substrate tube, such as SUPRASIL-F300 (Heraeus, Germany). Any large variations in the diameter of the capillaries will preclude the stacking process and so screening selects only those which lie within a tolerable diameter range (typically <1 % deviation). To this end, there are numerous reports in the literature detailing the capillary drawing process [18-

20], detailing both theoretical calculations and experimental data, including the seminal work by Fitt et al. [18]. Fitt et al. identify the parameters that influence the collapse of the capillary during the draw and define a collapse ratio that relates the effects of surface tension and viscosity of the glass. As the viscosity is strongly dependent on temperature, it is the furnace setting that principally governs the degree of collapse. Fitt et al. also showed that the hole collapse in the capillary is more sensitive to the tube feed speed than the draw speed as a direct consequence of the length of time the glass resides in the furnace hot-zone. A plain circularly symmetric substrate tube can be successfully drawn into a capillary with the upper end open to atmosphere by adjusting only the capstan speed and accepting some inevitable collapse. However, an over-pressure is normally applied to the upper end of the tube to counteract the surface tension effects, allowing the exact dimensions of the capillary to be fine-tuned.

Once obtained, the hollow capillaries are cleaned to remove contamination and residual glass fragments, and are then sealed (i.e. flame fused) at one end. This eliminates the sharp edges, but more importantly, when closed at the upper end the capillaries are able to expand during the drawing process to eliminate unwanted interstitial gaps. The prepared capillaries are then stacked in a hexagonal arrangement inside the jacket tube. (The hexagonal lattice structure is not exclusive, but represents the highest capillary fill-factor). The outer diameter of the capillaries and jacket tube are typically around 0.5 – 2 mm and 20 mm, respectively, and are largely dictated by the required draw-down ratio and glass sizes that are easily handled [19].

Depending on the required feature size, the assembled preform is either drawn directly into fibre, or drawn into a capillary and then re-drawn inside another jacket tube to further scale down the structure. The drawing process for HF, however, is nontrivial. Once the fibre drawing process is initiated, an unstable period begins as the gas trapped inside the sealed capillaries heats up and expands. This is counteracted by gas exiting through the lower (open) end of the glassware. The self-pressurising and regulating effect is beneficial in preventing the holes from collapsing shut, but as the volume of glass decreases (i.e. the remaining length of preform reduces), the pressure inside the capillaries continually changes and consequently the draw is always in a transient state [21]. This issue is compounded by the thermal gradient that exists radially across the preform, which governs the local viscosity of the glass, and translates into a different expansion for the capillaries depending on their exact position across the preform [22]. It is noted that even a modest change in furnace temperature of 10 °C can significantly alter the overall geometry of the fibre [19].

There are several steps involved in the stack-and-draw method which means that HF fabrication using this technique can be a time consuming process, sometimes taking weeks to complete. For HFs that require a large air-filling fraction and a small core diameter, the fabrication technique developed for SC-HF is a much simpler approach and less prone to complications. The steps involved in the conventional stack-and-draw are, fabrication and preparation of the hollow capillaries, assembly of the stacked preform, and fibre drawing. However, for SC-HF, the preform itself is prepared by drilling longitudinal holes into a glass substrate and thus the need to produce and stack capillaries is removed. The complexity of the fibre drawing stage in SC-HF is also reduced owing to its relatively simple transverse structure; whereas in conventional HF it is necessary to control the geometry of several rings of holes, the only requirement during SC-HF drawing is that the holes expand sufficiently to maximise the strut length. Further details of the fabrication process developed for SC-HF are described in the following section.

5.3 Experimental work

This section describes the fabrication and characterisation of SC-HF. Using computer modelling, the optical properties of the core modes in the fibre have been investigated, and confirm a high overlap with the air-cladding. The suitability of the SC-HF as an evanescent-field sensor has been verified by demonstrating an all-fibre acetylene-filled gas cell. A novel germanium-doped SC-HF has also been proposed, which was aimed at simplifying the construction of an all-fibre gas cell, as well as improving its compatibility with conventional solid optical fibre. The development, fabrication, and characterisation of SC-HF were undertaken by the author, including the evanescent-field sensing demonstration. The computer modelling was performed by Dr. Francesco Poletti.

5.3.1 Fabrication of suspended-core holey fibre

The processing steps for fabricating SC-HF are shown in Figure 5.3, and begin with defining the preform structure by creating three holes arranged in a triangular shape within a solid silica rod. The substrate glass should be of high-purity as, unlike preforms manufactured using MCVD where the signal light is transmitted through glass formed by the oxidation of $SiCl_4$, optical guidance in SC-HF occurs in the starting material itself. Commercially available synthetic fused silica rods (either HLQ-210 or SUPRASIL-F300 grade), purchased from Heraeus (Germany), have been used for this purpose.

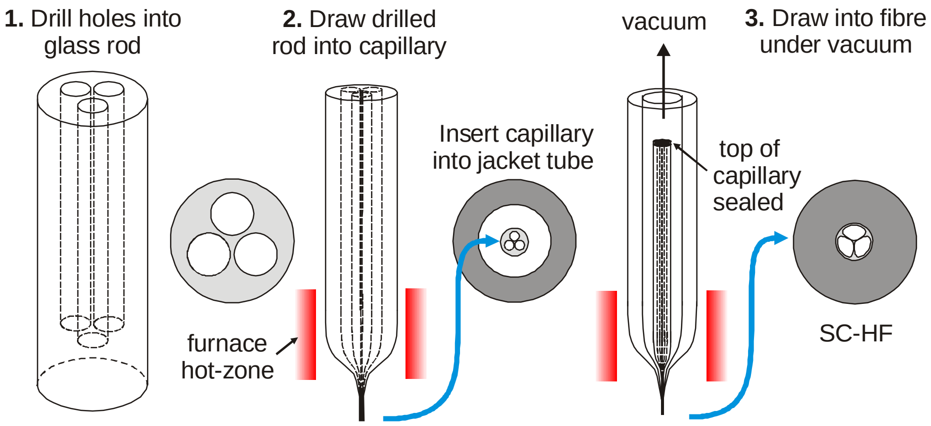

Figure 5.3: Illustration of the processing steps involved in the technique developed for fabricating Suspended-core holey fibre.

The holes in the glass rod were formed using high-precision in-house ultrasonic drilling equipment (SonicMill®, US) that is specifically designed for use with glass. The equipment is capable of grinding holes in glass, up to a depth of 150 mm, and uses a hollow drill impregnated with diamond grit at the tip. The nature of the process demands extremely slow drilling speeds (of between 200 - 500 $\mu m.min^{-1}$) and requires coolant to be continually flowed through the hollow drill piece to remove particulates and prevent overheating of the tool. Hole sizes ranging from 1 mm up to and above 10 mm in diameter are possible, and with careful alignment of the sample, a positional accuracy of better than 50 µm can be achieved.

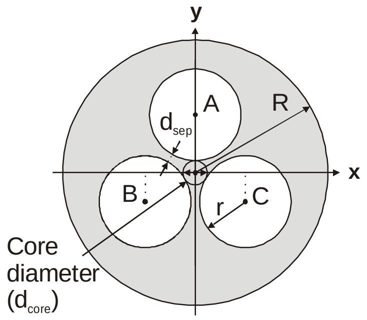

Hole	x-position	y-position
A	0	$(2rd_{sep})/\sqrt{3}$
B	$-(2r+d_{sep})/2$	$-(2r+d_{sep})/2\sqrt{3}$
C	$(2r+d_{sep})/2$	$-(2r+d_{sep})/2\sqrt{3}$

Figure 5.4: Arrangement and positional calculation for the location of holes in a SC-HF.

It is necessary to position the holes as close together as possible so that the web of glass between them will be sufficiently thin once it is scaled down into fibre. Figure 5.4 shows the calculation for the position of the holes, and was derived using trigonometry. It was found that a separation (d_{sep}) of 0.3 mm between adjacent holes was the minimum value possible, without sustaining cracks in the adjoining glass owing to the high pressure coolant used during the drilling process. The dimensions used for the glass rod and the diameter of the holes were in the range of 15 – 20 mm, and 4 – 8 mm, respectively.

With the use of a pristine tool bit, the surface quality of the holes after ultrasonic drilling is reasonable but visible scratches are normally still evident. Flame polishing the glass preform on a lathe was explored, but had the potential to distort the shape of the holes or trap air bubbles in the glass if the burner temperature was too high. Instead, it was found that a more suitable option was to mechanically polish the inner surface of the holes, and bespoke apparatus was constructed (see Figure 5.5). The glassware was clamped vertically and submerged within a receptacle containing SF1 polishing fluid (Logitech, UK). A nylon-bristled tube brush was then fitted to the head of the ultrasonic drill and slowly fed in and out of the hole whilst rotating at a speed of ~1000 rpm. The effect that polishing the preform has on the loss in the final fibre has not yet been quantified, but the image in Figure 5.5(c) shows the clearly visible improvement in surface quality.

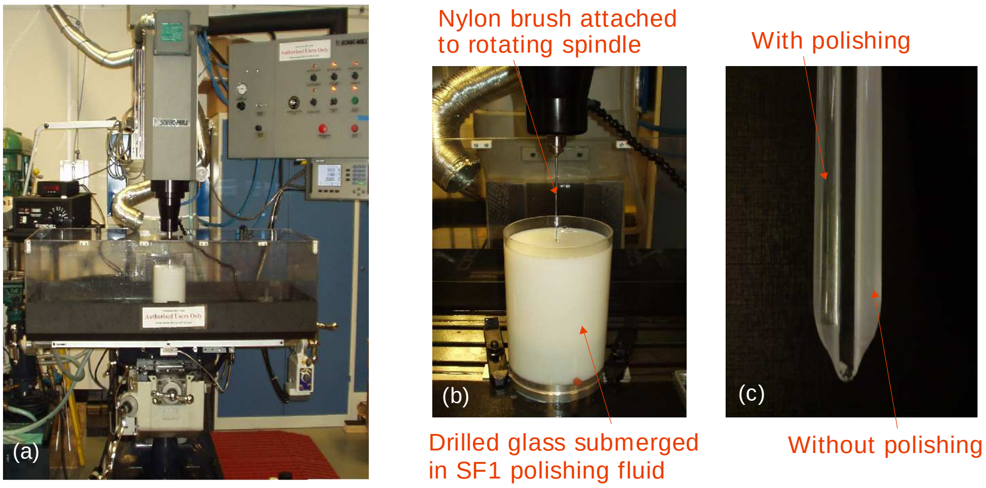

Figure 5.5: (a) Sonicmill® ultrasonic drilling equipment and (b) interchangable polishing apparatus constructued in-house. (c) Comparison of surface quality of drilled holes with and without polishing.

Once drilled and polished, the glass rod was drawn on a standard fibre drawing tower into a capillary of ~1 mm diameter using the mini-capstan. The upper end of the preform handle tube was left open to atmosphere, and the furnace temperature was optimised in order to retain the internal geometry of the drilled glass. A temperature of ≥100 °C below that used for the initial gravity drop was found to be appropriate. A preform feed speed of a few mm.min^{-1} was fast enough to avoid excessively deforming or collapsing the holes, although, as expected, the dominant parameter was the furnace temperature. The potential benefit in pressurising the holes during the capillary draw was explored, but the minimal gain in retaining the exact structure (or indeed expanding the holes) was deemed unnecessary when considering the eventual deformation of the capillary during the fibre drawing.

The final stage of the fabrication process is to further reduce the feature size of the core, and manipulate the shape of the holes in the capillary so that the fibre structure approximates that of a small core suspended by three thin struts. A length of capillary

(~200 – 300 mm long) was sealed at the upper end, in a flame, and inserted into a cladding tube. The action of sealing the capillary induces a build up of pressure when the preform traverses through the furnace hot-zone and prevents the capillary from collapsing internally [21]. In conventional holey fibre fabrication, the jacket tube is chosen to be a close fit to that of the capillary so as to avoid excessive expansion of the holes that would distort the final structure. In contrast, the approach used for realising SC-HF was to intentionally use a loose-fitting jacket tube with a large air gap (~2 mm) between the capillary and outer glass so that it expanded during the fibre draw and elongated the supporting glass struts. This expansion was aided by reducing the pressure between the capillary and the surrounding air space by applying a partial vacuum. A cladding tube with a comparatively large wall thickness was therefore needed so that the vacuum preferentially expanded the capillary and any collapse of the jacket tube was minimised. To this end, a dedicated mass flow controlled (MFC) pressure and vacuum system was constructed, which was connected to the top of a preform to allow a fine control of the pressure up to ±100 mbar relative to atmosphere. The preform feed and mini-capstan speeds used for drawing SC-HF were typically in the region of 2 mm.min^{-1} and 10 m.min^{-1}, respectively, and the fibre was coated with a high-index polymer (DSM-314) in the usual manner.

Capillary number	Substrate glass	Drilling parameters	Capillary diameter	Comments
F0595$^{\#}$	HLQ-210 rod 18 mm dia.	r = 2.5 mm d_{sep} = 0.5 mm	1.5 mm	First proof-of-concept capillary
F0648$^{\#}$	F300 rod 20 mm dia.	r = 4 mm d_{sep} = 0.5 mm	1.9 mm	Reduced outer wall thickness
T0252*	Ge:Si preform (LIEKKI) 15 mm dia.	r = 1.5 mm d_{sep} = 0.5 mm	1.5 mm	Glass cracked significantly during ultrasonic drilling
T0256*	F300 rod 15 mm dia.	r = 2.25 mm d_{sep} = 0.3 mm	1.2 mm	Establishing process parameters on new equipment

$^{\#}$all/partially lost in fire, *fabricated post-fire

Table 5.1: Summary of capillaries that were drawn and the parameters used to drill the glass preform.

Fibre number	Cladding tube quality/size	Capillary used	Fibre diameter	Comments
F0597#	F300 8.5 × 3.2 mm	F0595	~125 µm	Initial proof-of-concept SC-HF
F0656#	F300 8.5 × 3.2 mm	F0648	~125 µm	Explore pressurisation to expand strut length
F0753#	F300 6.9 × 3.5 mm	F0595	~125 µm	Process optimisation
F0793#	F300 12 × 4.8 mm	F0595	125 µm	Draw of SC-HF for characterisation and analysis
T0257*	CFQ 8 × 4.2 mm	T0256	125 µm	Establishing process parameters on new equipment
T0262*	CFQ 8 × 4.2 mm	T0256	125 µm	Establishing process parameters on new equipment
T0265*	F300 tube 8 × 4 mm	T0252	125 µm	Draw of Ge:Si core capillary

#all/partially lost in fire, *fabricated post-fire

Table 5.2: Summary of the fabricated suspended-core holey fibres and the associated capillary that was used.

Table 5.1 and Table 5.2 summarise the preforms and fibres, respectively, produced during the development of the SC-HF fabrication process. The optimum drawing conditions in each case were obtained empirically and were found to depend heavily on the cladding tube dimensions. Although the exact drawing conditions differed for each fibre the systematic approach detailed below was found to be sufficient to repeatedly achieve SC-HF with the desired geometry. (It is assumed that the glassware has been prepared as described previously, and with the capillary sealed at the upper end).

- Following the initial gravity drop, the furnace temperature is lowered by at least 50 ºC to increase the viscosity of the glass and lessen the effect of the subsequent vacuum. A transient period then follows whilst the shape of the neck-down region is stabilising.

- To reduce the complexity of the drawing regime, the preform feed and capstan speeds are fixed once the required fibre diameter is achieved, leaving only the furnace temperature and applied vacuum to adjust. A coated fibre tension in the region of 60 – 70 g, at a draw speed of around 10 m.min^{-1}, is sought.

- The air inside the preform is initially kept at atmospheric pressure whilst the fibre cross-section is continually monitored under an optical microscope. When the internal structure of the capillary is clearly visible, and without any obvious hole collapse, the vacuum pump is turned and a pressure inside the cladding tube of 30 – 60 mbar below atmospheric is targeted.

- Depending on the exact dimensions of the starting preform, a maximum value of 60 mbar for the applied vacuum is normally sufficient to create the desired fibre profile. If a higher differential pressure is required, it is preferable to increase the furnace temperature, in 5 ^{o}C increments, until the correct fibre structure is achieved.

The above methodology was found to be adequate to achieve to the intended fibre structure, but it is noted that active pressurisation of the internal capillary during the draw may be advantageous. However, this was not explored in this work as it was felt to detract from the intended straightforward nature of the current approach.

5.3.2 Fibre characterisation and simulation

A complete characterisation of all the capillaries and fibres detailed in Table 5.1 and Table 5.2 has not been possible, as many were fabricated prior to the Mountbatten building fire in October 2005 and were destroyed in the incident (see Appendix C.1). The transmission properties and gas sensing performance of the SC-HF reported here relates to measurements conducted on fibre F0597, prior to the fire, whilst the more recent simulation studies are based on the cross-sectional profile of fibre F0793 (see Table 5.2).

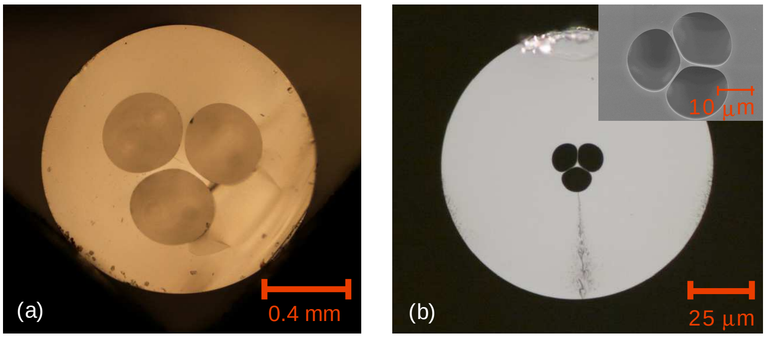

Figure 5.6: Cross-sectional images of (a) drawn capillary F0595, and (b) suspended-core holey fibre F0597 (inset: SEM micrograph).

Figure 5.6(a) shows a cross-sectional image of capillary F0595. The capillary was 1.5 mm in diameter and has the approximate structural dimensions of 100 µm and 500 µm, for the core diameter (d_{core}) and hole diameter (2r), respectively, disregarding any ovality. Figure 5.6(b) is the resultant SC-HF (F0597), which was drawn to a nominal outer diameter of 125 µm and coated with a high-index polymer (DSM-314). During the drawing process, various furnace temperatures and vacuum settings were explored, which resulted in fibres with measured core diameters and strut lengths ranging from 0.8 – 3 µm and 8 – 13 µm, respectively. Further analysis using a scanning electron microscope (SEM) revealed that the strut thickness was in the region of 200 nm.

The background loss in a 15 m length of SC-HF fibre (F0597), with d_{core} = 1.2 µm, was obtained using a standard white-light cutback measurement (Figure 5.7). The calculated propagation loss in the fibre was 0.33 dB.m^{-1} at λ = 1550 nm, and is in good agreement with recent reports of similar small-core structures [23]. It is believed that interface roughness scattering from the holes has a significant contribution to the overall loss, which has been reported by Roberts et al. [16] as the dominant loss mechanism for small-core HFs.

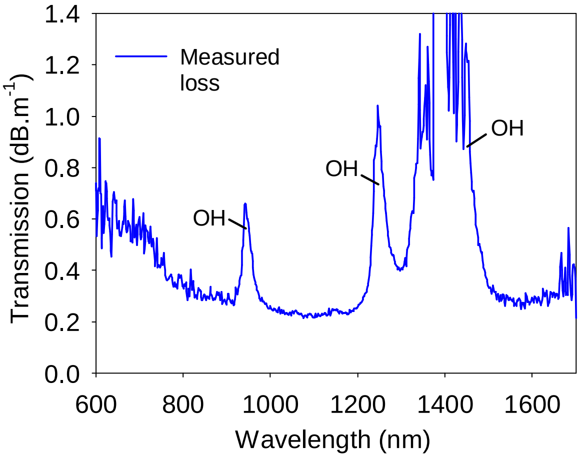

Figure 5.7: Measure wavelength dependent loss for SC-HF F0597 showing absorption peaks as a result of OH impurity.

The strong absorption bands observed at wavelengths of 1385 nm, 1245 nm and 945 nm, correspond to hydroxyl (OH) ions, and the intensity of the 1245 nm peak (which is visible without saturating the detector) equates to an OH concentration of ~300 parts per million (ppm), by weight. This value is in stark contrast to the quoted figure of 30 ppm in the manufacturer's data sheet for the bulk material (HLQ-210). A comparative OH measurement was performed on SC-HF F0793, which was fabricated using a high-purity F300 glass having a certified OH content of <1 ppm, by weight. The calculated concentration in this case was ~240 ppm. Incorporation of OH impurities in the fibre can originate from adsorbed hydroxyl ions in the preform prior to the drawing which subsequently diffuses into the glass at high temperatures. This effect has very recently been shown to be more detrimental for small core HFs (<2 µm) which incur a significant attenuation as a result [24]. Furthermore, surface absorbed OH from the atmosphere may also be present in the fibres following the draw which will also contribute to the measured result [25]. For the SC-HFs reported here, no specific steps were taken to actively remove OH contamination pre- or post-drawing, but its impact will be considered in future work.

In addition to the practical experiments, a theoretical analysis of the SC-HF was performed by Dr. Francesco Poletti using numerical simulations to examine the core mode properties of the fibre. The modelling was based on an outline of the fibre shape taken from an SEM micrograph of F0793. A full vector finite element method (FEM) was used to asses the fraction of light propagating in the air-cladding (see Figure 5.8). The feature size was scaled accordingly to obtain data for fibres with different values of d_{core}. The proportion of the light predicted to be travelling in the air for a fibre with $d_{core} = 1.2\ \mu m$ is 11.5 %, and increases to nearly 30 % when $d_{core} = 0.8\ \mu m$. At the time that this research was carried out, this result represented a higher core mode overlap than any other previously reported index guiding designs [2].

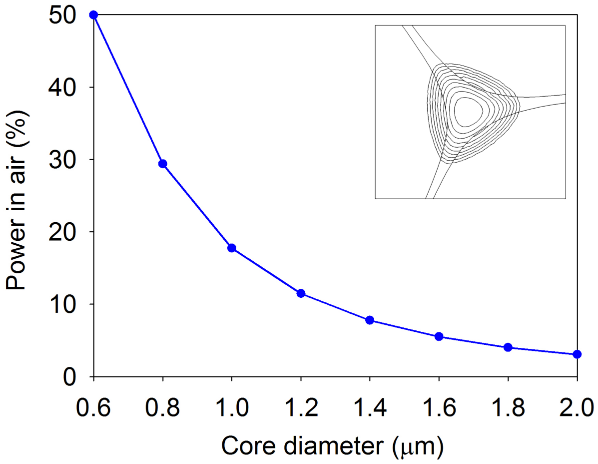

Figure 5.8: Fraction of power propagating in the holes of a SC-HF as a function of core diameter at λ = 1550 nm (inset: simulated mode profile in the core).

5.3.3 Evanescent-field gas sensing

There are numerous reports in the literature of evanescent-field sensing using MOF, many of which demonstrate the ability using acetylene gas [12-14]. The experimental setup that is used differs slightly in each case, but comprises of the same essential components: a tuneable laser source, an optical detector, and the sample fibre. The fibre is typically located in a gas-tight chamber with transparent windows, whilst free-space optics provides the means to couple light in and out of the core. This approach allows unrestricted access to the fibre ends to infuse the sample gas, and circumvents the problematic issue of splicing MOF to conventional solid core fibre [26]. However, the arrangement has practical limitations regarding long-term stability, and to realise an all-fibre gas cell, the need to splice to conventional solid fibre is unavoidable. The apparatus that was constructed for the SC-HF provided a convenient way of assessing the performance of the fibre initially, and used a simple method of aligning and launching light into the sample. The subject of splicing is addressed thereafter in subsection 5.3.4.

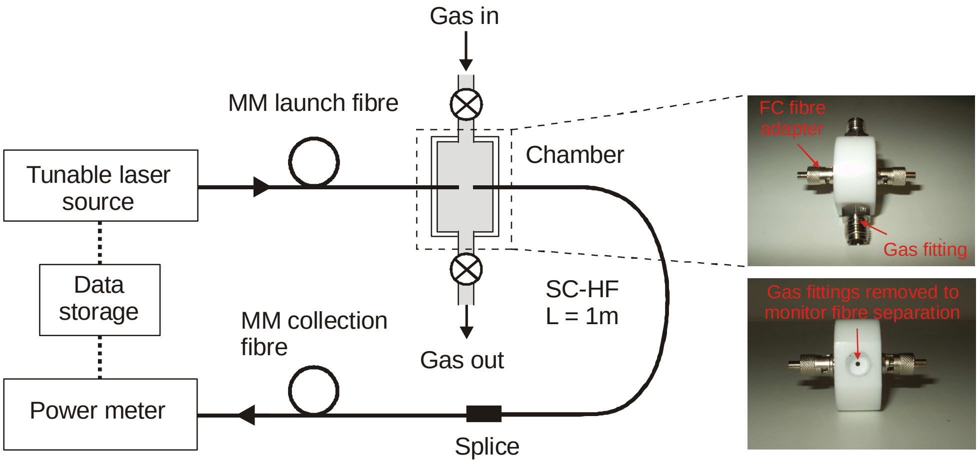

Figure 5.9: Schematic of the experimental setup used for SC-HF gas sensing, and photographs of the bespoke chamber that was designed specifically for the purpose.

Figure 5.9 shows the experimental setup used to measure the gas detecting capability of SC-HF. The fibre output from a tuneable laser source (Agilent 8164A, tuneable from λ = 1520 to 1545 nm) was delivered through a standard graded-index multimode (MM) fibre, which was in turn, free-space coupled to a 1 m length of F0597 (d_{core} = 1.2 μm, strut length = 8 μm). The fibre ends were located within a purpose-built chamber that had been constructed in-house and provided a flexible and quick way to test the sensing performance of HFs. The chamber itself was made from PTFE material to offer some compatibility with corrosive gases, and standard FC optical fibre connectors provided a straightforward way of securing and aligning the fibres whilst producing the gas-tight seal needed for gas filling. The distance between the launch and sample fibre was monitored through an optical microscope and their positions were adjusted as necessary (see photographs in Figure 5.9). The separation between the MM and sample fibre, in this case, was set to ~50 μm. MM fibre was used for the launch fibre to reduce the required alignment accuracy and maximise the available launch power. The other end of the SC-HF was spliced to the collection fibre using an Ericsson FSU995-PM arc-fusion splicer, and again standard MM fibre was used for this purpose (the SC-HF structure was collapsed during splicing, and the implications of this are discussed in the following section). The collection fibre was then attached to an optical power meter (HP 81531A).

To fill the fibre, a flow of 100 % acetylene (C_2H_2) gas was passed through the chamber, orthogonal to the fibre face, at a rate of 200 ml.min^{-1}. After 5 minutes, the chamber was sealed. Infiltration of the gas into the voids of the SC-HF relied solely on diffusion and thus a significant length of time was needed to completely fill the fibre. The internal volume of the chamber was significantly larger than that of the holes in the fibre, and as such any dilution of the acetylene gas was deemed to be negligible. The tuneable laser was scanned between wavelengths 1520 nm and 1545 nm with a resolution of 0.01 nm. The data from the power meter was recorded and stored, and the sweep repeated at hourly intervals.

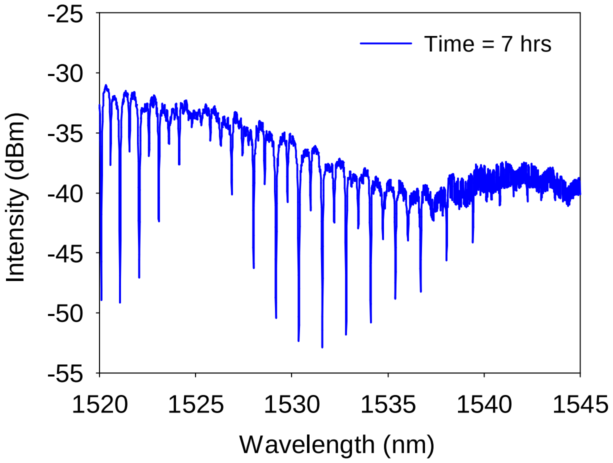

Figure 5.10: Experimentally measured spectrum of acetylene-filled SC-HF showing the characteristic absorption lines of C_2H_2 in the wavelegnth range of 1520 nm to 1545 nm.

The absorption spectrum from the fibre is shown in Figure 5.10 and clearly demonstrates the potential of SC-HF as an evanescent-field gas sensor [2]. The time lapsed measurement data is shown in Figure 5.11, and is centred on the absorption line at $\lambda = 1530.37$ nm. The intensity of the absorption can be seen to increase to its maximum value of 16 dBm over a period of hours as the acetylene gas diffused along the 1 m length of fibre. No significant change in absorption was seen after 7 hours.

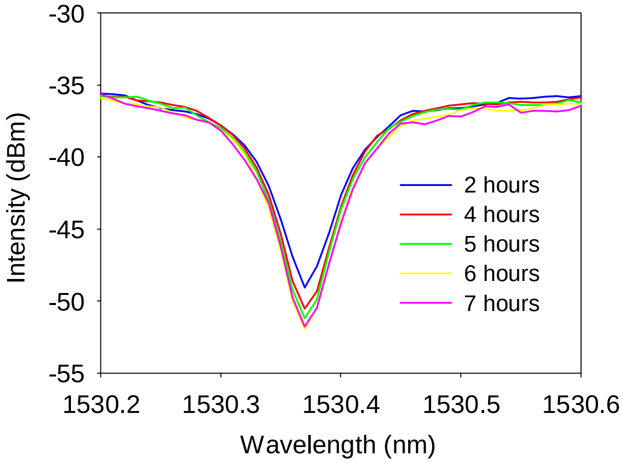

Figure 5.11: Time lapse data of acetylene absorption line λ = 1530.37 nm measured in a 1 m length of gas-filled SC-HF over a duration of 7 hours.

5.3.4 All-fibre acetylene gas cell

The experimental set up shown in Figure 5.9 was designed for conveniently evaluating the gas detecting capability of SC-HF, but not specifically to achieve the long-term stability required for an optical wavelength reference. In this section, the practical issues encountered with splicing SC-HF to conventional solid fibre are reported and an all-fibre acetylene-filled gas cell is demonstrated. The current advances in splicing MOF are firstly discussed.

In 2005, the first gas-filled microstructured fibre cell was reported [27] using photonic band gap fibre (PBGF). The high overlap of the propagating light with the hollow-core made it ideally suited for sensing applications, compared to the significantly lower mode overlap of index-guiding HFs at the time [14]. The basic construction of a microstructured all-fibre gas cell involves firstly, splicing one end of the MOF to conventional solid fibre and leaving the other end open so it can be infiltrated with the desired gas species. The air inside the holes of the MOF is then evacuated, and after filling with the sample gas the open end of the fibre is immediately fused closed using a fusion splicer to form a hermetic seal. The gas is usually loaded in to the fibre at a higher pressure than atmospheric to prevent the ingress of air.

The main obstacle in realising an all-fibre gas cell, or indeed any other integrated device based on HF, is splicing the air-cladding fibre to solid transmission fibre without incurring a significantly coupling loss. The inevitable need for compatibility between MOFs and conventional solid fibres was addressed soon after their inception by Bennett et al. [28], and there now exists an abundance of literature on electric arc fusion splicing techniques using commercially available equipment [26, 29-31]. Some of the key points on splicing HFs are summarised below.

A splice loss between a HF and a conventional single-mode fibre (SMF) is the result of either a mode field mismatch between the cores, or a collapse in the structure of the HF to such an extent that the light-guiding properties of the fibre are severely disrupted. To avoid the latter issue, a weak arc power and a short duration is used as the hole collapse is a direct consequence of surface tension effects in the glass as the fibre is heated above its softening point [26]. Frazao et al. [29] recommend that in addition to the reduced power density, the position of the fibre ends within the arc field should be displaced. The HF end-face is offset from the central axis of the arc discharge and thus the power intensity it experiences is reduced. Using this approach, Frazao et al. reported a minimum splice loss of 0.25 dB between a small-core HF ($d = 2.3\ \mu m$ and $d/\Lambda = 0.5$) and a standard SMF-28® (Corning) fibre using a Fujikura fusion splicer (FSM-40S).

In an effort to reduce the field mismatch between two fibres, specifically small-core HFs which have dissimilar mode-field diameters (MFD), Xiao et al. prescribed the use of repeated arc discharges [31]. Here, the fibres are initially fused together and then subjected to further heating in order to modify and expand the mode field of the propagating light. With the application of around 15 to 30 discharges, the fibre structure gradually deforms whilst the light throughput is continuously monitored to ascertain the optimum mode field match. Further studies into this technique have been carried out by

Tse et al. [32], who achieved an average splice loss of 1.3 dB between small-core HF (diameter = 1.3 μm) and commercial solid core fibre (Nufern-UHNA1, MFD = 4.8 μm), using a Furukawa FITEL-S177 fusion splicer. However, in contrast to Xiao et al., Tse et al. reported that a large overlap distance (compression) between the fibres (of >15 μm) was beneficial during splicing and compensates for the concave end-face that is formed during fusion in high-air filling fraction HFs [27].

Although the cited articles provided a valuable insight into the splicing process, the equipment settings were not found to be directly transferable to SC-HF and the model of fusion splicer available for this work (i.e. Ericsson FSU-995PM). Program settings suitable for splicing SC-HF to small-core transmission fibre, as well as those needed to controllably collapse the fibre holes for realising a gas cell, were experimentally determined for the Ericson FSU-995PM fusion splicer. The derived parameter values are shown in Table 5.3 along with the default settings. One point worth noting, and which appears to be overlooked in the literature, is the issue of fusion splicing fibre that contains a flammable gas species such as acetylene. It was found that a sustained arc from the fusion splicer, or an open fibre end positioned near the arc field, was indeed sufficient to ignite an acetylene-loaded fibre. This, however, was avoided when the arc power and duration were suitably low, such as in Program 1.

An acetylene-filled gas cell was successfully created using a 1 m length of SC-HF (F0793) which was fusion spliced to a small-core, high NA, transmission fibre (Fibercore SM600, MFD = 4.3 μm) using Program 1 listed in Table 5.3. The SC-HF end-face was offset from the electrode axis, as previously described. The SM600 fibre was chosen to minimise the mode field mismatch between the two fibres. The PTFE chamber shown in Figure 5.9 was adapted to facilitate filling the fibre with acetylene (C_2H_2) gas. Infiltration of the gas into the voids of the SC-HF relied, as before, on diffusion and as such it was left for several hours to ensure the entire length was filled. The fibre was then removed from the loading cell and immediately collapsed on the splicer using Program 2. To avoid ignition of the gas loaded fibre during this process, the fibre was clamped in the splicer such that the open end was positioned approximately 50 – 100 mm away from the arc field.

Splice parameters	Program 0 SM to SM (default)	Program 1 SC-HF to SM	Program 2 SC-HF collapse
Prefuse time (s)	0.2	0.2	0.2
Prefuse current (mA)	10.0	8.0	8.0
Gap (μm)	50.0	5.0	40.0
Overlap (μm)	10.0	10.0	0.0
Fusion time 1 (s)	0.3	0.3	0.3
Fusion current 1 (mA)	10.5	8.0	8.5
Fusion time 2 (s)	2.0	1.5	2.0
Fusion current 2 (mA)	16.3	10.0	12.0
Fusion time 3 (s)	2.0	0.0	0.0
Fusion current 3 (mA)	12.5	0.0	0.0

Table 5.3: Splicing parameters experimentally derived for splicing SMF to SC-HF, and controllably collapsing the end of SC-HF, using an Ericsson FSU-995PM arc fusion splicer.

The fibre was subsequently cleaved in the collapsed region using a FK-11 (Photon Kinetics) with a variable magnification camera focussed on the cleaver tip. The addition of the camera allowed the exact position of the cleave point to be accurately controlled so that the minimal amount of the collapsed region was retained, as shown in Figure 5.12(b). Collapsing the fibre structure invariably disrupted its optical guidance properties, but when viewed under an optical microscope the effect was not deemed to be excessive. Fibres that have been collapsed and cleaved in this way, with a retained solid section (d_{cleave}) of nominally 100 μm, 150 μm and 200 μm, were analysed. The photograph in Figure 5.12(c) shows the end face of a fibre with the maximum length of solid section examined (i.e. d_{cleave} = 200 μm). Although the light shows high divergence, the image suggests that most of the power is confined within a circular area of ~15 μm in diameter.

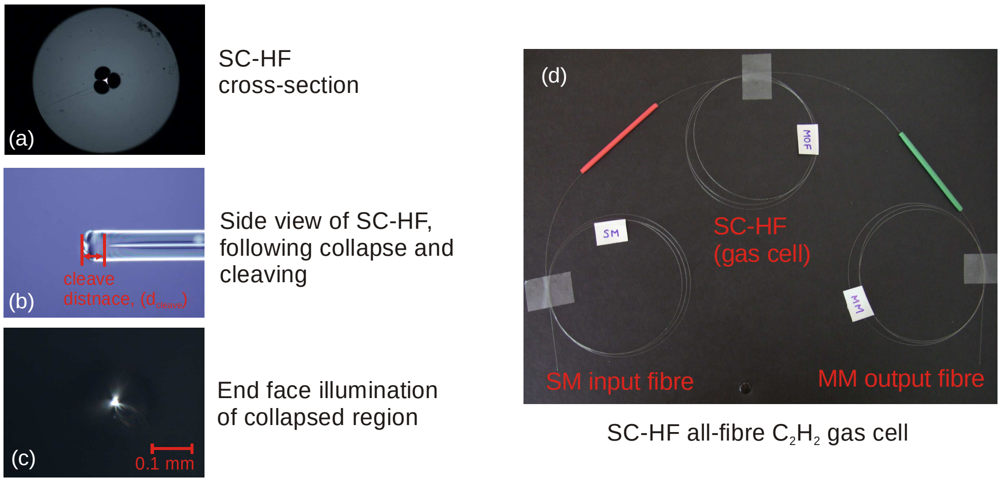

Figure 5.12: Images relating to the construction of a SC-HF gas cell, showing, (a) the fibre cross-section, (b) the collapsed region and cleave distance, (c) the end-face illumination after collapsing, and (d) the complete all-fibre acetylene-filled gas cell.

Finally, the pre-cleaved end of the gas-filled SC-HF was spliced to a length of transmission fibre. This output fibre served only as a conduit to deliver the light to the spectrum analyser and so a pure silica core fibre was used. An undoped F300 silica rod was drawn to a diameter of 125 µm and coated with a low index coating (PC-375), producing a NA of 0.49. The collection fibre was spliced to the collapsed end of the SC-HF using the standard SM-SM program (Program 0 in Table 5.3) and with the SC-HF offset from the arc field to avoid any further collapse.

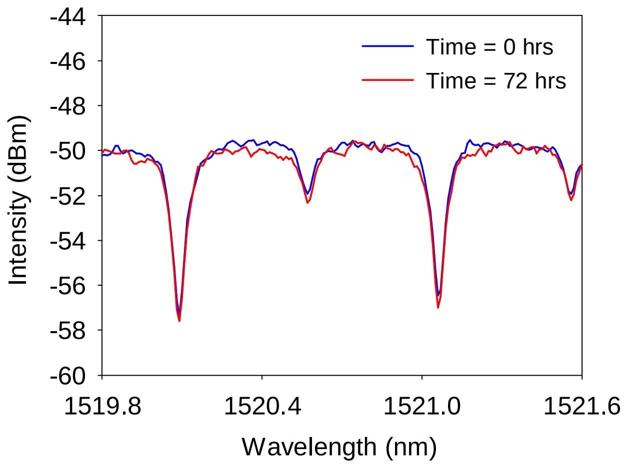

Figure 5.13: Evaluation of absorption over time in the assembled suspended-core holey fibre acetylene-filled gas cell.

The absorption spectrum from the acetylene-filled cell was monitored over a time period of 72 hours and the results are shown in Figure 5.13. The average change in absorption was less than 0.5 dB (~3 %) and is attributed to fluctuations in the output power from the laser. The splice loss between the SC-HF and transmission fibres was ascertained by a cut-back measurement, after the time-lapse trial was complete, and was of the order of 2 dB.

5.3.5 Germanium-doped suspended-core holey fibre

In this subsection, a novel fabrication approach is reported for realising a SC-HF with a germanium (Ge)-doped core that, following the collapse of the air holes, can produce a solid high-index region of several micrometers in diameter. Passive dopants have been reported in HFs previously, and are incorporated to either endow the fibre with further functionality (e.g. through the inscription of a Bragg grating), or enable the core to retain light-guiding properties in the event of the air-holes being collapsed during fusion splicing [33]. HFs that are fabricated using the stack-and-draw process facilitate the inclusion of a high-index core by substitution of one or more of the central elements with a doped glass rod during the preform assembly. A Ge-doped SC-HF fabricated using this substitution route was reported by Huy et al., and was designed for refractive index sensing [34]. The A_{eff} and Δn of the Ge-doped core in the fibre was 9 μm^2 and 9×10^{-3} (with respect to undoped silica), respectively. Although the fibre exhibited a high overlap of the core light with the air-cladding, the size and index contrast of core would be inadequate to confine the propagating light if the holes were collapsed.

The intended application of the SC-HF demonstrated here is an all-fibre gas cell and, as before, the structure exhibits a small diameter core (i.e. <2 μm). However, once the air holes are collapsed, during splicing, the central Ge-doped core region increases to >13 μm. This attribute allows the fibre ends to be intentionally collapsed to seal a sample gas inside, whilst the enduring high-index core enables it to be spliced to conventional transmission fibre. The profile of the Ge-doped SC-HF is formed by defining the initial three-hole arrangement entirely within the core area of a doped preform. In the drawn fibre, light propagation occurs in the suspended-core in the same way as the pure silica SC-HF. However, when the air holes are collapsed, the light is guided in the solid core as well as the combined Ge-doped region of glass that previously lay beyond the thin supporting struts.

A Ge-doped preform was purchased from the fibre manufacturer LIEKKI (Finland), with an outer diameter of 15 mm and a step-index core measuring 10 mm in diameter with a NA = 0.12. Holes were drilled in the preform which were 3 mm in diameter, with a d_{sep} of 0.5 mm, and were contained entirely within the germanium section of the glass. However, during the ultrasonic drilling process the preform suffered extensive cracking (see Figure 5.14(a)). This was attributed to a build up of stress in the glass resulting from the manufacturing process, and although the drilling process was repeated in other sections of the preform, the results were the same.

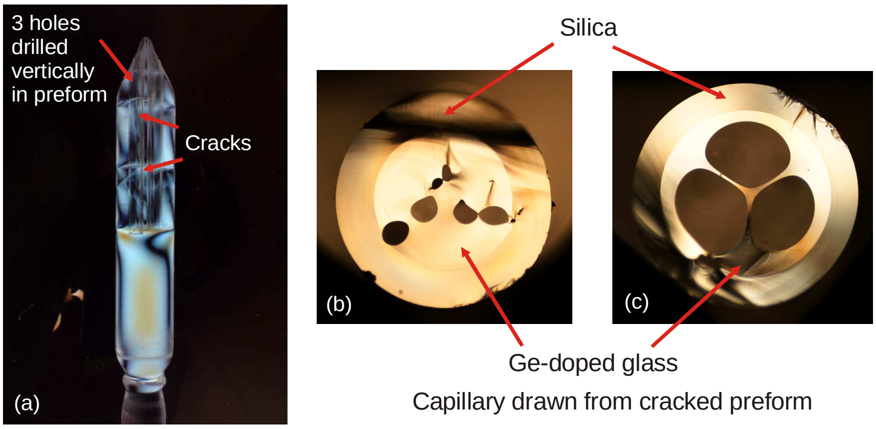

Figure 5.14: (a) Photograph illustrating the cracks that formed in the germanosilicate preform after ultrasonic drilling (viewed under cross-polarising lenses). (b) and (c) show the cross-sectional images of the resultant capillary, taken at various points during the draw.

Despite the cracking, the drilled preform was drawn into capillaries. The preform feed and mini-capstan speed, were 0.25 m.min^{-1} and 2 mm.min^{-1}, respectively, and a capillary of ~1.5 mm in diameter was obtained. The significant amount of germanium glass in the preform required the drawing temperature to be reduced to approximately 1990 ºC. The holes suffered significant collapsed during the draw and a pressure of 2 mbar was applied to the top of the preform to counteract the surface tension effects.

The majority of the material drawn was inevitably distorted, as shown in Figure 5.14(b), but a small 50 mm long section, was obtained with the desired profile (Figure 5.14(c)).

The 50 mm long capillary was sealed at one end and secured in an undoped silica cladding tube (F300-quality) that measured 8.0 × 4.2 mm in diameter. The preform assembly was then drawn at a temperature of 2065 ºC using a feed and capstan speed of 1.2 mm.min^{-1} and 5.0 m.min^{-1}, respectively. The final fibre diameter was a nominal 125 μm and was coated with a high index coating (DSM-314). After varying the applied vacuum to discover the optimum setting, a final value of 65 mbar below atmospheric was deemed appropriate. The short length of the capillary used in the preform assembly resulted in only a few meters of usable fibre (T0265). The dimensions of the fibre were measured using an optical microscope and revealed a core diameter of 1.6 μm and a variation in strut length of between 3.8 μm to 6.5 μm (Figure 5.15(a)).

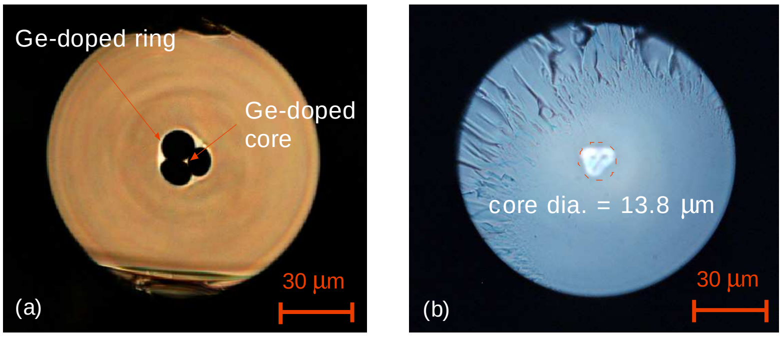

Figure 5.15: Cross-sectional images of (a) Ge-doped SC-HF and (b) the resultant high-index region following collapse of the holes using fusion splicing equipment.

The relatively short length of fibre obtained precluded any quantitative measurement of the transmission characteristics, although attempting to launch solely into the designated core proved difficult. A length of SM600 fibre (MFD = 4.3 μm) was used to couple white-light into the SC-HF whilst the output from the fibre was monitored with a microscope and camera. However, in only a few launch positions was the light guided predominantly in the core but still without significant coupling to the outer Ge-doped ring. This was attributed to a high confinement loss due to the length of the struts supporting the core of the SC-HF, which were only 3.8 μm at the shortest point. The guidance properties of the fibre were also analysed using light sources with operating wavelengths of 633 nm and 1550 nm, but with the same result.

A small length of fibre (T0265) was collapsed using Program 3 (see Table 5.3) on the fusion splicer and then cleaved within the solid section. Figure 5.15(b) shows the end-face of the illuminated fibre with the formed high-index region clearly visible. The solid Ge-doped core is approximated as being circular with a diameter of 13.8 µm. The ability to collapse the holes in a SC-HF for the purpose of enclosing a gas sample whilst still retaining a large high-index guiding section is not believed to have been previously reported. It is believed that the construction of an all-fibre index-guiding gas cell using Ge-doped SC-HF will be significantly simplified with this approach. Unfortunately there was insufficient fibre obtained from the draw to allow further investigation, but demonstration of this concept will be the subject of future work.

5.4 Summary

In this chapter, the fabrication of a silica SC-HF has been presented that uses a straightforward drilling technique to define the preform [2]. The simplicity of the fibre geometry allows long lengths to be drawn with minimal longitudinal variation, and the high-air filling fraction structure makes it ideally suited for evanescent-field sensing.

Characterisation of the SC-HF revealed a background loss of 0.33 $dB.m^{-1}$ (at $\lambda = 1550$ nm), which is comparable to other small-core HF structures [24]. The measured loss spectrum of the SC-HF also exhibited strong absorption bands in the near-infrared region that corresponded to OH ions in the glass, with a calculated concentration of ~300 ppm. The evaluated impurity was not believed to originate from the starting material but instead derived from either adsorbed OH ions in the preform prior to the drawing, that subsequently diffused into the glass at high temperatures, or surface adsorbed OH from the atmosphere present during characterisation [25].

The modal properties of SC-HF were studied using numerical simulations based on an outline of the core shape taken from a SEM micrograph. The fraction of light propagating in the air-cladding of a fibre was assessed using different core sizes. In a fibre with a core diameter of 1.2 µm, the overlap with the air-cladding was predicted to be 11.5 %, which increased to almost 30 % for a smaller core size of 0.8 µm (at $\lambda = 1550$ nm). This result places the SC-HF above other index guiding fibres available at the time as having the highest predicted core mode overlap.

The large structural air holes in SC-HF, and the high fraction of light that propagates within them, makes the fibre an ideal platform for sensing applications. This capability has been demonstrated using acetylene gas. The output from a high resolution tuneable laser source was used to successfully resolve the characteristic absorption lines between $\lambda = 1520$ and 1545 nm in a fibre loaded with C_2H_2 gas. These initial experiments were then extended to realise an all-fibre SC-HF gas cell which showed good stability over a time period of 72 hours. To construct the gas cell it was necessary to controllably collapse the holes in the SC-HF and splice it to conventional solid core fibre. A splicing loss of around 2 dB was achieved during this operation, which compares to Tse et al. who report a splice loss of 1.3 dB between small-core HF and commercial solid core fibre. More investigation is therefore needed to ascertain the exact loss incurred when splicing SC-HF and methods in which to reduce the loss.

Finally, a novel fabrication method for a small-core Ge-doped SC-HF has been demonstrated, which retains a large high-index central core following collapse of the air holes. The target application is again an all-fibre gas cell, where a chemical sample can be straightforwardly trapped in the holes of the fibre by intentionally collapsing the air-cladding using a commercial fusion splicer. This approach simplifies the process of constructing a gas cell and it is believed that the formed Ge-doped central region will facilitate low-loss splicing to transmission fibre. The fabrication route was successful, however, most of the fibre obtained was distorted and as such limited characterisation could be performed.

5.5 References

1. H. Ebendorff-Heidepriem, P. Petropoulos, S. Asimakis, V. Finazzi, R.C. Moore, K. Frampton, F. Koizumi, D.J. Richardson, and T.M. Monro. "Bismuth glass holey fibers with high nonlinearity". *Optics Express*, 12(21): 5082-5087, (2004).
2. A.S. Webb, F. Poletti, D.J. Richardson, and J.K. sahu. "Suspended-core holey fiber for evanescent-field sensing". *Optical Engineering Letters*, 46(1), (2007).
3. J.C. Knight, T.A. Birks, P. St.J. Russell, and D.M. Atkin. "All-silica single-mode optical fiber with photonic crystal cladding". *Optics Letters*, 21(19): 1547, (1996).
4. D. Richardson, F. Poletti, J.J.Y. Leong, X. Feng, H.E. Heidepreim, H.V. Finazzi, K.E. Frampton, S. Asimakis, and R.C. Moore. "Advances in microstructured fiber technology." in *Proceedings of IEEE/LEOS Workshop on Fibres and Optical Passive Components, Palermo*. 22-24 June, (2005).
5. T.A. Birks, J.C. Knight, and P.S.J. Russell. "Endlessly single-mode photonic crystal fiber". *Optics Letters*, 22(13): 961-963, (1997).
6. J.C. Baggett, T.M. Monro, K. Furusawa, and D.J. Richardson. "Comparative study of large-mode holey and conventional fibers". *Optics Letters*, 26(14): 1045-1047, (2001).
7. K. Furusawa, A. Malinowski, J.H.V. Price, T.M. Monro, J.K. Sahu, J. Nilsson, and D.J. Richardson. "Cladding pumped ytterbium-doped fiber laser with holey inner and outer cladding". *Optics Express*, 9(13): 714-720, (2001).
8. D.J. Richardson, K. Furusawa, H. Ebendorff-Heidepriem, P. Petropoulos, V. Finazzi, J.C. Baggett, W. Belardi, T.A. Kogure, J.H. Lee, Z. Yusoff, J. Nilsson, Y. Jeong, J.K. Sahu, and T.M. Monro. "Practical applications of holey optical fibers." in *Optical Fiber Communucation Conference (OFC), Washington, US*. Feb 26-27, 1-3, (2004).
9. K. Mukasa, M.N. Petrovich, F. Poletti, A.S. Webb, J. Hayes, A. Van Brakel, R.A. Correa, L. Provost, J. Sahu, P. Petropoulos, and D.J. Richardson. "Novel fabrication method of highly-nonlinear silica holey fibres." in *Conference on*

Lasers and Electro-Optics and Quantum Electronics and Laser Science, CLEO/QELS, Long Beach, CA, United states. paper CMC5, (2006).

10. V. Finazzi, T.M. Monro, and D.J. Richardson. "Small-core silica holey fibers: Nonlinearity and confinement loss trade-offs". *Journal of the Optical Society of America B: Optical Physics*, 20(7): 1427-1436, (2003).
11. C. Kerbage, A. Hale, A. Yablon, R.S. Windeler, and B.J. Eggleton. "Integrated all-fiber variable attenuator based on hybrid microstructure fiber". *Applied Physics Letters*, 79(19): 3191-3193, (2001).
12. Y.L. Hoo, W. Jin, H.L. Ho, D.N. Wang, and R.S. Windeler. "Evanescent-wave gas sensing using microstructure fiber". *Optical Engineering*, 41(1): 8-9, (2002).
13. G. Pickrell, W. Peng, and A. Wang. "Random-hole optical fiber evanescent-wave gas sensing". *Optics Letters*, 29(13): 1476-1478, (2004).
14. T. Ritari, G. Genty, and H. Ludvigsen. "Supercontinuum and gas cell in a single microstructured fiber". *Optics Letters*, 30(24): 3380-3382, (2005).
15. T.M. Monro, D.J. Richardson, and P.J. Bennett. "Developing holey fibres for evanescent field devices". *Electronics Letters*, 35(14): 1188-9, (1999).
16. P.J. Roberts, F. Couny, H. Sabert, B.J. Mangan, T.A. Birks, J.C. Knight, and P.S.J. Russell. "Loss in solid-core photonic crystal fibers due to interface roughness scattering". *Optics Express*, 13(20): 7779-7793, (2005).
17. X. Feng, A.K. Mairaj, D.W. Hewak, and T.M. Monro. "Nonsilica glasses for holey fibers". *Journal of Lightwave Technology*, 23(6): 2046-2054, (2005).
18. A.D. Fitt, K. Furusawa, T.M. Monro, and C.P. Please. "Modeling the fabrication of hollow fibers: Capillary drawing". *Journal of Lightwave Technology*, 19(12): 1924-1931, (2001).
19. K. Furusawa. "Development of rare-earth doped microstructured optical fibres". *Optoelectronics Research Centre*, PhD Thesis, (2003).
20. S.-Q. Lou, F. Hong, G. Tie-Ying, and J. Shui-Sheng. "Investigation on the Fabrication of Photonic Crystal Fibre". *Chinese Physics Letters*, 23(4): 860, (2006).

21. C.J. Voyce, A.D. Fitt, J.R. Hayes, and T.M. Monro. "Mathematical modeling of the self-pressurizing mechanism for microstructured fiber drawing". *Journal of Lightwave Technology*, 27(7): 871-878, (2009).

22. K. Lyytikainen, J. Canning, J. Digweed, and J. Zagari. "Geometry control of air-silica structured optical fibres using pressurisation." in *Proceedings of Microwave and Optoelectronics Conference, Foz do Iguacu, Brazil*. 1001-1005, (2003).

23. T.G. Euser, J.S.Y. Chen, M. Scharrer, P.S.J. Russell, N.J. Farrer, and P.J. Sadler. "Quantitative broadband chemical sensing in air-suspended solid-core fibers". *Journal of Applied Physics*, 103(10): 103108-1, (2008).

24. I. Gris-Sánchez, B.J. Mangan, and J.C. Knight. "Reducing spectral attenuation in small-core photonic crystal fibers". *Optical Materials Express*, 1(2): 179-184, (2011).

25. R.T. Bise and D.J. Trevor. "Surface absorption in microstructured optical fibers." in *Optical Fiber Communication Conference (OFC), Los Angeles, CA*. February 22nd, 714-716, (2004).

26. B. Bourliaguet, C. Pare, F. Emond, A. Croteau, A. Proulx, and R. Vallee. "Microstructured fiber splicing". *Optics Express*, 11(25): 3412-3417 (2003).

27. F. Benabid, F. Couny, J.C. Knight, T.A. Birks, and P.S.J. Russell. "Compact, stable and efficient all-fibre gas cells using hollow-core photonic crystal fibres". *Nature*, 434(7032): 488-91, (2005).

28. P.J. Bennett, T.M. Monro, and D.J. Richardson. "Toward practical holey fiber technology: fabrication, splicing, modeling, and characterization". *Optics Letters*, 24(17): 1203-5, (1999).

29. O. Frazao, J.P. Carvalho, and H.M. Salgado. "Low-loss splice in a microstructured fibre using a conventional fusion splicer". *Microwave and Optical Technology Letters*, 46(2): 172, (2005).

30. L. Xiao, M.S. Demokan, W. Jin, Y. Wang, and C.-L. Zhao. "Fusion Splicing Photonic Crystal Fibers and Conventional Single-Mode Fibers: Microhole Collapse Effect". *Journal of Lightwave Technology*, 25(11): 3563-3574, (2007).

31. L. Xiao, W. Jin, and M.S. Demokan. "Fusion splicing small-core photonic crystal fibers and single-mode fibers by repeated arc discharges". *Optics Letters*, 32(2): 115-117, (2007).

32. M. Tse, H.Y. Tam, L.B. Fu, B.K. Thomas, L. Dong, C. Lu, and P. Wai. "Fusion Splicing Holey Fibers and Single-Mode Fibers: A Simple Method to Reduce Loss and Increase Strength". *IEEE Photonics Technology Letters,* 21(3): 164-166, (2009).

33. Y. Wang, H. Bartelt, S. Brueckner, J. Kobelke, M. Rothhardt, K. Mörl, W. Ecke, and R. Willsch. "Splicing Ge-doped photonic crystal fibers using commercial fusion splicer with default discharge parameters". *Optics Express*, 16(10): 7258-7263, (2008).

34. M.C.P. Huy, G. Laffont, V. Dewynter, P. Ferdinand, P. Roy, J.-L. Auguste, D. Pagnoux, W. Blanc, and B. Dussardier. "Three-hole microstructured optical fiber for efficient fiber Bragg grating refractometer". *Optics Letters*, 32(16): 2390-2392, (2007).

Chapter 6

Flat Fibre

6.1 Introduction

In this chapter, a fabrication technique for an entirely new type of fibre is presented, which has been called *flat fibre*. Flat fibre exploits conventional Modified Chemical Vapour Deposition (MCVD) and optical fibre drawing technology to produce a novel planar optical substrate into which waveguiding channels can be written using direct ultraviolet (UV)-writing [1]. Flat fibre is fabricated by depositing photosensitive glass layers on the inside of a silica substrate tube which is subsequently collapsed flat geometry and drawn into planar geometry. The motivation behind the work was to combine the advantages of multifunctional planar optical circuits with the scalable nature of the optical fibre drawing process to develop a new platform for optical devices.

Optical planar devices, such as couplers, splitters, wavelength filters etc., are normally defined in thin layers of doped glass that have been deposited on a silicon wafer. Although the fabrication techniques for these types of optical components are well-established, the devices that are produced are ultimately constrained by the size (and even the rigidity) of the initial silicon substrate. In contrast, flat fibres can be produced in long lengths that are sufficiently thin that the material is mechanically flexible.

The first section in this chapter provides an overview of planar glass fabrication and waveguide writing, specifically flame hydrolysis deposition and direct UV-writing. The introduction is necessary in order to outline the prior art in planar waveguides, as well as convey the reasons for developing flat fibre and appreciate its merits. The experimental section then begins with a description of how flat fibre is fabricated. Optical waveguides have been demonstrated in passively-doped flat fibre samples (which were UV-written by others) and the transmission properties are reported. A more detailed analysis of the fabrication process is then presented, which examines how the processing conditions affect the geometry and glass composition of the resultant material. In relation to the obtained optical loss, specific characteristics of the core layer are examined and ways to improve on the results are discussed.

The unique properties of flat fibres, in terms of their extended lengths and mechanical flexibility, are discussed in the final subsection in the context of optical sensing. Owing to the overwhelming interest in the flat fibre concept by members of the Optoelectronics Research Centre (ORC), device realisation using flat fibre has been studied by other PhD students. An overview of this work and the preliminary results are reported.

6.2 Motivation and planar waveguide technology

In 1969, Steward E. Miller first shared his revolutionary outlook for an integrated optical platform that combined multiple optical components on a single planar substrate [2]. His vision was to replace the existing bulk optical components that were individually susceptible to the effects of temperature and vibration, with a single device that was inherently more stable. Forty years on, integrated optical devices have become ubiquitous in modern day optical telecommunication systems, and play a vital role alongside optical fibres.

Integrated optical circuits consist of an array of waveguiding channels that route, discriminate, and modulate optical signals, analogous to the electrical signals in a microelectronics integrated circuit (IC). Integrated optical devices are also fabricated in a similar way to ICs, using a combination of photolithography and reactive ion etching (RIE), and sharing some of the economic benefits that are afforded by the well-established semiconductor industry. The fabrication process for a planar optical circuit entails several individual processing steps which are shown schematically in Figure 6.1.

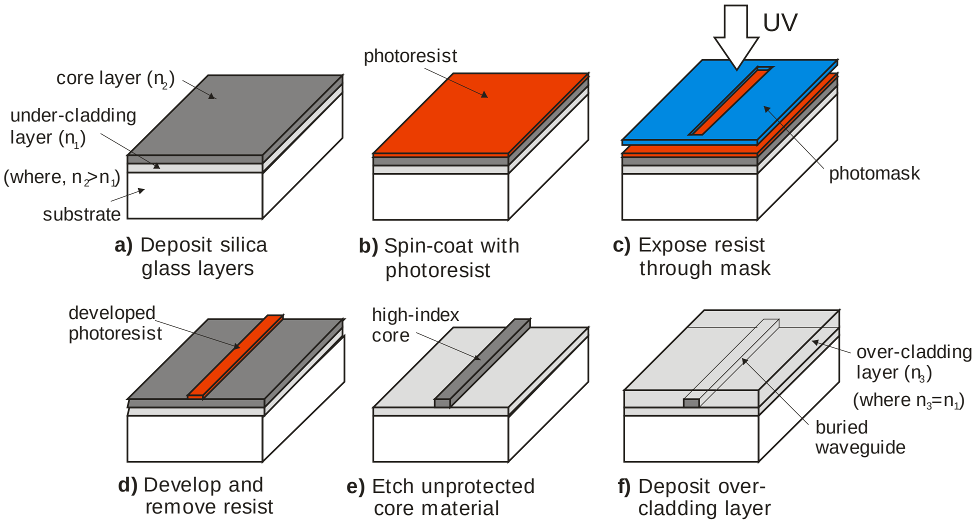

Figure 6.1: A schematic of the processing steps involved in fabricating a buried optical waveguide using photolithgraphy and etching.

The fabrication of a planar waveguide circuit begins with the deposition of silica glass layers on a silicon wafer using a Chemical Vapour Deposition (CVD)-based process, such as flame hydrolysis. An optical under-cladding is first deposited, followed by a second glass layer which is doped with germanium (Ge) to increase its index of refraction and which ultimately forms the core of the waveguide. The glass surface is then spin-coated with a thin layer (a few microns thick) of photoresist, on to which the predetermined waveguiding pattern is imprinted by exposure to UV radiation through a photomask. After the photoresist is developed, the areas that were shielded from the UV light are chemically washed away. RIE is then used to remove all core glass material other than that protected by the photoresist. Finally, an over-cladding glass layer, with the same refractive index as that of the under-cladding, is deposited on top of the exposed structure to form the buried waveguide circuit.

The processes of photolithography and etching for fabricating integrated optical circuits is well established technology, and is capable of producing multiple devices on a single substrate wafer to an exacting specification. A drawback to the process, however, is that any alteration to the waveguiding layout requires creating a new photomask; a task that requires extensive cleanroom equipment and a considerable time investment. In the last decade, an alternative method of defining optical waveguide channels, without the need for a photomask, has emerged, and is known as direct UV-writing [3]. Direct UV-writing uses a short-wavelength laser beam focussed on a photosensitive glass layer to induce a localised refractive index change. During irradiation, the glass substrate is translated relative to the laser beam and the predetermined waveguide pattern is traced out. Direct UV-writing is ideally suited for rapid prototyping of waveguide devices, and its software-driven apparatus allows any design changes to be implemented in a straightforward manner. Furthermore, by substituting the single-spot laser used in the traditional UV-writing setup for two overlapping beams, Bragg gratings can be simultaneously written into the waveguiding channel in a single step [4]. Direct UV-writing is an integral part of realising optical devices in flat fibre and is explained in more detail in subsection 6.2.2.

Within a production environment, many aspects of the glass deposition and waveguide fabrication processes described above are semi-automated to increase the yield and reduce operating costs. However, neither flame hydrolysis nor photolithography can be classed as scalable in the same way as optical fibre manufacture. For example, in optical fibre drawing, glass can effectively be drawn indefinitely as the total obtainable length simply scales proportionately with the preform dimensions. Similarly, the volume of a preform produced using MCVD can be scaled up by using a larger substrate tube and depositing more glass layers. However, the number of planar devices produced in a single fabrication run is determined (and limited) by the size of the substrate wafer and the onset of optical loss in the waveguiding channels if the component density is too high. These inherent fabrication differences between optical fibre and planar devices are not generally viewed as restrictive, as each is regarded as a separate technology designed to satisfy a particular demand i.e. long lengths of low-loss transmission media, or multifunctional optical waveguiding circuits. Nevertheless, an optical platform that possesses both of these qualities has the potential for realising unique waveguiding devices.

The aim of the work presented in this chapter was to explore ways in which to combine the scalable nature and advantages of the fibre drawing process with the inherent functionality of planar technology. Flat fibre is the result of that work [1], and exploits MCVD and optical fibre drawing equipment to generate extended lengths of doped planar material into which waveguiding channels can be written using direct UV-writing (see Figure 6.2). The entire process is inherently scalable, including the use of UV-writing in which it is only the physical movement range of the translation stages within the setup that determine the length of the channels that can be written. Flat fibre fabrication is therefore well suited to a production or manufacturing environment as the process, including drawing and waveguide writing, can be run continuously in exactly the same way as conventional fibre drawing. Unlike a FHD process, where the deposition area is restricted by the size of the wafer, the size of the flat fibre (i.e. length) is simply increased by increasing the glass volume of the preform. It can also be envisaged that the waveguide writing process could be integrated into the drawing tower and performed during the draw to mass produce multiple optical devices [5].

By using MCVD to deposit the core layers in flat fibre, the developed process has the capacity for creating glass layers with a lower loss than can be achievable by conventional planar methods, as well as allowing for superior control over the layer uniformity and composition for both passive and active constituents. Flat fibre also possesses many of the individual merits of planar and optical fibre technologies. A simple comparison between these three formats is shown in Table 6.1. The categories have knowingly been chosen with a bias towards flat fibre, as well as some positive assumptions being made about its potential loss performance, but only to reinforce the motivation behind the work.

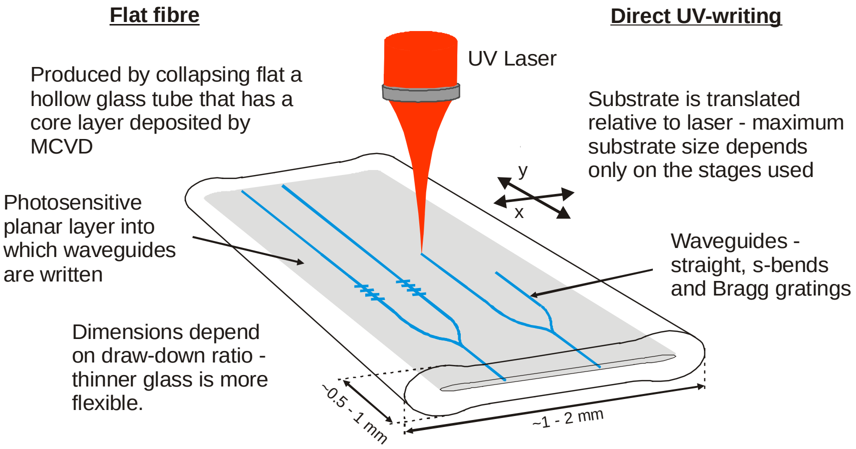

Figure 6.2: Flat fibre concept. Depiction of optical waveguide devices being written into a sample using direct UV-writing.

Capabilities of waveguide technology	Planar waveguide devices	Optical fibre	Flat fibre
Extended size/lengths	×	✓	✓
Coupling of waveguides (e.g. Y-splitter)	✓	×	✓
Low optical loss ($dB.m^{-1}$, or better)	×	✓	✓
Scalable process for substrate/preform	×	✓	✓
Scalable process for devices/fibre	✓	✓	✓
Passive and active devices	✓	✓	✓
Mechanically flexible	×	✓	✓
Cleave to size/length (i.e. no polishing)	×	✓	✓

Table 6.1: A summary of the properties of planar, optical fibre, and flat fibre formats indicating their relative capabilities.

The targeted application for flat fibre is initially optical sensing. The flexibility of the glass, and the ability to incorporate Bragg gratings during waveguide writing, means that flat fibre could be used to detect mechanical stress and strain [6]. In other applications, ‘windows’ could be introduced into long lengths of UV-written flat fibre samples to expose the core light and produce a functional evanescent-field sensor in a quasi-distributed arrangement. Both of these concepts represent devices, that are impractical to fabricate using rigid planar devices or conventional optical fibre technology, and are discussed further in subsection 6.3.5.

6.2.1 Fabricating planar glass substrates

The optical performance of a planar waveguide depends on the quality of the initial substrate glass. The glass layers should possess a high degree of thickness and compositional uniformity, and be of sufficiently low optical loss within the wavelength range of interest. In the context of silica fibre fabrication, the low-loss core layers are achieved in the preform through the use of MCVD. The equivalent deposition processes used for creating planar glass layers are Plasma Enhanced Chemical Vapour Deposition (PECVD) [7] and Flame Hydrolysis Deposition (FHD) [8]. An overview of FHD is given here, both to provide a more complete picture of planar silica deposition technology, as well as to reinforce the advantages of using MCVD for flat fibre fabrication. Furthermore, FHD is the process currently used for planar glass deposition within the ORC.

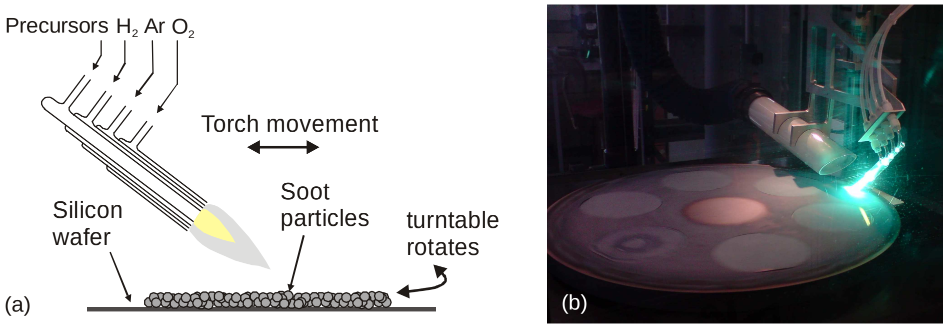

Figure 6.3: (a) Schematic of the flame hydrolysis deposition process and (b) a photograph of the equipment in use during the deposition stage.

Flame hydrolysis is the fundamental reaction in making fibre-preforms via Outside Vapour Deposition (OVD) and Vapour Axial Deposition (VAD). The chemical reaction has been recognised for many years, but it was not until the early 1980s that flame hydrolysis was adopted for planar glass deposition in the format now known as

FHD [9]. FHD involves injecting halide precursor vapours directly into an oxy-hydrogen torch where they undergo a chemical reaction to produce fine silica particles that are directed towards a flat substrate (see Figure 6.3). The low-density soot that is deposited is then sintered inside a high temperature furnace to form a glassy layer. Many discrete layers are built up in this way with repeated deposition and sintering cycles. The final composition of the glass is controlled by the dopant flow rates used during deposition.

The substrate material on to which the glass layers in FHD are deposited is normally silicon, rather than silica, owing to its availability at a low-cost and with a high planarity as a result of the demands from the microelectronics industry. This format is known as silica-on-silicon (SiO_2:Si). Before any actual glass deposition takes place, a thermal oxide is grown on the silicon wafer to improve its adhesive properties for the soot, and alleviate the effects of the difference in thermal expansion properties between silicon and silica. The surface of elemental silicon readily oxidises, and exposing the wafer to a high pressure oxygen-rich environment at a temperature of ~1000 °C for a period of several hours is sufficient to develop a thermal oxide a few microns thick [7].

The fabrication of buried waveguides, such as those illustrated in Figure 6.1, necessitates three (or more) distinct regions: an under-cladding, a core, and an over-cladding. These regions are deposited, in turn, on top of the thermal oxide, with each layer being fully sintered before depositing the next one. The composition of the cladding and core is governed by the concentration of SiO_2, GeO_2, P_2O_5 and B_2O_3 in the glass. Both the silica under- and over-cladding layers are doped with boron and phosphorous, and a similar glass refractive index to that of undoped silica (i.e. $n = 1.459$) is targeted. The primary reason for incorporating P_2O_5 and B_2O_3 is to significantly reduce the melting point of the oxide particles and facilitate sintering of the soot at a lower temperature than would be possible with pure silica. The core region will include the addition of GeO_2 to increase its refractive index relative to the cladding layers, and the final thickness of the glass layer will be around 5 – 7 μm depending on the application. The concentration of germanium in the core layer will depend on the application, but the refractive index increase will be in the region of 0.5 %Δ (Δ is defined as $(n_{core} - n_{clad})/n_{core}$ for weakly-guided waveguides).

The dopant vapours that are delivered to the torch originate from a source material in the same manner as described in Chapter 2 for the precursors used in MCVD. These vapours can derive from a solid, liquid, or gas source, and be either organic or inorganic in nature. The chemicals used in the FHD system within the ORC are: $SiCl_4$, $GeCl_4$, PCl_3 and BCl_3. The latter compound is gaseous at room temperature whilst the former chemicals are bubbled from a liquid source. Within the flame of the torch the dopant vapours undergo complex chemical reactions with direct oxidation occurring at high temperatures, and hydrolysis being the dominant reaction below ~1200 °C [7]. The balanced chemical reactions in the case of silicon tetrachloride are written below [7].

$$SiCl_4 + O_2 \rightarrow SiO_2 + 2Cl_2 \tag{6.1}$$

$$SiCl_4 + 2H_2O \rightarrow SiO_2 + 4HCl \tag{6.2}$$

In addition to the concentration of dopant vapour used during deposition, a number of physical factors will affect the morphology of the deposited soot (and resultant glass), such as the torch design and placement, as well as the fuel and carrier gas flow rates [10]. The sintering conditions will also affect the layer characteristics. For example, a furnace temperature that is too high will cause dopants to evaporate from the surface, whilst an incorrect ramp rate may result in the formation of defects. Understanding the effects of the various process parameters is paramount for producing high-quality planar layers using FHD. With optimised conditions, the refractive index and thickness variation is ~1 % and the typical waveguide loss in a germanium-doped SiO_2:Si layer is around 0.02 $dB.cm^{-1}$ [11].

6.2.2 Waveguide definition using direct UV-writing

Direct UV-writing is a single-step process for defining optical waveguide circuits in planar glass samples and was first demonstrated in a germanosilicate planar sample by Svalgaard et al. [3]. Unlike photolithography and etching techniques, UV-writing does not require the use of a photoresistive layer, a photomask, or a second glass deposition step to encase the formed waveguide. Instead, a permanent refractive index change is made in the pre-fabricated glass structure through exposure to a focussed argon-ion laser beam operating at $\lambda = 244$ nm. The substrate is translated relative to the UV light to produce the desired waveguide layout, which can consist of both straight and curved channels. The entire process is computer controlled and complex designs can be written with very high precision.

In order to induce a refractive index change in the glass, the UV-writing process exploits the photosensitivity that is exhibited by some materials. The glass sample typically consists of a three-layered structure with a germanium-doped silica layer (~5 μm thick) sandwiched between an under- and over-cladding. The exact mechanism responsible for the index change in germanium-doped glass is beyond the brief overview provided here, but is associated with defects within the silica glass matrix that lead to germanium oxygen-deficient centres (GODC). When irradiated by UV light, these defects are affected in such a way that their atomic bonding is modified, causing a localised refractive index change.

The extent to which the refractive index is changed during UV irradiation will depend on the amount of GODC in the glass, which will increase with the germanium concentration. The index change will also depend on the laser power and the energy transferred to the sample, and this exposure is quantified by the Fluence, F, measured in kJ.cm^{-2}. The fluence relates the translation speed of the substrate (υ) with the power density (I) and spot size (d) of the laser, and is expressed as $(I \times d) / \upsilon$. The index rise of UV-written waveguides can be as high as 0.02 [12] although an order of magnitude lower than this is more typical.

Direct UV-writing has been researched at the ORC, specifically the Planar Optical Materials Group, for many years, and its development has led to a technique known as Direct Grating Writing (DGW) [13]. DGW is an extension of direct UV-writing that enables channel waveguides and Bragg gratings to be defined simultaneously. By focussing two crossed laser beams on a single spot to create an interference pattern, intensity profile is created in the sample. The grating is then produced by translating the substrate whilst modulating the laser on and off such that the substrate is displaced by a distance equal to the period of the interference each time the laser is on. If the laser output is kept constant whilst the substrate is traversed then the interference pattern is averaged out and a straight waveguide is produced. The DGW equipment within the ORC has been used (by others) to inscribe the waveguides and gratings in the flat fibre samples that are reported in the following section.

6.3 Experimental work

The virtues of flat fibre lie in the combination of a novel fabrication route and existing waveguide writing technology. As each part is a distinct process, they are addressed here separately in the first two subsections. Subsection 6.3.1 presents the fabrication process developed for flat fibre, whilst subsection 6.3.2 reports on the characterisation of direct UV-written flat fibre samples. This experimental work was undertaken prior to, and continued shortly after the Mountbatten fire (see Appendix C.1), and was predominantly to provide a proof of concept [14]. Subsections 6.3.3 and 6.3.4 then report on the work undertaken to further understand the fabrication requirements for flat fibre and the findings are discussed in relation to the previously obtained measurement results from the UV-written waveguides. Finally, in subsection 6.3.5, an overview of the device work conducted by others on optical sensing in flat fibre is provided.

Owing to the disruption of the Mountbatten fire, any of the described fabrication process details refer to the MCVD system and optical fibre drawing equipment available at the time the work was carried out. Considerable optimisation of the off-site equipment was needed to continue research efforts, and consequently numerous preforms and fibres were fabricated. A selective few are reported in this chapter in order to convey the necessary results, whilst the full fabrication list is shown in Appendix B.4. It should be noted that all fabrication and characterisation work reported here on flat fibre was completed by the author, and any assistance that was provided by others is clearly disclosed. The UV-writing of all flat fibre samples, however, was kindly undertaken by the Planar Optical Materials group and in particular benefited from the committed efforts of Dr. Rafiq Adikan.

6.3.1 Flat fibre fabrication

The process developed for fabricating flat fibre involves two stages. The first stage involves depositing silica layers on the inside of a circular glass tube using conventional MCVD equipment. A high-quality SUPRASIL-F300 (Heraeus, Germany) glass substrate with low hydroxyl (OH) ion impurity was used in most cases and enabled direct comparisons to be made with conventional fibre preforms regarding the material loss, as well as exhibiting a high transparency at the wavelength used for UV-writing. The F300 substrate tube was subjected to the usual gas-phase etching (using sulphur hexafluoride) and flame polishing preparation steps, before several undoped silica cladding layers were deposited. The core layer was then doped with a high concentration of germanium to increase its photosensitivity and therefore its response to UV irradiation. The deposition process was halted after the core layer had been deposited, with the tube remaining uncollapsed.

The second stage of the fabrication process was to transfer the glassware to an optical fibre drawing tower (see Figure 6.4). The uncollapsed preform was then drawn down to a mm-scale using the mini-capstan whilst the atmosphere inside the tube was held under vacuum. A dedicated vacuum system was built for this purpose which allowed the pressure inside the tube to be regulated between 0 and -1000 mbar, relative to atmospheric. The drawing conditions were firstly left to stabilise without any differential pressure inside the tube until a circular capillary with the correct dimensions was achieved. This was verified under an optical microscope. The atmosphere inside the tube was then evacuated to initiate tube collapse. A period of several minutes was sufficient for the tube to collapse, as shown in Figure 6.4(b).

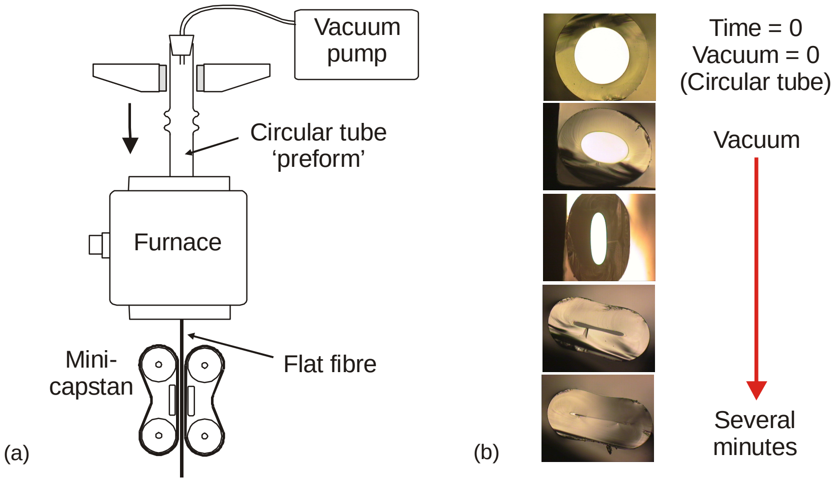

Figure 6.4: (a) Illustration of a circular tube (preform) being drawn into flat fibre, and (b) cross-sectional images of the glass as it gradually deforms into a planar geometry.

It was found that the drawing process remained stable once the vacuum pump was initiated and continued indefinitely without any measureable deviation in the geometry of the flat fibre. The uncoated flat fibre was cut into ~1 m lengths for ease of handling. The cross-sectional dimensions of the flat fibre depended on the size of the starting substrate and the associated preform feed and mini-capstan speed. A standard 20 × 16 mm tube typically produced flat fibre with outer dimensions of ~2 × 1 mm and was achieved using feed and draw speeds in the range of 1 – 5 mm.min^{-1} and 0.25 – 1 m.min^{-1}, respectively (see Figure 6.5(a)). The core thickness depended on the layer thickness deposited in the tube initially, but with a single Ge:Si layer, and the aforementioned scaling-down ratios, the final thickness was typically around 5 – 7 μm. This was chosen to match the spot size of the laser subsequently used for writing the waveguide.

By using a standard sized glass tube measuring 20 × 16 mm, and the aforementioned range of drawing conditions, a huge variation in fibre dimensions was possible. For convenience, the early experimental work focussed on the standard sized substrate, and the largest flat fibre samples obtained were approximately 4×2 mm, limited by manageable feed speeds during fabrication (i.e. <10 mm.min^{-1}). By using a larger diameter starting tube and, if necessary, a furnace with an increased internal bore, it is anticipated that the maximum achievable size of fibre could be increased (which is investigated further in subsection 6.3.4). However, the overall thickness of the material will affect its mechanical flexibility, and the glass will become more rigid as its dimensions increase. Therefore, smaller fibre dimensions may be preferable for certain applications. The unique flexibility of flat fibre is shown in Figure 6.5(b).

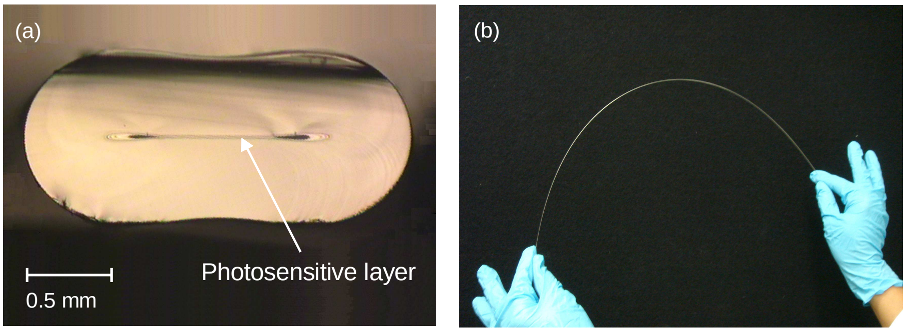

Figure 6.5: (a) Cross-sectional image of flat fibre showing the typical dimensions and shape. (b) Illustration of the mechanical flexibility of flat fibre.

6.3.2 Waveguide writing and characterisation

Most planar waveguide circuits, irrespective of their complexity, are composed of three distinct types of waveguides: splitting and coupling junctions, wavelength selectivity channels through the inclusion of a Bragg grating, and interconnecting waveguides that can be straight or S-bends. A myriad of optical functions can be realised using a combination of these fundamental elements, and it is these basic components that have been demonstrated in flat fibre to exemplify its potential [1].

Multiple waveguide channels have been UV-written in germanium-doped flat fibre samples (F0764) using DGW equipment. Both straight and Y-splitting channels were defined in 50 mm long samples. Bragg gratings were also defined in flat fibre samples with a designed Bragg wavelength (λ_b) and period (Λ) of 1550 nm of 529.37 nm, respectively. The UV-written waveguides were imaged and characterised using a dedicated setup that was assembled to combine interchangeable light sources and detectors for both alignment and measurement purposes. For conciseness, Figure 6.6 shows the complete array of components, including those used for the material and loss measurements reported later in this subsection.

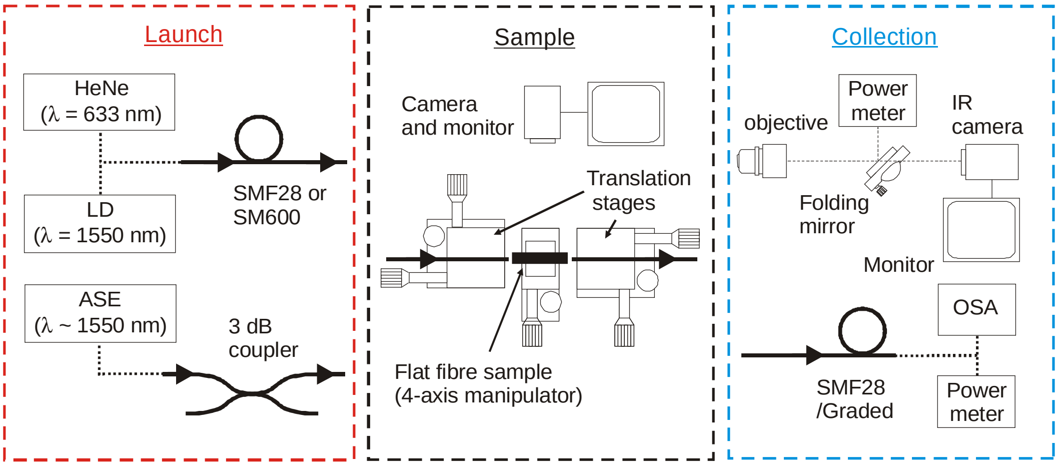

Figure 6.6: Experimental setup used for imaging and characterising flat fibre and UV-written waveguide samples. All apparatus are illustrated, and those components categorised as ‘launch’ or ‘collection’ were interchangeable depending on the required measurement.

Central to the experimental setup was a 4-axis translation stage which held the flat fibre sample and incorporated positional adjustments for pitch and yaw. A fibre-coupled He-Ne laser was used for alignment purposes, which could be interchanged with a laser diode or amplified spontaneous emission (ASE) source to perform near-infrared measurements without disturbing the launch conditions. The launch fibre was butt-coupled to the flat fibre sample and alignment was aided by a magnifying camera mounted above the sample. An index matching gel was used to improve the coupling efficiency. The waveguides were imaged using either a visible or infrared (IR) camera, depending on the light source being used, and intensity measurements were recorded using an optical spectrum analyser (OSA) or optical power meter.

Figure 6.7(a-c) shows images of the UV-written straight and splitting waveguides in flat fibre samples F0764, illuminated with visible (λ = 633 nm) and IR (λ = 1550 nm) light. The waveguides are visible as bright spots in the central core layer, although it is evident that light is also being guided in the high-index layer due to non-optimised launch conditions. Figure 6.7(d) shows the reflected spectrum from a UV-written Bragg grating obtained with assistance from Sumiaty Ambran and using the ASE source and a 3 dB coupler. The Bragg wavelength (λ_b) of the grating is related to the period and the effective refractive index of the mode (n_{eff}) by $2\Lambda n_{eff}$. The peak reflection of the grating was measured on the OSA as 1555.38 nm, equating to a n_{eff} of 1.469. Therefore, the refractive index contrast (Δn) of the UV-written waveguide, with respect to undoped silica (taken as 1.445 at λ = 1550 nm) is 0.024. This figure, however, includes the index rise from the germanosilicate core layer in the initial preform, which has been inferred from that of another preform (LN0005) fabricated with similar conditions as ~0.019. The resultant index modulation from the UV-writing is therefore 0.005.

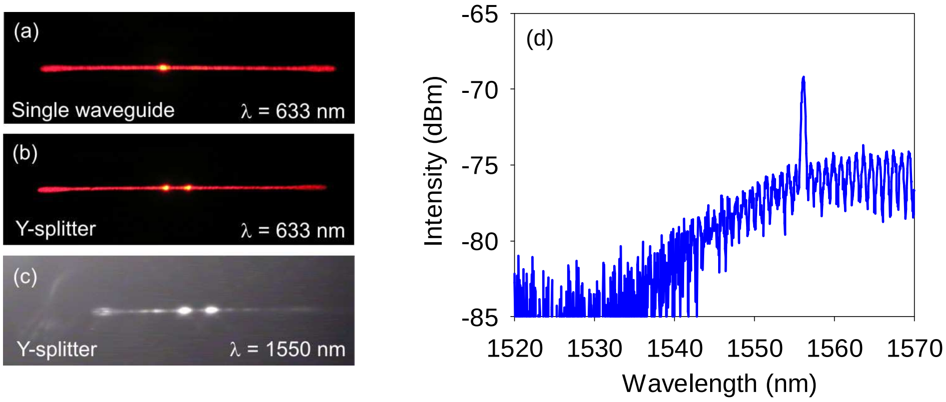

Figure 6.7: End face images of transmitted light from flat fibre samples (a) straight channel, and (b-c) Y-splitting channels. (d) Reflected spectrum from a UV-written Bragg grating.

In a conventional SiO_2:Si planar waveguide, the optical loss is not easily established using a cut-back measurement in the same way as optical fibre. Instead, the propagation loss is determined by butt-coupling standard single-mode fibres (SMF) to the input and output facets of the waveguide and comparing the measured transmission to that of the directly coupled SMF-to-SMF. The subtracted loss figure, however, is heavily dependent on the quality of the polished facets and the coupling efficiency to the waveguide. Therefore, a total throughput (i.e. SMF-waveguide-SMF) loss value is quoted, which is deemed acceptable given that the optical device will normally be connectorised with optical fibres.

Flat fibre can be cleaved easily by hand using a ceramic knife, and, as the core layer is in the centre of the glass, the UV-written waveguide remains unaffected. Using this method, a true loss measurement of the waveguide can be made by systematically cutting-back the sample to ascertain the transmitted power per unit length. This method was applied to a 50 mm long flat fibre sample (F0764) with a single UV-written channel. A SMF from the ASE laser source was pigtailed to the waveguide by Dr James Gates in order to provide a fixed launch position, and the power output from the flat fibre was recorded using both free-space optics as well as a butt-coupled fibre measurement. For the free-space measurement, the waveguide was firstly imaged through an objective lens and an adjustable iris onto an IR viewer. The lens position was then adjusted whilst viewing the waveguide on the monitor until focussed, and the aperture of the iris was then reduced to restrict the collected light to only that of the waveguide. Once positioned, the objective lens and camera position remained fixed and a flip-back mirror redirected the light exiting the flat fibre sample onto a large-area power meter. The intensity value was then recorded with both the free-space and fibre-coupled arrangement, and repeated after progressively cutting back the glass sample. The results are shown in Figure 6.8 and a linear regression has been applied using software.

The calculated waveguide loss from the free-space and fibre-coupled measurements of the flat fibre sample are 0.3 dB.cm^{-1} and 0.4 dB.cm^{-1}, respectively. Both of these values are higher than the propagation loss reported in the literature of 0.2 dB.cm^{-1} (at $\lambda = 1.54\ \mu m$) for a Ge:Si UV-written Si:SiO$_2$ sample [15]. The higher loss measured in the flat fibre is believed to be a result of non-optimised conditions used for the UV-writing. The contribution to the loss from the core glass material has also been measured using the same cut-back technique, and is reported below.

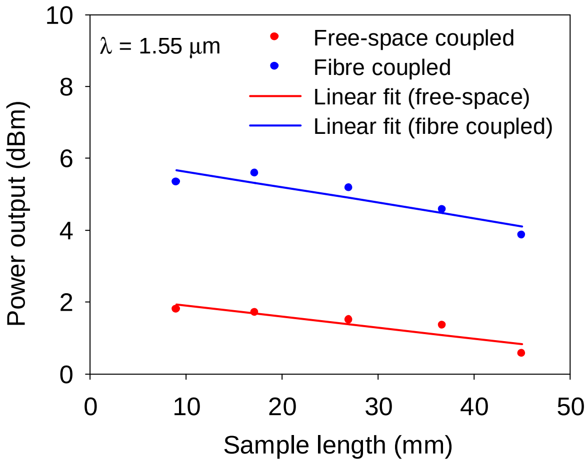

Figure 6.8: Propagation loss of UV-written channel waveguide in flat fibre sample (F0764) obtained using a cut-back measurement.

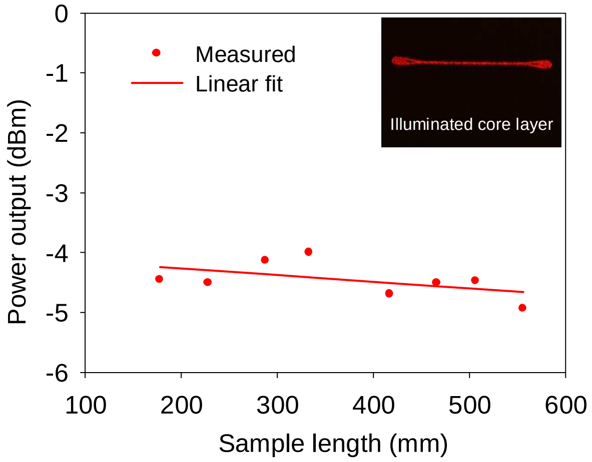

Figure 6.9: Material loss in the core layer of a flat fibre sample, measured using a cut-back technique (inset: image of the illuminated core layer).

A cut-back loss measurement was performed on a 400 mm long flat fibre sample (T0059). The core dimensions were ~800 × 6 µm and the glass had not been subject to any UV-writing. To provide a fixed launch position, the sample was pigtailed to SMF by Dr. James Gates. The light (at λ = 633 nm) exiting the flat fibre was captured on a large-area detector via an adjustable iris. The measurement results are presented in

Figure 6.9, and the calculated loss was 0.01 dB.cm^{-1}. This value is lower than that obtained by Tandon et. al of 0.02 dB.cm^{-1} for an optimised FHD deposited glass layer (i.e. buried waveguide) [11] and suggests that the previously measured waveguide loss was a consequence of the non-optimal writing conditions. A material loss of 0.01 dB.cm^{-1} obtained for the flat fibre sample is, however, considerably higher that expected from a glass prepared using MCVD. The possibility of scattering losses arising from a non-uniform dopant distribution in the core is examined in the next subsection.

6.3.3 Properties of the deposited core

To produce a UV-written waveguide with a high refractive index contrast, it is essential that the substrate glass exhibits a high degree of photosensitivity. The intensity of the UV absorption band centred on $\lambda = 244$ nm has a linear dependence on the molar fraction of GeO_2 in the glass, and so its photosensitivity can be enhanced by increasing the germanium concentration [7]. The gemanosilicate core layer in flat fibre is doped using an MCVD process, and as such a dopant concentration of up to ~30 mol% is possible [16]. In contrast, SMFs used for telecommunication purposes comprise of ~3 mol% of germanium. There is no recognised metric for photosensitivity, however, based on reports in the literature, a GeO_2 concentration in silica of around 5 – 10 mol% is appropriate for UV-writing [3, 7]. This value was the basis on which most of the flat fibres were fabricated.

The molar fraction of GeO_2 in silica glass can be inferred from its index of refraction. Therefore, as the dopant concentration in MCVD is governed by the ratio of $SiCl_4$ and $GeCl_4$ in the tube during deposition, by measuring the refractive index of the resultant glass, the precursor flow rates can be equated to the GeO_2 concentration. To determine the amount of Ge that was needed in the core of the flat fibre, a series of conventional preforms were fabricated and their refractive index profiles (RIP) compared to the precursor flow rates that were used during core deposition. $GeCl_4$:$SiCl_4$ ratios of 0.5:1, 1:1, 2:1, and 3:1, were used for preforms L30011, L30007, L30010, and L30013, respectively. The O_2 flow rate was maintained at 600 ml.min^{-1}, and the burner temperature used during deposition was between 1985 °C and 2025 °C. The RIPs of the preforms were measured using a PK2600 Preform Analyzer (Photon Kinetics, US) and the refractive index contrast as a function of $SiCl_4$:$GeCl_4$ vapour flow was plotted (see Figure 6.10).

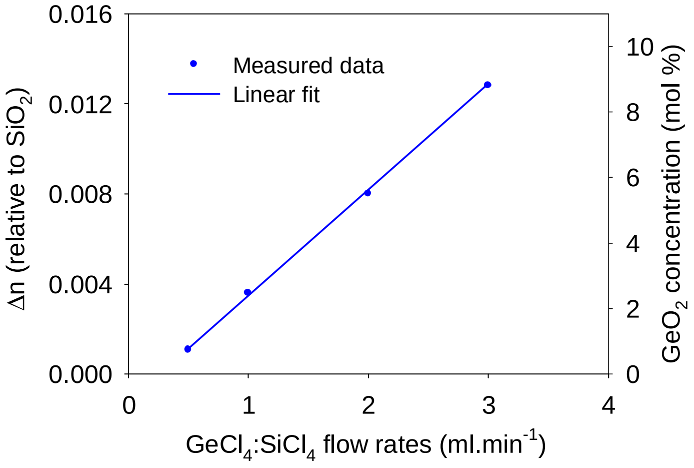

Figure 6.10: Measured (average) core refractive index of preforms L30011, L30007, L30010 and L30013 as a function of $GeCl_4$:$SiCl_4$ vapour flow rate. Right-hand axis: equivalent GeO_2 concentration as given by [17].

The measured data agrees well with that reported by Guryanov et al. [16], including the linear fitting that has been overlaid on the graph. The relationship between refractive index and oxide addition is reported by Huang et al. as $\Delta n = 0.148 \times \text{mol\%}$ [17] and has been added on the right-hand axis to the graph in Figure 6.10. Therefore, it was concluded that a volumetric ratio of >2 for the $GeCl_4$:$SiCl_4$ flow rates was required to achieve a GeO_2 concentration in the deposited glass of between 5 – 10 mol%, which was deemed necessary for successful UV-writing in flat fibre samples.

Although GeO_2 is added to silica glass to increase its photosensitivity, the associated index rise is not necessarily desirable. In FHD, boron is added to the core layer to reduce its refractive index and ensure it closely matches that of the surrounding layers. This results in a waveguide with a more symmetric mode field, and minimises the coupling loss when connected to standard optical fibre [18]. Boron, in the form of B_2O_3 in silica glass, has a molar refractivity of $\Delta n = -0.0375 \times \text{mol\%}$ [19] and is readily available in MCVD systems with a BBr_3 precursor. Furthermore, boron co-doping enhances the photosensitivity of silica glass, and it has been reported that in a fibre containing ~16 mol% of GeO_2 the UV-induced index modulation is increased by 7×10^{-4} [20].

Flat fibres have been fabricated (T0384) from a boron co-doped germanosilicate preform (G30168) produced using conventional MCVD equipment. The preform contained three layers that were deposited using $SiCl_4$, $GeCl_4$, and BBr_3 precursor flow rates of 100 ml.min^{-1}, 200 ml.min^{-1}, and, 100 ml.min^{-1}, respectively. The burner temperature was 1800 °C and the carriage traverse speed was 150 mm.min^{-1}. The RIP of a flat fibre sample drawn from the preform was measured using an S14 Profiler (Photon Kinetics, US). The index rise in the core was 0.003, which compares to an anticipated index rise in the absence of boron of 0.008. Using the molar refractivity for GeO_2 and B_2O_3 quoted above, the calculated oxide additions to flat fibre sample T0384 are 5.4 mol%, and 13.3 mol%, respectively. Optical waveguides have been UV-written in these flat fibre samples and have shown an enhanced index modulation compared to those without boron co-doping. Work is ongoing to quantify these preliminary findings.

A consequence of doping silica with high concentrations of either GeO_2 or B_2O_3 is an increase in the thermal expansion coefficient of the glass. In flat fibre, the equivalent over- and under-cladding regions are formed by the silica substrate tube, and as such some mismatch with the core is inevitable. The difference between the thermal expansion coefficients of the deposited core and the cladding tube is a function of the dopant concentration in the core, and can be equated to a weight factor of the incorporated constituent [21]. The contributions from GeO_2 and B_2O_3 can be expressed in the units of °C.mol^{-1}, and are reported as 0.71×10^{-7} °C.mol^{-1} and 1.8×10^{-7} °C.mol^{-1}, respectively [22]. Using these values, the thermal expansion mismatch introduced into preform G30168 as a result of the contributions from GeO_2 and B_2O_3 was calculated as ~3×10^{-6} °C^{-1}. Flat fibre was successfully drawn from this preform (i.e. T0384) immediately after fabrication, however, the following day the remaining glass tube had developed visible cracks in the deposited layer. It was found that generally glass layers deposited using high ratios of $GeCl_4$ or BBr_3 vapour to $SiCl_4$ vapour (i.e. 5 or more) were prone to cracking. In most cases, the glass preform appeared unaffected immediately after deposition but deteriorated over a period of hours. These findings imposed a practical upper limit on the dopant concentration that could be used in flat fibre using the current technique.

As well as an increase in the thermal expansion mismatch, the addition of GeO_2 and B_2O_3 has another undesired effect for flat fibre; a reduction in the melting point of the glass. In FHD samples, this change is essentially to reduce the sintering temperature of the deposited soot particles to below that of the silicon wafer substrate (i.e. 1410 °C). However, in MCVD, high working temperatures (i.e. >2000 °C) are unavoidable and often lead to the preferential evaporation of dopants from the silica, causing the well known ‘central dip’ in the RIP [16]. Techniques exist to limit this effect, such as over-doping or pre-etching of the core before the final seal pass [23], but none of these treatments are appropriate for flat fibre fabrication as the collapse stage is performed on the drawing tower.

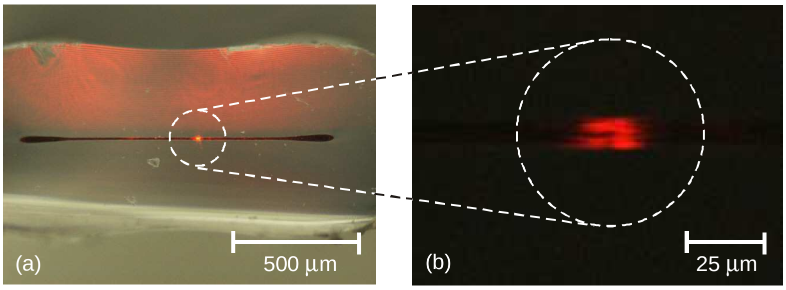

Figure 6.11: (a) Cross-sectional image of UV-written channel waveguide in flat fibre sample F0764, and (b) magnification of the waveguiding region showing evidence of a central dip in the deposited layers and the non-uniform illumination from the core.

Figure 6.11 shows the cross-sectional image of a UV-written waveguide in flat fibre sample F0764, illuminated with a He-Ne laser. Inspection of the core light under high magnification revealed that the intensity distribution was not uniform and there was some evidence of a central dip (see Figure 6.11(b)). These guiding characteristics may have contributed to the measured waveguide loss in subsection 6.3.2. The depletion of dopants from the central core region is symptomatic of collapsing a glass tube at high temperature, and is undoubtedly accentuated by the reduced pressure inside the tube during the flat fibre drawing process. By using a lower furnace temperature, it may be possible to reduce the severity of the central dip, or perhaps lessen its apparent effect by increasing the number of core layers in the preform so that the require draw-down ratio is increased.

6.3.4 Fibre drawing parameters

The size and shape of flat fibre is determined by the drawing conditions. As the glass is drawn uncoated, the main process variables are: preform feed rate, capstan speed, furnace temperature, and the relative pressure inside the tube. The effect that these parameters have on the final geometry of the fibre was investigated and the findings are discussed below.

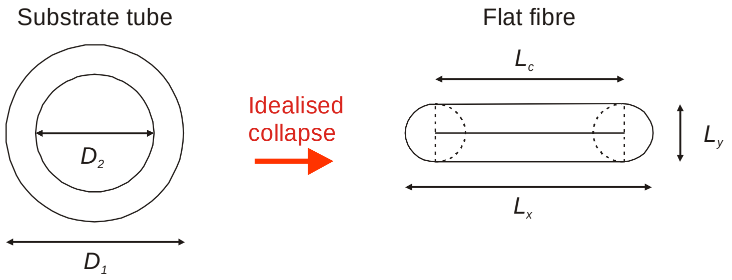

Figure 6.12: Depiction of a circular substrate tube and the idealised shape when reshaped into a flat profile.

The flat fibre drawing process involves feeding a circular glass tube into the furnace of a drawing tower at a constant rate. The tube is subsequently collapsed into a flat profile (aided by a reduced pressure inside the tube) and the size of the glass exiting the furnace is determined by the speed of the capstan. For the purpose of modelling, the drawing process has been considered as two separate stages: the initial collapse of the glass tube, and its subsequent reduction in size, i.e. scaling-down factor. The first stage is shown in Figure 6.12 and depicts a circular tube flattened into an idealised shape. The dimensions of the flattened tube have been defined as L_c, L_y, and L_x, and are related to the circular tube by equations (6.1), (6.2) and (6.3), respectively. For the purposes of simplicity, the core thickness has been approximated as zero.

$$L_c = \frac{\pi}{2} \times D_2 \tag{6.1}$$

$$L_y = D_1 - D_2 \tag{6.2}$$

$$L_x = \left(\frac{\pi}{2} \times D_2 \right) + \left(D_1 - D_2 \right) \tag{6.3}$$

The dimensions of the drawn fibre are dictated by the rate at which the glass is fed into the furnace, and the speed of the capstan, and are related by the conservation of mass as explained in Chapter 2. By defining a scaling-down factor, the dimensions of the flat fibre can be predicted for a given tube size using the equations above. This has been done for 3 different sized substrate tubes and the results are shown in Figure 6.13. The findings suggest that a huge range of flat fibre sizes are possible by selecting the appropriate scaling-down factor. However, in practice, certain constraints were placed on the allowable values. For example, it was found that a capstan speed of >5 m.min^{-1} became unmanageable owing to the need to cut the glass by hand at regular intervals. A capstan speed <0.2 m.min^{-1} was also problematic, and failed to produce sufficient tension in the fibre, even when the furnace temperature was relatively low.

Similarly, practical limitations also applied to the preform feed rate. A feed speed that was in excess of 9 mm.min^{-1} caused the draw to become unstable, owing to the short resident time of the glass in the furnace and an insufficiently formed neck-down region. However, no issues were found with feed speeds at the lower end of the scale, and values of 0.1 mm.min^{-1} or less were possible. The restrictions imposed by practical issues are indicated by a greyed region in Figure 6.13.

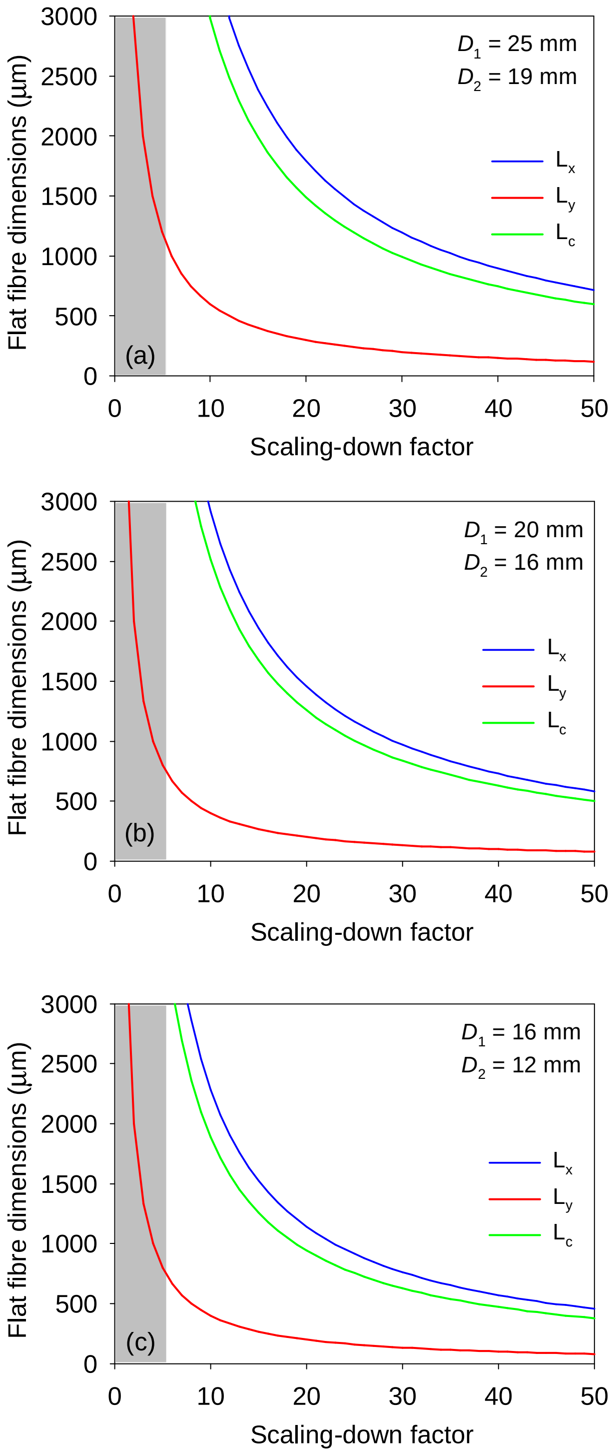

Figure 6.13: Flat fibre dimensions as a function of scaling-down factor for starting tubes measuring (a) 25 × 19 mm, (b) 20 × 16 mm and (c) 16 × 12 mm. The greyed region signifies scaling-down factors that are impractical using the current equipment.

The effect of furnace temperature and applied vacuum on the collapse of the tube has also been investigated. In conventional preform fabrication, the surface tension effects in the glass at high temperatures act to collapse the tube in a symmetrical manner. Creation of the planar geometry required for flat fibre, however, requires a negative differential pressure between the inside of the glass tube and its exterior. At high furnace temperatures, it was found that even a modest differential pressure of a few millibar (mbar) was sufficient to initiate planar collapse of the tube. The extent of the collapse was influenced by the magnitude of the applied vacuum, as well as the furnace temperature. It was important to understand the relative impact of these changes and establish whether the geometric calculations presented previously are valid.

Two independent drawing trials were performed on CFQ-quality (Heraeus, Germany) silica tubes to examine the effect of furnace temperature and applied vacuum (the nominal diameter was 20×16 mm, although there was a slight variation in diameters which is apparent in the results). In the first trial, a differential pressure of -10 mbar, (relative to atmospheric) was maintained inside the tube whilst the furnace temperature was varied from 2020 °C to 2140 °C. In the second trial, the furnace temperature was kept constant at 2020 °C whilst the applied vacuum was varied from 0 to -40 mbar (relative to atmospheric). Glass samples were examined after making incremental changes, and the average wall thickness was measured using an optical microscope. The results are shown in Figure 6.14 and Figure 6.15.

The results indicate that an increase in either the furnace temperature or the applied vacuum is sufficient to deform the circular tube, and is accompanied by an increase in the wall thickness of the glass. For the sizes of tubes tested, either an increase in furnace temperature of 140 °C, or a reduction of the internal pressure by 40 mbar was sufficient to produce flat fibre. The resultant increase in wall thickness, however, was different in each case. Increasing the vacuum in order to collapse the fibre increased the wall thickness by 45 %, compared to 23 % for an increase in the furnace temperature. These findings need to be taken into consideration when calculating the required preform feed and capstan speeds.

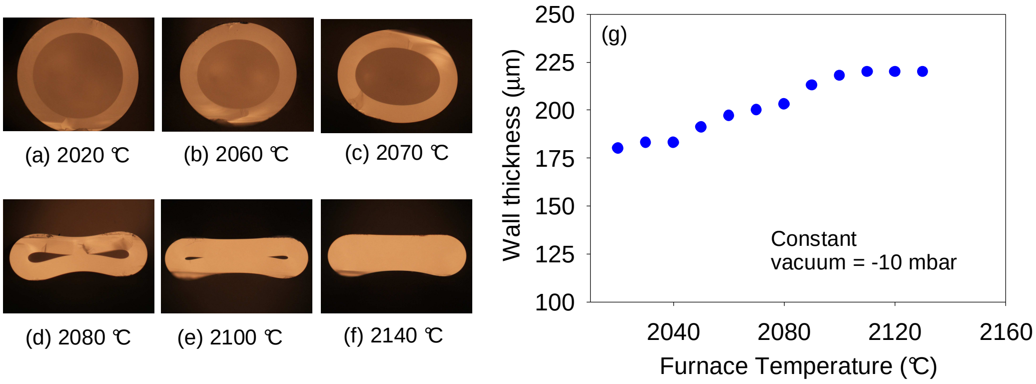

Figure 6.14: Examining the effects of tube collapse with constant differential pressure and varying furnace temperature. (a to f) Selected cross-sectional images showing the extent of collapse, and (g) a plot of the measured wall thickness.

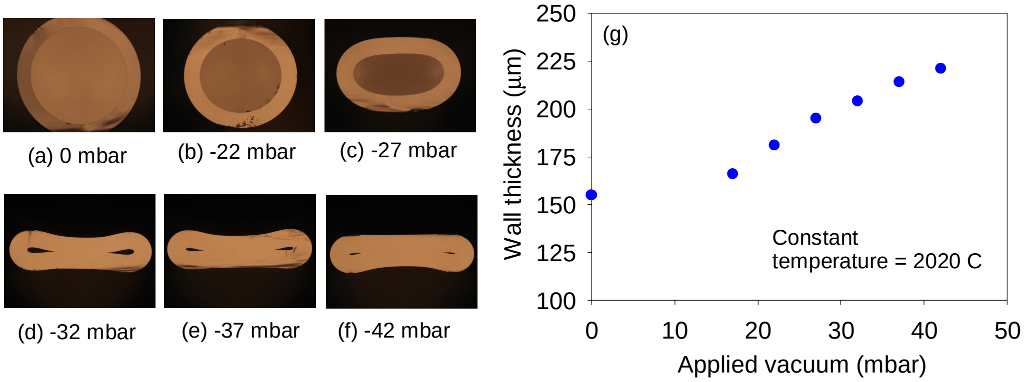

Figure 6.15: Examining the effects of tube collapse with constant furnace temperature and varying applied vacuum. (a to f) Selected cross-sectional images showing the extent of collapse, and (g) a plot of the measured wall thickness.

6.3.5 Sensing devices using flat fibre

The main application identified for flat fibre was optical sensing. It was envisaged that extended lengths of flexible glass substrates could be used for quasi-distributed sensing, with functionality enabled through the inscription of densely-packed UV-written waveguides and Bragg gratings. In a quasi-distributed sensing, or point-sensing scheme, the optical waveguide incorporates multiple nodes that are sensitive to a localised change in the environment. These changes are detected by either an alteration to the properties of the waveguide (normally via a Bragg grating), or through direct interaction with the evanescent-field. Evanescent-field sensing, which was introduced in Chapter 2, involves partially exposing the propagating wave so that it can interact with its surroundings. To realise a flat fibre sensor, this approach requires the silica over-cladding to be removed at regular intervals to provide detection 'windows' through which the evanescent-field can be accessed. Although full device realisation was not within the aims of this thesis, the preliminary work towards a flat fibre sensor has begun and the progress so far is summarised below.

Chemical etching and RIE techniques have both been explored to selectively remove the over-cladding from flat fibre samples, with varying degrees of success. The associated problems were: efficiently masking off the area of glass to be etched, and etching the over-cladding to the correct depth with sufficient accuracy. Chemical etching of a flat fibre sample was explored using hydrofluoric (HF) acid. Owing to the aggressive nature of HF, very few materials were found that were entirely resistant to its effects, and screening a specific area for etching proved difficult. Wax was found to be the most promising material and also adhered well to the glass surface. A flat fibre sample was partially coated in wax and SMFs were connected to each end of sample to enable the etching progress to be monitored by measuring the light throughput. The attempts to chemically etch the sample were mainly unsuccessful, and issues relating to the surface tension of the liquid, which prevented 'wetting' of the sample, and evaporation of the acid were experienced.

Preliminary trials were conducted using RIE to selectively remove regions of the over-cladding in flat fibre samples. Glass samples, of ~75 mm in length, were masked by hand using Kapton tape to leave multiple exposed windows, each with a size of around 500×100 μm. The depth of the core in these particular samples was ~25 μm from the surface. The RIE equipment was operated by Mr. Neil Sessions, and several etching runs were performed on flat fibres using various time durations. Unlike the experiments with HF acid, where the etching progress was monitored continuously, RIE relied on establishing an etching rate. After processing, the size and depth of the etched windows was measured using a P16 Surface Profiler (Omniscan, UK). Depths of between 12 μm and 29 μm were achieved and the calculated etch rate was 0.1 $\mu m.min^{-1}$. From these early studies, it is believed that RIE is capable of achieving the micron accuracy required to selectively etch the over-cladding in flat fibres to a specific depth.

As RIE is not practical for removing glass that is several tens of microns thick, the over-cladding of the flat fibre needs to be minimised. This can be achieved by depositing a thicker core layer, which subsequently requires a higher scaling-down factor, or using a thinner-walled substrate tube initially. Reducing the over-cladding thickness in the final fibre is also possible, and the Planar Optical Materials group have pursued this approach using mechanical polishing. A flat-fibre sample was side-polished on one edge to gain access to the evanescent-field of a UV-written waveguide. The initial results show that a wavelength shift in the peak reflection of a Bragg grating was detectable when the sample was exposed to a refractive index liquid of $n = 1.3$ compared to that of air ($n = 1$) [24].

Bragg gratings are inherently sensitive to changes in strain and temperature and can thus be used for sensing applications. A change in the period of the grating can be detected, either through the flexing of the waveguiding medium or a difference in its expansion as a result of a temperature change. These types of sensors have important applications in monitoring the structural health of buildings and equipment. The first results of a bending and twisting sensor using the flat fibre platform have been demonstrated by the Planar Optical Materials group [6]. The findings reveal a proportional relationship between the mechanical flexing of the sample and the measured wavelength shift of the Bragg grating. These preliminary results, and those reported above, demonstrate the potential of flat fibre sensing devices and further research in this area is on-going.

6.4 Summary

This chapter has reported on the fabrication process for a novel flat fibre platform. In combination with direct UV-writing, flat fibre provides a new type of planar glass substrate into which waveguides and Bragg gratings can be defined in order to produce unique optical devices. The successful fabrication of germanosilicate and boron co-doped flat fibre samples has been demonstrated and UV-written waveguide channels have been characterised.

The propagation loss of a UV-written optical waveguide in a Ge:Si flat fibre sample has been measured as <0.4 $dB.cm^{-1}$ using the cut-back method. It was acknowledged that this value is higher than that reported by Svalgaard et al. [15] of 0.2 $dB.cm^{-1}$, and the discrepancy was attributed to non-optimised UV-writing conditions. However, a more recent measurement of the loss in a B:Ge:Si flat fibre reveals a figure of 0.12 $dB.cm^{-1}$ [25]. The material loss in a (non UV-written) flat fibre sample was also measured using the cut-back method, and the result of 0.01 $dB.cm^{-1}$ is lower than that reported for an optimised FHD glass sample [11].

The core deposition and fibre drawing processes for flat fibre have been investigated with respect to the resultant dopant composition and fibre geometry. Properties of the core glass, such as its refractive index, photosensitivity, and thermal expansion coefficient, have been investigated and the design parameters were discussed. Practical limits were observed with regards to the maximum dopant concentration that could be attained, and non-uniformity was observed in the illumination from a UV-written waveguide highlighting the detrimental effects of a high dopant concentration. The drawing parameters were investigated and it was shown how they influence the final size and geometry of flat fibre. A basic geometric model was derived to calculate the range of flat fibre sizes that were possible using the current equipment, and also to understand the practical limitations on the glass size and flexibility.

The primary device application for flat fibre was optical sensing. It was envisaged that the unique attributes of flat fibre could be utilised for producing functional waveguiding circuits on a substrate that was not constrained by length or rigidity. As the work presented in this chapter mainly focussed on the fabrication technique and a proof-of-concept, the majority of the device implementation was conducted by the Planar Optical Materials group. This preliminary work was summarised. During the development of flat fibre there was also intense interest from other researchers and institutions. In particular, the work presented in subsections 6.3.1 and 6.3.2 is being continued by the University of Malaysia to explore the potential applications for flat fibre technology [26]. Furthermore, the work on flat fibre has generated commercial interest and has led to a European patent which has now been licensed [5].

6.5 References

1. A.S. Webb, F.R. Mahamd Adikan, J.K. Sahu, R.J. Standish, C.B.E. Gawith, J.C. Gates, P.G.R. Smith, and D.N. Payne. "MCVD planar substrates for UV-written waveguide devices". *Electronics Letters*, 43(9): 517-519, (2007).
2. S.E. Miller. "Integrated optics: Introduction". *Bell Syst. Tech. J.*, 48(7): 2059-2069, (1969).
3. M. Svalgaard, C.V. Poulsen, A. Bjarklev, and O. Poulsen. "Direct UV writing of buried singlemode channel waveguides in Ge-doped silica films". *Electronics Letters*, 30(17): 1401, (1994).
4. G.D. Emmerson, C.B.E. Gawith, I.J.G. Sparrow, R.B. Williams, and P.G.R. Smith. "Physical observation of single step UV-written integrated planar Bragg structures and their application as a refractive-index sensor". *Applied Optics*, 44(24): 5042, (2005).
5. A.S. Webb, M.F.R. Adikan, J.K. Sahu, C.B.E. Gawith, P.G.R. Smith, and D.N. Payne, *Method of fabricating a planar substrate having optical waveguides*. (Patent Number WO2008035067), 2007.

6. S. Ambran, C. Holmes, J.C. Gates, A.S. Webb, J.K. Sahu, and P.G.R. Smith. "UV-written Bragg gratings in a flat-fiber platform as a bending and twisting sensor." in *Conference on Lasers and Electro-Optics Europe and Quantum Electronics Conference, May 22 - 26, Munich, Germany*. (2011).
7. I.J.G. Sparrow. "Development and applications of UV written waveguides". *Optoelectronics Research Centre*, PhD Thesis, (2005).
8. Y. Wu, H. Xin, L. Zhang, Z. Zhuo, Y. Yu, W. Zheng, G. Liu, and Y. Zhang. "Fabrication of planar optical waveguide material on silicon by flame hydrolysis deposition." in *Proceedings SPIE - Optoelectronics, Materials, and Devices for Communications, China*. 251, (2001).
9. M. Kawachi, M. Yasu, and T. Edahiro. "Fabrication of SiO2-TiO2 glass planar optical waveguides by flame hydrolysis deposition". *Electronics Letters*, 19(15): 583-584, (1983).
10. S.P. Watts. "Flame hydrolysis deposition of photosensitive silicate layers suitable for the definition of waveguiding structures through direct ultraviolet writing". *Optoelectronics Research Centre*, PhD Thesis, (2002).
11. P. Tandon and H. Boek. "Experimental and theoretical studies of flame hydrolysis deposition process for making glasses for optical planar devices". *J. Non-Cryst. Solids*, 317(3): 275-289, (2003).
12. M. Svalgaard and K. Færch. "High index contrast UV-written waveguides." in *European Conference on Integrated Optics (ECIO'05), Grenoble, France*. 522-524, (2005).
13. G.D. Emmerson, S.P. Watts, C.B.E. Gawith, V. Albanis, M. Ibsen, R.B. Williams, and P.G.R. Smith. "Fabrication of directly UV-written channel waveguides with simultaneously defined integral Bragg gratings". *Electronics Letters*, 38(24): 1531-2, (2002).
14. M.F.R. Adikan, A.S. Webb, C.B.E. Gawith, J.C. Gates, J.K. Sahu, P.G.R. Smith, and D.N. Payne. "First demonstration of direct UV written Bragg gratings in collapsed fobre planar samples." in *32nd European Conference and Exhibition on Optical Communication ECOC, Cannes, France*. (2006).

15. M. Svalgaard and M. Kristensen. "Directly UV written silica-on-silicon planar waveguides with low loss". *Electronics Letters*, 33(10): 861-863, (1997).

16. A. Gur’yanov, M. Salganskii, V. Khopin, M. Bubnov, and M. Likhachev. "GeO2-rich low-loss single-mode optical fibers". *Inorganic Materials*, 44(3): 278-284, (2008).

17. Y.Y. Huang, A. Sarkar, and P.C. Schultz. "Relationship between composition, density and refractive index for germania silica glasses". *J. Non-Cryst. Solids*, 27(1): 29-37, (1978).

18. D. Zauner, M. Svalgaard, and M. Kristensen. "Directly UV written silica-on-silicon planar waveguides with low insertion loss." in *Proceedings of the Optical Fiber Communication Conference*, *Feb 22-27*, *San Jose, CA*. 149-150, (1998).

19. L.G. Van Uitert, D.A. Pinnow, J.C. Williams, T.C. Rich, R.E. Jaeger, and W.H. Grodkiewicz. "Borosilicate glasses for fiber optical waveguides". *Materials Research Bulletin*, 8(4): 469-476, (1973).

20. D.L. Williams, B.J. Ainslie, J.R. Armitage, R. Kashyap, and R. Campbell. "Enhanced UV photosensitivity in boron codoped germanosilicate fibres". *Electronics Letters*, 29(1): 45, (1993).

21. S. Yoo, A.S. Webb, A.J. Boyland, R.J. Standish, A. Dhar, and J.K. Sahu. "Linearly polarized ytterbium-doped fiber laser in a pedestal design with aluminosilicate inner cladding". *Laser Physics Letters*, 8(6): 453-457, (2011).

22. N.P. Bansal and R.H. Doremus, *Handbook of glass properties.* Academic Press. (1986).

23. S. Hopland. "Removal of the refractive index dip by an etching method". *Electronics Letters*, 14(24): 757-759, (1978).

24. C. Holmes, F.R.M. Adikan, A.S. Webb, J.C. Gates, C.B.E. Gawith, J.K. Sahu, P.G.R. Smith, and D.N. Payne. "Evanescent field sensing in novel flat fiber." in *Conference on Quantum Electronics and Laser Science Conference on Lasers and Electro-Optics, CLEO/QELS, San Jose, CA, United states*. (2008).

25. S. Ambran, H.L. Rogers, A.S. Webb, J.C. Gates, C. Holmes, P.G.R. Smith, and J.K. Sahu, *A loss comparison of flat-fibre and silica-on-silicon direct UV written*

waveguides using a novel Bragg grating measurement technique, in *Photon 10*. 2010: University of Southampton, Southampton.

26. F. Mahamd Adikan, S. Sandoghchi, W. Chong, R. Simpson, M. Mahdi, A. Webb, J. Gates, and C. Holmes. "Direct UV Written Optical Waveguides in Flexible Glass Flat Fiber Chips". *Selected Topics in Quantum Electronics, IEEE Journal of*, PP(99): 1-1, (2011).

Chapter 7

Conclusions and Future Work

7.1 Introduction

The aims of this thesis have been met through the development of four novel fabrication techniques for silica preforms and fibres. Details of the techniques have been described and example fibre devices have been demonstrated. Conclusions from the work are provided here and the possible directions for future research are outlined based on a continuation of the current themes.

7.2 In-situ solution doping technique

An in-situ solution doping technique has been developed for producing multilayered rare-earth (RE)-doped preforms suitable for fibre laser applications. A geometrical model of the layer deposition process was derived in order to calculate the fabrication requirements of preforms with complex refractive index profiles (RIP). The influence that the substrate tube dimensions and precursor flow rates had on the final preform RIP were established, and the implications of these findings was experimentally verified.

The potential of the in-situ solution doping technique for producing multiple RE-doped layers was demonstrated with a large-core fibre suitable for large-mode area (LMA) applications. The fibre comprised of ten Yb-doped layers which was, at the time of fabrication, limited only by a gradual collapse in the substrate tube during the high-temperature sintering passes. However, with control over the internal tube pressure, as is now possible on the current MCVD system, it is expected that tens of RE-doped layers can be achieved. Theoretical calculations predict that a in-situ solution doped preform core diameter of around 5 mm is entirely possible in a reasonable timescale. Any further scaling of the diameter is likely to be limited only by practical issues, such as time constraints, or the diminishing return of depositing multiple layers (i.e. each layer that is deposited contributes less to the overall core diameter than the previous layer).

The geometrical model was implemented when fabricating selectively-doped pedestal RIP preforms. These consisted of an Yb-doped core and an aluminosilicate (Al:Si) inner-cladding, which was favoured over germanosilicate (Ge:Si) or phosphosilicate (P:Si), and produced a glass preform which was tolerant to post-processing. This unique approach was exploited for fibre structures that featured a non-circular inner-cladding. More investigation is needed to assess whether removing the circular symmetry of the inner-cladding can enhance the pump absorption efficiency, although it is expected to be important in fibres with a larger inner-cladding diameter. Future work relating to pedestal RIP fibres will be based on a P:Si host glass for the Yb-doped core in order to mitigate possible photodarkening effects at high powers. Soot layers that are P-doped are more sensitive to the burner temperature than pure silica, and further optimisation will be required, but the lower sintering temperature of the soot will allow an increased number of layers to be deposited without significant tube collapse.

7.3 Chemical-in-crucible process

The vapour-phase deposition of RE ions in fibre-preforms has been demonstrated using a novel chemical-in-crucible (CIC) process. Modifications were made to the standard MCVD setup which allowed the dopant precursor source to be situated within the substrate glassware and transported directly to the reaction-zone in the vapour-phase. Yb-doped preforms with a concentration of up to 25,000 ppm (by weight) were achieved using an organometalic Yb(TRIS) precursor. Passively-doped preforms were fabricated using $AlCl_3$, and a maximum concentration of 16.5 mol% was achieved using a crucible temperature of 190 °C. Characterisation of the Al:Si fibres is still required to ascertain the optical loss and OH impurity.

The optical loss measured in fibres doped using Yb(TRIS) was found to be higher than expected at near-infrared wavelengths, and the relatively low purity of commercially available Yb(TRIS) was cited as a possible cause. Further work will examine the use of alternative precursors, and in particular, anhydrous ytterbium chloride ($YbCl_3$), which was identified in subsection 4.3.3. The intrinsically low vapour pressure of $YbCl_3$ (10 kPa at 1000 °C) will require the chemical to be heated to several hundred degrees Celsius to produce sufficient vapour. Preliminary work has begun on a high temperature crucible design and early trials suggest that the high temperature regime that is required can be implemented into the current CIC setup. Experimental work is on-going to assess whether the vapour from precursors such as $YbCl_3$ can be transported efficiently to the substrate tube without condensing and oxidising prematurely.

Further studies on Yb-doped P:Si preforms will also explore the use of an Al:Si inner-cladding to achieve a pedestal RIP which is tolerant to post-processing of the glass. This will necessitate dual heated crucibles inside the glassware so that the vapour from $AlCl_3$ and Yb(TRIS) can be delivered simultaneously.

7.4 Suspended-core holey fibre

A straightforward fabrication technique for producing silica suspended-core holey fibre (SC-HF) has been presented. Using computer simulation, the air-filling fraction of the fabricated fibre was predicted to be up to 30 % (for a core size of 0.8 μm). The high overlap of the propagating light with the air-holes was employed to demonstrate gas sensing using the SC-HF, and an all-fibre acetylene-filled gas cell was realised. The difficulties in splicing SC-HF to conventional solid core fibre were overcome and the methods used are reported.

A novel fabrication technique for Ge-doped SC-HF was also presented. The fibre exhibits the same high air-filling fraction as the undoped SC-HF, and the structure is achieved by defining the holes within the core region of a doped preform. The fibre features a small-diameter core, but upon collapse of the holes it retains a larger diameter high-index region that is compatibility with conventional solid core fibre. A sample gas can be straightforwardly trapped in the fibre by intentionally collapsing the air-cladding using a commercial fusion splicer. Although, only a few short lengths of Ge-doped SC-HF were produced, due to the preform cracking during the drilling process, future research will continue this work using an Al-doped preform which should be tolerant to ultrasonic drilling. The preform will be fabricated initially using the in-situ solution doping technique, and a ~5 mm core will be targeted. The merits of a SC-HF with a doped core will be demonstrated by constructing an all-fibre gas cell and testing its long-term stability.

7.5 Flat fibre

A novel fabrication route has been presented for producing extended lengths of planar glass substrates using MCVD and conventional fibre drawing equipment. In combination with direct UV-writing, flat fibre can be used as a platform for multifunctional waveguiding devices that are mechanically flexible. Straight and splitting waveguide channels as well as Bragg gratings have all been demonstrated in flat fibre samples that have a highly-doped Ge:Si core.

The fabrication issues and considerations pertaining to the photosensitivity of the core layer were discussed, as well the physical dimensions of flat fibre that can be currently drawn. In particular, those areas relating to the composition of the core glass will be investigated as part of future work. These include: enhancing the photosensitivity through optimisation of B- and Ge-doping, increasing the aspect ratio of the flat fibre to enlarge the usable area for UV-writing, and refractive index matching of the deposited layer to that of the undoped silica cladding to improve compatibility with conventional optical fibre.

The potential of flat fibre for sensing applications was discussed, and the progress in realising an evanescent-field sensor was summarised. The concept of a long flexible flat fibre sensor with detection ‘windows’ distributed along the length and integrated optical waveguides circuits was envisaged, although this has not yet been realised. Preliminary trials to introduce detection windows in flat fibre samples have been conducted using reactive ion etching (RIE). This method appears to be a suitable way to remove a few tens of microns of silica glass over-cladding with an accurate control over the etch depth. This route will be followed in future work, as well as methods to reduce the over-cladding thickness of the flat fibre samples. It will also be necessary to reduce the waveguiding loss to allow long lengths of flat fibre samples to be used. This will be addressed primarily through optimisation of the UV-writing parameters.

Appendix A

Publications

A.1 Journal articles specific to thesis

Linearly polarized ytterbium-doped fiber laser characterised by a pedestal design and aluminosilicate inner cladding.
S. Yoo, A. S. Webb, A. J. Boyland, R. J. Standish, A. Dhar, J. K. Sahu.
Laser Physics Letters, 8(6), 453-457, (2011).

Optical fiber fabrication using novel gas phase deposition technique.
A. J. Boyland, A. S. Webb, S. Yoo, R. J. Standish, J. K. Sahu.
Journal of Lightwave Technology, 29(6), 912-915, (2011).

MCVD in-situ solution doping process for the fabrication of complex design large core rare-earth doped fibers.
A. S. Webb, A. J. Boyland, R. J. Standish, S. Yoo, J. K. Sahu, D. N. Payne.
Journal of Non-Crystalline Solids, 356(18-19), 848-851 (2010).

Suspended-core holey fiber for evanescent-field sensing.

A. S. Webb, F. Poletti, D. J. Richardson, J. K. Sahu.

Optical Engineering Letters, Vol. 46(010503-2), 1-3 (2007).

MCVD planar substrates for UV-written waveguide devices.

A. S. Webb, M. F. R. Adikan, J. K.Sahu, R. J. Standish, C. B. E. Gawith, J. C. Gates, P. G. R. Smith, D. N. Payne.

Electronics Letters, Vol.43(9), 517-519, (2007).

A.2 Conferences proceedings specific to thesis

Polarization-maintaining ytterbium-doped fibre with an aluminosilicate Inner-cladding fabricated using In-situ Doping Technique.

S. Yoo, A. S. Webb, A. J. Boyland, R. J. Standish, J. K. Sahu.

CLEO/Europe-EQEC 2011, Munich, Germany, 22-26 May, CJ2.4.

In-situ Solution Doping Technique for novel geometry rare-earth doped fiber fabrication.

A. S. Webb, A. J. Boyland, R. J. Standish, D. Lin, S. Alam and J. K. Sahu.

CLEO/QELS 2010, San Jose, CA, 16-21 May, JTuD35.

Rare-earth doped optical fiber fabrication using novel gas-phase deposition technique.

A. J. Boyland, A. S. Webb, M. P. Kalita, S. Yoo, C. A. Codemard, R. J. Standish, J. Nilsson and J. K. Sahu.

CLEO/QELS 2010, San Jose, CA, 16-21 May, CThV7.

First demonstration of direct UV written Bragg gratings in collapsed fibre planar samples.

M. F. R. Adikan, A. S. Webb, C. B. E. Gawith, J. C. Gates, J. K. Sahu, P. G. R. Smith, D. N. Payne.

ECOC 2006, Cannes, France, 24-28 Sep.

A.3 Published patents

Method of fabricating a planar substrate having optical waveguides.

A. S. Webb, M. F. R. Adikan, J. K. Sahu, R.J. Standish, C. B. E. Gawith, J. C. Gates, P. G. R. Smith, and D. N. Payne.

European Patent 2064158 B1 (WO 2008/035067), Filing Date 18/09/07.

A.4 Magazine articles

Fiber and Preform Fabrication: Novel fiber fabrication methods benefit fiber lasers.

M. P. Kalita, A. S. Webb, A. J. Boyland, S. Yoo, J. K. Sahu.

Laser Focus World, 46(11), 63-65, (2010).

Flat Fibre: A more flattering light.

The Engineer, March 2007, page 12

Flat Fibre: Best of both worlds.

Materials World, May 2007, page 5

Flat optical fibre is good for networks.

Engineering Weekly, February 2007

A.5 Other publications

Erbium-doped multi-element fiber amplifiers for space-division multiplexing operations.

S. Jain, T.C. May-Smith, A. Dhar, A. S. Webb, B. Usmani and J.K. Sahu.

Optics Letters - submitted.

Gain and noise figure study of Er-doped multi-element fiber amplifier.

S. Jain, T.C. May-Smith, A. Dhar, A. S. Webb, B. Usmani and J.K. Sahu.

Asia Communications and Photonics Conference (ACP) Guangzhou, China, 7-10 November 2012 ATh2A.1.

Tandem-pumped ytterbium-doped aluminosilciate fiber amplifier with low quantum defect.

T. Yao, J. Ji, J. K. Sahu, A. S. Webb, J. Nilsson.

CLEO-QELS 2012 San Jose, CA, 6-11 May.

Q-switched neodymium-doped $Y_3Al_5O_{12}$ based silica fiber laser.

S. Yoo, A. S. Webb, R. J. Standish, T. C. May-Smith, and J. K. Sahu.

Optics Letters, Vol.37(12), 2181-2183, (2012).

5.4 W cladding-pumped Nd:YAG silica fiber laser.

S. Yoo, A. S. Webb, R. J. Standish, T. C. May-Smith, J. K. Sahu

CLEO/Europe-EQEC 2012 San Jose, CA, 6-11 May, CM2N.2

Fabrication of a multimode interference device in a low loss flat-fiber platform using physical micromachining technique.

S. Ambran, C. Holmes, J. C. Gates, A. S. Webb, M. F. R. Adikan, P. G. R. Smith, J. K. Sahu.

Journal of Lightwave Technology, Vol. 30(17), 2870-2845 (2012).

Direct UV-written optical waveguides in flexible glass flat fiber chips.

M. F. R. Adikan, S. Sandoghchi, W. Chong, R. Simpson, M. Mahdi, A. S. Webb, J. C. Gates, C. Holmes.

IEEE Journal of Selected Topics in Quantum Electronics, Vol. 18(5), 1534-1539, (2011).

Fibers for high-power lasers and amplifiers.

J. K. Sahu, S. Yoo, A. Boyland, A. S. Webb.

OECC 2011, Kaohsiung, Taiwan, 7 July, 7C1_3.

UV-written Bragg gratings in a flat-fiber platform as a bending and twisting sensor.

S. Ambran, C. Holmes, J. C. Gates, A. S. Webb, J. K. Sahu, P. G. R. Smith.

CLEO/Europe-EQEC 2011, Munich, Germany, 22-26 May.

Temperature effect on the Brillouin gain spectra of highly doped aluminosilicate fibers.

F. H. Mountfort, S. Yoo, A. J. Boyland, A. S. Webb, J. Nilsson, J. K. Sahu.

CLEO/Europe-EQEC 2011, Munich, Germany, 22-26 May, CE.P.23.

Liquid-nitrogen-cooled high-concentration erbium-doped fibre laser.

R. Steinborn, T. F. Yao, A. S. Webb, J. K. Sahu, J. Nilsson.

CLEO/Europe-EQEC 2011, Munich, Germany, 22-26 May, CJ6.3.

Ytterbium-doped Y_2O_3 nanoparticle silica optical fibers for high power fiber lasers with suppressed photodarkening.

S. Yoo, M. P. Kalita, A. J. Boyland, A. S. Webb, R. J. Standish, J. K. Sahu, M. C. Paul, S. Das, S. K. Bhadra.

Optics Communications, Vol. 283(18), 3423-3427, (2010).

Micromachined multimode interference device in flat-fibre.

S. Ambran, C. Holmes, J. C. Gates, A. S. Webb, M. F. R. Adikan, P. G. R. Smith, J. K. Sahu.

Photonics Global Conference 2010, Singapore, 14 – 16 Dec.

A loss comparison of flat-fibre and silica-on-silicon direct UV written waveguides using a novel Bragg grating measurement technique.

S. Ambran, H. L. Rogers, A. S. Webb, J. C. Gates, C. Holmes, P. G. R. Smith, J. K. Sahu.

Photon 2010, Southampton, UK, 23-26 Aug.

Ytterbium-doped Low-NA P-Al-silicate large-mode-area fiber for high power applications.

J. K. Sahu, S. Yoo, A. J. Boyland, A. S. Webb, C. Codemard, R. J. Standish, J. Nilsson.

CLEO/QELS 2010, San Jose, CA, 16-21 May, CTuP3.

Ytterbium-doped nano-crystalline optical fiber for reduced photodarkening.

S. Yoo, M. P. Kalita, A. J. Boyland, A. S. Webb, R. J. Standish, and J. K. Sahu.

CLEO/QELS 2010, San Jose, CA, 16-21 May, JWA98.

Near-diffraction-limited supercontinuum generation in a cladding-pumped nonlinear fiber converter.

J. Ji, C. Codemard, A. S. Webb, J. K. Sahu, J. Nilsson.

CLEO/QELS 2010, San Jose, CA, 16-21 May, CMM5.

Modification of spectroscopic properties of Bismuth doped silica fiber by post-fabrication process and different fabrication methods.

M. P. Kalita, S. Yoo, A. S. Webb, R. J. Standish, M. Ibsen, J. K. Sahu.

OFC 2010, San Diego, CA, 21-25 Mar, OMG2.

Ytterbium-doped nanostructured optical fibers for high power fiber lasers.
J. K. Sahu, M. C. Paul, M. P. Kalita, A. J. Boyland, C. Codemard, S. Yoo, A. S. Webb, R. J. Standish, J. Nilsson, S. Das, S. K. Bhadra, M. Pal, A. Dhar, R. Sen.
CLEO/Europe-EQEC 2009, Munich, Germany, 14-19 Jun, CJ2.1.

Influence of temperature on the post-irradiation temporal loss evolution in Yb-doped aluminosilicate fibers photodarkened by 488nm CW irradiation.
C. Basu, S. Yoo, A. J. Boyland, A. S. Webb, C. L. Sones, J. K. Sahu.
CLEO/Europe-EQEC 2009, Munich, Germany, 14-19 Jun CJ1.2.

Fiber design for high power fiber lasers.
J. K. Sahu, S. Yoo, A. J. Boyland, A. S. Webb, M. Kalita, J. N. Maran, Y. Jeong, J. Nilsson, W. A. Clarkson, D. N. Payne.
Photonics West 2009, San Jose, CA, 24-29 Jan, 7195-17 (Invited).

Advances in active fibres for high-power and high-brightness fibre sources.
J. K. Sahu, S. Yoo, A. J. Boyland, A. S. Webb, M. Kalita, Y. Jeong, J. Nilsson, D. N. Payne.
Photonics 2008, New Delhi, India, 13-17 Dec (Invited).

High power tunable Er-Yb ribbon fibre laser.
J. W. Kim, A. J. Boyland, A. S. Webb, J. K. Sahu, W. A. Clarkson.
Europhoton Conference (EP 2008), Paris, France, 30 Aug - 5 Sep, TUoC4.

Evanescent field sensing in novel flat fiber.
C. Holmes, M. F. R. Adikan, A. S. Webb, J. C. Gates, C. B. E. Gawith, J. K. Sahu, P. G. R. Smith, D. N. Payne.
CLEO/QELS 2008, San Jose, CA, 4-9 May, CMJJ3.

488 nm irradiation induced photodarkening study of Yb-doped aluminosilicate and phosphosilicate fibers.

J. K. Sahu, S. Yoo, A. J. Boyland, M. P. Kalita, C. Basu, A. S. Webb, C. L. Sones, J. Nilsson, D. N. Payne.

CLEO/QELS 2008, San Jose, CA, 4-9 May.

Direct UV written waveguides and Bragg gratings in novel substrates.

J. C. Gates, C. Holmes, A. S. Webb, M. F. R. Adikan, C. B. E. Gawith, J. K. Sahu, P. G. R. Smith.

Photonex Exhibition and Conference 2007, Coventry, UK, 17 Oct.

Recent developments in direct-UV-written planar waveguides, gratings, sensors and substrates.

M. F. R. Adikan, J. C. Gates, A. S. Webb, H. E .Major, C. Holmes, M. A. G. Ramirez, B. D. Snow, D. O. Kundys, C. B. E. Gawith, P. G. R. Smith.

ECIO 2007, Copenhagen, Denmark, 25-27 Apr.

Flat fiber - the flexible format for distributed lab-on-a-chip.

C. B. E. Gawith, A. S. Webb, M. F. R. Adikan, J. C. Gates, J. K.Sahu, P. G. R. Smith.

SPIE Europe Optics & Optoelectronics Conference 2007, Prague, 16-20 Apr.

Progress in active fibers.

J. K. Sahu, S. Yoo, J. Kim, A. J. Boyland, A. S. Webb, J. Nilsson, Y. Jeong, D. J. Richardson, D. N. Payne.

OFC 2007, Anaheim, CA, 25-29 Mar 2007, OWA3 (Invited).

High-power and high-brightness fiber sources.

J. K. Sahu, J. Nilsson, Y. Jeong, J. Kim, P. Dupriez, S. Yoo, A. J. Boyland, A. S. Webb, D. N. Payne.

Photonics 2006, Hyderabad, India, 13-16 Dec (Invited).

Opportunities in high-power fiber lasers.

J. K. Sahu, J. Kim, S. Yoo, A. S. Webb, C. Codemard, P. Dupriez, Y. Jeong, J. Nilsson, D. J. Richardson, D. N. Payne.

Proceedings of SPIE - Active and Passive Optical Components for Communications VI, Vol. 6389, Massachusetts, 1-4 Oct 2006 (Invited).

Novel fabrication method of highly-nonlinear silica holey fibres.

K. Mukasa, M. N. Petrovich, F. Poletti, A. S. Webb, J. R. Hayes, A. Van Brakel, R. Amezcua-Correa, L. Provost, J. K. Sahu, P. Petropoulos, D. J. Richardson.

CLEO/QELS 2006, Long Beach, CA, 21-25 May, CMC5.

Appendix B

Fabrication Summary

B.1 Chapter 3

The table below details the full list of fabricated preforms and fibres pertaining to the experimental work on in-situ solution doping reported in Chapter 3. (For brevity, the dopant solutions containing $AlCl_3.H_2O$ or $YbCl_3.H_2O$ are abbreviated to Al and Yb, respectively, and unless otherwise stated, are dissolved in 200 ml of methanol. Where multiple layers were used, the solution concentration for each layer is detailed and refers to an un-doped silica soot unless stated as being phosphosilicate, P:Si).

Preform number	Target preform profile	Number of core layers	Core dopant solution	Number of inner-cladding layers	Inner-cladding dopant solution	Fibre number
L30089	Process test	2	4g Al/2g Yb	-	-	T0117
L30096	Graded index	3	4g Al/2.2g Yb 4g Al/2.2g Yb 4g Al/2.4g Yb	-	-	T0130
L30097	Pedestal	1	20g Al/4g Yb	3	45g Al (450 ml)	T0134

Preform number	Target preform profile	Number of core layers	Core dopant solution	Number of inner-cladding layers	Inner-cladding dopant solution	Fibre number
L30102	Graded index	4	2g Al/1g Yb 3g Al/1g Yb 4g Al/1g Yb 5g Al/1g Yb	-	-	T0150
L30108	Process test	1 (P:Si)	6g Al/4g Yb	-	-	T0174
L30133	Large core	3	1g Al/1g Yb	-	-	T0193
L30135	Pedestal	1	10g Al/3.6g Yb	1	10g Al	-
L30152	Large core	10	2.5g Al/2.5g Yb (1000 ml)	-	-	-
L30153	Large core	3	2.5g $AlCl_3$ 2.5g $YbCl_3$ (1000 ml)	-	-	-
L30154	Large core	10	2.5g Al/2.5g Yb (1000 ml)	-	-	T0215
L30163	Pedestal	1	12g Al/4g Yb	5	12g Al	T0240 T0244 T0251
L30169 (failed)	Pedestal	1	16g Al/4g Yb	5	16g Al	No preform
L30171 (failed)	Process test	1	16g Al/4g Yb	5	16g Al	No preform
L30172	Process test	1	10g Al/2g Yb	-	-	T0257
L30182	Pedestal	1	12g Al/4g Yb	2	15g Al	-
L30183	Pedestal	1	12g Al/4g Yb	5	15g Al	-
L30184	Pedestal	1	12g Al/4g Yb	14	15g Al	T0283 T0285
L30186	Soot temp comparison	1	12g Al/4g Yb	-	-	T0296
L30187	Soot temp comparison	1	12g Al/4g Yb	-	-	T0297
L30190	Bismuth oxide	1	0.8g Bi_2O_3 (200 ml H_2O)	-	-	T0298
L30196	Vertical comparison	1	12g Al/4g Yb	-	-	T0308
L30200	Multiple soots and soakings	10	12g Al/4g Yb	-	-	T0313
L30202	Multiple soots and soakings	5	12g Al/4g Yb	-	-	T0314

Preform number	Target preform profile	Number of core layers	Core dopant solution	Number of inner-cladding layers	Inner-cladding dopant solution	Fibre number
L30206	Process test	1 (P:Si)	4g Al/6g Yb	-	-	T0316
L30207	Process test	5	12g Al/4g Yb	-	-	T0319
L30208	Multiple doping	1 (P:Si)	4g Al/6g Yb	-	-	T0321
L30219	Pedestal	1	12g Al/4g Yb	7	20g Al	-
L30222	Multiple doping	1	12g Al/4g Yb	-	-	T0344 T0345
L30223	Pedestal	1	12g Al/4g Yb	5	20g Al	T0349
L30225	Pedestal	1	12g Al/4g Yb	5	20g Al	T0361

(Fibres were drawn with the assistance of Mr. Robert Standish)

B.2 Chapter 4

The table below summarises the preforms and fibres fabricated using the chemical-in-crucible process. (The crucible type (A, B, C or D) refers to those shown in Figure 4.4, and the process flow rates of $SiCl_4$ and $POCl_3$, in ml.min^{-1}, are abbreviated to Si and P, respectively, for conciseness).

Preform number	Fibre number	Crucible temperature (°C) and type	Dopant precursor	Reagents flow (sccm)	Remarks
L30083	-	377 (A)	Al(TRIS)	Si (200)	No conclusive index rise
L30085	-	210 (A)	Al(TRIS)	Si (50)	No conclusive index rise
L30094	T0124 T0137	343 (A)	Yb(TRIS)	P:Si (100:100)	-
L30099	-	284-409 (A)	$YbCl_3H_2O$/ $AlCl_3H_2O$	Si (200)	To confirm theory
L30101	T0145	228 (A)	Yb(TRIS)	P:Si (50:25)	White core
L30104	T0169	284 (A)	F:Yb(TRIS)	P:Si (200:25)	White core
L30105	-	199 (A)	Yb(TRIS)	P:Si (100:25)	Vapour ignited

Preform number	Fibre number	Crucible temperature (°C) and type	Dopant precursor	Reagents flow (sccm)	Remarks
L30110	T0168	332 (A)	Er:Yb(TRIS)	P:Si (100:25)	Vapour ignited. White core
L30114	T0171	230 (A)	$AlCl_3$	Si (100)	Partially white core
L30156	T0216	235 (B)	Yb(TRIS)	P:Si (200:50)	White core
L30157	T0220	400 (A)	$BiCl_3$	P:Si (200:100)	-
L30159	T0221	20% (B)	Yb(TRIS)	P:Si (600:300)	Blue colouring in core
L30168	T0246	230 (D) w/o fb	Yb(TRIS)	P:Si (500:200)	-
L30193	T0299 T0300 T0383	200 (D)	Yb(TRIS)	P:Si (450:150)	-
L30194	T0302 T0303 T0327	250 (D)	Yb(TRIS)	P:Si (450:150)	-
L30258	A0003 A0067	170 (D)	$AlCl_3$	Si (200)	-
L30259	A0004	140 (D)	$AlCl_3$	Si (200)	-
L30260	-	190 (D)	$AlCl_3$	Si (200)	-

(Fibres were drawn with the assistance of Mr. Robert Standish)

B.3 Chapter 5

The table below lists the capillaries and fibres fabricated in Chapter 5. All details were included in the chapter itself but are repeated here for completeness.

Capillary number	Substrate glass	Drilling parameters	Capillary diameter	Remarks
F0595[#]	HLQ-210 rod 18 mm dia.	$r = 2.5$ mm $d_{sep} = 0.5$ mm	1.5 mm	First proof-of-concept capillary
F0648[#]	F300 rod 20 mm dia.	$r = 4$ mm $d_{sep} = 0.5$ mm	1.9 mm	Reduced outer wall thickness
T0252[*]	Ge:Si preform (LIEKKI) 15 mm dia.	$r = 1.5$ mm $d_{sep} = 0.5$ mm	1.5 mm	Glass cracked significantly during ultrasonic drilling
T0256[*]	F300 rod 15 mm dia.	$r = 2.25$ mm $d_{sep} = 0.3$ mm	1.2 mm	Establishing process parameters on new equipment

Fibre number	Cladding tube	Capillary used	Fibre diameter	Remarks
F0597[#]	F300 8.5 × 3.2 mm	F0595	~125 µm	Initial proof-of-concept SC-HF
F0656[#]	F300 8.5 × 3.2 mm	F0648	~125 µm	Exploring pressurisation to expand strut length
F0753[#]	F300 6.9 × 3.5 mm	F0595	~125 µm	Process optimisation
F0793[#]	F300 12 × 4.8 mm	F0595	125 µm	Draw of SC-HF for characterisation and analysis
T0257[*]	CFQ 8 × 4.2 mm	T0256	125 µm	Establishing process parameters on new equipment
T0262[*]	CFQ 8 × 4.2 mm	T0256	125 µm	Establishing process parameters on new equipment
T0265[*]	F300 tube 8 × 4 mm	T0252	125 µm	Draw of Ge:Si core capillary

[#]all/partially lost in fire, [*]fabricated post-fire

B.4 Chapter 6

The table below lists the capillary and fibres pertaining to the experimental work presented in Chapter 6.

Capillary number	Substrate glass	Drilling parameters	Notes
*G2046	ORC lathe 2	Ge-doped tube preparation	3 core layers Ge:Si = 10:1
*F0651-G2046	ORC 5m tower	Investigation of drawing parameters	Furnace = 2050 °C Applied vaccum 0 to -100 mbar
*LN0025	ORC lathe 2	Ge-doped tube preparation	10 core layers Ge:Si = 1:1
*F0673-LN0025	ORC 5m tower	Investigation of drawing parameters	Furnace = 1990 °C Applied vacuum -10 mbar
*LN0028	ORC lathe 2	Ge-doped tube preparation	3 core layers Ge:Si = 2:1 Pre-core collapse
*F0764-LN0028	ORC 5m tower	Investigating the collapse sequence	Furnace = 1970 °C Applied vacuum -15 mbar
L30007	Temp Lathe 3	Ge-doped calibration preform	Ge:Si = 1:1
L30010	Temp Lathe 3	Ge-doped calibration preform	Ge:Si = 2:1
L30011	Temp Lathe 3	Ge-doped calibration preform	Ge:Si = 0.5:1
L30013	Temp Lathe 3	Ge-doped calibration preform	Ge:Si = 3:1
Draw-of-G30000	Temp 12m tower	Investigation of temperature and vacuum	Furnace = 2020 °C Applied vacuum 0 to -60 mbar
Draw-of-G30000	Temp 12m tower	Investigation of furnace temperature	Furnace = 2020 to 2140 °C Applied vacuum -10 mbar
G3003	Temp Lathe 3	Ge-doped tube preparation	3 core layers Ge:Si = 2:1 Pre-core collapse
Draw-of-G30003	Temp 12m tower	Investigation of wall thickness at low temperature	Furnace = 2000 °C and below
G30004	Temp Lathe 3	Investigating deposited layer thickness	3 core layers Ge:Si = 2:1
G30005	Temp Lathe 3	Ge-doped tube preparation	2 core layers Ge:Si = 2:1
G30006	Temp Lathe 3	P-doped tube preparation	2 core layers P:Si = 2:1

Capillary number	Substrate glass	Drilling parameters	Notes
Draw-of-G3005	Temp 12m tower	Investigation of drawing parameters	Furnace = 2020 °C
G30007	Temp Lathe 3	Ge-doped tube preparation	3 core layers Ge:Si = 2:1
G3009	Temp Lathe 3	Collapsing tube on lathe	Various
Draw-of-G3007	Temp 12m tower	Draw of flat fibre for UV-writing	Applied vacuum -10 mbar Feed = 8.4 mm.min^{-1}
G30010	Temp Lathe 3	Ge-doped tube preparation (thin wall)	2 core layers Ge:Si = 2:1
Draw-of-G3010	Temp 12m tower	Samples for UV-writing trials	Applied vacuum 0 to -20 mbar Furnace = 2040 °C
G30012	Temp Lathe 3	P-doped tube preparation	6 core layers P:Si = 2:1
Draw-of- G30012	Temp 12m tower	Investigation of drawing parameters	Applied vacuum 0 to -20 mbar Furnace = 2045 °C
G30021	Temp Lathe 3	Ge-doped rube preparation	3 core layers Ge:Si = 2:1 Pre-core collapse
T0059-G30021	Temp 12m tower	Draw of flat fibre for UV-writing and cut-back measurement	Applied vacuum -30 mbar Furnace = 2060 °C
G30024	Temp Lathe 3	Investigation of thick P-doped core	10 core layers P:Si = 2:1 Pre-core collapse
T0065-G30024	Temp 12m tower	Draw of thick P-doped tube	Applied vacuum -35 mbar Furnace = 2060 °C
G30168	Temp Lathe 3	Boron co-doped trials	3 core layers B:Ge:Si = 1:2:1
L30093	Temp Lathe 3	Trial of collapsing on lathe	2 core layers Ge:Si = 2:1
T0129-L30093	Temp 12m tower	Draw of drilled preform	Furnace = 2070 °C
T0268	Temp 12m tower	Draw of milled preform	Furnace = 2000 °C
T0384	Temp 12m tower	Draw of boron co-doped tube	Applied vacuum -25 mbar Furnace = 2030 °C

Appendix C

Fire Related Issues

C.1 Mountbatten building fire

In October 2005, a major fire at the University of Southampton devastated the ORC's facilities and the Mountbatten building. The cleanroom area that housed the silica optical fibre fabrication equipment was entirely destroyed, along with the preform and fibre samples stored within. The measurement laboratories and offices, included those used by the author, were also badly damaged and they were subsequently demolished together with the rest of the building.

Following the fire, work promptly began to re-house staff and students, and temporary buildings were erected adjacent to the ORC headquarters, providing over a 100 people with much needed office and laboratory space. The Silica Fibre Fabrication group was fortunate enough to be offered the use of cleanroom facilities at an off-site location, and by June 2006 the ability to fabricate preforms and fibre was restored. Both these locations remained home to the author, and the rest of the Silica Group members, until the new Mountbatten building was complete and research in the cleanroom complex could resume in June 2010.

Although the author's PhD studies continued after the Mountbatten fire, the event had a significant impact on the research activities. For example, not all of the equipment previously used was accessible until very recently and as such the research directions and topics followed were largely dictated by the available resources, which may be reflected in the thesis. The key issues that were encountered are summarised below.

1) All preform and fibre samples fabricated by the author prior to October 2005 were lost in the fire. Consequently characterisation of some samples, particularly those fibres pertaining to Chapter 5, remains incomplete.

2) The temporary office and laboratory space in building 47 was a major asset following the fire, however, in reality it took longer than expected to re-order all the necessary measurement equipment and as such research progress was slow.

3) The temporary off-site facilities presented a technical challenge in having to learn the operation of new equipment, as well as re-establishing fabrication processes. In particular, the replacement MCVD system required considerable optimisation and the drawing tower available for use was significant larger, in height, than the 5 m tower used previously at the ORC.

4) Technical challenges were also encountered once the new fabrication equipment was installed into the Mountbatten building. These systems were manufactured by SG Controls (Cambridge, UK), rather than Heathway (NJ, USA) as used previously, and as such time was needed to gain familiarisation with the equipment and the control interface.